A MACRO-SCALE PLASTICITY MODEL FOR HIGH PERFORMANCE FIBER REINFORCED CEMENT COMPOSITES

by

Kittinun Sirijaroonchai

A dissertation submitted in partial fulfillment
of the requirements for the degree of
Doctor of Philosophy
(Civil Engineering)
in The University of Michigan
2009

Doctoral Committee:

Professor Sherif El-Tawil, Chair
Emeritus Professor Antoine E. Naaman
Associate Professor Gustavo J. Parra-Montesinos
Associate Professor John A. Shaw

DEDICATION

To my parents
Jirayuth and Poonsuk Sirijaroonchai

To my brothers and my little sister
Kittisak, Kittidej and Saifon Sirijaroonchai

ACKNOWLEDGMENTS

I always consider myself as a lucky person to have Prof. Sherif El-Tawil as my advisor. His willingness to meet and discuss with me on a daily basis will be what I miss the most. I would also like to acknowledge my committees Prof. Antoine E. Naaman for introducing me to the world of HPFRCC, Prof. Gustavo J. Parra-Montesinos for providing me test data, and Prof. John Shaw for teaching me how to solve $\frac{\partial J_2}{\partial \boldsymbol{\sigma}}$ (without this tensor, it would be impossible for me to solve plasticity problem).

The author would also like to thank technicians of the Structural Engineering Laboratory, Robert Spence, Robert Fischer, and Jan Pantolin for helping me with the tests. Thanks are also due to Prof. James LaFave and his students Adrianne Wheeler and Ray Foltz of University of Illinois at Urbana-Champaign for helping me with the biaxial tests.

Special Thanks to his colleagues Dr. Visit Likhitruangsilp, Dr. Kulsiri Chandrangsu, Supat Suwannakarn, and Remy Lequesne for their help during this study; his officemates Dr. Kapil Khandelwal, Dr. Ekin Ekiz, Chung-Chan Hung, Dongjoo Kim, and Philip Park and his fellow friends Chachrist Srisuwanrat, Monthian Setkit, Thaweesak Jirathanathaworn, and Thiradet Jiarasuksakun for their friendship and helping throughout this study.

Last but not least, I would like to dedicate this work to my family, who always give me unconditional love and encouragement. I would not come this far without your guys.

TABLE OF CONTENTS

LIST OF FIGURES

LIST OF TABLES

LIST OF APPENDICES

ABSTRACT

A macro-scale plasticity model for High Performance Fiber Reinforced Cement Composites (HPFRCC) is developed. The proposed model is a phenomenological, multi-axial, constitutive model capable of representing important phenomena associated with HPRFCC response such as tension-related cracking, hardening, and softening as well as compression-related confinement and crushing behavior. The proposed model is based on the results of experiments conducted in this study under various loading conditions in both compression and tension. The material parameters in the experimental program pertain to two types of commercially available fibers, namely Hooked and Spectra fibers, and three fiber volume fractions ranging from 1.0% to 2.0%. Test results reveal that the inclusion of fibers increases ductility in the softening regime in compression and significantly improves ductility and strain hardening in tension, which makes HPFRCC amenable to general plasticity theory. The proposed plasticity model is constructed by modifying an existing model of concrete in compression and extending it to encompass tensile response. A unique feature of the model is that a single yield surface is used to cover both compressive and tensile responses for both hardening and softening regimes. The accumulated effective plastic strain is used as a damage index for controlling the evolution of the plasticity surfaces. To ensure the validity of the proposed model, computational results are compared to results of several structural tests including tests of a two-span continuous beam, a slab subjected to punching loads, a structural wall, and a coupling beam. The model is shown to be able to capture with reasonable accuracy the experimentally observed responses, including load deflection behavior and mode of failure. The proposed model requires modest computational resources compared to existing micro-mechanical models for HPFRCC that explicitly address fiber and matrix responses, and the interaction between them through bond. It can therefore be applied for large-scale computational structural simulations providing a good balance between accuracy, detail, and computational demands.

CHAPTER 1

INTRODUCTION

1.1 Introduction

Cement-based materials such as concrete and mortar are brittle materials that crack under low tensile stress. One common way to mitigate this deficiency is by adding fibers to the matrix. Fiber Reinforced Cement Composites (FRCC) resist tensile stresses through composite action between the cementitious matrix and the embedded fibers. The transmission of forces between these two components occurs through interfacial bond stress defined as the shearing stress between the fiber surface area and the surrounding matrix. Fibers play a major role in the post-cracking behavior of FRCC by bridging the cracks and providing resistance to crack opening. Hence, the FRCC does not fail abruptly after the first crack.

A key characteristic of High Performance Fiber Reinforced Cement Composites (HPFRCC) is that they can achieve quasi-ductile response that is they exhibit strain-hardening response accompanied by multiple cracks and relatively large energy absorption prior to fracture localization. Figure 1.1 shows a comparison of the stress-strain response in tension of both normal FRCC and HPFRCC composites. According to Naaman and Reinhardt (1996), there are two methods to identify if a composite behaves as a high performance material. The first method is to examine the response of the composite in tension. If the post-cracking strength (σ_{pc}) is higher than that at first cracking (σ_{cc}), then the composite is considered to be a high performance material. An alternative method to classify a high performance material is proposed by Tjiptobroto and Hansen (1993). In this method, it is assumed that if the energy needed to form a new crack is less than the energy needed to propagate the crack, then multiple cracking type of failure is more likely to form (Figure 1.1b) and the composite is classified as "high performance." Based on these two methods, several parameters that control the formation of multiple cracks can be identified. These parameters include the total number of fibers in the composites, the strength of the interfacial bond, the toughness of the matrix, and the mechanical properties of the fibers.

At present, HPFRCC technology is still considered to be at an early stage where there is intense interest in material development, testing, and characterization. Analysis formulations are still few compared to more traditional materials, but the rate of development is picking up as the demand of HPFRCC construction grows. Inelastic analysis models for HPFRCCs can be broadly categorized by their resolution in modeling nonlinear behavior as micro-scale models, macro-scale models, and structural-scale model. Micro-scale models describe the interaction among the three phases of the material, i.e. fiber, matrix, and interfacial zones. Macro-scale models, on the other hand, focus on the phenomenological behavior at the point level. The point level in this context is defined as an element that contains several fibers embedded in cement matrix. They are capable of explicitly accounting for key behavior phenomena such as cracking, softening, hardening post-cracking responses, and crushing behavior. Structural-scale models implicitly capture the essence of structural behavior at the domain level, for example, cross-sectional moment versus curvature behavior and panel shear force versus distortion relationships. They are generally favored by practitioners because they are computationally expedient and because they produce data that is intuitive and that deals directly with design variables such as moments, rotations, etc.

1.2 Motivations and Objectives

Since micro-scale models focus on the behavior of the constituents of HPFRCC, they have high computational demands which severely limit their use in analysis applications involving large structures. Structural-scale models can capture only the overall behavior at the domain level, and do not provide detailed enough information about structural behavior. Macro-scale model, however, can provide such details and are more computationally efficient than micro-scale models. Such models can also be practically applied to model structural behavior in the continuum finite element simulations.

With the above motivation, the main objective of this research is to develop a macro-scale, multi-axial constitutive model for High Performance Fiber Reinforced Cement Composites (HPFRCC) that is suitable for application in computational structural simulations. The research program includes both experimental and analytical components that are intended to achieve this objective. The experimental programs include three different types of tests: uniaxial, biaxial, and triaxial tests. After understanding the behavior of HPFRCC through these tests, a macro model will be developed based upon concepts in plasticity. The proposed model is verified against actual structural tests that involved the use of HPFRCC.

1.3 Structure of Dissertation

This dissertation composes of 5 chapters as follows:

Chapter 1: Introduction. This chapter provides an overview of the research. The objectives and a structure of the dissertation are also provided.

Chapter 2: Literature review. This chapter provides background regarding High Performance Fiber Reinforced Cement Composites (HPFRCC) including analytical techniques applicable at various scale lengths. Particular emphasis is placed con mcro-scale models and testing techniques of cementitious materials.

Chapter 3: Experiments. This chapter describes four testing techniques that have been widely used in concrete and that are adopted here for testing HPFRCC. These techniques include uniaxial compression, uniaxial tension, biaxial compression, and triaxial compression tests.

Chapter 4: Macro-scale plasticity model for HPFRCC. This chapter provides an overview of general plasticity theory and the four-parameter compressive yield surface for concrete proposed by Hsieh et al. (1979), which is further developed for HPFRCC materials. The chapter concludes with an extension of the compressive yield surface to the tension side.

Chapter 5: Model Calibration and Verification. This chapter discusses the procedures to calibrate material parameters. In addition, evidence is provided to show that the proposed calibrated model works. Several exercises which include a two-span continuous beam, punching shear slab, slender wall, and coupling beam are simulated and their results compared with the test results.

Chapter 6: Conclusion. This chapter provides a summary of this research study. Conclusions related to the macro-scale plasticity model for HPFRCC are drawn and future work is recommended.

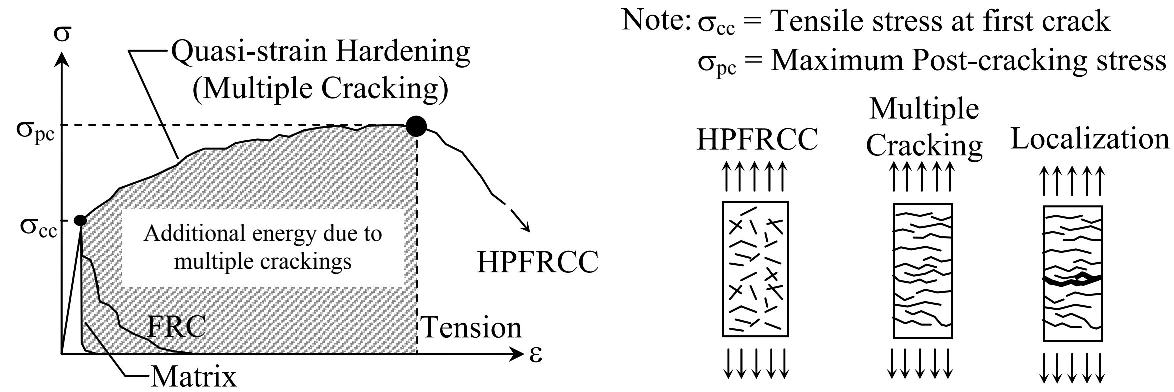

Note: σ_{cc} = Tensile stress at first crack
σ_{pc} = Maximum Post-cracking stress

(a) A comparison between stress-strain response of HPFRCC and normal FRC in tension.

(b) Multiple cracks are formed during the hardening process and followed by the localization, which leads to failure at high tensile strain

Figure 1.1 Typical Stress-strain response in tension of high performance fiber reinforced cement composites (HPFRCC) (Naaman and Reinhardt, 1996)

CHAPTER 2

LITERATURE REVIEWS

Important aspects regarding the behavior and modeling of concrete and High Performance Fiber Reinforced Cement Composites (HPFRCC) at different length scales are reviewed in this chapter (Figure 2.1). Particular attention is paid to macro-scale models for concrete as they are the basis for constructing the HPFRCC macro-scale model presented in Chapter 4. Testing techniques under various loading conditions for concrete and fiber reinforced cement composites are discussed in the final section of this chapter.

2.1 Classification of Models

Depending upon the size, i.e. length, along which the dominant physical processes of interest take place, analysis techniques for High Performance Fiber Reinforced Cementitious Composites (HPFRCC) can be generally classified into three categories: structural-scale, macro-scale, and micro-scale models. The characteristic length scale of typical structural components in civil engineering is usually specified on the order of 10^0 to 10^1 m. At this scale level, the responses of interest include load carrying capacity, drift, durability, etc. The pertinent parameters that influence structural response at this scale include member strength, stiffness, and ductility. At the macro-scale (10^{-1} – 10^{-2} m), it is possible to distinguish between the responses of members made of fiber reinforced cement composites and conventional reinforced concrete members. Phenomena like strain-hardening and softening play a dominant role at this length scale. At the micro-scale level $(10^{-3} - 10^{-6})$, each component of HPFRCC, i.e. fiber, matrix, and interfacial bond, can be distinguished. Propagation of matrix cracks from preexisting defect cracks and pullout of fibers that bridge these cracks are the major mechanisms that influence response at this length scale.

The simply supported beam shown in Figure 2.2 demonstrates further the ideas presented in the previous paragraph. As the length scale progressively decreases more details of the beam are revealed. At the structural-scale level, all parts of the beam including HPFRCC and reinforcements are lumped together and represented by beam elements. Appropriate boundary conditions are enforced at the joints at both ends of the beam. At the macro-scale level, the rebars and HPFRCC are distinguished and are separately modeled with beam and solid elements, respectively. The interaction between reinforcement and HPFRCC is modeled by using appropriate kinematic constraints. However, the fibers and the matrix inside the HPFRCC at this scale length are still indistinguishable, i.e. HPFRCC is considered as a homogeneous medium. At the micro-scale level, the fibers and the matrix and the interaction between them are explicitly modeled.

Several methods have been proposed in the past to link models that describe HPFRCC responses across the various length scales. One of these methods is the spatial averaging concept (Kabele, 2003). Each component of a spatial element called a Representative Volume Element (RVE) can be identified on a finer length scale. The constitutive law, which defines the relationship between overall stress and overall deformation of the RVE, is obtained by averaging the local quantities on the finer length scale. Another method is to use Homogenization Theory to link the micro and macro levels (Alwan, 1994). In this method, a composite material element is formed by the repetition of micro cells. Depending on the complexity of the model, the macro element can be composed of a few to several hundred unique unit cells arranged in a certain predefined pattern. An example given in Figure 2.3 shows a composite material element that composes two different unit cells arranged in a zigzag pattern. Each unit cell represents different properties such as Young's modulus and Poisson's ratio for the isotropic elastic materials. The load-displacement response of the macro-scale unit is obtained by combining all unit cells together. Further information regarding the basic concept of this theory can be found in Benssousan (1978); Sanchez-Palencia (1980); Lions (1981); Duvaut (1984); Oleinik (1984); Murat and Tartar (1985); and Levy (1985). Numerical approaches for Homogenization can be found in Triantafyllidis (1985, 1994); Wu et al (1989); Guedes and Kikushi (1990); and Leguillon (1992).

The two methods given above only provide a linkage from micro-scale to macro-scale models but they do not cover the transition from macro-scale to structural scale. The Finite Element Method is commonly used to make this transition. The advantage of this method is that it can handle structural members with arbitrary geometry, materials, and boundary and loading conditions.

2.2 Models of Fiber Reinforced Cementitious Composites (FRCC)

Models of FRCC encompassing three different length scales will be discussed in this section: (a) Structural-scale models, (b) Macro-scale models, and (c) Micro-scale models.

2.2.1 Structural-scale Models

In structural-scale models, each component of a structure is represented using domain-level elements that are characterized by load-deflection or moment-curvature responses depending on the type of the component. There are few examples of structural-scale models for HPFRCC including Stang and Olesen (1998) who developed closed form moment-rotation relationships for the plastic hinge region in HPFRCC members in pure flexure, and Olesen (2001) who extended these relationships to account for the effect of axial force.

2.2.2 Macro-scale Models

In macro-scale models, the constitutive models of each component of the structure, such as steel reinforcements and FRCC components, are uniquely defined and characteristics such as strain hardening in HPFRCC or strain softening in FRCC under tensile response can be distinguished. Macro-scale models can be divided into one-, two-, and three-dimensional. In one-dimensional models, the uniaxial responses of both FRCC and HPFRCC under both tension and compression are accounted for in a fiber section framework (Para-Montasinos, 1999 and Chandrangsu, 2003). In fiber section analysis, the equilibrium and strain compatibility between reinforcing bars and the FRCC components are enforced. The final product of such analysis is moment-curvature response for a beam section, which can be used as the input for structural-scale models.

Soranakoom and Mobasher (2007) used the same concept to derive a closed form solution for flexural beam responses of FRCC.

In two-dimensional models, the responses of FRCC under biaxial loading conditions are considered. Two general constitutive models for FRCC include hypoelastic and plasticity models. By using the former, Han et al. (2003) incorporated a co-axial stress-strain model proposed by Feenstra et al. (1998) with the uniaxial compressive and the uniaxial tensile behaviors of FRCC to model cyclic member responses. In the co-axial stress-strain model, the corresponding principal strains are first determined based on a given state of strains. For each principal strain direction, the corresponding principal stress is then determined from the uniaxial constitutive model. Once all principal stresses are known, the original state of stresses is then calculated by rotating from the principal strain axis back to the original axis. The main assumption of this model is that the principal strain direction coincides with the principal stress direction. The drawback of this model is that it does not consider the increase in compressive strength under biaxial compression. By using a two dimensional plasticity formulation, Hu et al. (2003) proposed a single smooth biaxial failure surface for steel fiber reinforced concrete (SFRC), which was derived from the multiplication of elliptical and power functions. The model required a total of six material parameters determined from the test under biaxial loading combinations. The associative flow rule was used in this model based on the assumption that volumetric strain is not of concern.

In three-dimensional models, the responses of FRCC under all triaxial loading combinations are considered. Seow and Swaddiwudhipong (2005) proposed a five-parameter compressive failure criterion for FRC constructed with straight hooked fibers.

Beside the concrete parameters, a few additional parameters pertaining to fibers, such as the volume fractions, aspect ratios, ultimate bond strength, and types of fibers, were also taken into consideration for constructing the failure surface. For the tension response, the improvement of FRCC over conventional concrete was not modeled by using a plasticity model but by simply adding tensile softening once the stress reaches the tensile strength. The model was then verified against test results of FRCC cubes and a simply supported beam with two loads. Another example is by Minelli and Vecchio (2006) who used the modified compression field theory (MCFT) and the distributed stress field model (DSFM) combined with an adjusted tension softening model for steel fiber-reinforced concrete (SFRC) to model members under shear loading.

2.2.3 Micro-scale Models

By using the so-called representative volume element (RVE) approach, FRCC can be modeled as a collection of cell each comprised of three different components, i.e. a fiber, the surrounding matrix, and the interfacial bond between fiber and matrix. The first component, that is the surrounding matrix, usually represents either mortar or concrete. This component is modeled as linearly elastic up to the peak strength followed by strain softening to represent the brittleness of the matrix. The second component, which is the fiber, is also modeled as linearly elastic up to the yield strength of the fiber. However, the post-yield stress-strain response of the fiber is dependent on the fiber type. For example, steel fibers can be assumed as perfectly plastic up to the failure strain but the polymeric fibers fracture once they reach the yield strength. The last component in the RVE is the interfacial bond between fiber and matrix, which is mobilized when the matrix cracks. Once cracking occurs in the matrix, the fiber, which previously received stresses from the matrix before cracking, now transmits the stresses across the cracks (Sujivorakul, 2002). The post-cracking process is mainly composed of two stages, i.e. debonding and pull-out stages, as shown in Figure 2.4. In the former stage, the separation between fiber and surrounding matrix occurs when the applied force reaches a critical value. This critical value can be calculated by two different approaches, i.e. the stress-based or energy-based approaches (Stang et al, 1990; Leung and Geng, 1998). In the stress-based criterion, separation occurs once the applied stress reaches some critical value. Examples of the stress-based model are the anchorage bond at the ends of hooked fibers, or the mechanical bond along the length of twisted fibers (Alwan et al, 1999 and Sujivorakul, 2002). In the energy-based approach, debonding occurs once the external work done by the applied force overcomes the interfacial fracture energy. A comparison between these two approaches can be found in Stang et al. (1990). In the pull-out stage, once full debonding has occurred, the fiber starts to slide out of the matrix. Force resistance is mainly provided by the friction between fiber and matrix. Under small slip, the relationship between resisted force and sliding is mainly dependent upon the types of fibers (Sujivorakul, 2002), for example, the pullout load in the smooth steel fibers decreases as the embedded length decreases. However, in twisted fibers, the pullout load increases as the embedded length decreases.

So far, only a RVE composed of a single fiber surrounded by matrix has been discussed. An averaging method can be employed in order to extend the micro-scale model to a corresponding macro-scale model (Li et al, 1991). The required material parameters in this method include properties of the matrix and fiber as well as the interfacial properties between fiber and matrix. These interfacial properties include size, volume fractions, and distribution of fibers; and bonding strength or bonding toughness between fiber and matrix (Leung and Geng, 1998). With all these material parameters, the stress-strain curve of the pre-cracking behavior and the stress-displacement curve of the post-cracking behavior in the composite material can be obtained by integrating over the volume.

Instead of the averaging method, an alternative method proposed by Bolander and Saito (1997) is to model fibers as truss elements dispersed throughout a matrix model. The orientation and the distribution of short fibers are random to represent actual fiber distribution in a real FRCC. The response of a fiber controlled by kinematic constraints from the matrix is divided into two parts, i.e. pre-cracking, and post-cracking. In the pre-cracking stage, the interaction between fiber and matrix is modeled using shear lag theory, whereas in the post-cracking regime, the pullout response between fiber and matrix is used instead.

2.3 Macro-Scale Models for Concrete

Four common macro-scale models that can be used for modeling concrete are covered in this section: plasticity, microplane, fracture mechanics, and damage mechanics. In a typical case, one or more of these models can be combined together to create an appropriate constitutive model. For example, the plasticity model is used for compression while the fracture mechanics approach is used for tension.

2.3.1 Plasticity Models

Plasticity theory was originally developed to model the constitutive response of metallic materials. In the past few decades, the theory has been extended to model concrete behavior due to its computational expediency. In plasticity theory, there are three essential ingredients used to describe the nonlinear behavior of concrete. The first ingredient is the plastic flow rule, used to determine the direction of plastic flow once the state of stress reaches the yield surface. This rule can be divided into two different types, i.e. associative, and non-associative. In the former, the loading surface is the same as the yield surface and hence, the plastic flow direction is always perpendicular to the current yield surface. In the latter, the loading surface is different from the yield surface and thus, the plastic flow direction is not normal to the current yield surface. In this case, a potential function is used to define the loading surface. Smith et al. (1989) observed that the plastic flow direction of concrete is not perpendicular to the yield surface as shown in Figure 2.5. Grassl (2003) confirmed that use of the associative flow rule over predicted the volumetric response of concrete under triaxial loading conditions. Therefore, a non-associative flow rule is more suitable for modeling concrete behavior than the associative flow rule. Some examples of potential functions used for defining non-associative flow can be found in Schreyer and Babcock (1985); Ohtani and Chen (1986); Imran and Pantanzopoulou (2001).

The second ingredient in the plasticity theory is the hardening rule. Once the direction of plastic flow has been determined in a plasticity model, a hardening rule must be employed to determine the kinematic of the yield surface. There are three commonly used hardening models, i.e. isotropic, kinematic, and mixed hardening, to describe the behavior of the yield surface (Figure 2.6). It should be noted that differences in response between these three models can be seen only if unloading occurs, i.e. the stress-strain responses under monotonic loading for these three models are identical. In isotropic hardening, the yield surface expands equally in all direction but the center of the yield surface is fixed. In contrast, kinematic hardening requires the size of yield surface to remain constant, but the center point of the yield surface moves as the load increases. The result of moving the center of yield surface is to capture the cyclic behavior called the Bauschinger's effect that occurs in steel. Lastly, mixed hardening is a combination of both isotropic and kinematic hardening. Hence, the yield surface grows and moves at the same time as the load increases. Derivation of hardening rules can be found in Hill (1950) for isotropic; Prager (1955, 1956) and Ziegler (1959) for kinematic; and Hodge (1957) for mixed hardening. Some examples of hardening rules in concrete models include Schwer and Murray (1994), who used a mixed hardening rule where the translation of center of the yield surface is calculated by multiplying a scalar quantity with the incremental plastic strains; Grassl et al. (2002) who used the volumetric components of plastic strains, instead of using the length of plastic strain tensors, as an alternative hardening parameter.

The third ingredient in the plasticity theory, which is the most important item in developing a plasticity model for concrete, is the yield criterion. The yield criterion is used to define the elastic boundary of the concrete. When the stress reaches the yield surface, also known as the failure surface, permanent deformation will take place as the load increases. The classification of the yield criterion of concrete is based on the number of material parameters required to define the yield surface. These material parameters range from one to five parameters. However, one- and two-parameter models are not versatile enough to fit the observed experimental data. Hence, the minimum number of parameters needed to describe a concrete yield function is at least three parameters. Some examples of concrete yield functions can be found in Chen and Chen (1975), Chang et al. (1987), Lade (1981), and Grassl (2003) for three-parameter models; Ottosen (1977), Hsieh et al. (1979) for four-parameter models; Balan et al. (2001), Barzegar and Maddipudi (1997), and Pivonka et al. (2004) for five-parameter models.

Since the main finite element software used in this study is LS-DYNA, it is worthwhile to explore the existing concrete models available in the program. In LS-DYNA, several plasticity models, such as the Geologic Cap model (MAT25) and its extension, the Continuous Surface Cap Model (MAT145), the K&C Concrete Model (MAT72 and MAT72R3), are currently available for modeling concrete behavior with solid elements (Hallquist, 2007). In MAT25, the Drucker-Prager yield surface combined with the cap surface is used to model geomaterials such as soils and concrete (Figure 2.7a). The Drucker-Prager yield criterion is a two-parameter pressure dependent model that accounts for strength enhancement associated with the increase in confining pressure. The model is an extension of the one-parameter pressure independent J_2 yield criterion. The cap surface is included for controlling dilatancy of concrete (Dimaggio and Sandler, 1971). The algorithm of MAT 25 is based on the work of Simo et al. (1988). Some drawbacks of this model pointed out by Schwer and Murray (1994) are the intersection between the shear yield surface and the cap surface, which creates a kink in the surface, and the exclusion of the third invariant J_3 term, which causes the cross-section of the yield surface to be circular in the π-plane contrary to observed test data.

As a result of the limitations on the MAT25 model, the continuous cap model (MAT145) was introduced to overcome those problems. In the meridian plane, the shear and cap surface are blended together (Figure 2.7b) and in the π-plane, the circular cross-section is converted into a triangle with smooth corners. In addition, mixed hardening and strain rate effect are also embedded in this material model. More details on how to obtain material parameters and background of MAT25 and MAT145 can be found in Schwer (2002). Lastly, MAT72 (Figure 2.8) is a three-invariant model that uses three different yield surfaces, namely initial, maximum, and residual yield surfaces. Depending on the current location of stress (hardening or softening), the current state of stress is obtained by interpolating among the three surfaces. Full details on development and material parameters of this model can be obtained from Crawford and Malvar (2006).

2.3.2 Microplane Models

Another way to derive the relationship between the stress-strain tensors is to use the Microplane model, which was first introduced by Bazant in 1984. Unlike plasticity theory that is formulated in terms of invariants of the stress and strain tensor, the microplane model provides relations between stress and strain components on a plane with pre-specified orientations. The origin of this model can be traced back to the Taylor's slip theory of plasticity (1938), based on which the plasticity of polycrystalline metals was formulated. It should be noted that the prefix "micro" in this context does not refer to the actual microstructure geometry, but rather implies a separate characterization of the inelastic deformations on planes of various orientations within the microstructure.

The basic procedure of the microplane model is as follows. First, the strain components on microplanes with various orientations are obtained from the projection of the continuum strain tensors. Then, the corresponding normal, volumetric, deviatoric, and shear stresses of each plane are obtained by applying the kinematic constraints. Finally, the stress components on the microplanes are converted back to continuum stress tensors by using the principle of virtual work. The evolution of microplane model can be found in Bazant and Oh (1983, 1985), Bazant and Prat (1988), Bazant et al. (1996), and Bazant et al. (2000), whereas some applications of this model can be found in Carol et. al. (1992); Cofer and Kohut (1994); Bazant and Ozbolt (1990); and Liu and Foster (2000). The main drawbacks of the microplane model (Bazant and Tsubaki, 1980) are that the formulation cannot be written as an explicit expression and the constitutive equations require many material constants.

2.3.3 Fracture Mechanics

Fracture mechanics is a commonly used method for determining the tensile stress causing crack formation or crack growth in structural components. There are two different types of fracture mechanics, i.e. Linear Elastic Fracture Mechanics (LEFM), and Nonlinear Fracture Mechanics.

In the LEFM approach, the toughness of linear materials can be described by two methods, i.e. energy and stress intensity factors. In the former approach, initiation of a single crack or growth of the existing crack can occur if and only if such a process causes the total energy to decrease or remain constant (Griffith, 1920). Therefore, the critical condition in the energy approach is defined as the point where the crack growth occurs under the equilibrium condition with no net change in the total energy. Irwin (1956) further defined an energy release rate G as a measurement of the energy available for an increment of the crack extension. This parameter G can also be considered as the crack driving force. In the stress intensity factor approach, fracture occurs if the stress intensity factor K_I reaches the fracture toughness of the material K_{IC}. The subscript of K defines the failure modes, which consist of opening (K_I), in-plane shear (K_{II}), and out of plane shear (K_{III}).

Some examples of the applications of LEFM to cementitious composites include Hillerborg et al (1976) who studied the size effect on the formation and propagation of cracks in an unreinforced concrete beam using LEFM and the Finite Element Method. He used his results to explain the difference between bending strength and tensile strength and also the variation of bending strength with beam depth; Kim et al (1999) studied the size effect on the compressive strength of concrete cylinders and proposed empirical formulae to predict the compressive strength as a function of diameter and height/diameter ratios; Reis and Ferreira (2003) studied the influence of notch depth on the fracture mechanics properties of polymer concrete and found out that the fracture energy G_f is in direct proportion to the notch depth; Li et al (1991) used the bridging fracture energy combined with a micromechanical model to derive the post-peak response of FRCCs. Paris and Erdogan (1963) related the fatigue life of a structure with pertinent fracture mechanics parameters. Their model is commonly known as Paris law. Several researchers further extended Paris law to model concrete (Baluch et al., 1987; Bazant and Schell, 1993; Bazant and Xu, 1991; Perdikaris and Calmino, 1987). Matsumoto and Li (1998) modified Paris law by introducing the stress intensity factor due to fiber bridging to predict the fatigue life of fiber reinforced concrete. Zhang et al. (2001) studied the size effect on fatigue in bending of concrete.

In Nonlinear Fracture Mechanics, the process of fracture in the nonlinear materials is described by two approaches, i.e. the Crack Tip Opening Displacement (CTOD) and J contour integral (J-Integral). In the CTOD approach, the initial sharp crack is blunted due to the plastic deformation at the crack tip (Well, 1961). The degree of blunting is in direct proportion to the material toughness. Since nonlinear deformation occurs, the LEFM factors, G and K, are no longer suitable factor to measure toughness of the materials. Hence, the CTOD is more meaningful term to measure the fracture toughness of the plastic materials. Some examples of CTOD approach include Ouyang and Shah (1992) who used the critical CTOD $(\mathrm{CTOD_C})$ and the critical stress intensity parameter $(\mathrm{K_{IC}})$ to derive the resistance curve (R-Curve). Jeng and Shah (1985) showed that the critical crack length $(\mathrm{a_c})$ cannot be used as a factor to replace the $\mathrm{CTOD_C}$ since $\mathrm{a_c}$ is dependent on the geometry of the specimen and the size of the initial flaw.

The second nonlinear fracture mechanic approach is the J Integral proposed by Rice (1968). The J integral parameter is a path-independent method that can be used to define toughness of both linear and nonlinear materials. In LEFM, J integral can be viewed as either energy or stress intensity parameters (Rice, 1968; Hutchinson, 1968; and Rice and Rosengren, 1968). Some examples of J-Integral applications include Li et al. (1987) who were the first to use J-based technique to explain the tension-softening response of fiber reinforced composites. Marshall and Cox (1988) used the J-integral to explain how to achieve multiple cracking or pseudo strain hardening. The crack driving force $(\mathrm{J_b})$ that accounts for the energy dissipation in the fiber bridging zone must be equal to the crack tip toughness $\left(\mathrm{J_{Tip}}\right)$. If this condition is not satisfied, the Griffith type crack will overcome (Li and Leung, 1992). Other works related to multiple cracking can be found in Maalej and Li (1995); Mishra and Li (1995); Leung (1996); Kanda (1998).

Once the cracking point is determined, two different techniques can be employed for modeling crack propagation in Finite Element Analysis: the discrete and smeared cracking approaches. In the former approach, each dominant crack surface and its orientation are predefined and are explicitly modeled (Ngo and Scordelis, 1967). At each cracking interface, the nodal displacements of adjoining elements are progressively disconnected as the crack propagates as shown in Figure 2.9. In other words, as the tensile load increases, the displacements at the cracking interface will increase and adjacent elements near the crack that were joined before are now separated. Thus, an adaptive meshing approach must be employed. However, this makes the model extremely complex and time consuming (Ngo, 1975). In addition, the finite elements used in this model require higher-order interpolation fields, which again impose high computational demand. In general, the discrete-cracking model can be used for solving problem involving with only a few dominant cracks.

In the smeared cracking approach, cracking is accounted for by modifying the material properties to reflect the occurrence of cracking. Once a crack occurs, the strength of concrete perpendicular to the cracking surface diminishes and the shear stiffness is reduced by a shear reduction factor. The main advantages of this approach is that (Bolander and Wight, 1989): (1) cracks can occur at any direction; (2) multiple cracks can simultaneously take place at any integration point; (3) the topology of the finite element mesh remains unchanged throughout the analysis; (4) the smeared crack approach can handle situations involving widely spread cracking.

2.3.4 Damage Mechanics

Concrete behaves as a quasi-brittle material in the sense that it cannot withstand a significant amount of plastic deformation at the macro-scale, but at the micro-scale, localized damage growth can occur (Lemaitre, 1992). The gradual degradation of the material at the macro-scale results from decohesion between aggregates and cement matrix. Continuum Damage Mechanics (CDM) is one of the methods that can be used to capture this degradation, also known as the strain softening type behavior. The CDM was first introduced by Kachanov (1958) as a scalar field quantity to model creep rupture failure in ductile materials and Krajcinovic (1983) was the first to use CDM to model brittle materials such as concrete.

The CDM model is derived from the thermodynamics of irreversible processes and internal state variable theory and can be worked into two space domains (Simo and Ju, 1987), i.e. stress- and strain-space. Typically, the strain-driven mechanism is preferred since damage in the material is directly linked to the history of strain, not the stress history. In the strain-based model, the main hypothesis is that the strain associated with a damage state under the applied stress is equivalent to the strain associated with its undamaged state under the effective stress (Lemaitre, 1971). Besides having two space domains, damage mechanics is classified in two different categories based on material type. The first model is the isotropic damage model, which is used for modeling ductile material. In this model, a scalar variable is use to capture the growth of damage. The second model is anisotropic damage model, which is used for modeling brittle material. Unlike the former model, a forth order tensor is required in order to account for damage growth in all directions. Obviously, concrete must be modeled by using anisotropic damage mechanics.

One drawback of CDM is that the mathematical expression becomes ill-posed at a certain level of accumulated damage. Ellipticity of the governing equations in quasi-static problems cannot be assured, whereas hyperbolicity in dynamic problems can be lost locally. In numerical simulations, this shortcoming can be observed as extreme sensitivity to the fineness and orientation of the mesh (Borst et al. 1995 and Peerling et al. 1998). To overcome this problem, several approaches have been introduced in the past: for example, nonlocal approaches (Pijaudier-Cabot and Bazant 1987, Simo 1988); rate-dependent approaches (Needlemen 1988, Sluys 1992); and continuum models enhanced with higher-order deformation gradients (Aifantis 1984, 1987, 1992, de Borst et al. 1995, Peerling et al. 1998).

In the nonlocal approach, the state variables that fluctuate at the microscale are spatially averaged by using a weight function. A characteristic length, which is an essential parameter for the weight function, is influenced by spacing, size and shape of inclusions (fibers in the case of FRCC). A major problem of this approach is how to determine a suitable weight function. Furthermore, additional experiments are needed to obtain the characteristic length. In rate-dependent damage models, a damage function is incorporated as a result of classical viscoplasticity. It requires one additional material parameter, i.e. the damage fluidity coefficient (μ). As μ approaches zero, the model exhibits instantaneous elastic response, and as μ approaches infinity it is equivalent to a rate-independent damage model. In the gradient-enhanced damage model, the equivalent strain is used and can be obtained by using Taylor's expansion up to the second order terms. Hence, the equivalent strain is composed of the local strain and its gradient. To determine the gradient term, additional boundary conditions are required in the boundary value problems. However, the physical interpretation of these boundary conditions remains an open issue (Peerling et al. 1998).

2.4 Testing Techniques

In order to obtain the material parameters necessary to model the complete behavior of HPFRCCs in three dimensions, several tests, which consist of uniaxial, biaxial, and triaxial tests, must be performed under both compression and tension. This section provides background about these testing techniques for normal- and high-strength concretes, with and without fibers.

2.4.1 Uniaxial Tests

The uniaxial compression test is widely used in the civil engineering field. In fact, current design guidelines such as ACI 318-05 (2005) and AASHTO standards (2000) are based on the parameters obtained from this test. These parameters include the unconfined compressive strength and the Young's modulus. The testing procedure can be found in ASTM D4832-02 standard (2002). Several issues regarding the geometry of the specimen and the boundary conditions were pointed out by Van Mier et al. (1997). They found that the friction at the interface between concrete specimen and the loading platens play an important role influencing the strength and ductility of the post-peak response of concrete. As a result of the frictional interface between the specimen and loading platens, the slenderness ratio of the specimen influences both strength and ductility of the post-peak response. In addition, prism shaped specimens give higher strength than cylindrical shape specimens.

Unlike ordinary concrete, FRCCs and HPFRCCs are not brittle so the direct tensile test must be performed to study tensile behavior. Since there is no standard test procedure in direction tension, several issues must be taken into account when designing the test setup. These issues include the geometry and alignment of the specimen, and the boundary conditions. In terms of geometry, Chandrangsu (2003) showed that the size of specimens affects the strain value at the peak stress and the difference between small and large specimens could be as high as three times with small specimens being more ductile than large specimens. In term of alignment, Toutanji et al (1993) applied a small confining pressure to the side of a specimen to ensure that the loading direction is always parallel to the specimen. Since FRCC are not homogeneous, secondary flexural moment can be developed when fixed loading platens are used. This will cause redistribution of stress within a specimen and lead to higher fracture toughness than can be achieved with free rotating boundary conditions (Van Mier and Van Vliet, 2002).

2.4.2 Biaxial Tests

Prior to 1969, solid steel platens were used to apply the compressive loads on concrete specimens (Kupfer et al, 1969). Hence, the true biaxial loading conditions were not satisfied because the solid platens restricted transverse expansions due to Poisson's effect and induced additional stresses in the specimen. Kupfer et al. (1969) proposed the use of brush-like platens composed of steel filaments as the loading plates, which would allow the specimens to move freely in the transverse direction. These platens are attached to two independent actuators for loading. Under combinations of both compression and tension, there are three segments in load space, i.e. compression-compression, compression-tension, and tension-tension (Figure 2.10). It should be noted that due to symmetry of loadings, only the shaded area needs to be tested.

Under compression-compression, Kupfer et al (1969) reported that the biaxial strength of normal-strength concrete increases by about 16-27 % over the uniaxial compressive strength depending on the loading ratio. Lee et al. (2004) confirmed that under equal biaxial compression, the compressive strength is about 17% higher than uniaxial compressive strength. Hussein and Marzouk (2000) tested high-strength concrete and found that the improvement of equal biaxial compressive strength of high-strength concrete is less pronounced compared with normal-strength concrete (Figure 2.10). However, the failure modes and crack patterns of both normal- and high-strength concrete were almost the same. Yan and Lin (2007) conducted biaxial compression test on concrete under dynamic loading with strain rates ranging from $10^{-5}/\mathrm{s}$ to $10^{2}/\mathrm{s}$. They concluded that the dynamic strength increases as the strain rate and lateral confinement increase. However, the initial tangential stiffness and the failure modes are not affected by the strain rate. Lan and Guo (1999) tested concrete under repeated biaxial load and noted that the failure envelopes of concrete subjected to repeated loads had no significant difference from those subjected to monotonic loads. They also noted that the shape of the stress-strain envelope curves under repeated biaxial loads is similar to that under repeated uniaxial loads.

For steel-fiber reinforced concretes, Torrenti and Djebri (1995) utilized the same test setup as Kupfer et al. (1969) and found out that addition of steel fibers increases ductility substantially. In addition, orientations and types of fibers influence both failure modes and the biaxial compressive strength. Yin et al (1989) also tested steel fiber reinforced concrete under biaxial compression but they used different loading mechanism. Instead of using two separate actuators to apply biaxial compressive loads, they used two pairs of crescent shaped distribution beams to convert uniaxial compressive force to biaxial compressive loads. This loading mechanism is known as a load bifurcation mechanism. The main drawback of this loading mechanism is the limitation of the compressive loading ratios between two directions. Moreover, only compressive forces can be applied using this kind of loading mechanism. It should be noted that this loading mechanism originated from Su and Hsu (1988) for testing fatigue under biaxial compression of concrete. The same conclusion that addition of fibers increased ductility and strength was drawn.

Under compression-tension, the second and the forth quadrants in Figure 2.10 are identical due to symmetry of loading. For normal-strength concrete, the compressive strength decreases as the tensile stress in the other direction is increased (Kupfer et al., 1969). Introduction of even small amount of tension in one direction could reduce the compressive strength on the other direction more dramatically for high-strength concrete than normal-strength concrete (Hussein and Marzouk, 2000). Demeke and Tegos (1999) tested steel fiber-reinforced concrete (FRC) and noted that the strength of FRC is much higher than regular concrete strength. They saw enhancements of strength ranging from one to three times depending on the volume fractions of fibers.

Another test setup for biaxial compression-tension test was proposed by Tschegg et al. (1995) to test fracture properties under multi-axial stress fields. In this test, a rectangular concrete block was pre-notched on the top where a tensile force was applied laterally by using a wedge. The compressive load from an actuator was applied to the wedge and the top area of the specimen, which created a compressive reaction force at the bottom of specimen. Hence, the biaxial compression-tension state could be achieved. Another attempt of fracture testing under biaxial compression-tension was done by Subramaniam et al (2002). A hollow concrete specimen was subjected to torsional loading, which creates biaxial compression-tension in the principal direction. They concluded that the fracture parameters, such as stress intensity factor (K_I) and the resistance curve of the cracking opening failure mode could be obtained by this method.

In the tension-tension regime, the tensile strength under any given loading combinations of biaxial tension is almost the same as the uniaxial tensile strength for normal-strength concrete (Kupfer et al, 1969 and Lee et al., 2004). In addition, material parameters such as K_I and the Paris coefficient in the Paris fatigue law are similar to those obtained from uniaxial tension (Subramaniam and Shah, 2003).

2.4.3 Triaxial Tests

In triaxial compression tests, there are two methods to apply confining pressure, namely active and passive confinement (Figure 2.11). In active confinement, a concrete specimen is placed in a pressure cell filled with pressurized fluid, i.e. the lateral load is achieved through hydrostatic pressure. Once the pre-defined confining pressure is reached, longitudinal load is then applied and the axial stress-strain curve and lateral strain history are obtained. The following conclusions can be drawn from existing literature (Smith et al., 1989; Imran and Pantazopoulou, 1996; Sfer et al., 2002; and Gabet et al, 2006): (1) increasing the confining pressure changes the failure mode of concrete from brittle to ductile strain hardening; (2) the volumetric strain starts with contraction up to the peak strength, followed by expansion; (3) the flow direction of plastic is not perpendicular to the yield surface; hence, using associative flow will overestimate the volumetric strain; (4) there is little difference in the yield surfaces of normal- and high-strength concrete (Li and Ansari, 1999); (5) increasing confining pressure decreases the permeability due to collapse of internal pores inside concrete (Mahboubi and Ajorloo, 2005); (6) the envelope curves of cyclic response for unconfined and confined normal concrete are the same as the monotonic response curves. However, this observation is valid only for the ascending branch of the envelope curve of confined high-strength concrete subjected to cyclic loading. The descending branch needs to scale down for each unloading/reloading cycle (Lokuge et al, 2003).

For passive confinement, lateral load is provided by either a steel tube or fiber reinforced polymer tube wrapped around a concrete specimen. A critital difference between these two materials is the peak strength, which in turn affects the maximum confining pressure. As axial load is applied, the concrete expands laterally due to the Poisson's effect, but is arrested by the wrapping material, which leads to an increase in the confining pressure. The passive confining test provides more effective means for studying concrete behavior under confinement than the active confinement test because the confining pressure increases with the damage buildup (Pantazopoulou and Zanganeh, 2001). This is favorable for concrete under compression because the ductility increases. Example of passive confining test setups using steel tube can be found in Ahmad and Shah (1982); and Panazopoulou and Zanganeh (2001). For FRP wrapping, some examples for test setups include Spoelstra and Monti (1999); and Panazopoulou and Zanganeh (2001).

Beside these two common triaxial tests, there is another triaxial test setup that uses three independent actuators applying load to a concrete cube specimen. This test setup is described by Schwer (2002) as the "true triaxial test" since the common triaxial tests previously mentioned can only control two of the three principal stresses. However, Lan and Guo (1997) observed that the test results under multi-axial compressions between proportional and non-proportional loading appear to have no effect on response.

However, the concrete responses under combination of compression and tension are sensitive to the stress paths. Lin et al (2002) studied the effect of triaxial compressive loading history on the reduction of tensile strength by correlating ultrasonic velocity with the degree of damage. Once the level of damage is known, the reduction of tensile strength can be determined.

2.5 Conclusion

This chapter surveyed the different techniques for modeling the constitutive response of concrete and HPFRCC. Model classification based upon by the scale was first discussed followed by models for HPFRCC at the structural, macro, and micro-scale. An extensive discussion for macro-scale models for concrete was also presented. A variety of concrete models including plasticity, micro-plane, fracture mechanics, and damage models were introduced. The chapter closed with a survey of the test techniques used to obtain the parameters necessary to calibrate the surveyed models.

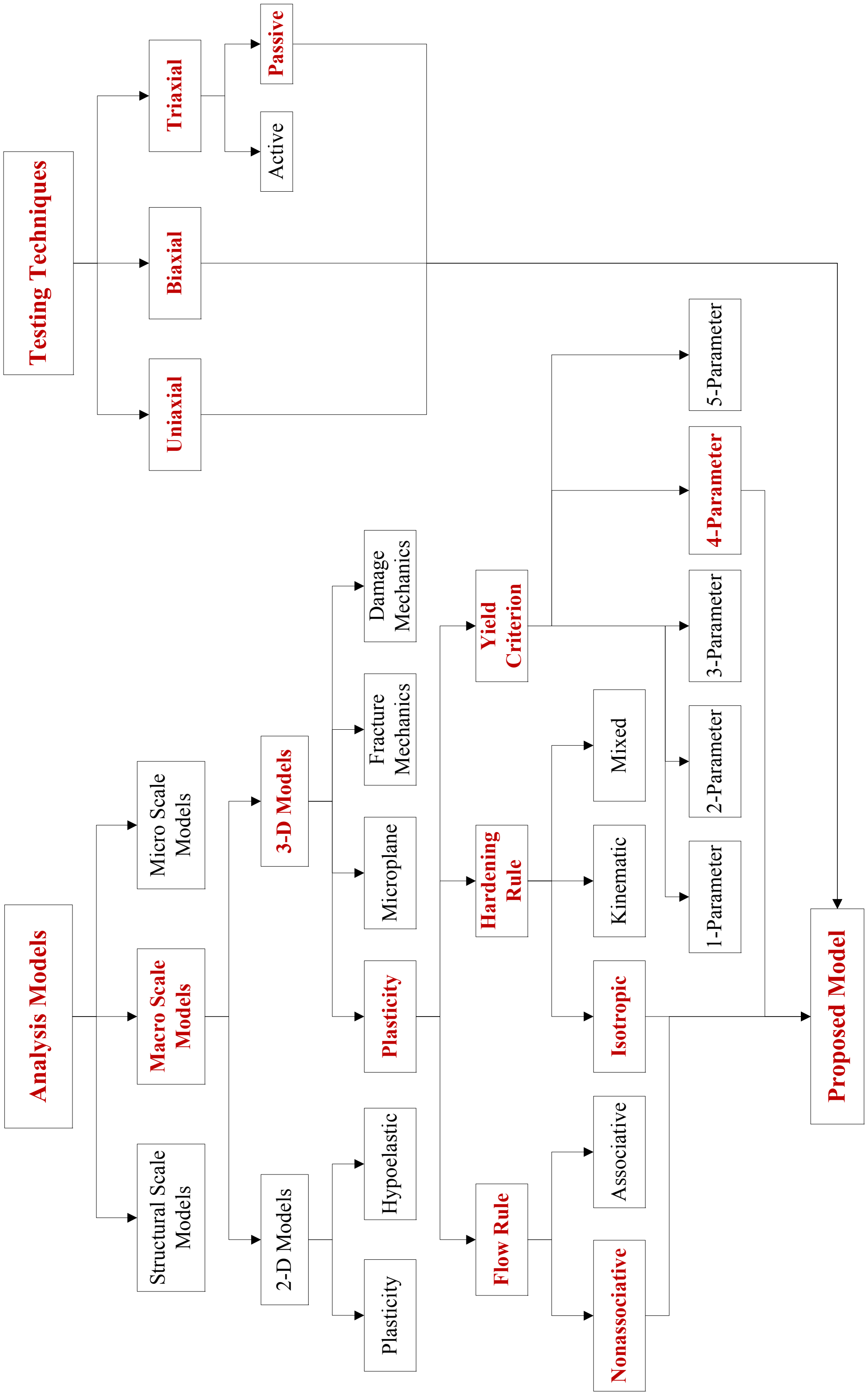

Figure 2.1 Hierarchy of modeling and testing techniques and their relation to the model proposed in this dissertation

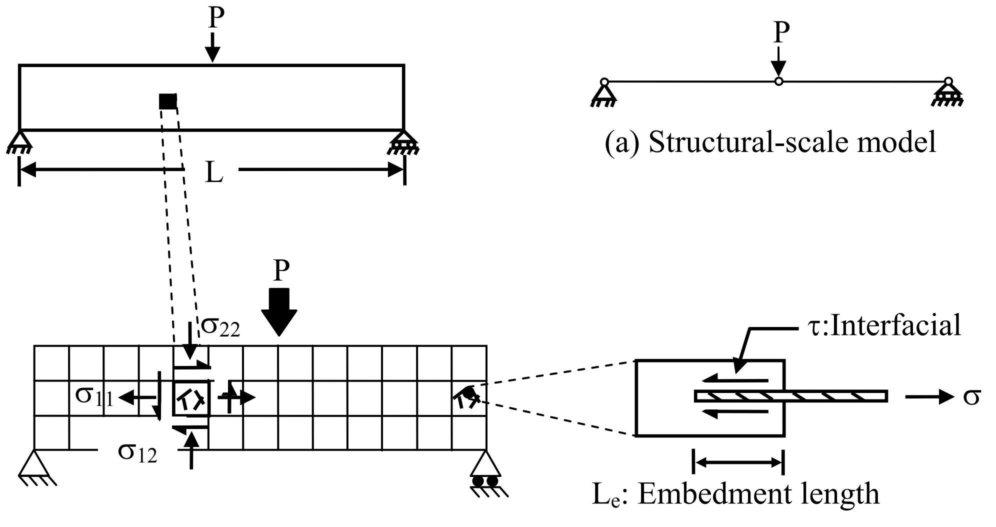

(a) Structural-scale model

(b) Macro-scale model

(c) Micro-scale model

Figure 2.2 Two-dimensional simply supported beam with different length scale

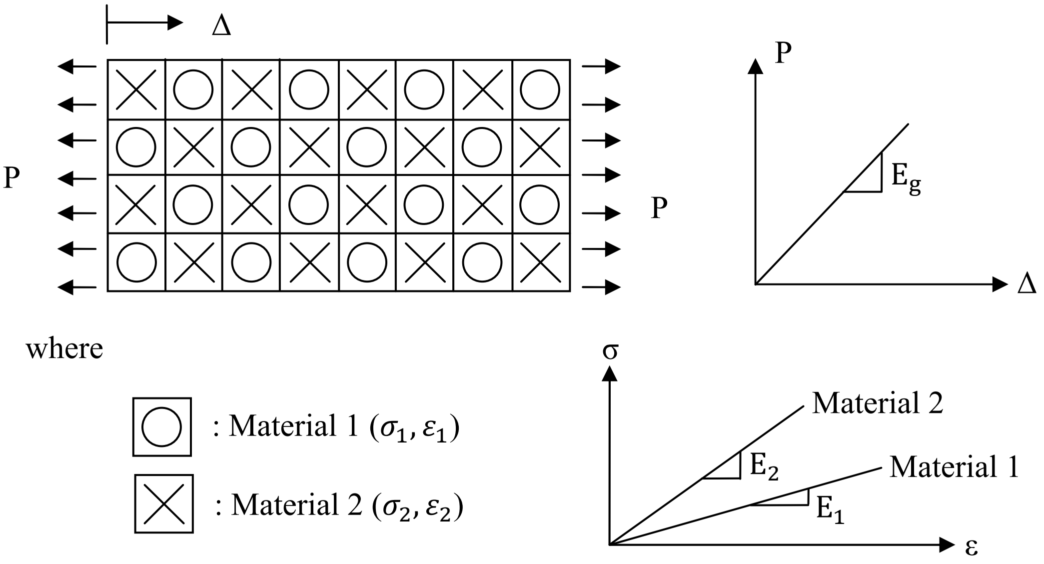

Figure 2.3 Example of composite materials compose of two different types of unit cell merging by homogenization theory (Alwan, 1994)

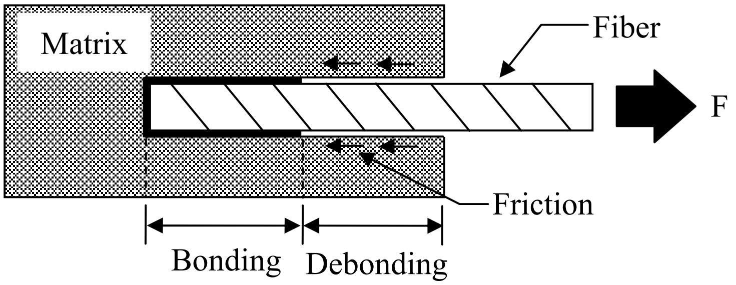

Figure 2.4 Interaction of a single fiber surrounded by matrix during the post-cracking process

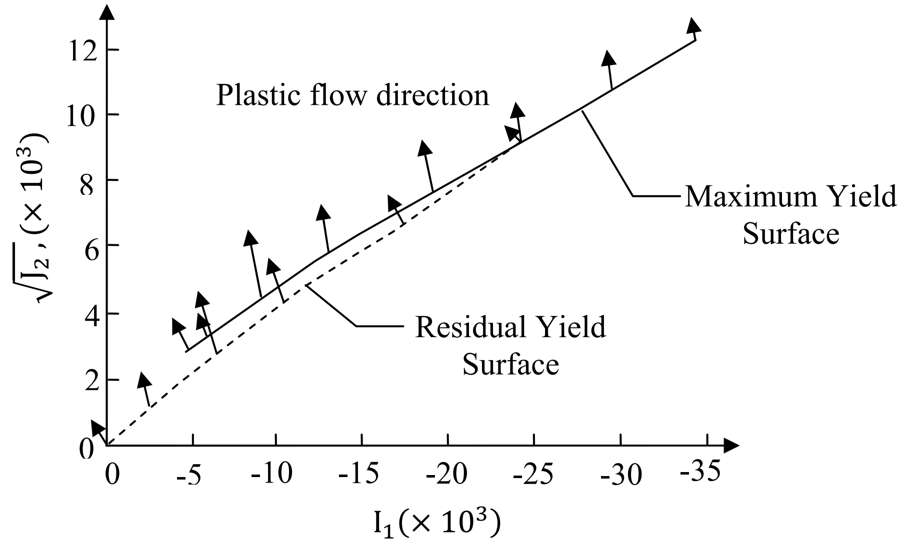

Figure 2.5 Plastic flow direction of the plastic strain components at peak and at post-peak range is not normal to the yield surfaces (Smith et al, 1989)

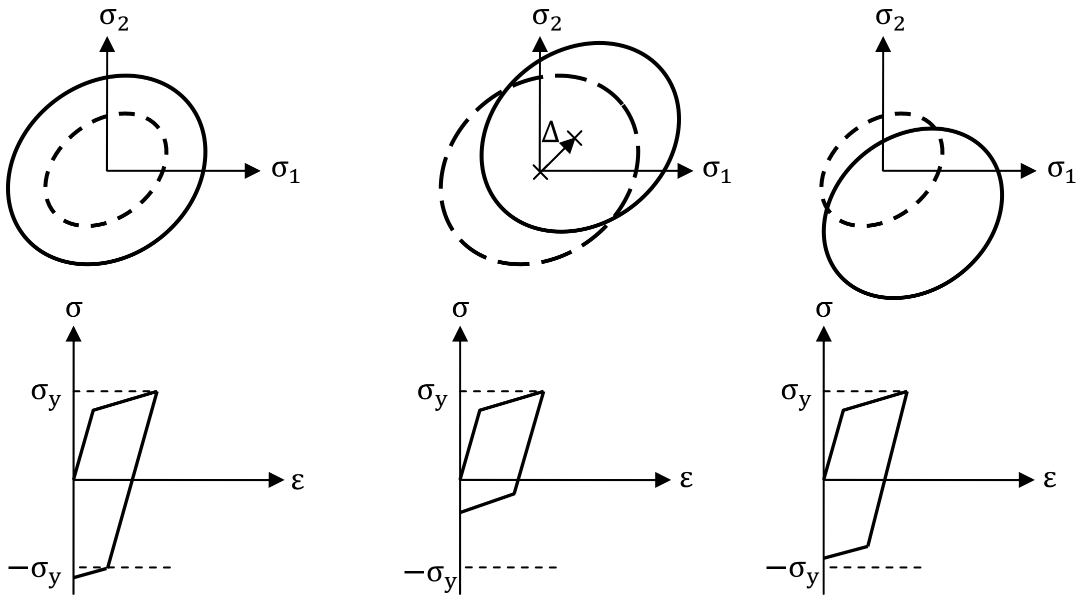

(a) Isotropic hardening (b) Kinematic hardening (c) Mixed hardening

Figure 2.6 Various forms of hardening (Schwer, 2003)

$I_{1,L}$: Intersection between failure and cap envelopes

$I_{1,L}$: Intersection between cap envelopes and I_1-axis

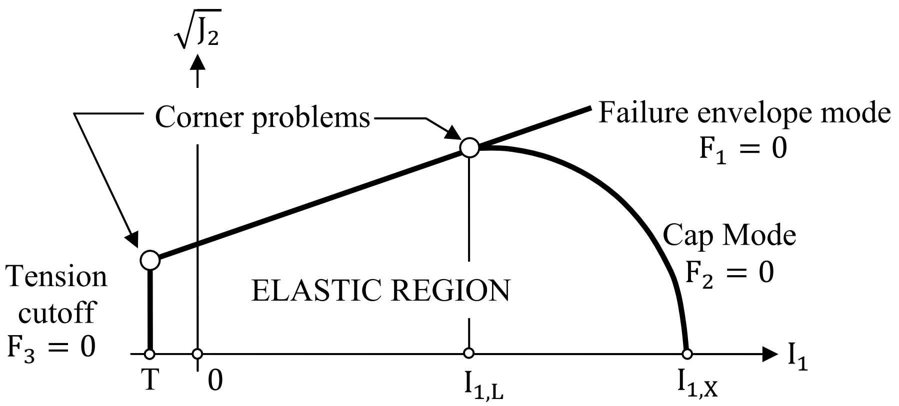

(a) Original cap model or MAT 25 in LS-DYNA (Simo et al, 1988)

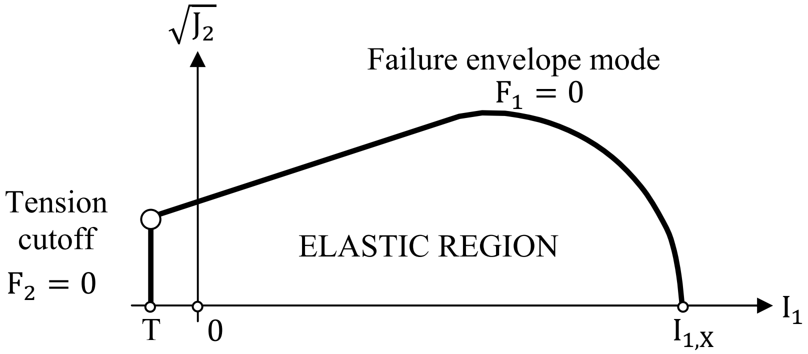

(b) Continuous surface cap model or MAT 145 in LS-DYNA (Schwer and Murray, 1994)

Figure 2.7 Cap models for concrete available in LS-DYNA

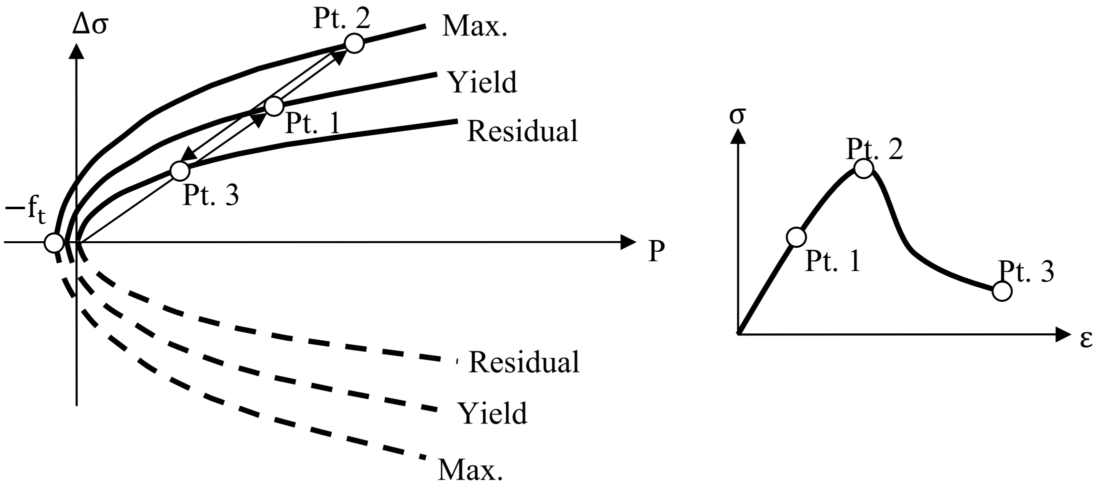

Figure 2.8 K&C Concrete model available in LS-DYNA (Crawford & Malvar, 2006)

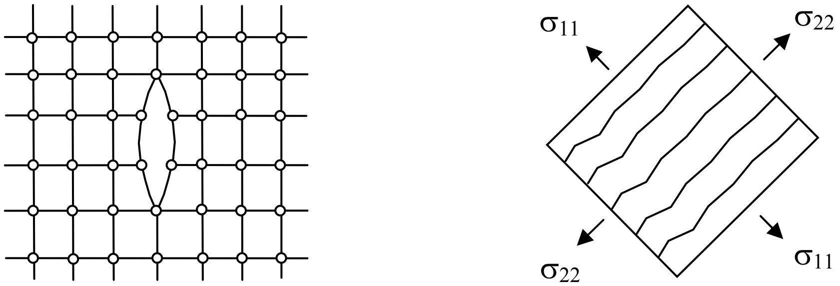

(a) Discrete crack model

(b) Smeared crack model

Figure 2.9 One-directional crack model (Bangash, 2001)

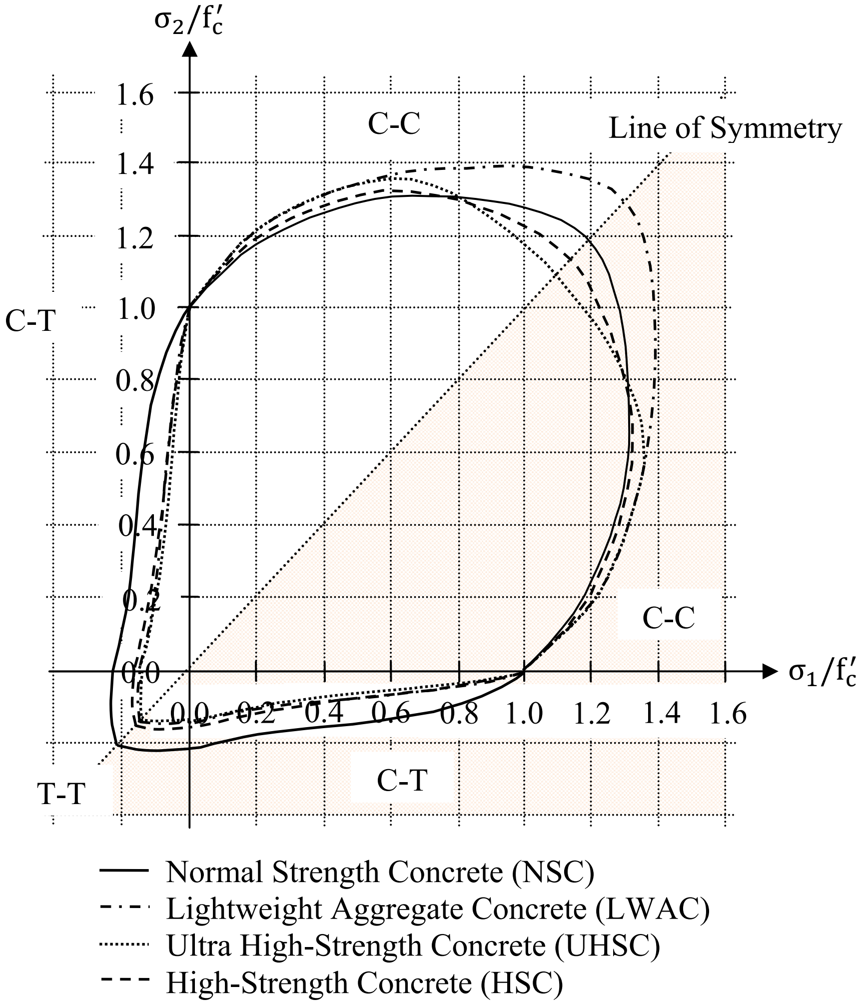

Figure 2.10 Biaxial strength envelopes for four different types of concrete under combinations of compression and tension (Hussein & Marzouk, 2000)

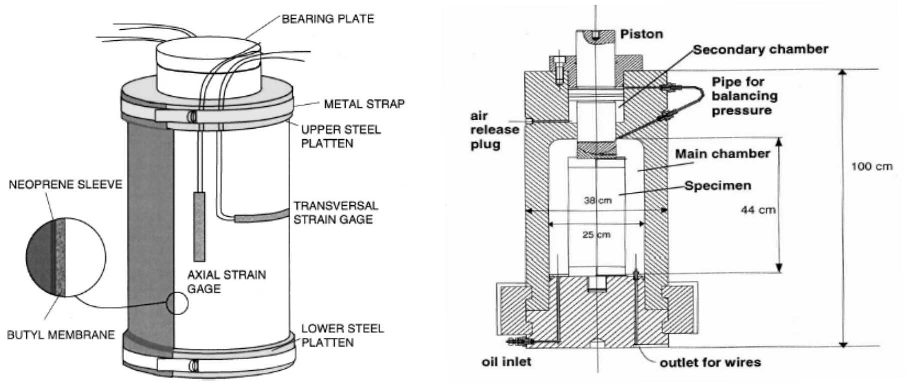

(a) Active triaxial tests (Domingo et al, 2002)

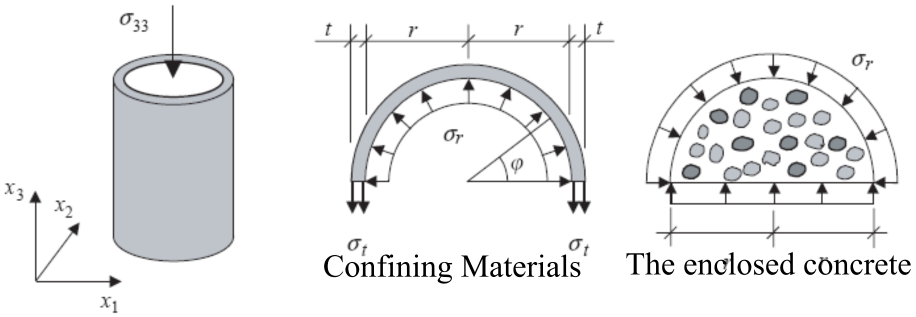

(b) Passive triaxial tests (Grassl, 2003)

Figure 2.11 Triaxial test setups

CHAPTER 3

EXPERIMENTS

This chapter reports on experiments performed under various loading paths to understand the complete behavior of HPFRCC in three-dimensional space. The loading paths selected include uniaxial, biaxial, and triaxial loading conditions (Figure 3.1). The test are conducted for HPFRCC with both hooked and Spectra fibers. The results from these tests are then used to construct the failure surfaces, hardening and softening functions presented in Chapter 4.

3.1 Experimental Program and Preparation of Specimens

3.1.1 Mix Proportions and Properties of fibers

Two different types of fiber are considered in this work, namely hooked and Spectra. The fibers are embedded in a matrix with 8 ksi strength. The mix proportions for the mortar mix are given in Table 3.1 and include early age cement type III, fly ash type C, and Flint sand with ASTM 30-70 gradation. Superplasticizers are employed to increase flowability.

The main parameters in this study were fiber type and volume fractions. As shown in Figure 3.2, the two types of fiber are 1.5 in-long high strength steel hooked and 1.5 in-long Spectra fiber. The Dramix® hooked fibers are made of high strength steel and are a trademark of Bekaert, Belgium. The Spectra® fibers are made of high molecular weight polyethylene and are a trademark of Honeywell, US. Compared with other polymeric fibers, Spectra® fibers have higher strength and higher elastic modulus and typically used in the aerospace industries. Properties of both types of fibers are given in Table 3.2. Previous studies (Chandrangsu, 2003) showed that the optimal length for Spectra fiber for HPFRCC applications is 1.5 inches for the mix proportion chosen. Three volume fractions are considered in the tests, i.e. 1.0%, 1.5%, and 2.0%. As a result, each loading path was composed of seven series as shown in Figure 3.1 (including 3 for Spectra, 3 for hooked and base mortar test). The test series are indentified using three abbreviated terms: the first term represents the loading conditions (UXC for uniaxial compression), UXT for uniaxial tension, BXC-C for biaxial compression-compression, TXCS for triaxial compression with confining pressure of 6 ksi, and TXCM for triaxial compression with confining pressure of 7.5 ksi); the second term represents the fiber type (S for Spectra, H for hooked, and M for mortar without fiber); and the third term represents the volume fraction of fiber. For examples, BXC-C-S1 represents HPFRCC with 1% Spectra fiber under biaxial compression-compression test, and TXCS-H1.5 denotes HPFRCC with 1.5% hooked fiber under 6-ksi triaxial compression test.

3.1.2 Specimen Preparation

Water was first pre-mixed with super-plasticizer so that when the liquid part was mixed with the cement, the chemical reaction between super-plasticizer and cement could be fully developed. In the mixing process, all dry components (cement, sand, and fly ash) were first mixed together in the mixing machine for a few minutes. About half of the liquid part was then added. Once the dry components were fully mixed with the liquid part, fibers were slowly added in a small amount at a time and the rest of liquid part was then intermittently added as well. Extra care was taken to prevent Spectra fiber form lumping into big balls. Once the mixing process was achieved, the specimens were cast into plastic molds on a shaking table in order to achieve good compaction.

The specimens were kept in their molds and covered with plastic sheets for about 24 hours. They were then removed from the molds and were placed in water tank for curing for at least another 28 days. Afterwards, they were removed from the tank and left to dry for 48 hours prior to testing. In addition, for the uniaxial compression test specimens, both ends of the cylinder were capped with sulfur before testing to ensure an even loading surface.

3.2 Uniaxial Tests

3.2.1 Testing procedures

The uniaxial tests were divided into compression and tension tests based on the loading path. A standard cylinder specimen (3 in × 6 in) was used for the uniaxial compression test. Three LVDTs were attached along the side of specimen to measure the longitudinal deformation up to the peak load. To prevent damage to the LVDTs from rapid deformation increases after the peak load, the LVDTs were removed and the post-peak deformation was obtained from the machine displacement instead. The full stress-strain response was then obtained by joining the two parts. In the pre-peak regime, strain was obtained by dividing the average of the three LVDT deformations with the LVDT gauge length. In the post-peak regime, strain was obtained by dividing the machine deformation by the total specimen height. The stress was directly obtained by dividing the machine load with the cross-sectional area. To ensure the consistency of the results, at least three specimens within the same series were tested and the average curve was used.

A dog-bone shape specimen was used for the uniaxial tension test. The dimensions of dog-bone shape specimen are shown in Figure 3.3. Two LDVTs with gauge length of 7 in were attached along the sides of the specimen in the loading direction. Tests were carried out in an MTS machine with a stroke rate of 0.025 inch per minute. A data acquisition system was used to record the applied load from the machine. The deformation of specimen was obtained by averaging the readings of the two LVDTs. Again, to make sure that the test results were consistent, at least six tests were repeated for each series.

The average curves for both test results are finally used as inputs to determine the parameters of the plasticity model (Chapter 4). In addition, Young's modulus is also obtained from the unconfined uniaxial compressive test.

3.2.2 Test Results

Figure 3.4 shows the average uniaxial compressive stress-strain responses of mortar and HPFRCC with different types and volume fractions of fibers. Additional details on each type and each volume fraction of fiber can be found in Appendix A. The peak strength and its corresponding strain clearly increase in the HPFRCC mixes compared to the plain mortar specimen. For example, the peak strength of UXC-H for all volume fractions increased by 25% whereas the corresponding strain at peak was increased by 50% over the corresponding mortar values. The failure mode was observed to shift from brittle to ductile once the fibers were added. This was clearly evident in the softening part of the stress-strain curve. Both enhancements, i.e. the strength and the gradual softening, were due to the fact that the dispersed fibers hindered lateral expansion, which in turn increased the confining pressure. Since the mortar is a pressure dependent material, increasing confining pressure enhances both the strength and the ductility of the material (Table 3.3).

Figure 3.5 shows the average uniaxial tensile stress-strain responses of mortar and HPRCC with different types and volume fractions of fibers. Clearly, the response of mortar without fiber is brittle under tension. The response of plain mortar (UXT-M) is linear elastic up the first crack, followed by an abrupt drop associated with the crack localization. The addition of fibers changed the response dramatically and eliminated localization after the first cracking. In this study, specimens mixed with both types of fibers (UXT-H and UXT-S) showed strain-hardening behavior along with multiple crackings (Figure 3.6). Other enhancements were evident too. For example, the strength of UXT-H was at least five times that of plain mortar. Similarly, the strength of UXT-S was four times higher than plain mortar strength. In term of ductility, UXT-S showed greater ductility than UXT-H. Specifically, at 2% strain, UXT-S could maintain a stress level of 75% of the tensile strength whereas UXT-H could sustain only 25% (Table 3.4).

3.3 Biaxial Tests

3.3.1 Testing procedures

A total number of 90 specimens with the size of 5.5 in × 5.5 in × 1.5 in were tested using an existing test setup at UI-MUST-SIM facility at the University of Illinois. This test setup was composed of four independent actuators each with loading capacity of 112 kips (500 kN) situated on the loading frame. Each actuator was attached with a brush-like platen that was designed in such a way that when the load was applied in the longitudinal direction, the specimen could expand freely in the transverse direction. The test setup was similar to that used by Kupfer et al. (1969). A non-contact displacement measurement system called Krypton® system was used for detailed measurement of the deformation in the test panels (Figure 3.7a). The signal receivers were placed in the middle of the specimen 1.5 in apart from each other as shown in Figure 3.7c. In each direction, receivers were aligned into three lines and the two outer receivers were used to measure the in-plane deformation along each line. The deformation along each line was then converted to strain and the in-plane strain was obtained by averaging three strains in each direction. Hence, the horizontal deformation was obtained by averaging the deformation of receivers (1-3, 4-6, and 7-9 receivers) whereas the vertical deformation was obtained by averaging the deformations of receivers (1-7, 2-8, and 3-9 receivers). In addition, an LVDT was attached at the back panel of the specimen to measure the out-of-plane expansion (Figure 3.7b). The out-of-plane deformation was obtained by adding the z-direction movement of the middle receiver (No. 5) with the deformation of the LVDT.

The main parameter varied during the tests was the ratio between principal strains. Due to symmetry in biaxial strain space, the four loading paths shown in Figure 3.8 are sufficient to provide the necessary information regarding the biaxial compression-compression behavior of HPFRCC. The loading paths are classified as the ratio of the vertical to the horizontal strain: C-C for ratio of 1; C-0.4C for the ratio of 0.4; C-0.6C for the ratio of 0.6; UXC for the ratio of 0.

3.3.2 Test results

During the first trial experiments, it was found that all specimens exhibited failure by out-of-plane splitting. This was manifested in the load-displacement curve as a sudden drop after the peak point (Figure 3.9). This problem was due to the fact that the length of the fibers was about the same size as the thickness of the specimen. Thus, the fibers were aligned in the in-plane direction of the specimen. In other words, there was no fiber in the out-of-plane direction to prevent the splitting crack. To alleviate this problem, each series was recast into one big specimen with dimensions of 6.5 in × 6.5 in × 18 in and then sliced into 10 specimens each of size 5.5 in × 5.5 in × 1.5 in. This improved the results dramatically as show in Figure 3.10. Table 3.5 summarizes the key parameters of the peak point of HPFRCC under uniaxial and equal biaxial compression.

The uniaxial compressive responses of HPFRCC tested with the biaxial test setup are shown in Figure 3.11. The longitudinal stress is plotted against both longitudinal and transverse strains. As can be seen, the strength of UXC-H increases as the fiber volume fraction increases. However, the strengths of UXC-S under all fiber volume fractions are about the same value. In term of the effect of the test setups and geometry of specimens, the comparison of uniaxial response between cylinders and rectangular panels is shown in Figure 3.12. In the pre-peak region, the Young’s moduli obtained from both setups are almost identical but the cylinder specimens give higher compressive strength than that of rectangular specimens. In addition, the amount of fibers in cylinder specimens does not affect the compressive strength. In the post-peak region, the rectangular panels are more ductile than the cylinders in the hooked fiber case. However, the ductility in Spectra is less affected by the setup or geometry of specimens when compare with the hooked fiber.

The equal biaxial compressive responses of both fiber types are plotted against the uniaxial compression in Figure 3.13. In the pre-peak regime, the initial slope of both uniaxial and equal biaxial compressions is identical for both types of fibers. However, the peak stress of both fibers is improved over the uniaxial compressive strength. In the post-peak regime, except the BXC-C-S1 and BXC-C-S1.5, the ductility under equal biaxial compressions is similar to that under uniaxial compression. For the BXC-C-S1 and BXC-C-S1.5, the receivers were detached from the specimens after reaching the peak load. Hence, the post-peak strains were discarded in the graph. The failure envelopes of specimens with both fibers under biaxial state of stress are compared with normal concrete in Figure 3.14. Under equal biaxial compression (BXC), the ratio between the peak strength and the unconfined compressive strength is improved from 1.1 in high strength concrete to 1.5 and 1.6 in HPFRCC constructed with hooked and Spectra, respectively. The failure envelopes of regular concrete were obtained from Hussein & Marzouk (2000). The enhancement is attributed to the fibers, which prevent out-of-plane expansion, which in turn helps to improve the confinement and thus increases the compressive capacity.

3.4 Triaxial Tests

3.4.1 Testing procedures

Passive triaxial tests were performed using a 500-kip compression machine. A steel tube 3 in in nominal diameter and 7 in in height was used to encase the HPFRCC specimens to the necessary confinement (Figure 3.15). The level of passive confinement was varied by changing the thickness of the tube. Two thicknesses of steel tubes used in this study are 1/8 and 1/16 in, which are denoted on the first term of ID as “S” and “M”, respectively (see Figure 3.1). During the casting process, a thin Teflon sheet was placed inside the steel tube to minimize friction between specimen and the tube. The HPFRCC material was cast inside the tube. A clear depth of 0.5 in was left on each end so that a steel loading plate could fit inside the tube and directly load the specimens.

Three LVDTs were placed along the side of the tube for measuring longitudinal deformation and two strain gauges were attached to the tube at the mid-height (on opposite sides of the tube) in both longitudinal and circumferential directions. The longitudinal strain gauge was used to evaluate the effect of friction between specimen and the tube whereas the circumferential strain gauge was used to measure the expansion of the tube which was then converted to confining pressure.

The dog-bone shape steel pieces were cut from the tube and direct tension tests were performed to obtain the stress-strain curve of the steel tube. Once the stress-strain curve of steel tube was known, the circumferential strain of the steel tube could then be converted to circumferential stress and this stress was then converted to confining pressure using the following formula:

$$\mathrm{P} = \frac{\sigma \mathrm{t}}{\mathrm{R}} \tag{3.1}$$

where P is the confining pressure, σ is the circumferential stress, R and t are the radius and thickness of steel tube, respectively. From the direct tension tests and the above formula, the maximum confining pressure of 1/8-in and 1/16-in thick are 6 and 7.5 ksi, respectively.

3.4.2 Test results

The stress-strain responses of HPFRCC under triaxial compression test are plotted in Figure 3.16. The overall stress-strain response is not influenced by the type and volume fractions of fiber. This is attributed to the heavy confinement provided by the steel tube which over shadowed the effect of the fibers. Nevertheless, the strength of both hooked and Spectra specimens under both confining pressures is slightly greater than regular mortar. Figure 3.17 illustrates the responses of HPFRCC with 2% Spectra under all loading conditions tested in this study. The initial slope of the responses under all loading conditions is the same but the strength is improved as the confining pressure increases. Another observation is that the minimum volumetric strain $\left(\varepsilon_{\mathrm{v,min}}\right)$ of Spectra specimens, which indicates the ability of specimen to expand laterally in the hardening regime, was double that of mortar (Figure 3.18). This volumetric strain $(\varepsilon_{\mathrm{v}})$ is calculated by adding the longitudinal strain with the lateral expansions, which are identical in both transverse directions. The minimum volumetric strain indicated as the lowest contraction point of the volume strain is numerically defined as the lowest negative number of ε_{v}. Similar to the uniaxial compressive response, ε_{v} starts with the contraction as the lateral expansion at the initial state is still less pronounced than the longitudinal strain. However, as the load increases, the lateral expansions increase at a higher rate than the longitudinal deformation and subsequently, the volumetric strain switches from negative to positive. Table 3.6 summarizes the key parameters that are used to obtain the material parameters for the failure surface.

3.5 Conclusion

The chapter begins with discussion of the fiber properties and mix proportions used in this study. The mixing process to achieve the high performance response is given. In particular, it is noted that special care should be taken during mixing to avoid problems, such as segregation due to excessive liquid and balling of fibers, which could jeopardize the performance of the HPFRCC. The uniaxial tests under both compression and tension are discussed next. It is noted that the addition of short fibers into the mortar improves not only the strength but also the ductility in both loading paths, especially the tensile one. The biaxial compression-compression tests are discussed next, and the special loading platens that allow specimens to expand freely in the loading plane are described. The test results reveal that including the fiber significantly increases the material strength under biaxial loading because the fibers prevent the out-of-plane expansion inducing a confinement effect. The last section covers the triaxial compression tests, based upon which, it is concluded that under high pressure confining pressure, the effect of fibers is diminished. As a consequence, the shape of the yield surface depends mostly on the strength of the matrix and not on the fiber content.

Table 3.1 Mixed proportions by weight of cement

Matrix type		Mortar
Cement type 3		1
Aggregates	Silica sand (Flint)	1
	Coarse aggregate	-
Fly ash class C		0.15
Chemical admixtures	Super-plasticizer	Added when the mix is too dried
Water		0.4
Fibers	Types of fibers	Hooked & Spectra
	Volume Fraction V_f (%)	1.0, 1.5, and 2.0
Compressive strength f'_c ksi (MPa)		8 (55.2)

Table 3.2 Properties of fibers

Fiber Type	Diameter in (mm)	Length in(mm)	Density g/cc	Tensile strength ksi (MPa)	Elastic Modulus ksi (GPa)
Hooked	0.015 (0.38)	1.18 (30)	7.9	304 (2100)	29000 (200)
Spectra	0.0015 (0.038)	1.50 (38)	0.97	374 (2585)	16960 (117)

Table 3.3 Summary of the key parameters of the average test results of mortar and HPFRCC from uniaxial compression tests

Types of fiber	Fiber volume fraction (%)	ID	Young's modulus ksi (MPa)	Peak point		Post-peak strain at 40% of f_c' (%)
				Strength (f_c') ksi (MPa)	Strain (%)	
Spectra	1.00	UXC-S1	5421 (37376)	8.01 (55.19)	0.31	1.23
	1.50	UXC-S1.5	6528 (45009)	7.57 (52.21)	0.22	1.79
	2.00	UXC-S2	4292 (29592)	7.24 (49.93)	0.27	1.88
Hooked	1.00	UXC-H1	3083 (21257)	8.25 (56.91)	0.29	0.52
	1.50	UXC-H1.5	5360 (36956)	8.75 (60.30)	0.31	0.62
	2.00	UXC-H2	5288 (36459)	8.30 (57.23)	0.26	0.85
Mortar		UXC-M	3856 (26586)	6.27 (43.25)	0.21	0.43

Table 3.4 Summary of the key parameters of the average test results of mortar and HPFRCC from uniaxial tension tests

Types of fiber	Fiber volume fraction (%)	ID	First crack		Peak strength	
			Stress (σ_{cc})* ksi (MPa)	Strain (ε_{cc})* (%)	Stress $(\sigma_{pc})^*$ ksi (MPa)	Strain $(\varepsilon_{pc})^*$ (%)
Spectra	1.00	UXT-H1	0.15 (1.03)	0.024	0.46 (3.15)	1.61
	1.50	UXT-H1.5	0.14 (0.96)	0.021	0.48 (3.24)	1.24
	2.00	UXT-H2	0.13 (0.93)	0.019	0.45 (3.09)	0.61
Hooked	1.00	UXT-S1	0.16 (1.13)	0.010	0.51 (3.48)	0.28
	1.50	UXT-S1.5	0.19 (1.33)	0.013	0.61 (4.24)	0.29
	2.00	UXT-S2	0.18 (1.25)	0.017	0.58 (4.00)	0.30
Mortar		UXT-M	0.12 (0.82)	0.013	-	-

* referring to Figure 1.1

Table 3.5 Summary of the key parameters of the average test results of HPFRCC from biaxial compression tests

Types of fiber	Volume fraction (%)	Peak point							
		Uniaxial compression				Compression-Compression			
		Horizontal		Vertical		Horizontal		Vertical	
		Stress ksi (MPa)	Strain (%)	Stress ksi (MPa)	Strain (%)	Stress ksi (MPa)	Strain (%)	Stress ksi (MPa)	Strain (%)
Spectra	1.00	-	-0.53	6.35 (43.77)	0.53	9.42 (64.97)	0.28	9.36 (64.50)	0.49
	1.50	-	-0.31	5.39 (37.16)	0.43	8.61 (59.37)	0.68	9.98 (68.78)	0.64
	2.00	-	-0.36	5.64 (38.91)	0.68	9.57 (66.01)	0.71	8.40 (57.90)	0.93
Hooked	1.00	-	-0.37	5.23 (36.06)	0.44	9.98 (68.80)	0.58	10.37 (71.52)	0.70
	1.50	-	-0.29	7.24 (49.88)	0.56	10.06 (69.33)	0.53	10.24 (70.63)	0.70
	2.00	-	-0.42	7.48 (51.59)	0.72	9.40 (64.84)	0.81	9.54 (65.76)	0.73

Note: Negative number in ε for uniaxial compression case represents tension (expansion).

Table 3.6 Summary of the key parameters of the average test results of mortar and HPFRCC from triaxial compression test

Type of fiber	Volume fraction (%)	Confining pressure					
		6 ksi (41 MPa)			7.5 ksi (52 MPa)		
		f_{max} ksi (MPa)	ε_{max} (-)	$\varepsilon_{v,min}$ (%)	f_{max} ksi (MPa)	ε_{max} (-)	$\varepsilon_{v,min}$ (%)
Spectra	1.00	21.17 (145.95)	0.025	-0. 53	32.17 (221.83)	0.037	-0. 91
	1.50	21.48 (148.10)	0.040	-0. 61	32.62 (224.89)	0.042	-0. 71
	2.00	20.47 (141.16)	0.045	-0. 61	31.67 (218.36)	0.048	-0. 92
Hooked	1.00	21.51 (148.33)	0.015	-0. 55	30.01 (215.38)	0.033	-0. 54
	1.50	22.10 (152.41)	0.022	-0. 55	31.24 (215.39)	0.040	-0. 40
	2.00	22.83 (157.40)	0.018	-0. 59	32.21 (222.05)	0.041	-0. 43
Mortar		18.90 (130.31)	0.013	-0. 33	28.76 (198.28)	0.034	-0. 71

f_{max}: Maximum stress

ε_{max}: Corresponding longitudinal strain at maximum stress (positive number represents contraction).

$\varepsilon_{v,min}$: Minimum volumetric strain (negative number represents contraction).

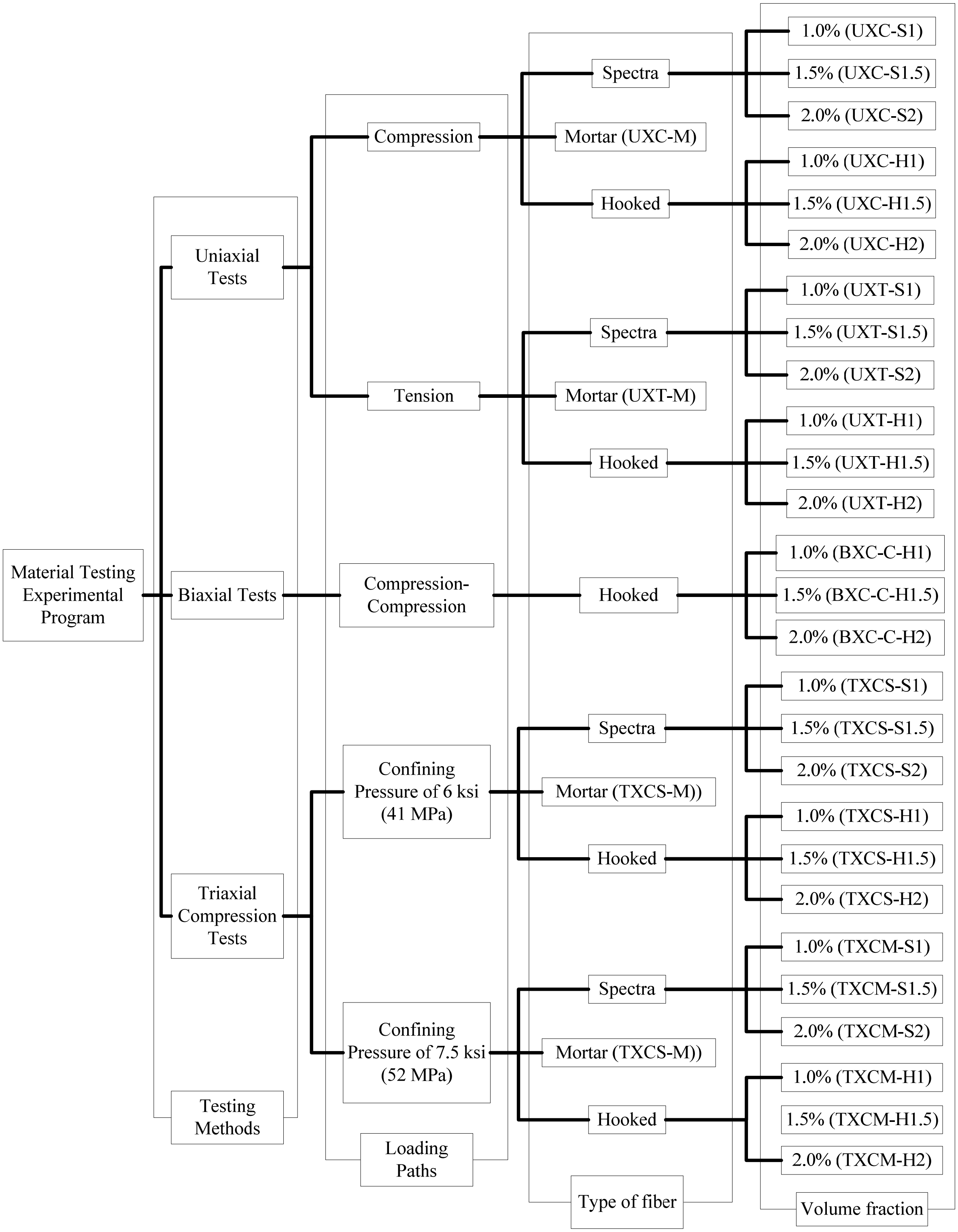

Figure 3.1 Flowchart of experimental program with ID

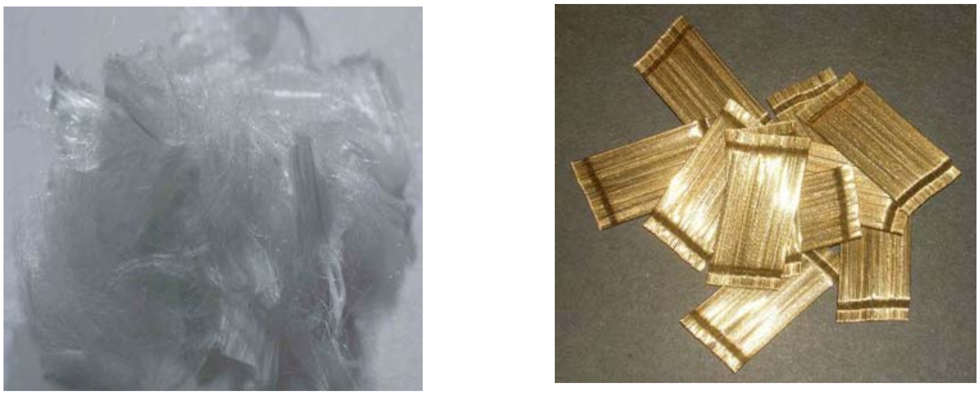

(a) Spectra fibers (b) Hooked fibers

Figure 3.2 Photos of (a) 1.5-in. long Spectra fibers and (b) 1.5-in. long hooked fibers

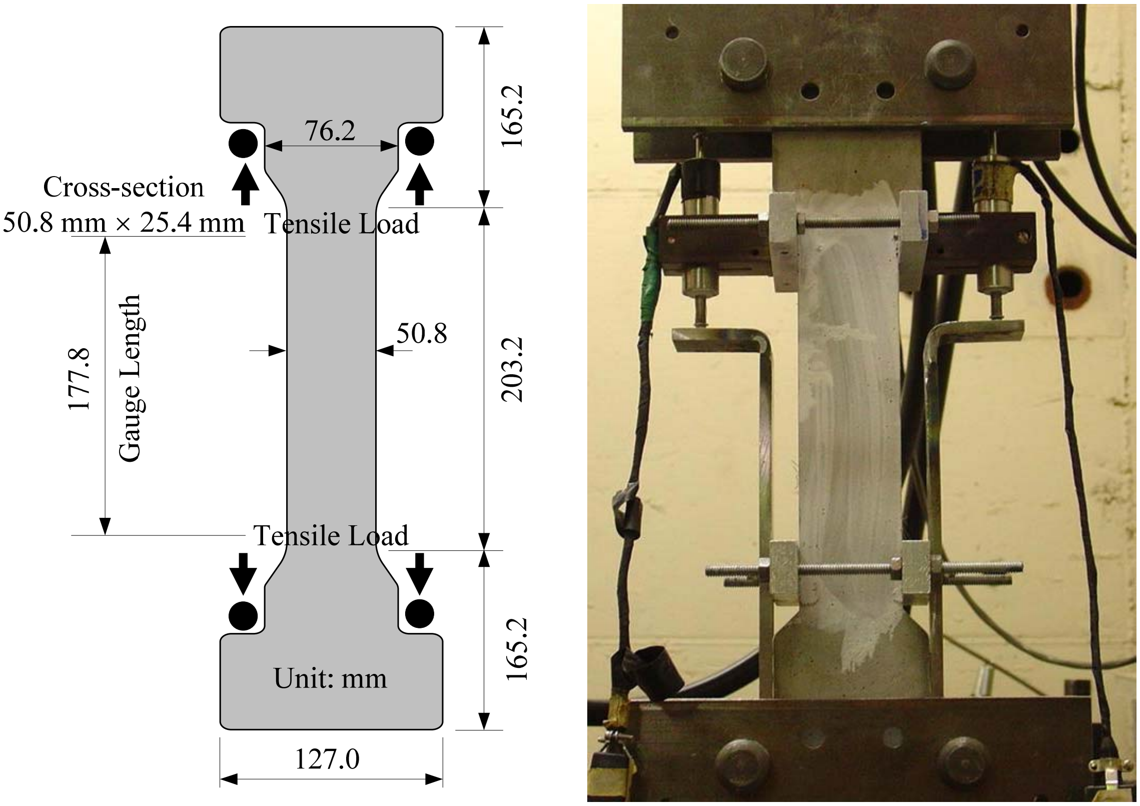

(a) Dimension of dog-bone specimen (b) Test setup (Likhitruangsilp, 2006)

Figure 3.3 Configuration of tensile specimen

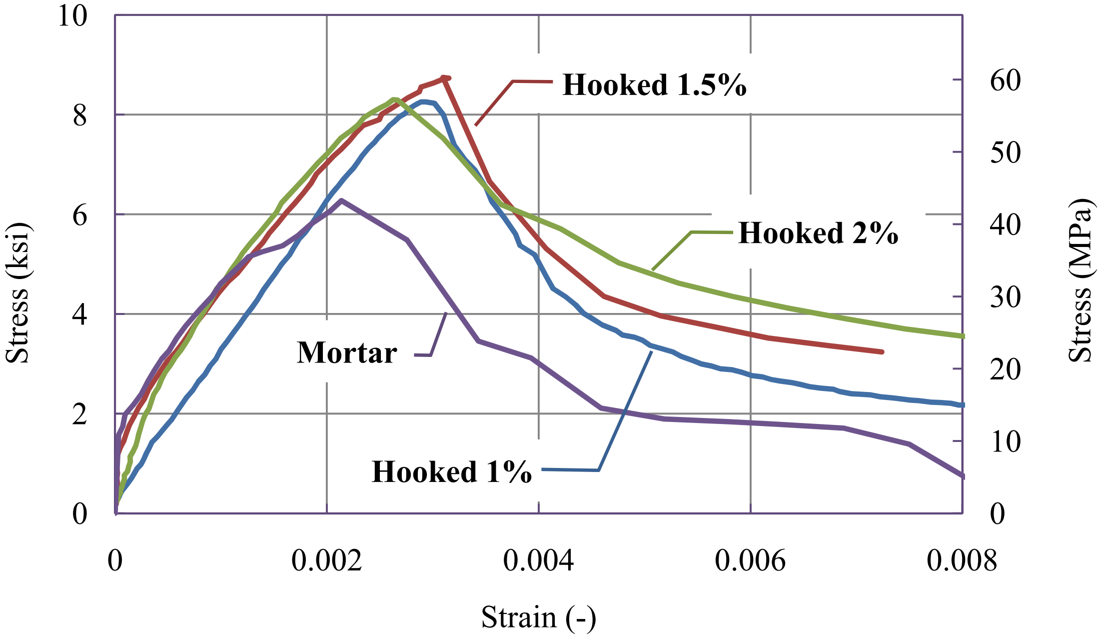

(a) Hooked fiber

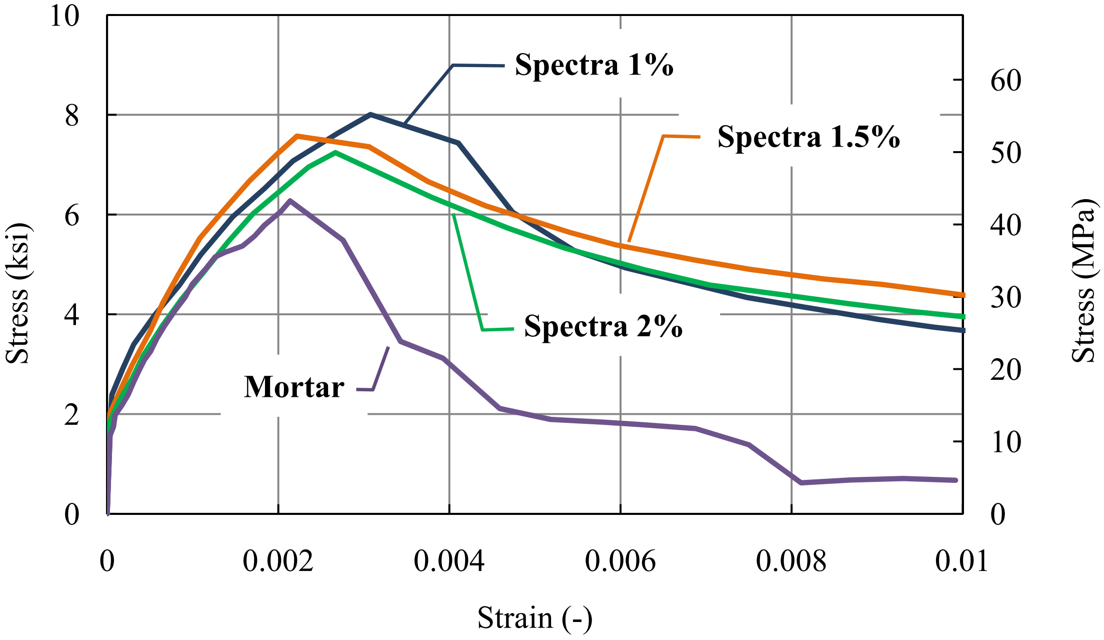

(b) Spectra fiber

Figure 3.4 Effect of volume fractions of fibers on uniaxial compressive behavior of HPFRCC

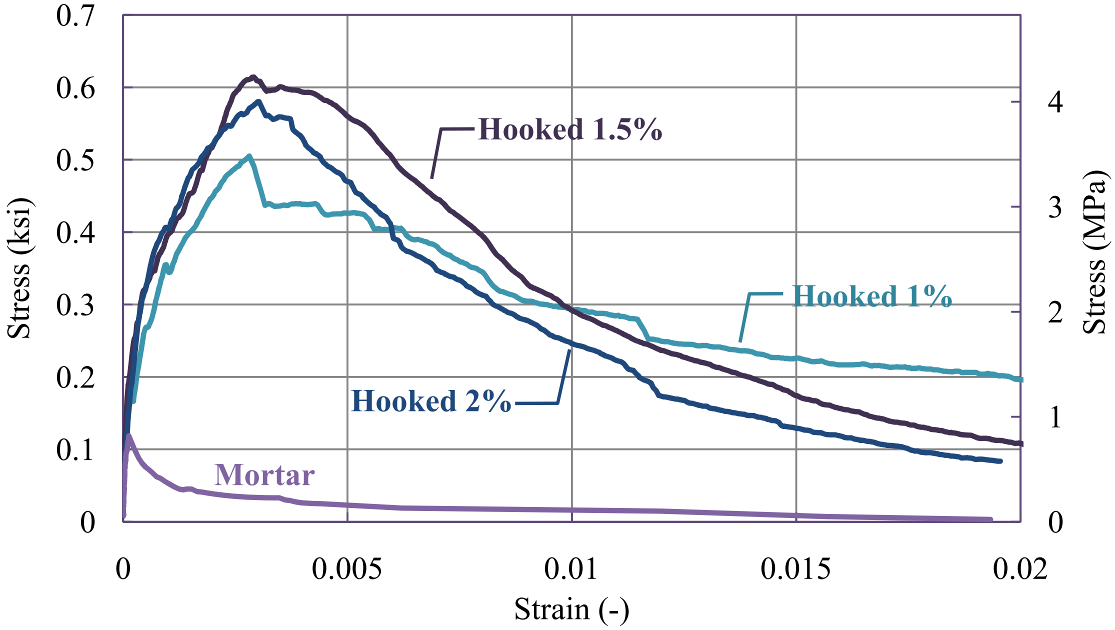

(a) Hooked fiber

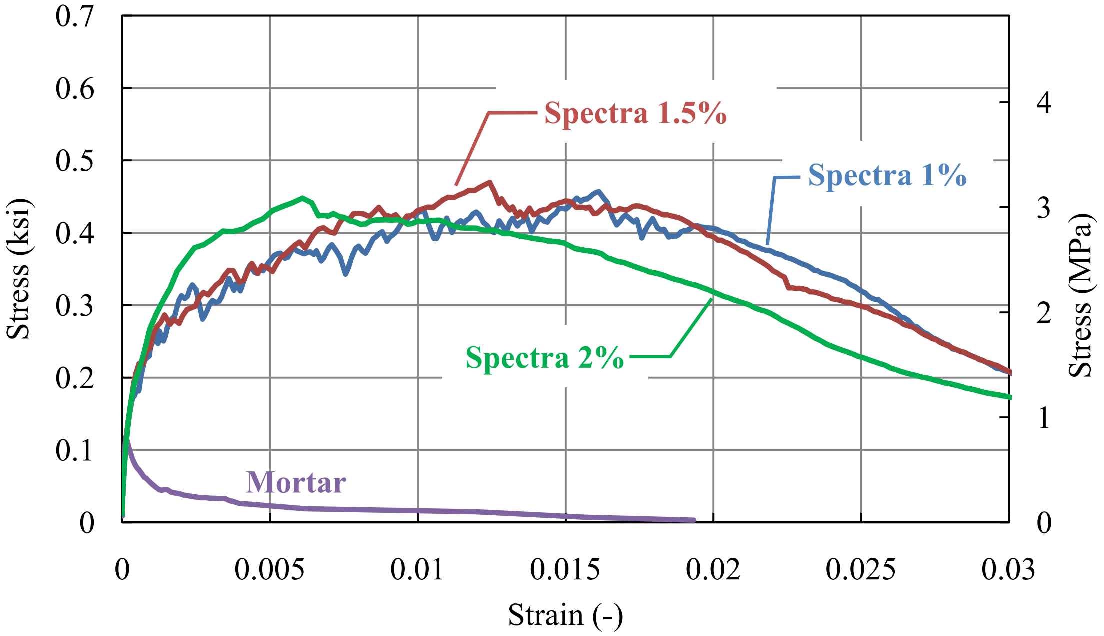

(b) Spectra fiber

Figure 3.5 Effect of volume fractions of fibers on uniaxial tensile behavior of HPFRCC

(a) First few cracks (b) Saturated cracks (c) Localization

Note: Light color line represents minor crack
Dark color line represents major crack

Figure 3.6 Photos showing multiple cracks at different loading states observed in HPFRCC with Spectra 1% in tensile test

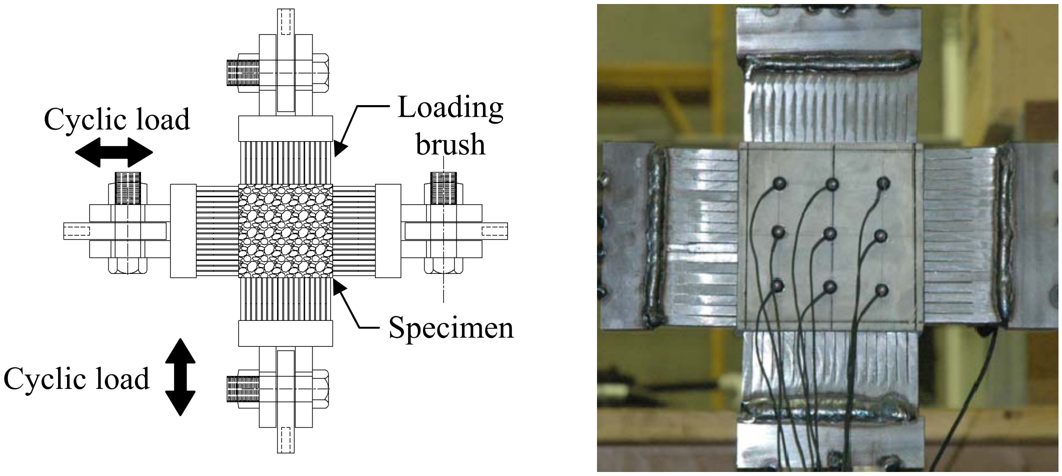

(a) Nine Krypton receivers measure the 3D deformations (front panel)

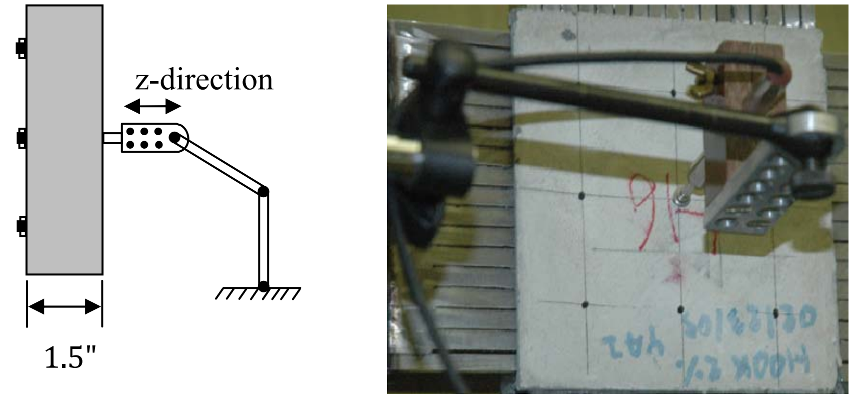

(b) LVDT attached at the middle point of the back panel measures the out-of-plane expansion (back panel)

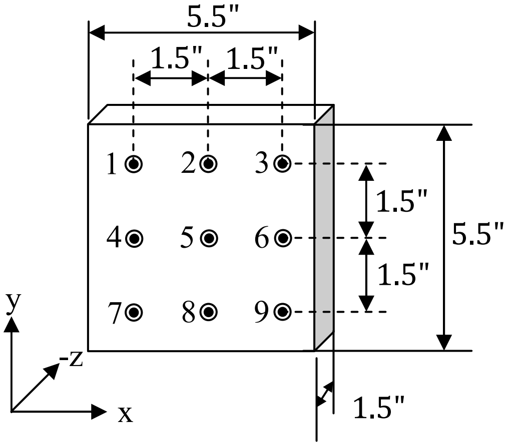

(c) Positions of Krypton receivers at the front panel

Figure 3.7 Biaxial test setup with the measuring systems

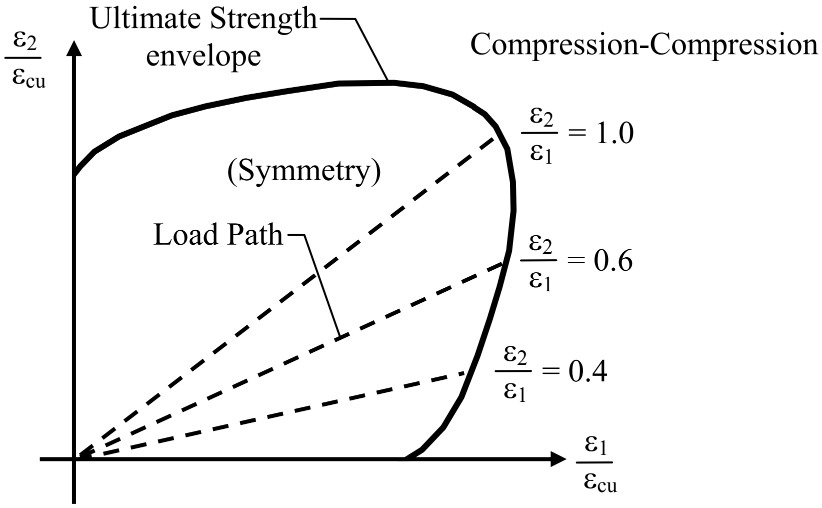

Figure 3.8 Nominal loading paths in strain space under biaxial compression-compression state of stress

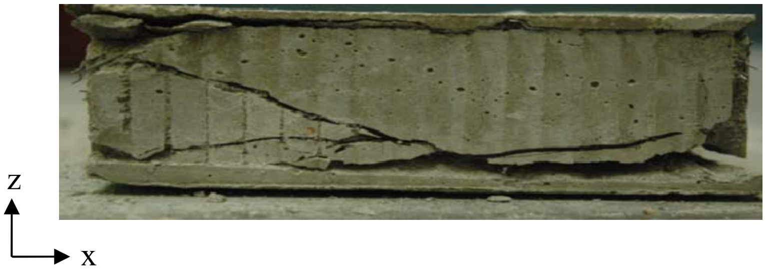

(a) Splitting in the out-of-plane direction

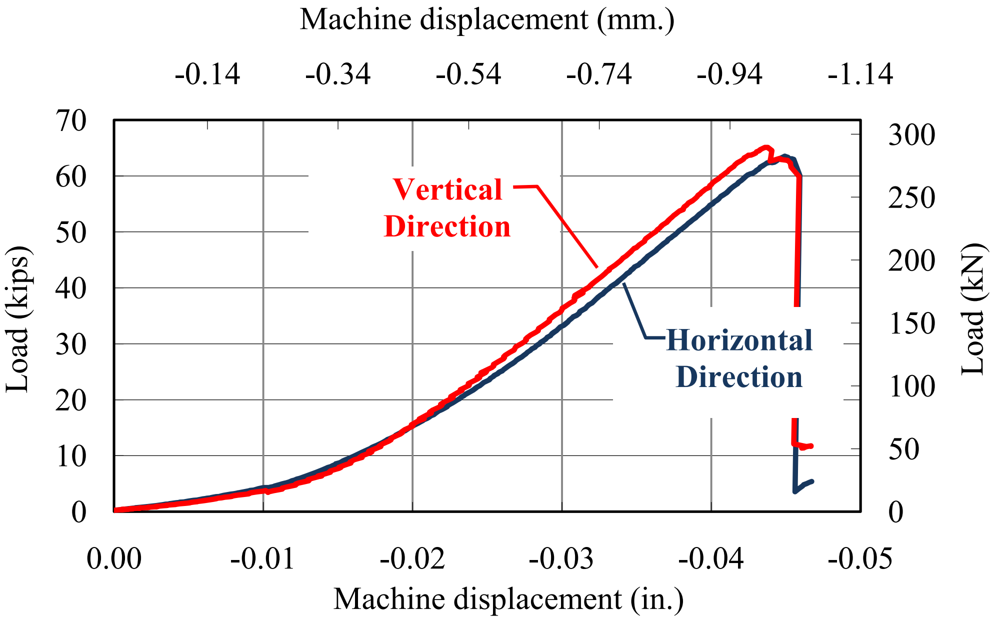

(b) Sudden drop of loading after the peak load (BXC-C-H1)

Figure 3.9 Problem with individual casting of specimen is the out-of-plane splitting failure caused sudden drop of load after its peak

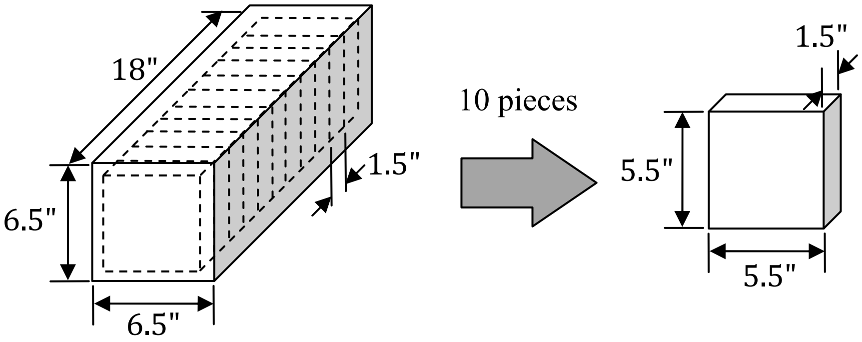

(a) Solution to solve splitting crack is to cast 6.5" × 6.5" × 18" specimen and then slices into 10 pieces (5.5" × 5.5" × 1.5" each)

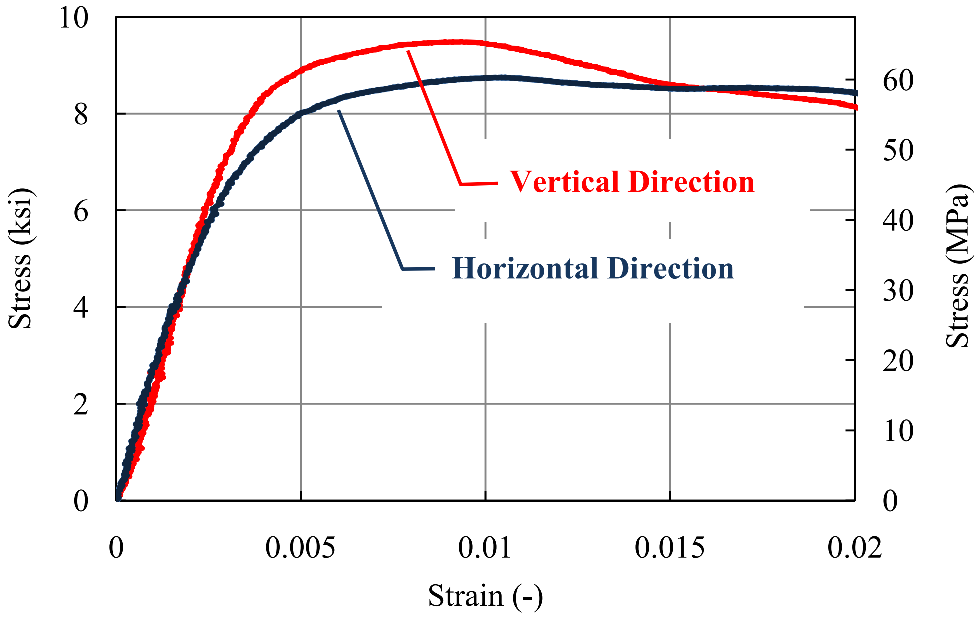

(b) No sudden drop of stress after the peak point (BXC-C-SP2)

Figure 3.10 Solution to solve the splitting crack in the out-of-plane direction

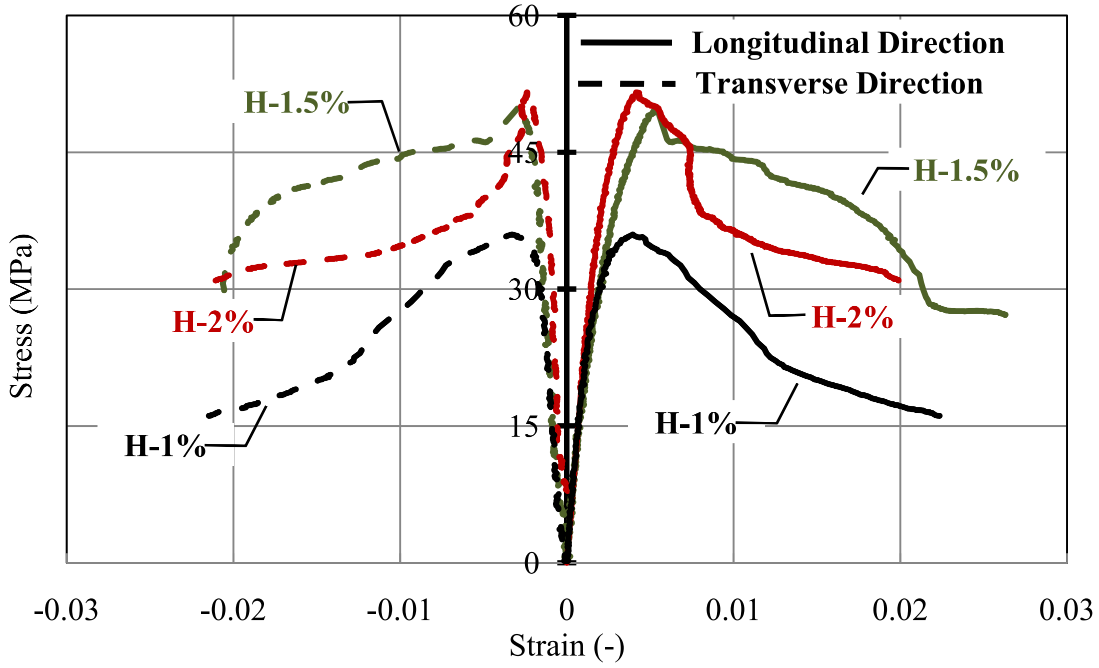

(a) Hooked fiber

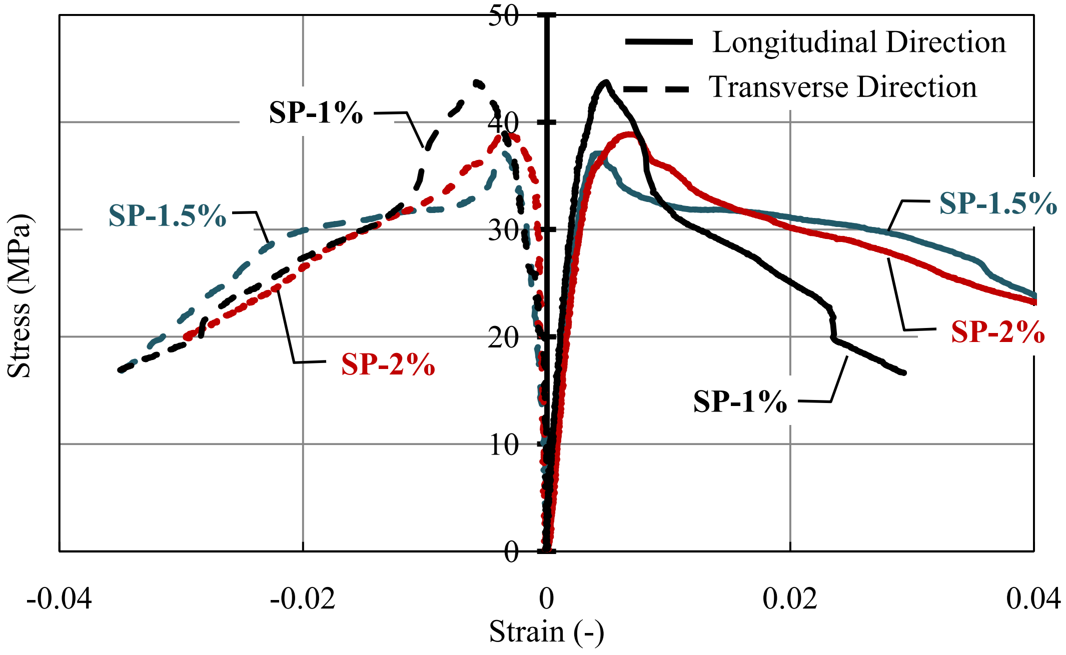

(b) Spectra fiber

Figure 3.11 Uniaxial compressive responses of HPFRCC

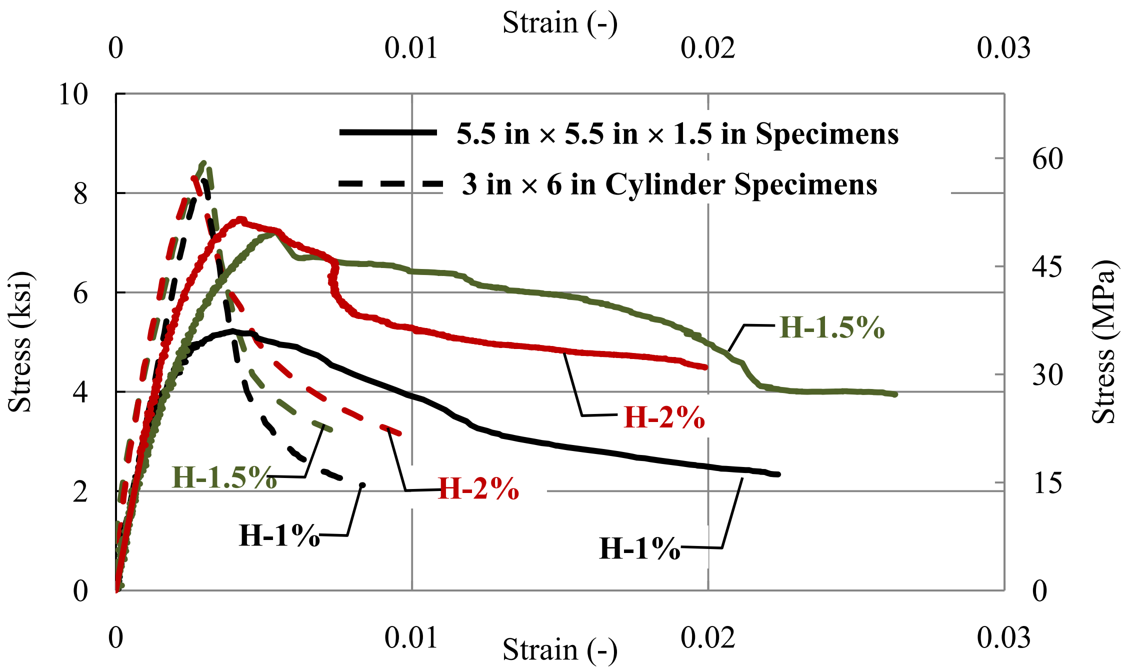

(a) Hooked Fiber

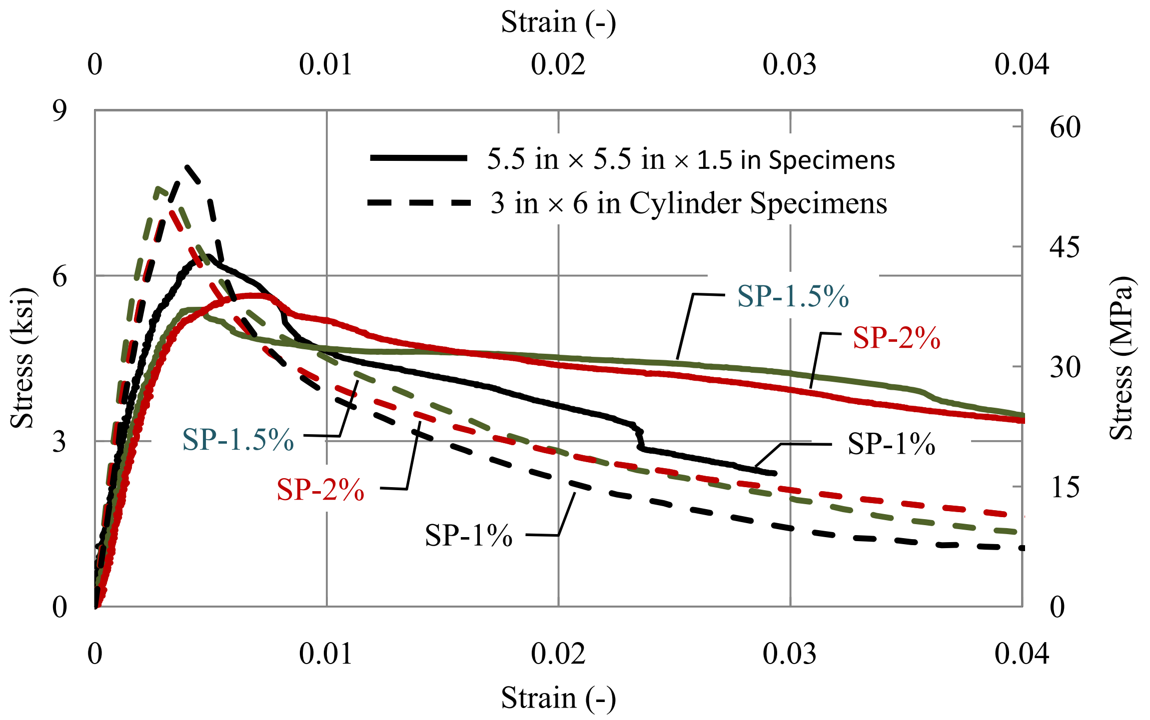

(b) Spectra fiber

Figure 3.12 Comparison of the uniaxial compressive responses between cylinder and rectangular panel specimens

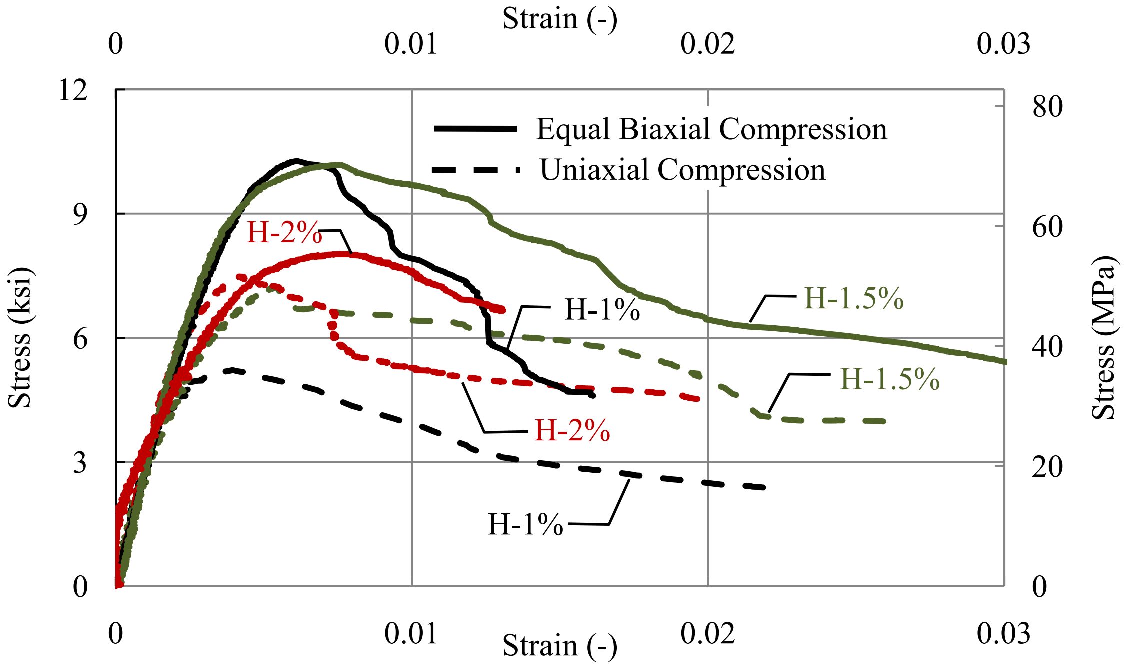

(a) Hooked Fiber

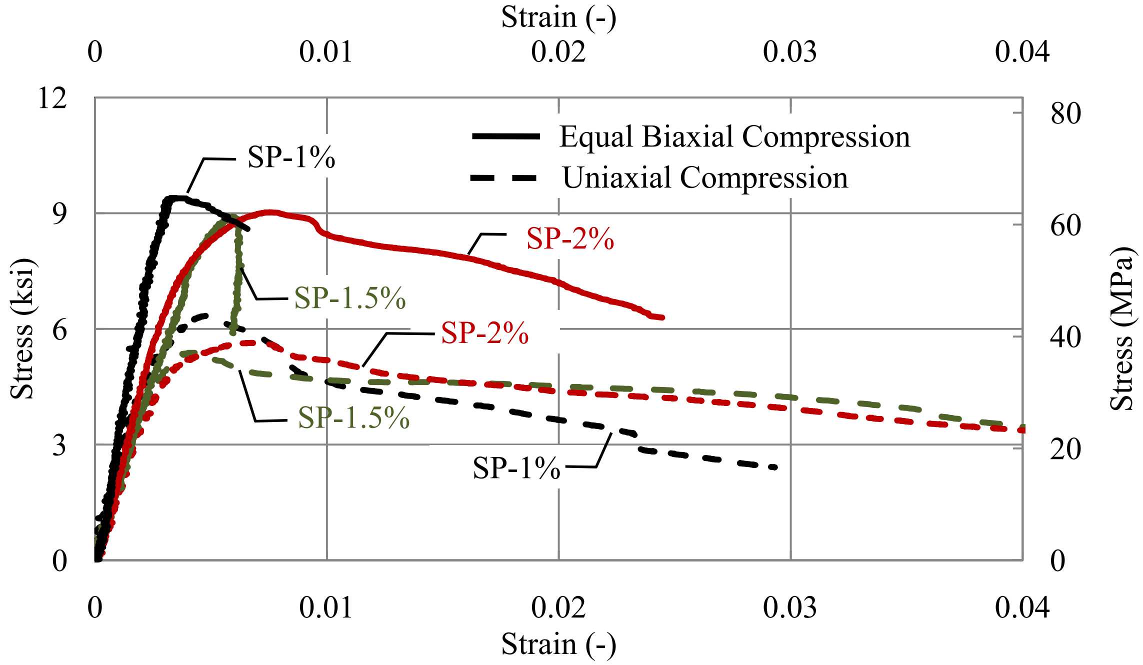

(b) Spectra Fiber

Figure 3.13 Comparison between equal biaxial compressive responses and uniaxial compressive responses of HPFRCC in rectangular panel specimens

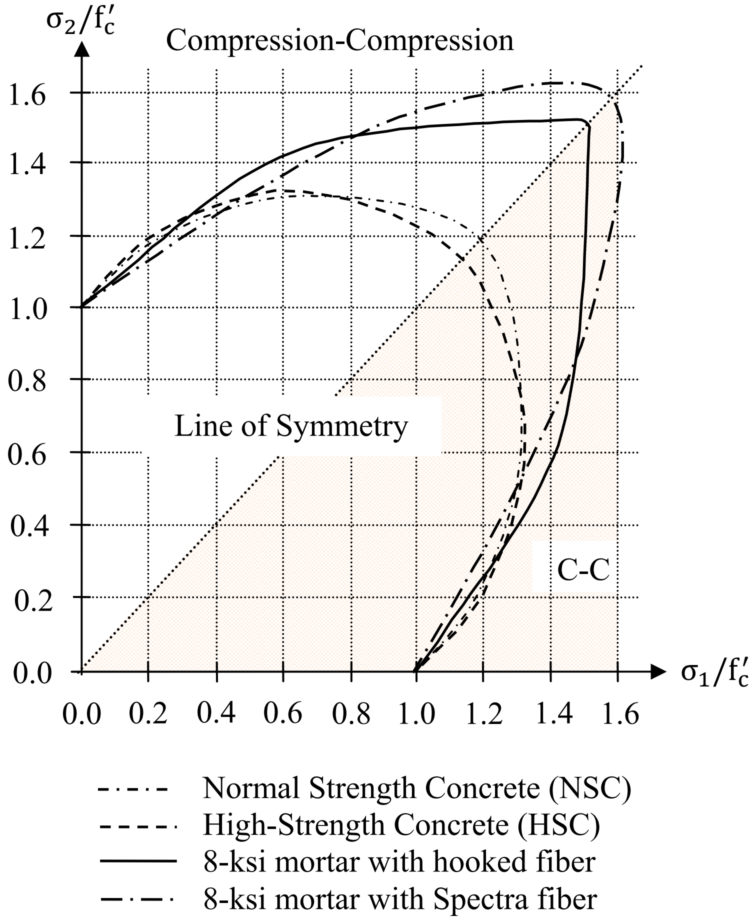

Figure 3.14 Failure envelopes of HPFRCC constructed with hooked and Spectra fibers under biaxial state of stress compared with ordinary concrete

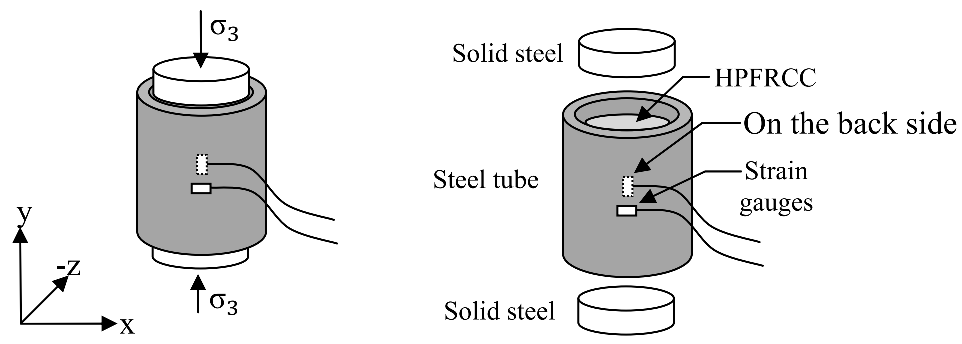

(a) Steel tube wrapped around the specimen provides confinement and two solid steel plates transmit load. Two strain gauges measure circumferential and longitudinal expansion of steel tube

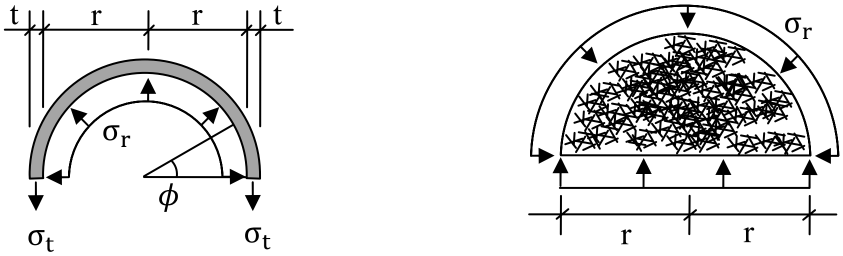

(b) Steel tube provides confining pressure (Grassl, 2003)

(c) Specimen subjected to confining pressure (Grassl, 2003)

Figure 3.15 Passive triaxial test setup

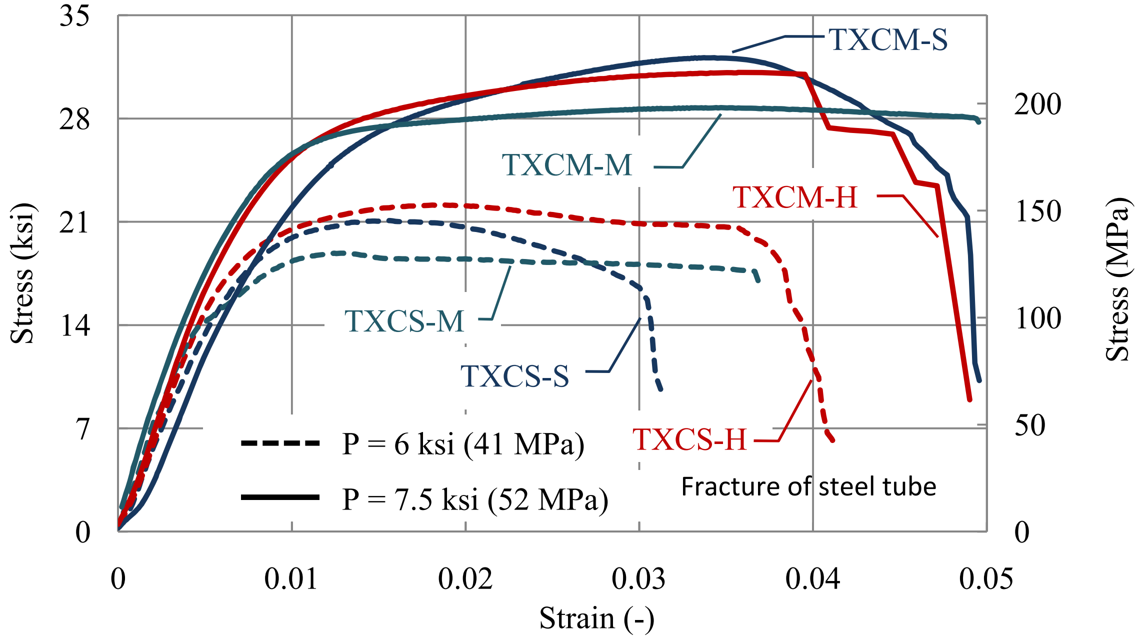

Figure 3.16 Stress-strain responses in longitudinal direction under two levels of confining pressure (6 ksi and 7.5 ksi)

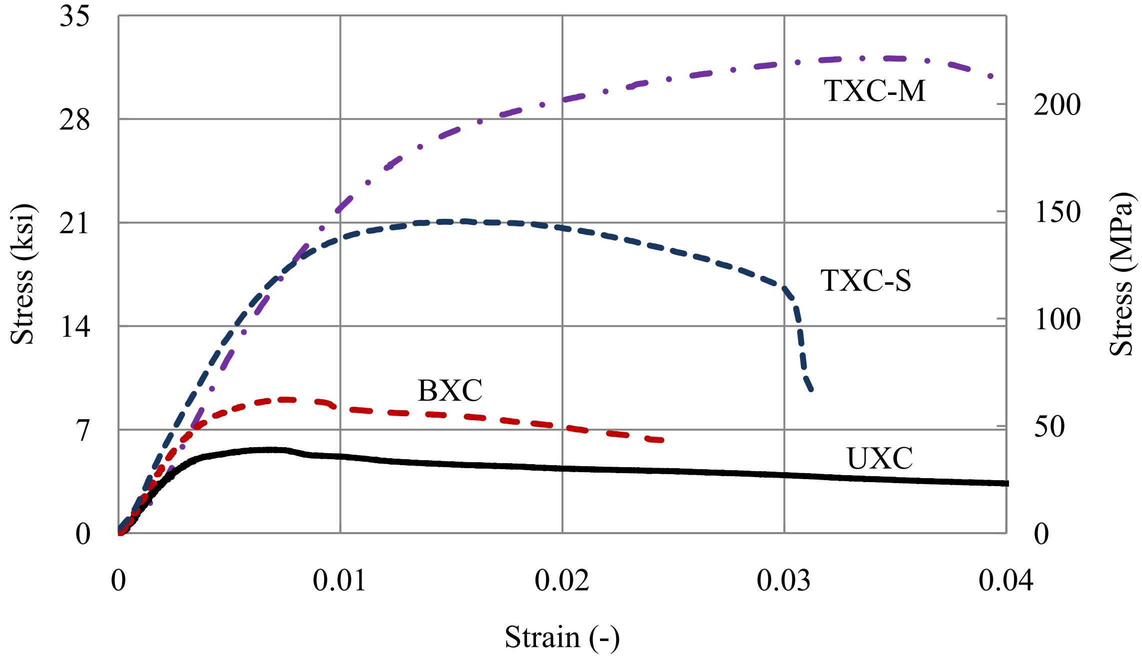

Figure 3.17 Comparison of stress-strain responses of 2% Spectra under various compressive loading conditions

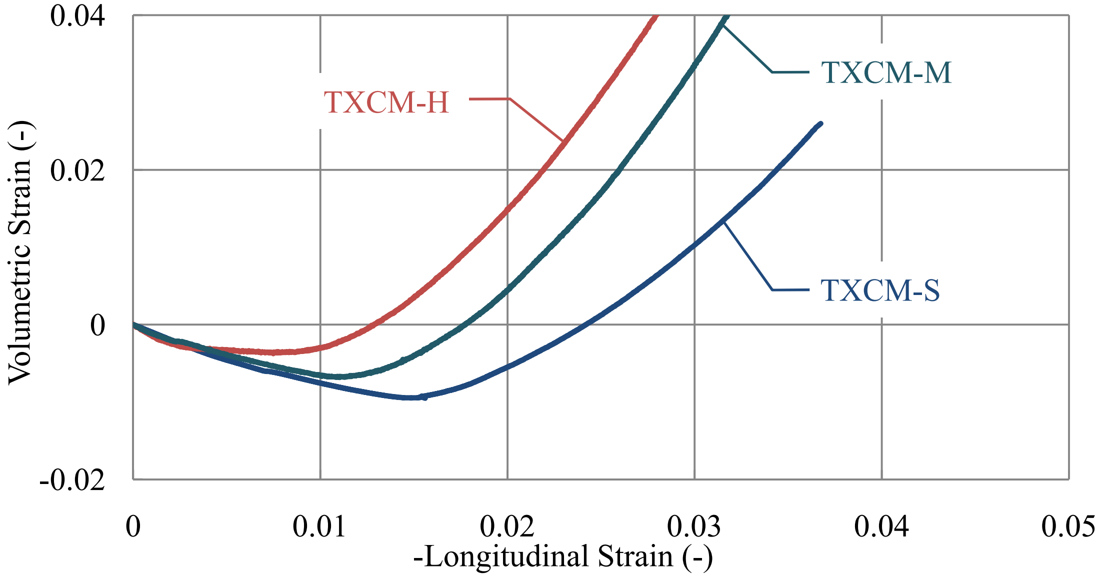

(a) Confining pressure of 7.5 ksi (52 MPa)

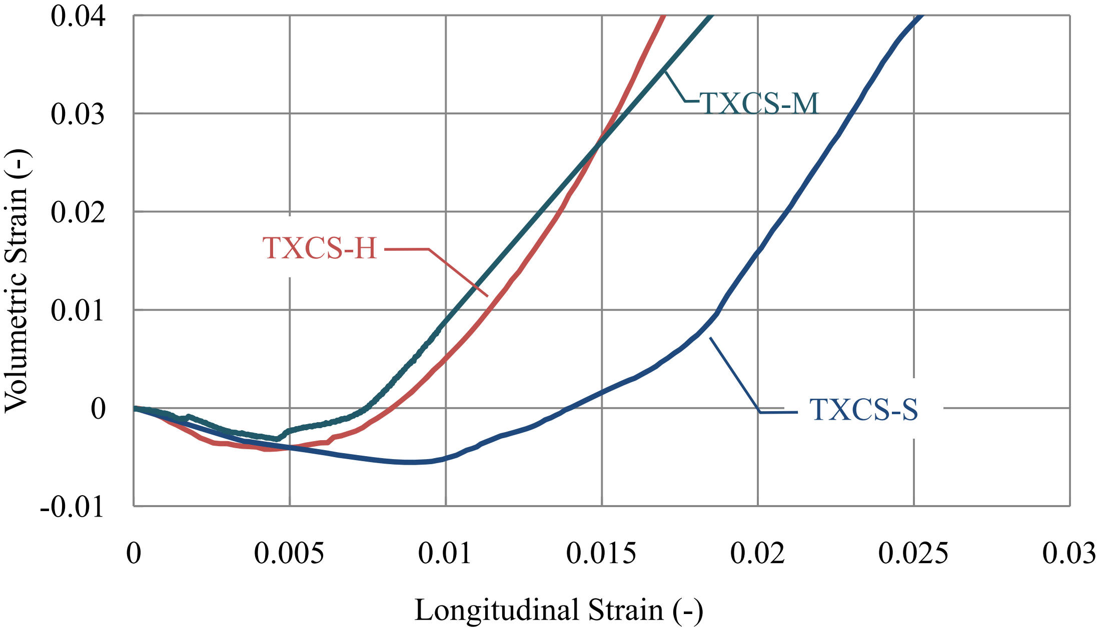

(b) Confining pressure of 6 ksi (41 MPa)

Figure 3.18 Volumetric strain versus longitudinal strain under triaxial compression tests

CHAPTER 4

THEORY OF MACRO-SCALE PLASTICTY MODEL FOR HPFRCC

A macro-scale plasticity model for High Performance Fiber Reinforced Cement Composites (HPFRCC) is presented in this chapter. First, a brief overview of general requirement for the plasticity model is given. Then, a four-parameter compressive yield surface for concrete proposed by Hsieh et al. is discussed and is further modified to develop a macro-scale plasticity model for HPFRCC. Finally, the tension yield surface is proposed and added into the developed model in the last section of this chapter.

4.1 Introduction

Because HPFRCC behaves like many geomaterials in an inelastic nonlinear manner, a simple linear elastic model is not sufficient to describe its stress-strain behavior. Therefore, a macro-scale plasticity model that is based on phenomenological observations of HPFRCC behavior is introduced. Phenomenological models employ a mathematical formulation to describe the macro-scale behavior of a given material without regard to how it behaves at the micro-scale level (Ogden, 1984). One essential requirement of this theory is material homogeneity in which material components are uniformly distributed. In the case of HPFRCC, this requirement is satisfied, in that fibers are not organized in any specific patterns and are distributed randomly. Even though, phenomenological models heavily depend on engineering judgment, such models have been successfully used by many researchers and are widely accepted to provide good accuracy with less computational demand than micro-scale models.

4.2 Plasticity Model for Compressive Response of HPFRCC

The behavior of ordinary concrete is first discussed in this section with emphasis on the requirements for concrete yield surfaces. These requirements are then used to extend an existing model for concrete to model HPFRCC response. Since HPFRCC behaves differently in compression and tension, a separate model for tension response is also proposed.

4.2.1 General characteristics of the plasticity model in concrete

The response of regular concrete under uniaxial compression shown in Figure 4.1 can be divided into two different sides, i.e., compression and tension. In the compression regime, the response is initially linear elastic up to point A, i.e. the loading/unloading are on the same path (Figure 4.1). Beyond point A, the concrete starts to develop permanent plastic deformations as a result of micro-cracks and collapsing air voids inside the concrete. In other words, the concrete will not be able to fully revert back to the starting stage when unloading occurs. Under such conditions, the loading and unloading paths no longer coincide. Concrete will soften in compression beyond the peak stress.

The yield surface of concrete must have the following characteristics: (1) smooth and convex; (2) pressure-dependent; (3) able to model the difference between compressive and tensile strength; (4) nonlinear in the meridian plane; and (5) able to capture the change in volumetric strain. The first condition is derived from the consequences of Drucker's postulates and ensures that the concrete material is stable. However, this condition does not necessarily apply under the softening regime. The second condition arises from triaxial compression test results (Schwer, 2002). In Figure 4.2, the load starts at stage I where the particles inside concrete resist the load up to pressure P_1. At this stage, no permanent deformations have taken place yet and therefore, the concrete material is assumed to behave as an elastic material. Once the pressure exceeds P_1, air voids inside the concrete starts to collapse and hence, the bulk modulus, which is the slope between pressure and volumetric strain, reduces. Stage II can also be referred as work-hardening stage. At pressure P_2, the concrete particles are fully compacted; thus the load is now solely resisted by concrete particles and crushing starts to take place. The third and forth conditions, which are logically necessary conditions, can be achieved by using a non-circular cross-section with a larger radius on the compressive meridian. In addition, test results reveal that at low hydrostatic pressure, the yield surface shape is nearly triangular. However, as the pressure increases, the yield surface bulges (becomes more circular). The last characteristic also stems from experimental data, where it has been observed that the volumetric strain starts with contraction up to peak stress, followed by dilation (expansion) beyond (Figure 4.3). Moreover, triaxial test results show that the volumetric strain direction does not coincide with the direction of plastic flow (Smith et. al, 1989). Therefore, the non-associative flow rule should be used to model concrete.

Concrete plasticity models can be classified according to the number of parameters required to define the yield surface. The number of parameters range from two up to five parameters in the literature. A one-parameter model is not enough to fully define a concrete yield surface, since concrete is a pressure-dependent material. Some examples of two-parameter models are the Mohr-Coulomb and Drucker-Prager models; further examples can be found in Chen (1982), Jansen (1975), and Schreyer and Babcock (1985). Examples of three-parameter models can be found in William and Warnke (1975); Chen and Chen (1975); Chen et al. (1980); Elnashai and Nicholson (1986); Lade (1982); and Lade et al. (1994). Examples of four-parameter models can be found in Ottosen (1977); Hsieh et al. (1979); Voyiadjis and Abu-Lebdeh (1994); and Imran and Pantanzopoulou (2001). Examples of five-parameter models can be found in William and Warnke (1975); Barzegar and Maddipudi (1997); and Balan et al. (2000).

4.2.2 Original HTC model

Hsieh et al. (1979) proposed the four-parameter HTC model by combining an equilateral triangular cross-section with a circular shape to represent the surface shape in the deviatoric plane. In the derivation of this yield function, three of five requirements listed in the previous section are considered. First, the compressive meridian must be higher than the tensile meridian under the same level of pressure. Consider the two extreme yield surfaces in the deviatoric plane as shown in Figure 4.4a. The two cross-sections represent a circle ($\mathrm{r} = \mathrm{k}$) and an equilateral triangle ($\mathrm{r}(\cos\theta) = \mathrm{k}$). To satisfy this first condition, these two cross-sections are merged and the new cross-section equation becomes $\mathrm{r}(\mathrm{a}\cos\theta + \mathrm{b}) = \mathrm{k}$. Second, the yield surface drawn in the meridian plane is nonlinear. This was achieved by introducing a square term of 'r' into the cross-section equation. Third, the yield function is pressure-dependent, which was accomplished by adding the pressure term 'ρ' into the equation. The new yield function of the HTC model is:

$$F(\rho, r, \theta) = ar^2 + (\alpha\cos\theta + \beta)r + C\rho - 1 = 0 \qquad (4.1)$$

where r and ρ represent the deviatoric and the hydrostatic components of stress tensors, respectively $\left(r = \sqrt{2J_2}, \rho = \frac{I_1}{3}\right)$. Material constants a, α, β, C can be directly obtained from experiments. It should be noted that even though the smoothness and convexity conditions were not considered when deriving the yield function, Eq. (4.1) does satisfy this requirement. The yield function can also be expressed as a function of invariants as:

$$F(I_1, J_2, \sigma_1) = A\frac{J_2}{(f_c')^2} + B\frac{\sqrt{J_2}}{f_c'} + C\frac{\sigma_1}{f_c'} + D\frac{I_1}{f_c'} - 1 = 0 \qquad (4.2)$$

where A, B, C, and D are material parameters that can be evaluated from four different loading conditions: unconfined uniaxial compression, equal biaxial compression, confined triaxial compression, and uniaxial tension (Hsieh et al., 1982).

Three drawbacks of this original model can be identified. First, this model does not consider post-peak behavior, i.e. post peak response. Secondly, the model does not consider the evolution of volumetric strain. Lastly, since the associative flow rule is used, the plastic flow direction is perpendicular to the yield surface, which is contradictory to actual test results.

4.2.3 Modified HTC model

To address the drawbacks of the original HTC model, Imran and Pantazopoulou (2001) modified the HTC model by adding softening and potential functions to capture the post-peak behavior and the change in volumetric strain, respectively. The yield function of the modified HTC model is composed of two parts: the hardening (F_1) and the softening parts (F_2) and the new equation can be written as:

$$F(\boldsymbol{\sigma}, k, r) = F_1(\boldsymbol{\sigma}, k) + F_2(\boldsymbol{\sigma}, r) \qquad (4.3)$$

where

$$F_1(\boldsymbol{\sigma}, k) = \frac{AJ_2}{kf_c'} + B\sqrt{J_2} + Ck\sigma_1 + DkI_1 + E_{htc}\frac{1-k}{kf_c'}I_1^2 - kf_c' \tag{4.4}$$

and

$$F_2(\boldsymbol{\sigma}, r) = -(1-r)\frac{I_1}{I_1^{trans}}f_c' + (1-r)f_c' \tag{4.5}$$

The first term $F_1(\boldsymbol{\sigma}, k)$ remains almost the same as the original equation. The second term $F_2(\boldsymbol{\sigma}, r)$ was introduced to capture the post-peak response. The parameter I_1^{trans} in the second term was introduced to capture the failure mode of the post-peak response of concrete. This parameter represents the magnitude of hydrostatic stress at the transition point between brittle and ductile failure modes. If the confining pressure is three times greater than I_1^{trans}, the failure mode of concrete shifts from brittle to ductile. The hardening and the softening parameters are derived from Hognestad's parabolic equation and the Cosine function, respectively (Figure 4.5).

$$k = \frac{\left(2\sqrt{\varepsilon_p\varepsilon_{p,max}} - \varepsilon_p\right)}{\varepsilon_{p,max}}(1-k_0) + k_0 \tag{4.6}$$

$$r = \frac{1}{2} + \frac{1}{2}\cos\left(\pi\frac{\varepsilon_p - \varepsilon_{p,max}}{\varepsilon_{p,ult} - \varepsilon_{p,max}}\right) \tag{4.7}$$

In Eq. (4.6) and (4.7), the scalar parameter ε_p is a measure of the plastic deformation that can be obtained from the equivalent inelastic work. As shown in Figure 4.5, $\varepsilon_{p,max}$ and $\varepsilon_{p,ult}$ correspond to the value of ε_p at the peak and residual strength, respectively and k_0 represents the value of k at the initial yield surface. The equivalent plastic work can be defined as follows:

$$\varepsilon_p = \int d\varepsilon_p \equiv \int \frac{\boldsymbol{\sigma}: \mathbf{d\varepsilon^p}}{kf_c'} \tag{4.8}$$

The evolution of the yield surface with respect to the hardening parameter k is shown in Figure 4.6. Unlike the J_2-plasticity model, this model uses a cap surface to limit the material strength in the hydrostatic loading case. Figure 4.7 and Figure 4.8 show the yield surface under various softening stages. If the hydrostatic pressure exceeds the transition pressure (I_1^{trans}), the effect of softening factor 'r' is diminished. In other words, the concrete behaves as a perfectly plastic material when the concrete is triaxially loaded under high hydrostatic pressure that is three times greater than I_1^{trans}.

Another feature added in this model is the non-associative flow rule. The Drucker-Prager yield surface is selected as the potential function which is used to control not only the direction of the plastic flow but also the amount of volumetric plastic strain. The Drucker-Prager function is defined as:

$$g(\boldsymbol{\sigma}) = a_C \frac{I_1}{\sqrt{3}} + \sqrt{2J_2} - c \tag{4.9}$$

where c does not need to be defined since only the gradient of the potential function is used. The parameter 'a_C' is the slope of the flow direction which in turn controls the amount of volumetric plastic strain and can be defined as:

$$a_C = \frac{a_u}{(1-\eta)} \left(\frac{\varepsilon_p}{\varepsilon_{p,max}} - \eta \right) \tag{4.10}$$

where a_u is the value of 'a_C' under uniaxial loading and η is the ratio of $\frac{\varepsilon_p}{\varepsilon_{p,max}}$ at zero volumetric plastic strain, which is also the same point where the stress reaches the peak point (Figure 4.3).

4.2.4 Modified HTC model for HPFRCCs

The experimental results of HPFRCCs under uniaxial compression reveal that the fibers help to prevent the sudden drop that occurs after the load reaches its peak point.

The fibers act in a manner similar to a thin confining tube surrounding specimen as shown in Figure 4.9. Because the presence of fibers does not significantly increase the strength, although it does increase ductility, a third term is introduced into the modified HTC described in Eq. (4.3). Since the softening shape of HPFRCCs is different from that of regular concrete, an exponential function is applied in the third term. Hence, the yield surface is now composed of three different functions, i.e. a hardening function (F_1), a cosine softening function (F_2), and an exponential softening function (F_3).

$$F(\boldsymbol{\sigma}, k, r) = F_1(\boldsymbol{\sigma}, k) + F_2(\boldsymbol{\sigma}, r) + F_3(\boldsymbol{\sigma}, s) \tag{4.11}$$

$$F_1(\boldsymbol{\sigma}, k) = \frac{AJ_2}{kf_c'} + B\sqrt{J_2} + Ck\sigma_1 + DkI_1 + E_{htc}\frac{1-k}{kf_c'}I_1^2 - kf_c' \tag{4.12}$$

$$F_2(\boldsymbol{\sigma}, r) = -(1 - Imp)(1 - r)f_c'\left[\frac{I_1}{I_1^{trans}} - 1\right] \tag{4.13}$$

$$F_3(\boldsymbol{\sigma}, s) = -Imp(1 - s)f_c'\left[\frac{I_1}{I_1^{trans}} - 1\right] \tag{4.14}$$

The parameter Imp controls the level of the stress at the beginning of the exponential softening curve as shown in Figure 4.10, whereas the exponential factor ‘s’ controls the slope of the softening curve that is expressed as a function of ε_p (Figure 4.5):

$$s = Exp^{-1}\left[\frac{-\omega(\varepsilon_p - \varepsilon_{p,int})}{\varepsilon_{p,ult} - \varepsilon_{p,int}}\right] \tag{4.15}$$

where the factor ‘ω’ controls the slope of exponential curve (Figure 4.11). $\varepsilon_{p,ult}$ indicates the plastic strain at the residual state. At this state, the material becomes perfectly plastic, i.e. stress does not increase or decrease with an increase in strain.

For the ease of fitting data, the definition of ε_p is changed from the equivalent inelastic work to the effective plastic strain and is expressed as:

$$\varepsilon_p = \int d\varepsilon_p \equiv \int \sqrt{\frac{2}{3}\mathbf{d\boldsymbol{\varepsilon}^p}:\mathbf{d\boldsymbol{\varepsilon}^p}} \tag{4.16}$$

Therefore, under uniaxial compression response, the material parameters $\varepsilon_{p,max}$, $\varepsilon_{p,int}$, and $\varepsilon_{p,ult}$ can be obtained by simply subtracting the elastic strain from the total strain.

4.3 Plasticity Model for Tensile Response of HPFRCC

In contrast to regular concrete where localization and subsequent sudden softening occur once the strain reaches the first crack, HPFRCC exhibits strain hardening tensile behavior until crack saturation occurs. In other words, the tensile behavior of HPFRCC showing strain hardening and then gradual softening makes it a good candidate for a tension plasticity model. Several points are considered in constructing the maximum tension yield surface as follows. First, the tension surface has to merge into the compression surface. In order to prevent sudden change in stress between compression and tension, the zero pressure point A, which represents the dividing point between both yield surfaces (Figure 4.12), is chosen. By substituting zero pressure $(I_1 = 0)$ into the modified HTC yield function (Eq. 4.11), the corresponding $\sqrt{J_2}$ at this point A is determined as

$$\sqrt{J_{2,1}} = \sqrt{J_{2,HTC}} = \frac{-2c}{b + \sqrt{b^2 - 4ac}} \tag{4.17}$$

where

$$a = \frac{A}{kf_c'} \tag{4.18.1}$$

$$b = B + \frac{2Ck}{\sqrt{3}} \sin\left(\theta + \frac{2\pi}{3}\right) \tag{4.18.2}$$

$$c = -kf_c' + [(1 - \mathrm{IMP})(1 - r)f_c'] + [\mathrm{IMP}(1 - s)f_c'] \tag{4.18.3}$$

Second, using the same method used for constructing the cap surface for the compression yield surface, the limit point for the tension yield surface is selected as point B in Figure 4.12 (where $J_2 = 0$). At this point, the material is under triaxial tension (TXT). Since there are no test results for this case, it is assumed in this study that the maximum principal stress is the same as the uniaxial tensile strength. Therefore, the second point is expressed as

$$\left(I_{1,2}, \sqrt{J_{2,2}}\right) = (3f_t, 0) \tag{4.19}$$

Third, an intermediate point C $\left(I_{1,3}, \sqrt{J_{2,3}}\right)$ located between the transition and TXT points is defined by using uniaxial and equal biaxial tensions. At uniaxial tension (UXT), the first invariant (I_1) and square root of the second invariant $\left(\sqrt{J_2}\right)$ are f_t and $f_t/\sqrt{3}$, respectively, whereas at equal biaxial tension (BXT), I_1 and $\sqrt{J_2}$ are $2\alpha f_t$ and $\alpha f_t/\sqrt{3}$, respectively. The parameter α represents the strength ratio between equal biaxial and uniaxial tensions. From Table 4.1, the lode angles of UXT and BXT, which are at the extreme limits of the lode angle (i.e. $\theta = \pi/6 \text{ and } -\pi/6$, respectively), are constant. Unlike points A and B, where the lode angles are not constant, the linear interpolation using the sine function between UXT and BXT points is employed to obtain the intermediate point. Therefore, the intermediate point is expressed as

$$I_{1,3} = f_t\left[1 + (2\alpha - 1)\left(\sin\theta + \frac{1}{2}\right)\right] \tag{4.20}$$

$$\sqrt{J_{2,3}} = \frac{f_t}{\sqrt{3}}\left[1 + (\alpha - 1)\left(\sin\theta + \frac{1}{2}\right)\right] \tag{4.21}$$

With these three points, the tension yield surface is proposed to be as follows

$$\mathrm{F_t} = \mathrm{x}\mathrm{I}_1^2 + \mathrm{y}\mathrm{I}_1 + \mathrm{z} - \sqrt{\mathrm{J}_2} = 0 \tag{4.22}$$

where the material parameters x, y, and z are obtained by substituting I_1 and the corresponding $\sqrt{\mathrm{J}_2}$ of the three identified points into the yield function.

$$\begin{bmatrix} \mathrm{I}_{1,1}^2 & \mathrm{I}_{1,1} & 1 \\ \mathrm{I}_{1,2}^2 & \mathrm{I}_{1,2} & 1 \\ \mathrm{I}_{1,3}^2 & \mathrm{I}_{1,3} & 1 \end{bmatrix} \begin{Bmatrix} \mathrm{x} \\ \mathrm{y} \\ \mathrm{z} \end{Bmatrix} = \begin{Bmatrix} \sqrt{\mathrm{J}_{2,1}} \\ \sqrt{\mathrm{J}_{2,2}} \\ \sqrt{\mathrm{J}_{2,3}} \end{Bmatrix} \tag{4.23}$$

By inverting the first matrix of the right hand side equation, the solutions of x, y, and z are obtained.

$$\begin{Bmatrix} \mathrm{x} \\ \mathrm{y} \\ \mathrm{z} \end{Bmatrix} = \begin{bmatrix} \mathrm{I}_{1,1}^2 & \mathrm{I}_{1,1} & 1 \\ \mathrm{I}_{1,2}^2 & \mathrm{I}_{1,2} & 1 \\ \mathrm{I}_{1,3}^2 & \mathrm{I}_{1,3} & 1 \end{bmatrix}^{-1} \begin{Bmatrix} \sqrt{\mathrm{J}_{2,1}} \\ \sqrt{\mathrm{J}_{2,2}} \\ \sqrt{\mathrm{J}_{2,3}} \end{Bmatrix} \tag{4.24}$$

where

$$\mathrm{x} = \frac{1}{\mathrm{d}}\left[\left(\mathrm{I}_{1,2} - \mathrm{I}_{1,4}\right)\sqrt{\mathrm{J}_{2,1}} + \left(-\mathrm{I}_{1,1} + \mathrm{I}_{1,4}\right)\sqrt{\mathrm{J}_{2,2}}\right] \tag{4.25.1}$$

$$\mathrm{y} = \frac{1}{\mathrm{d}}\left[\left(-\mathrm{I}_{1,2}^2 + \mathrm{I}_{1,4}^2\right)\sqrt{\mathrm{J}_{2,1}} + \left(\mathrm{I}_{1,1}^2 - \mathrm{I}_{1,4}^2\right)\sqrt{\mathrm{J}_{2,2}}\right] \tag{4.25.2}$$

$$\mathrm{z} = \frac{1}{\mathrm{d}}\left[\left(\mathrm{I}_{1,2}^2\mathrm{I}_{1,4} - \mathrm{I}_{1,2}\mathrm{I}_{1,4}^2\right)\sqrt{\mathrm{J}_{2,1}} + \left(-\mathrm{I}_{1,1}^2\mathrm{I}_{1,4} + \mathrm{I}_{1,1}\mathrm{I}_{1,4}^2\right)\sqrt{\mathrm{J}_{2,2}}\right] \tag{4.25.3}$$

$$\mathrm{d} = \left(\mathrm{I}_{1,1} - \mathrm{I}_{1,2}\right)\left(\mathrm{I}_{1,1} - \mathrm{I}_{1,4}\right)\left(\mathrm{I}_{1,2} - \mathrm{I}_{1,4}\right) \tag{4.25.4}$$

To rid the denominator term ‘d’ of parameters x, y, and z, multiplying Eq. (4.22) with ‘d’ and let’s define $\mathrm{x}' \equiv \mathrm{xd},\ \mathrm{y}' \equiv\ \mathrm{yd},\ \text{and}\ \mathrm{z}' \equiv \mathrm{zd}$. Then, the tension yield function now becomes

$$\mathrm{F_t} = \mathrm{x}'\mathrm{I}_1^2 + \mathrm{y}'\mathrm{I}_1 + \mathrm{z}' - \mathrm{d}\sqrt{\mathrm{J}_2} = 0 \tag{4.26}$$

By substituting the value of I_1 and the corresponding $\sqrt{\mathrm{J}_2}$ at three points from Table 4.1, material parameters $\mathrm{x}', \mathrm{y}', \mathrm{z}'$, and d can be obtained as

$$x' \equiv xd = f_t[(2\alpha - 1)\beta - 2]\sqrt{J_{2,HTC}} + \sqrt{3}f_t^2[1 + (\alpha - 1)\beta] \quad (4.26.1)$$

$$y' \equiv yd = f_t^2[8 - 2\beta(2\alpha - 1) - \beta^2(2\alpha - 1)^2]\sqrt{J_{2,HTC}} - 3\sqrt{3}f_t^3[1 + (\alpha - 1)\beta] \quad (4.26.2)$$

$$z' \equiv zd = 3f_t^3[1 - (2\alpha - 1)\beta][(2\alpha - 1)\beta - 2]\sqrt{J_{2,HTC}} \quad (4.26.3)$$

$$d = 3f_t^3[1 - (2\alpha - 1)\beta][(2\alpha - 1)\beta - 2] \quad (4.26.4)$$

$$\beta \equiv (\sin\theta) + \frac{1}{2} \quad (4.26.5)$$

So far only the construction of the maximum tensile yield surface is given, the evolution of the tension yield surface is not yet discussed. In order to make sure that the continuity between compression and tension yield surfaces exists at every loading state, the development of the tension yield surfaces, i.e. expansion under hardening regime and contraction under softening regime, must be taken into consideration. As the tension yield surface expands, the compression yield surface must be expanded also to maintain continuity between these two yield surfaces. Therefore, the hardening and softening parameters (k, r , and s) are shared for both compression and tension yield functions. By introducing the hardening and softening parameters into Eq. (4.26), a complete tension yield function is written as:

$$F_t(\boldsymbol{\sigma}, k, r, s) = x'I_1^2 + \left[(y' + z')\sqrt{rs} - z'\right]I_1 + kz' - d\sqrt{J_2} = 0 \quad (4.27)$$

where the material parameters $x', y', z',$ and d are obtained from Eq. (4.25). Although the hardening and the softening parameters of both compression and tension yield functions are the same, the shapes of the both responses are not the same. Under uniaxial compression, the shape of the response starts with the parabolic function, followed by a mix of cosine and exponential functions. However, under uniaxial tension, the shape of the response composes of bilinear hardening, followed by an exponential softening shape.

Therefore, the hardening (k) and the softening parameters (r and s) are redefined under tension as

$$k = \frac{(k_1 - k_0)}{\varepsilon'_{p,1}} \varepsilon'_p + k_0 \qquad : \quad 0 \le \varepsilon'_p \le \varepsilon'_{p,1} \tag{4.28}$$

$$k = \frac{1 - k_1}{\varepsilon'_{p,2} - \varepsilon'_{p,1}} \left(\varepsilon_p - \varepsilon_{p,1}\right) + k_1 \quad : \quad \varepsilon'_{p,1} < \varepsilon'_p \le \varepsilon'_{p,2} \tag{4.29}$$

$$r = s = \mathrm{Exp}\left[-\gamma \frac{\left(\varepsilon'_p - \varepsilon'_{p,2}\right)}{\left(\varepsilon'_{p,3} - \varepsilon'_{p,2}\right)}\right] \quad : \quad \varepsilon'_{p,2} < \varepsilon'_p \le \varepsilon'_{p,3} \tag{4.30}$$

where k_0, k_1, $\varepsilon'_{p,1}$, $\varepsilon'_{p,2}$, and $\varepsilon'_{p,3}$ are defined in Figure 4.13. The parameter γ is defined as the slope of exponential softening function. The definition of tension effective plastic strain is defined the same way as in compression. Hence, both compression and tension effective plastic strains are defined as:

$$\varepsilon_p = \int d\varepsilon_p \equiv \int \sqrt{\frac{2}{3} \mathbf{d\varepsilon^p} : \mathbf{d\varepsilon^p}} \quad : \ P \ge 0 \tag{4.31}$$

$$\varepsilon'_p = \int d\varepsilon'_p \equiv \int \sqrt{\frac{2}{3} \mathbf{d\varepsilon^p} : \mathbf{d\varepsilon^p}} \quad : \ P < 0 \tag{4.32}$$

Since the effective compression plastic strain $\left(\varepsilon_p\right)$ is not the same as the tension effective plastic strain $\left(\varepsilon'_p\right)$, ε_p must be updated as the tension yield surface evolves. For the hardening region (Eq. 4.6), the inverse relationship between ε_p and k can be obtained as

$$\varepsilon_p = \varepsilon_{p,\max} \left(1 - \sqrt{\frac{(1 - k)}{(1 - k_0)}}\right)^2 \tag{4.33}$$

For the softening region (Eq. 4.7 and 4.15), the inverse relationship between ε_p and softening parameters (r and s) can be obtained as

$$\varepsilon_{\mathrm{p}} = \max\begin{cases} \varepsilon_{\mathrm{p,max}} + \dfrac{\left(\varepsilon_{\mathrm{p,ult}} - \varepsilon_{\mathrm{p,max}}\right)}{\pi}\cos^{-1}(2\mathrm{r} - 1) \\ \varepsilon_{\mathrm{p,int}} - \dfrac{\left(\varepsilon_{\mathrm{p,ult}} - \varepsilon_{\mathrm{p,int}}\right)}{\omega}\ln(\mathrm{s}) \end{cases} \tag{4.34}$$

Conversely, if the compression yield surface evolves, the tension effective plastic strain $\varepsilon'_{\mathrm{p}}$ must be updated. Under the hardening region, two separate equations are used to obtain the corresponding $\varepsilon'_{\mathrm{p}}$. The first equation is when the hardening parameter k is between k_0 and k_1

$$\varepsilon'_{\mathrm{p}} = \varepsilon'_{\mathrm{p,1}}\frac{(\mathrm{k} - \mathrm{k}_0)}{\mathrm{k}_1 - \mathrm{k}_0} \tag{4.35}$$

The second equation is when k is between k_1 and 1 and can be expressed as

$$\varepsilon'_{\mathrm{p}} = \varepsilon'_{\mathrm{p,1}} + \frac{(\mathrm{k} - \mathrm{k}_0)}{(1 - \mathrm{k}_1)}\left(\varepsilon'_{\mathrm{p,2}} - \varepsilon'_{\mathrm{p,1}}\right) \tag{4.36}$$

Under the softening region, the minimum value of r and s is taken and the corresponding $\varepsilon'_{\mathrm{p}}$ is obtained as

$$\varepsilon'_{\mathrm{p}} = \varepsilon'_{\mathrm{p,2}} - \frac{\left(\varepsilon'_{\mathrm{p,3}} - \varepsilon'_{\mathrm{p,2}}\right)}{\gamma}\ln[\min(\mathrm{r}, \mathrm{s})] \tag{4.37}$$

The same potential function used for compression (Drucker-Prager model) is used for tension. However, the slope of plastic flow direction ($\mathrm{a_T}$) is defined as a constant value since there is no information on how the volumetric strain expands or contracts respected to the longitudinal strain. Nevertheless, the potential function defined here is for future expansion of the model. Once the relationship between volumetric and longitudinal strains is known, the parameter '$\mathrm{a_T}$' can be easily adjusted to fit with the experimental results. Therefore, the potential function for tension is defined as:

$$\mathrm{g}(\boldsymbol{\sigma}) = \mathrm{a_T}\frac{\mathrm{I}_1}{\sqrt{3}} + \sqrt{2\mathrm{J}_2} - \mathrm{c} \tag{4.38}$$

where a_T is the slope of the plastic flow direction used to control the amount of volumetric plastic strain.

One of a few drawbacks of the proposed model is the kink at the connection between compression and tension yield surfaces (Figure 4.12). Since only the zeroth degree continuity is considered when constructed tension yield surface, the slope at the transition is not smooth. Another drawback is the number of material parameters required for modeling complete behavior of HPFRCC. However, out of 22 material parameters, only six are required for determining compression yield surface and only two are required for tension. The remaining parameters can be obtained from simple uniaxial compression and tension tests.

Another limitation of this model is that it cannot simulate cyclic behavior. The consequence of sharing hardening and softening parameters of both yield functions together appears when cyclic loading occurs. To illustrate this effect, one element subjected to uniaxial cyclic loading is simulated as shown in Figure 4.14. The load first starts with compression until reaching the hardening regime, followed by unloading until it reaches the tension side (Figure 4.14b). At the beginning, a compressive stress develops as the compressive strain increases and once the stress reaches the initial yield surface, the hardening parameter increases and the compressive yield surface starts to grow. Since both yield functions share the same hardening parameter, the tension yield surface also grows. Once unloading takes place, the pressure drops and the hardening parameter stops developing (Figure 4.14c). As the pressure drops and switches from positive to negative (from compression to tension), the algorithm is switched from compression to tension as well. Since the current tension yield surface is not at the initial state, but at the last point where the yield surface stops expanding from the last compressive stress, the stress-strain response under cyclic loading differs from the monotonic loading scenario shown as a dotted line in Figure 4.14d. In other words, the tensile elastic region increases in size when compared with the monotonic case. However, the strength capacity remains the same as the monotonic case. It should be noted that the strain in the cyclic loading case is obtained by subtracting the total strain from the permanent damage strain caused by the compression regime. Since this dissertation focuses only on monotonic loading behavior, correcting this unrealistic cyclic response is beyond the scope of this study and is something that can be addressed in future work. Nevertheless, the proposed model is sufficient to accurately represent monotonic loading behavior under both compression and tension for HPFRCC.

4.4 Conclusion

A macro-scale plasticity model for High Performance Fiber Reinforced Cement Composites (HPFRCC) is given in this chapter. The material model is divided into two parts, i.e. compression and tension. In the former, an existing model is modified for modeling HPFRCC compressive response. The shape of the compression yield surface is taken similar to the modified HTC model proposed by Imran and Pantazopoulou (2001). However, the softening part of the yield function is modified to accommodate the difference between mortar and HPFRCC. Unlike mortar where the stress drops abruptly after reaching the peak, the post-peak response of HPFRCC gradually softens. In tension the modified HTC model is extended to cover tensile behavior. The evolution of variables shared by both tension and compression surfaces is described.

Table 4.1 Four points for constructing the tension yield function

Experiment	First invariant (I_1)	Second invariant $\left(\sqrt{J_2}\right)$	Lode angle (θ)
1. Compression yield surface	0	$\sqrt{J_{2,HTC}}$	$\left[-\frac{\pi}{6},\frac{\pi}{6}\right]$
2. Uniaxial tension (UXT)	f_t	$\frac{f_t}{\sqrt{3}}$	$-\frac{\pi}{6}$
3. Equal biaxial tension (BXT)	$2\alpha f_t$	$\frac{\alpha f_t}{\sqrt{3}}$	$\frac{\pi}{6}$
4. Equal triaxial tension (TXT)	$3f_t$	0	$\left[-\frac{\pi}{6},\frac{\pi}{6}\right]$

where α is the strength ratio between equal biaxial tension-tension and uniaxial tension

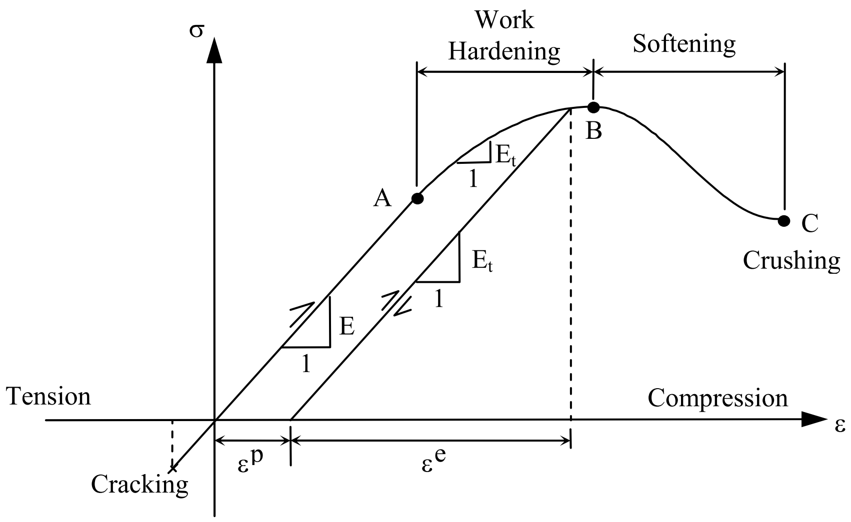

Figure 4.1 Idealized uniaxial stress-strain of regular concrete (Chen, 1982)

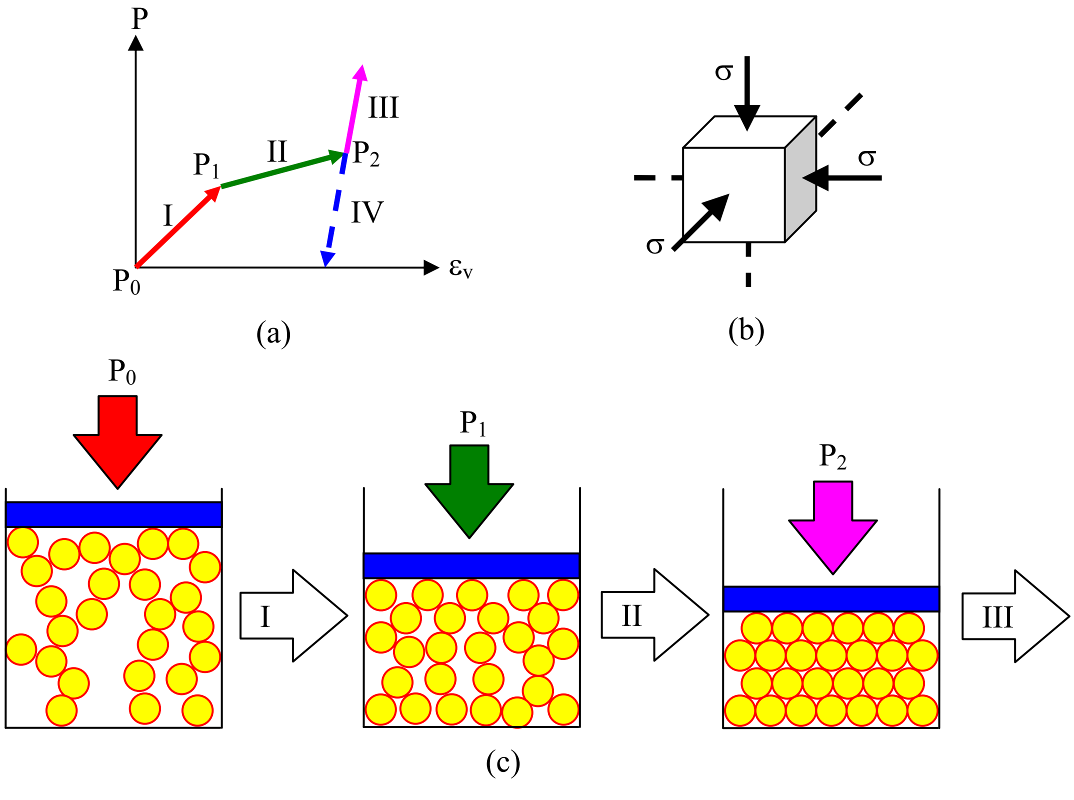

Figure 4.2 Schematic of geomaterial particle compaction and corresponding pressure-volume response under triaxial loading condition (Schwer, 2002)

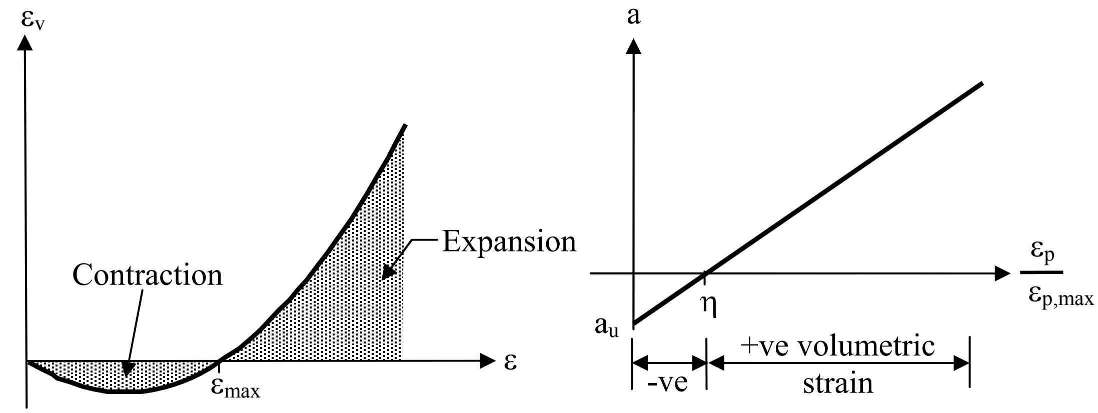

(a) Contraction and Expansion of volumetric strain under uniaxial compression

(b) Slope of flow direction as a function of $\varepsilon_p/\varepsilon_{p,max}$

Figure 4.3 Amount of volumetric strain under uniaxial compression controlled by ′a′ (Imran, 1994)

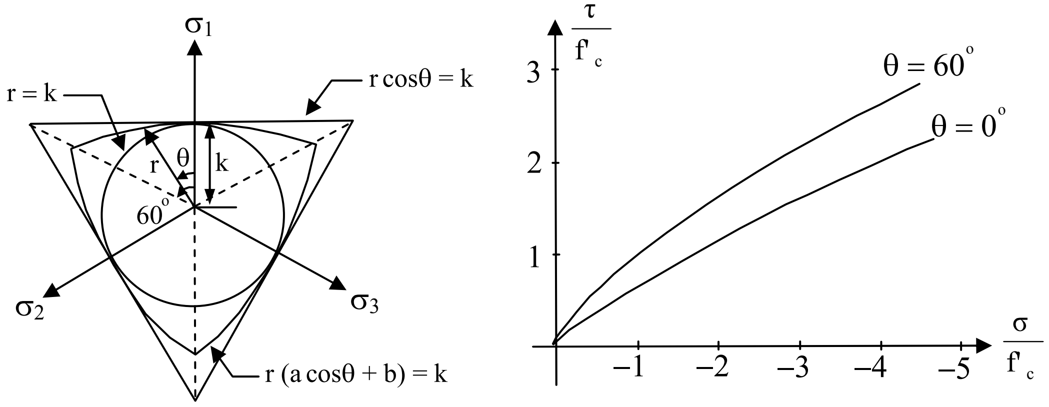

(a) Geometric on deviatoric plane

(b) Geometric on meridian plane

Figure 4.4 Original yield surface of HTC model (Hsieh et al., 1982)

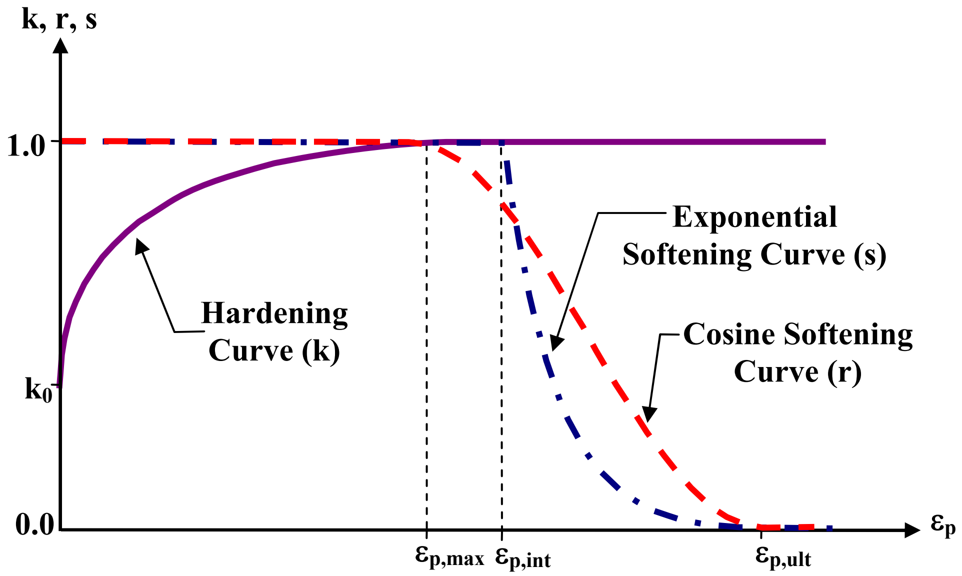

Figure 4.5 Plot of hardening and softening parameters as a function of ε_p

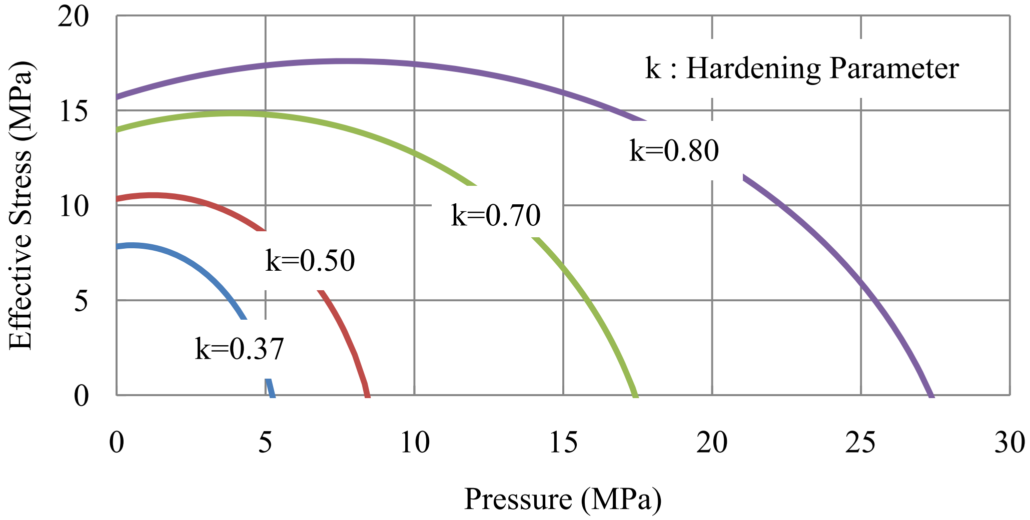

Figure 4.6 Evolution of loading surface during the hardening on the meridian plane (Imran, 1994)

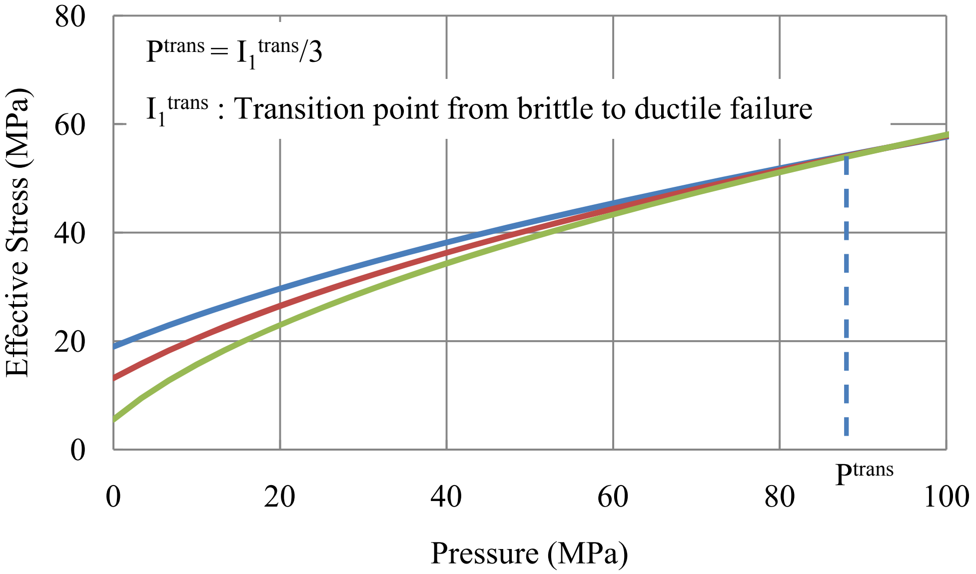

Figure 4.7 Evolution of loading surface during the softening on the meridian plane (Imran, 1994)

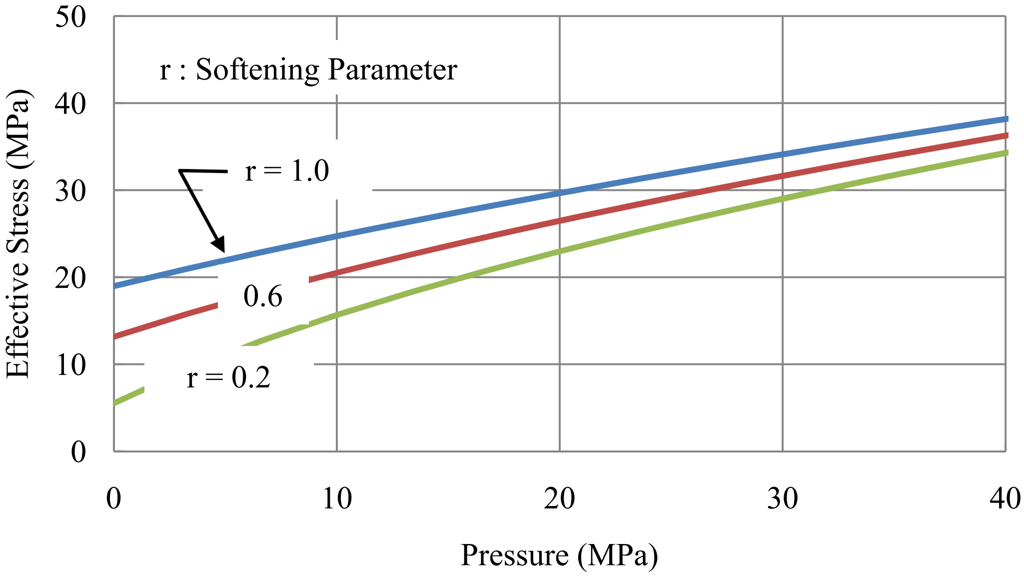

Figure 4.8 Evolution of loading surface during the softening on the meridian plane at the lower level of confinement (Imran, 1994)

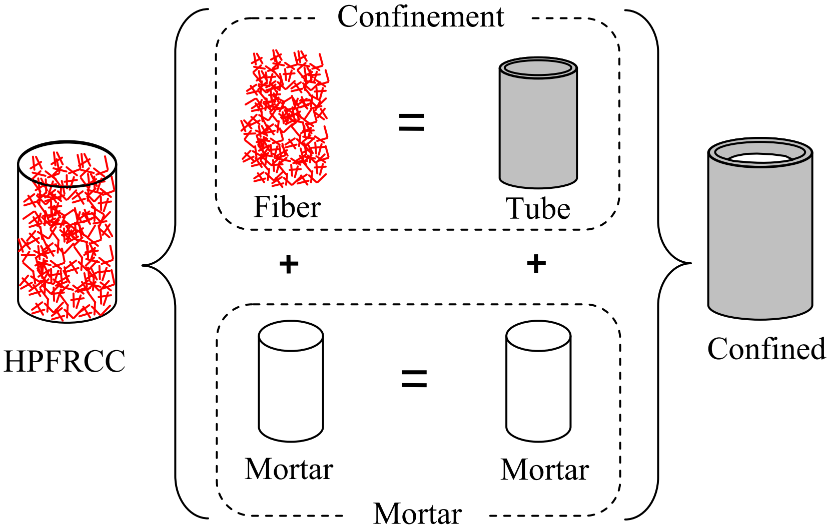

Figure 4.9 Fibers provide the effective confinement under uniaxial loading condition

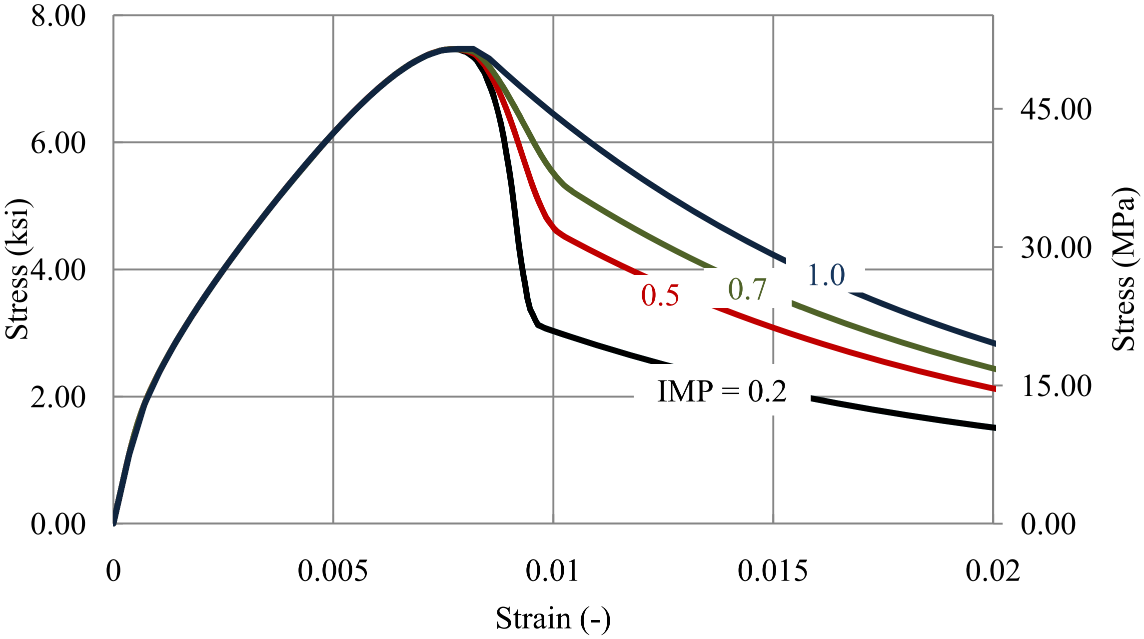

Figure 4.10 Effect of IMP under uniaxial compression

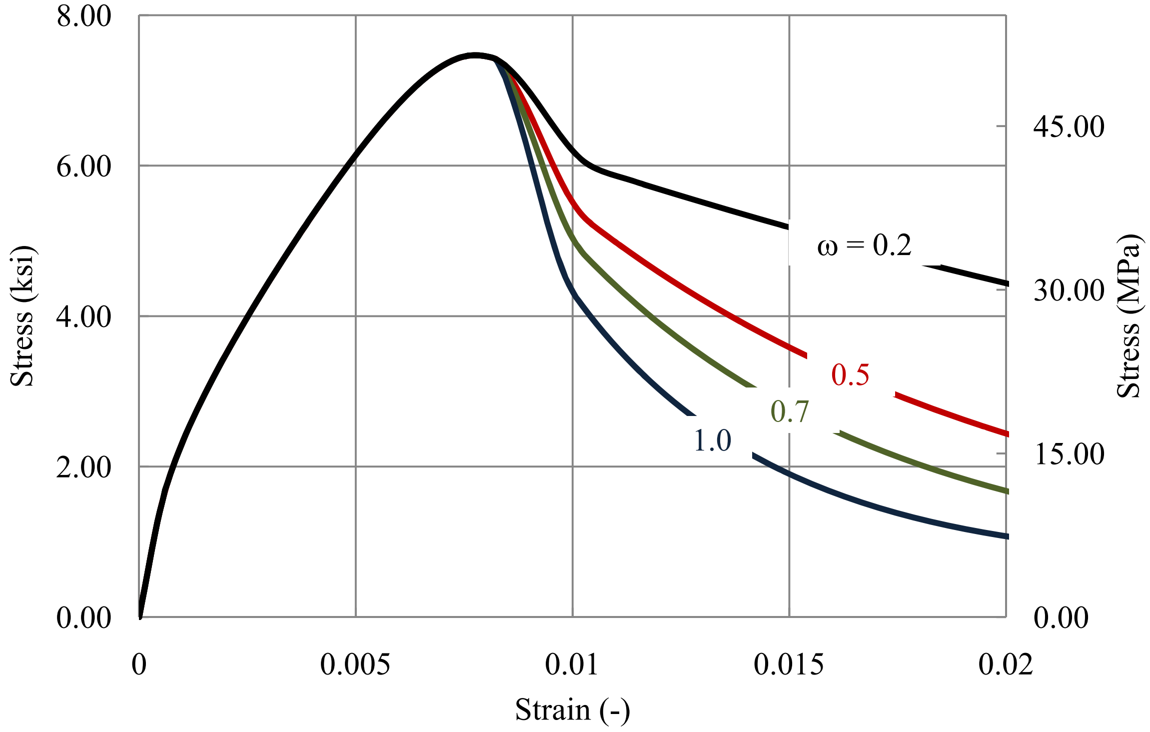

Figure 4.11 Effect of ‘ω’ factor under uniaxial compression

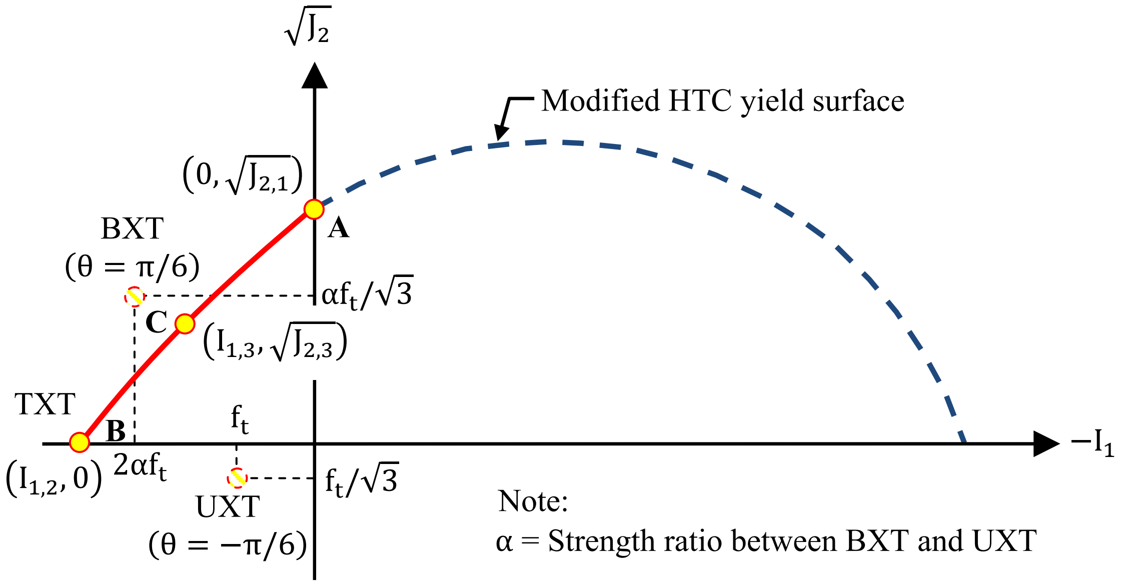

Figure 4.12 Compression and tension yield surfaces on the meridian plane at $\theta = 0$

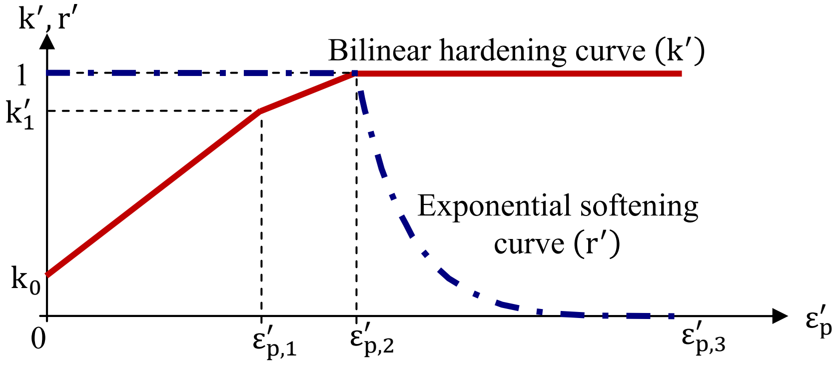

Figure 4.13 Plot of hardening and softening parameters of the tension yield surface as a function of effective plastic strain (ε_p)

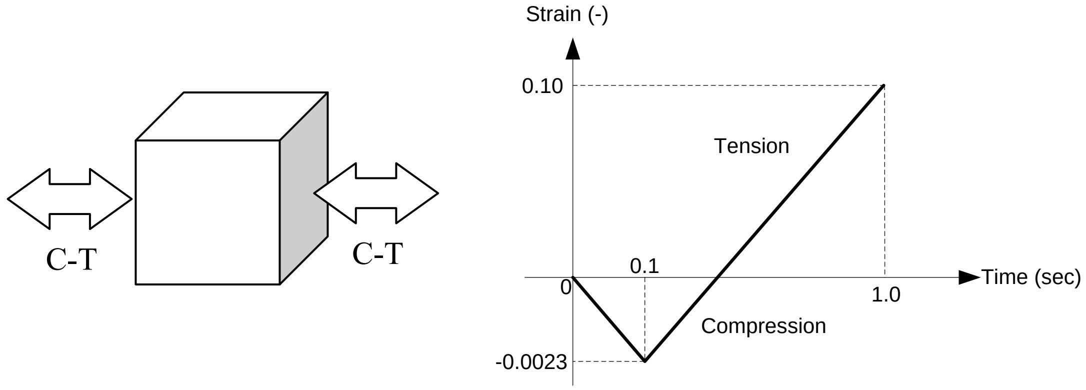

(a) One element simulation

(b) Prescribed strain vs. time

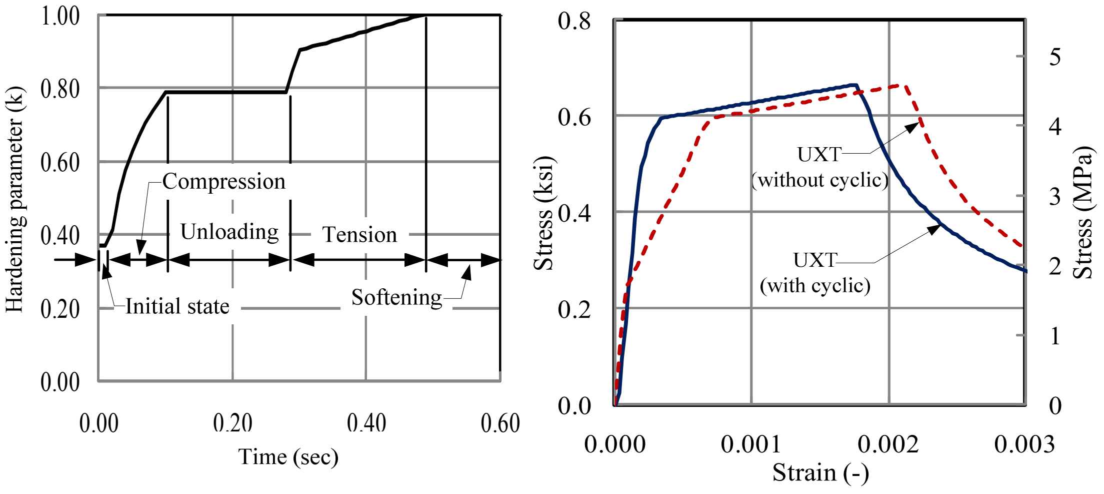

(c) Hardening parameter (k) vs. time

(d) Comparison of responses under cyclic and monotonic loadings

Figure 4.14 Uniaxial response under cyclic loading

CHAPTER 5

IDENTIFICATION OF MATERIAL PARAMETERS AND MODEL VERIFICATIONS

The model discussed in the previous chapter is calibrated and validated in this chapter. After implementing the model in the commercial Finite Element software, LS-DYNA, several exercises are conducted to ensure that the model gives good results with respect to test data. These exercises include a variety of specimens including two-span continuous beam, punching shear slab, slender wall, and a coupling beam.

5.1 Identification of Material Parameters

5.1.1 Material Parameters for Compressive Yield Function

As discussed in Chapter 4, a total of 22 material parameters are required to define the yield and potential functions of both compression and tension parts of the model. The yield surfaces define the boundary of the elastic region whereas the potential functions define the plastic flow direction as well as control the magnitude of the volumetric plastic strain. The material parameters A, B, C, D for the compression yield function are obtained in two different stages, i.e. at the peak and residual points. These two stages are selected for two reasons. The first is to ensure that the peak strengths under the three basic loading combinations, namely uniaxial (UXC), equal biaxial (BXC), and triaxial compressions (TXC), match with the experimental results. The second reason is to guarantee that the lowest softening stress can be achieved. Since the uniaxial compression state of stress gives the lowest confining pressure out of these three loading combinations, the lowest possible stress will be controlled by this loading scenario. Therefore, at the peak point where all the internal hardening and softening parameters are unity (k = r = s = 1), the yield function becomes:

$$F(\sigma, k = 1, r = 1, s = 1) = \frac{A}{f_c'} J_2 + B\sqrt{J_2} + C\sigma_1 + DI_1 - f_c' = 0 \qquad (5.1)$$

At the residual point, the hardening parameter remains unity $(k = 1)$ but the softening parameters are zero $(r = s = 0)$ and the yield function is expressed as:

$$F(\sigma, k = 1, r = 0, s = 0) = \frac{A}{f_c'} J_2 + B\sqrt{J_2} + C\sigma_1 + DI_1 - f_c' \frac{I_1}{I_{1,\mathrm{trans}}} \qquad (5.2)$$

By substituting the material strengths for the UXC, BXC, and TXC cases into Eq. (5.1) and the residual strength under UXC into Eq. (5.2), the material parameters A, B, C, and D can be obtained by solving the following equation:

$$\begin{bmatrix} \frac{0.1}{3} & \frac{1}{\sqrt{3}} & 0 & -1 \\ \frac{f_c'}{3} & \frac{f_c'}{\sqrt{3}} & 0 & -f_c' \\ \frac{{f_{cb}'}^2}{3f_c'} & \frac{f_{cb}'}{\sqrt{3}} & 0 & -2f_{cb}' \\ \frac{(\sigma_1 - \sigma_2)^2}{3f_c'} & \frac{(\sigma_1 - \sigma_2)}{\sqrt{3}} & -\sigma_2 & -\sigma_1 - 2\sigma_2 \end{bmatrix} \begin{Bmatrix} A \\ B \\ C \\ D \end{Bmatrix} = \begin{Bmatrix} -\frac{f_c'}{I_{1,\mathrm{trans}}} \\ f_c' \\ f_c' \\ f_c' \end{Bmatrix} \qquad (5.3)$$

where f_c' is the compressive strength; f_{cb}' is the biaxial compressive strength; σ_1 and σ_2 are the maximum longitudinal stress and its corresponding lateral stress under TXC, respectively. In this study, the residual strength is taken as at one percent of the unaixial compressive strength.

$$\begin{Bmatrix} A \\ B \\ C \\ D \end{Bmatrix} = \begin{bmatrix} \frac{0.1}{3} & \frac{1}{\sqrt{3}} & 0 & -1 \\ \frac{f'_c}{3} & \frac{f'_c}{\sqrt{3}} & 0 & -f'_c \\ \frac{{f'_{cb}}^2}{3f'_c} & \frac{f'_{cb}}{\sqrt{3}} & 0 & -2f'_{cb} \\ \frac{(\sigma_1-\sigma_2)^2}{3f'_c} & \frac{(\sigma_1-\sigma_2)}{\sqrt{3}} & -\sigma_2 & -\sigma_1-2\sigma_2 \end{bmatrix}^{-1} \begin{Bmatrix} -\frac{f'_c}{I_{1,trans}} \\ f'_c \\ f'_c \\ f'_c \end{Bmatrix} \tag{5.4}$$

The remaining two material parameters for the compression yield function, E_{htc} and $I_{1,trans}$, can be obtained once the material parameters A, B, C, and D are known. For the hardening region, E_{htc}, which defines the cap of the yield surface in the meridian plane, is determined at the initial yield function. At the initial point, the hardening parameter is prescribed as k_0 and the yield function is expressed as:

$$F(\sigma, k_0) = \frac{AJ_2}{k_0 f'_c} + B\sqrt{J_2} + Ck_0\sigma_1 + Dk_0 I_1 + \frac{E_{htc}(1-k_o)I_1^2}{k_0 f'_c} - k_0 f'_c = 0 \tag{5.5}$$

Under uniaxial compression, the principal stress first reaches the yield surface at $k_0 f'_c$. By replacing the invariants I_1 and J_2 with the uniaxial state of stress ($k_0 f'_c$), E_{htc} can be derived as:

$$E_{htc} = \frac{1}{(k_0-1)}\left[\frac{A}{3} + \frac{B}{\sqrt{3}} - Dk_0 - 1\right] \tag{5.6}$$

The variable $I_{1,trans}$, which defines the first invariant at the transition zone, is directly obtained from the triaxial compression test. The transition zone is defined as a point in which the post peak behavior changes from softening to perfectly plastic. Once the first invariant reaches $I_{1,trans}$, the softening response is eliminated and HPFRCC behaves as a perfectly plastic material.

The remaining compression parameters are the effective plastic strains $\left(\varepsilon_{\mathrm{p,max}}, \varepsilon_{\mathrm{p,int}}, \text{and } \varepsilon_{\mathrm{p,ult}}\right)$ and the slope of the exponential softening parameter (s). These parameters are directly obtained by fitting the stress-strain response with the observed response under uniaxial compression and are shown in Table 5.2 as a function of fiber type and volume fraction.

5.1.2 Materials Parameters for Tensile Yield Function

Only the tensile strength and the ratio between equal biaxial to uniaxial tensions are needed for the tension yield function. The hardening parameter k_1', the effective plastic strains$\left(\varepsilon_{\mathrm{p,1}}', \varepsilon_{\mathrm{p,2}}', \text{and } \varepsilon_{\mathrm{p,3}}'\right)$, and the softening slope (s) are obtained by fitting with the uniaxial test result (Figure 4.13). The initial hardening parameter k_0' is shared with the compressive yield function and takes the same value. The tension material parameters are given in Table 5.3 as a function of type of fiber and volume fraction.

5.1.3 Mesh Size Dependency in Softening Response

To eliminate the mesh size dependency associated with softening behavior, the material parameters related to the softening slope under both compression and tension are modified to account for this effect. The diagonal length of the element is selected to represent mesh size. To determine the sensitivity of the softening responses to mesh size, two simulations, i.e. uniaxial compression cylinder and dog-bone tensile specimen, are simulated. Under compression, a cylinder with the same dimensions used in the testing in Chapter 3 is simulated. Three different sizes of elements are used ranging from 0.25, 0.5, and 1 in. From the simulated results, it turns out that the mesh size has little effect on the compressive softening slope (Figure 5.1). Therefore, the parameter ω controlling the compressive softening parameter is defined as a constant for each type and volume content of fibers. Under tension, the dog-bone specimen is simulated where the same element sizes used in the compression simulations are used as well. The simulations show that the tensile softening slope does depend on the size of the element as shown in Figure 5.2. From the trend lines in both fibers, the softening parameter is directly proportional to the element size. Hence, the tensile softening slope 's' given in Table 5.3 is expressed in term of diagonal length of the element.

5.2 Implementation and Simulation in LS-DYNA

5.2.1 Implementation

The proposed model is implemented in LS-DYNA as a user-defined material subroutine called UMAT. Within the subroutine, the user-defined model is compiled with INTEL-FORTRAN and linked to the LS-DYNA executable file as a static library as shown in Figure 5.3 (Moraes & Nicholson, 2001). The user-defined subroutine is called at every time step for each integration point. Users need to know priori what input parameters are required and transferred from the main program to the UMAT subroutine because some static libraries are not available from LS-DYNA. If that is the case, users need to write their own additional static library. By default, the given inputs from the main program are the incremental strain ($\boldsymbol{\Delta\varepsilon}$), the previous state of stresses $\left(\boldsymbol{\sigma}^{i-1}\right)$ and strains $\left(\boldsymbol{\varepsilon}^{i-1}\right)$, and the history variables. The outputs from UMAT are the current material state, e.g. state of stresses $\left(\boldsymbol{\sigma}^{i}\right)$, strains $\left(\boldsymbol{\varepsilon}^{i}\right)$ and history variables, which are needed for the next increment. In the current version (LS-DYNA 971), LS-DYNA allows user to write up to ten subroutines simultaneously and up to 48 history variables for each

UMAT. Since LS-DYNA is written in FORTRAN, user-defined subroutines require a FORTRAN compiler running on the users' machine.

5.2.2 Material Model for Reinforcing Bars

In all simulations given in section 5.5, a bar reinforcement is modeled by using the J_2 plasticity model (MAT 24) in LS-DYNA. The yield function of this model is expressed as follows (Hallquist, 2007):

$$F(\boldsymbol{\sigma}, \sigma_Y) = J_2 - \frac{\sigma_Y^2}{3} \leq 0 \tag{5.7}$$

where J_2 is the second invariant of the deviatoric stresses and σ_Y is the yield strength, which is defined as

$$\sigma_Y = \beta\left[\sigma_0 - f_h\left(\varepsilon_{eff}^p\right)\right] \tag{5.8}$$

From Eq. (5.8), the yield strength is related to three parameters, i.e. the strain rate factor (β), the initial yield strength (σ_0), and the hardening function $f_h\left(\varepsilon_{eff}^p\right)$. Since the simulation is under static loading condition, β is set to one. The hardening function is expressed in term of the effective plastic strain ε_{eff}^p, which is defined as:

$$\varepsilon_{eff}^p = \int_0^t \sqrt{\frac{2}{3}\boldsymbol{\varepsilon}^{\mathbf{p}} : \boldsymbol{\varepsilon}^{\mathbf{p}}} dt \tag{5.9}$$

where $\boldsymbol{\varepsilon}^{\mathbf{p}}$ is the plastic strain tensor. Example of the tabular form $f_h\left(\varepsilon_{eff}^p\right)$ for the reinforcement is given in Table 5.4.

5.2.3 Contact Algorithm

The CONTACT_AUTOMATIC_SINGLE_SURFACE algorithm is used to prevent inter-penetration between parts in this study. The algorithm employs the penalty method in which slave and master surfaces are automatically defined within the code. When the slave node penetrates the master surface, the code automatically detects and calculates the required force to push the slave nodes back to the master surface. This required force is determined from fictitious spring stiffness and the penetration displacement (Figure 5.4). The stiffness of the fictitious spring is calculated from the bulk modulus, contact area, and volume of the elements on the master surface. Further details regarding to this contact algorithm can be found in Hallquist (2007). A static coefficient of friction between all solid parts is assumed to be 0.3.

5.2.4 Element Formulations

To avoid hour-glassing during simulation, a full quadrature is used for an 8-node solid element (Figure 5.5a). The Hughes-Liu beam element formulation with 2 × 2 Gauss quadrature integration is used to model reinforcements. This beam element formulation is selected because it is based on a degenerated brick element formulation (Tavarez, 2001). Hence, it is compatible with the solid elements used elsewhere. The beam element contains six degree of freedoms in both translation and rotation. The orientation of the beam element is defined as shown in Figure 5.5b. The main geometry input parameter of this element is the nominal diameter of the rebar, not the radius as specified in the manual (Hallquist, 2007).

5.3 Single Element Exercises

The first exercise to ensure that the proposed model works is to exercise a single three-dimensional solid element subjected to various loading conditions, i.e. uniaxial, biaxial, triaxial, and shear loading combinations as shown in Figure 5.6. In all loading combinations except shear, the load case is further divided into compression and tension.

A fully integrated solid element with the dimension of 1 in. × 1 in. × 1 in. is used where a prescribed displacement is specified at nodal points depending on loading conditions.

In the uniaxial loading cases, the prescribed displacements are equally applied at nodes on two faces opposite to each other in the opposite direction. The computed stress-strain responses under compression and tension are plotted in Figure 5.7a. In the equal biaxial case, the prescribed displacement is now applied at four faces in the same plane in the opposite direction. The biaxial stress-strain responses under compression and tension are plotted in Figure 5.7b. Notice that strength enhancement occurs under equal biaxial compression due to the increase in pressure. On the contrary, strength reduction occurs under equal biaxial tension. This is to be expected since the strength ratio α in the tension yield function is defined to be 0.5.

In the triaxial case, two different confining pressures are applied to demonstrate the effect of confining pressure on the strength and ductility response under both compression and tension. The confining pressure is first applied at the four horizontal faces. Once the confining pressure reaches the specified level, it is kept constant and the prescribed displacement in the vertical direction (z-axis) is applied next. Under compression, the two confining pressure levels are 5 and 10 MPa (Figure 5.7c). Obviously, increasing the confining pressure improves both strength and ductility. Under tension, the two confining pressure levels are 1 and -1 MPa. It should be noted that the sign convention of confining pressure is positive under compression and negative under tension. Two things can be pointed out from the stress-strain responses. First, the strength and its corresponding strain are dependent upon the confining pressure. As shown in Figure 4.12, decreasing the confining pressure (or increasing I_1) will reduce the corresponding $\sqrt{J_2}$ on the yield surface and thus, the strength will also be reduced. Second, the residual strength under tension is usually set to zero. However, for the confining pressure of -1 MPa case, the triaxial tension state of stress is reached (all principal stresses are at 1 MPa) before the softening variables reach zero. At this particular point, the triaxial tension algorithm is triggered and the state of stress is kept constant. In the shear case, the shear strength is a direct result from combining the compression and tension yield surfaces together. This loading case should not be confused with the pure shear force case since the simulation is performed under displacement controlled. The normal stresses are not zero in this case.

5.4 Simulations of Uniaxial Compression and Uniaxial Tension Tests

In this exercise, two simulations with the same dimension as used in the experiments are performed to see if the material model can capture the observed overall responses. In the first simulation, a 3 in × 6 in cylinder is compressed by two steel plates. Fully integrated solid elements are used as shown in Figure 5.8. A linearly elastic isotropic material model with the properties of steel is used for steel plates. Two boundary conditions are enforced at the end nodes of the steel plates. A fully fixed boundary condition is enforced at the bottom nodes whereas the prescribed displacements are enforced at the top nodes.

Figure 5.8 illustrates the contour lines of both hardening and softening parameters under various loading stages. Since the friction between specimen and both steel plates inhibits the expansion on the top and bottom of the specimen, the hardening parameter first reaches unity in the middle portion of the specimen. After the peak, softening starts to take place as the deformation kept increasing. Figure 5.8c and Figure 5.8d show the contour lines of the Cosine softening parameter (r) and exponential softening parameter (s), respectively. Notice that the parameter ‘r’ softens faster than the parameter ‘s’. This is due to the fact that the development of ‘r’ takes place right after ‘k’ reaches unity but the development of ‘s’ takes place much later (at $\varepsilon_{p,int}$).

In the second simulation, the dog-bone shape specimen with same dimensions as given in Figure 3.3 is simulated. To duplicate the real boundary conditions used in the test, four cylindrical steel supports are also included in the simulation. Figure 5.9 shows the contour lines of the hardening and softening parameters at various loading stages. In the hardening stage, the stress is concentrated at the middle portion of the specimen. However, in the softening stage, the stress is concentrated at one particular area and this causes the localization at the end of the simulation.

5.5 Validation using Structural Tests

Several validation exercises are presented in this section to show that the developed formulation is applicable to a wide range of loading conditions.

5.5.1 Two-Span Continuous Beam

5.5.1.1 Experiments

Chandrangsu (2003) proposed a bridge deck system using HPFRCC to replace the negative reinforcements. According to AASHTO (2000), reinforcements in the bridge deck must be provided in both top and bottom layers. However, in this proposed system, the negative reinforcement, which was required for temperature and shrinkage controls, was entirely eliminated and replaced with HPFRCC. Only the positive reinforcement, which was used to resist bending moment, was provided. To evaluate the performance of this system, one strip of the bridge deck, which was equivalent to two-span continuous beam, was tested under monotonic loading (Figure 5.10a).

- **Experimental Setup**

A two-span continuous beam with dimensions of 4 in × 7 in × 10.5 ft subjected to monotonic loading was tested as shown in Figure 5.10b. The beam rested on three supports was subjected to prescribed displacements applied through two loading platens. Two exterior supports were placed on each side 3 in from the edge and one interior support was placed at the mid-span. Each loading platen was placed on each span 1.875 ft apart from the center of the beam. These two loading platens were attached to a hydraulic Instron machine, which was used to apply the prescribed displacement. Two LVDTs were placed under the beam at each loading point to measure the deflection at each span.

- **Materials**

The beam was constructed with HPFRCC with 1.5% Spectra fiber and a No.3 rebar was placed at 2.5 in from the bottom fiber. The material compositions by weight of HPFRCC were 1-cement: 1-sand: 0.15-fly ash: 0.4-water. The experimentally obtained uniaxial stress-strain curves of HPFRCC along with the simulated results are shown in Figure 5.11. For the compressive response, the strain at maximum stress given in the literature is three times higher than that given in Chapter 3 because the strain in the literature was obtained from the machine displacement, which always gave higher value than LVDT deformation. From the direct tension tests, the stress-strain responses showed the size dependent effect. The upper bound curve denoted as (H) was obtained from the small dog-bone size whereas the lower bound curve denoted as (L) was obtained from the large specimen. Further discussion regarding the specimen size and the size effect can be found in Chandrangsu (2003). No.3 rebar had the Young's modulus of 29,000 ksi and the yield strength of 60 ksi. The ultimate strength was 105 ksi with the corresponding plastic strain of 4.2%.

5.5.1.2 Finite Element Model

- **Mesh Description**

The three-dimensional finite element beam consists of beam elements to represent the No. 3 rebar and solid elements to represent HPFRCC matrix and fixtures. Figure 5.12a shows the finite element mesh with the boundary supports and the loading fixtures. The beam rests on half cylindrical shaped supports and is pushed down by two half cylindrical shaped fixtures (Figure 5.12b). Since full bond between the rebar and the matrix is assumed, the size of the solid element is dictated by the location of the rebar. Hence, the solid elements are split along the height into two sections based on the clear cover. The first section extends from the top fiber to the rebar and is meshed with 8 elements along the height. The second section extends from the rebar to the bottom fiber and is meshed with 4 elements along the height. Both sections are meshed with 8 elements across the width (Figure 5.12c). Along the length of the beam, both reinforcement and matrix is meshed with 200 elements. Hence, this beam consists of 19200 solid elements and 200 beam elements. The smallest mesh size of solid element is 0.63 in × 0.63 in × 0.47 in. Hence, the diagonal length of the smallest element, which is 1 in, will be used for obtaining the tensile softening parameter's' in Table 5.3.

The fixed boundary conditions were applied by fixing all the bottom nodal displacements of the supports whereas the top nodes of the loading platens were fixed all horizontal movements. In addition, the top nodes were enforced with the prescribed vertical displacement as shown in Figure 5.13.

- **Material Models**

Three material models are used in this simulation corresponding to three main components. The modified HTC model for HPFRCC proposed in Chapter 4 is used for the matrix component of the beam. The material parameters are directly obtained from Table 5.2 and Table 5.3 where the tensile softening parameter is obtained based on the diagonal element length of 1 in. To provide a more objective comparison, the model in Chapter 4 is recalibrated to uniaxial test data in Chandrangsu (2003). In other words, the simulations in this exercise are performed based on two material parameter sets: (1) One based on a direct calibration to test data in Chandrangsu (2003); and (2) Material parameters directly obtained from Table 5.2 and Table 5.3 without any modifications.

A J_2 plasticity model (MAT24 in LS-DYNA) is used for the reinforcement where the initial yield strength of No.3 rebar is 60 ksi and the tabular form $f_h\left(\varepsilon_{eff}^{p}\right)$ is given in Table 5.4. Notice that once the stress reaches the ultimate strength, the perfectly plastic condition is applied. A linearly isotropic elastic model (MAT 1 in LS-DYNA) is used for supports and loading fixtures where the elastic properties are the same as used in the rebars.

5.5.1.3 Results and Discussions

Figure 5.14 shows the contour plots of the hardening and softening parameter (k and r, respectively) at various stages. At the beginning, the hardening parameter is at the initial value (Figure 5.14a). As the prescribed displacement increases, the hardening variable starts to propagate not only from the contact areas at the supports and at loading platens, but also from the negative and positive moment sections (Figure 5.14b). Once the hardening parameter reaches unity, softening starts to take over and propagates from the extreme fiber of the beam in both positive and negative moment sections (Figure 5.14c). It should be noted that the hardening parameter in the compression side reaching one does not represent crushing of the HPFRCC. Crushing occurs when the softening parameter reaches zero. However, the hardening parameter in the tension side reaching one does represent the localization due to formation of a major crack.

The load vs. deflection in span under the point load is shown in Figure 5.15. In the first case in which material parameters are recalibrated on test results provided in the literature, both simulation results give similar trend as the experimental results but the response of the beam with the lower bound tensile capacity (L) is closer to the test results than with upper bound tensile capacity (H). The notations (L) and (H) indicate the two different tensile curves of HPFRCC used in the simulations. In the second case where material parameters are obtained from Table 5.2 and Table 5.3, the simulation result also gives similar trend as in the first case. Although the compressive Young's modulus in the first case is lower than the second case, the load-deflection responses are similar in both cases. Because the beam is designed as under-reinforced, the tensile response of HPFRCC matrix governs the overall behavior of the beam. The comparison of deformed shape at the final stage between test and simulation is shown in Figure 5.16. At this stage, major cracks in the testing beam occurred at three locations: at the top fiber of the mid-span, at the bottom fiber of the left and the right loading platens. The simulation results match these three locations.

5.5.2 Punching Shear Slab

5.5.2.1 Experiments

A HPFRCC slab subjected to concentrated load was tested as a part of the proposed bridge deck system described in the previous section (Likhitruangsilp, 2006). The deck configuration for the punching tests is the same as given in the previous section (Figure 5.10a). Two different reinforcement layouts, i.e. no reinforcement (0T-0L), one layer of reinforcement (1T-1L), are considered in this test. For specimens with reinforcements, rebars are aligned in both directions perpendicular to each other (Figure 5.17).

- **Experimental Setup**

As shown in Figure 5.18, a square slab with dimensions 31 in × 31 in × 7 in was tested under a concentrated load placed at the center of the slab. The slab rested on a steel frame, which was intended to simulate as simply supported conditions. The dimension of this frame was 32 in × 32 in with an opening in the transverse direction of 6 in at the middle. The width of this frame was 2 in. A square 4 × 4 in^2 steel plate placing at the center of the top of the slab was pushed down at a rate of 0.01 in/min. An LVDT was placed at the bottom center of the slab to measure the deflection.

- **Materials**

The slab was constructed using HPFRCC with 1.75% volume fraction of 1.5-in Spectra fibers. The mixture proportions by weight of this matrix were 1-cement: 2-sand: 1-aggregate: 0.5-water. The compressive strength was 6.5 ksi. Figure 5.20 shows the uniaxial stress-strain response of HPFRCC. For reinforcements, No. 3 steel rebars with the Young's modulus of 29,000 ksi and the yield strength of 60 ksi were placed in both transverse and longitudinal directions at the spacing of 4 in. center-to-center. As stated earlier, there are three configurations of steel layout considered in this test. With one layer of reinforcement, the clear cover from the bottom of the slab was 2-5/16 in. The layout of reinforcement is shown in Figure 5.17.

5.5.2.2 Finite Element Model

- **Mesh Description**

As shown in Figure 5.19a, the punching shear slab model consists of beam and solid elements. For one layer of reinforcement case, the Hugh-Liu beam elements are used to represent the No. 3 reinforcements whereas the fully integrated solid elements are used to represent the HFPFRCC matrix, the steel frame, and the loading plate. Full bond between matrix and reinforcement is assumed as in the previous simulation and thus, the size of the solid element is selected to be 1 in × 1 in × 1 in. To simplify the meshing process, the centroid of the rebars is moved up to 2 in measured from the bottom fiber. Hence, the slab model consists of 6727 solid elements and 620 beam elements.

In terms of boundary conditions, the bottom nodes of the steel frame are imposed with a fixed boundary condition. The top nodes of the steel plate are pushed down with the prescribed displacement and prevented from moving horizontally. The CONTACT_AUTOMATIC_SINGLE_SURFACE algorithm was used to provide the contact between the slab, the steel frame, and the loading plate (Figure 5.19).

- **Material Models**

The same material models used in the two-span continuous beam simulations are used here. The material properties of the modified HTC model are obtained from Table 5.2 and Table 5.3. Since there is no existing data for 1.75% Spectra fibers, the material parameters used in this simulation are based on the response of HPFRCC with 1.5% Spectra fibers. A minor re-calibration of the material parameters is performed to fit with the uniaxial responses given in the literature (Figure 5.20). For the reinforcement, since the literature provides only the yield strength, the steel is assumed here to behave as elastic perfectly plastic material. Therefore, the hardening function $f_h\left(\varepsilon_{eff}^{p}\right)$ was set to be independent of the effective plastic strain. For the steel frame and loading plate, the material properties are the same as used for the rebars.

5.5.2.3 Results and Discussions

The comparisons of load vs. mid-span deflection curves between simulation and experiment are shown in Figure 5.21. For the case of 0T-0L, the load-deflection response is matched well with the experimental result. This is because the biaxial ratio factor (α) is adjusted to be 0.5. In other words, since the HPFRCC component at the bottom center of the slab is mostly subjected to biaxial tensile loading condition, the α ratio dictates the maximum loading capacity. Therefore, the α parameter is adjusted until the maximum load is fitted with the experimental result. For the case of 1T-1L, the initial slope and the peak load of simulated response are matched well with the experiment but the softening response of simulation is less ductile than the test results. This may be attributed to the fact that the material model for reinforcement is assumed to be perfectly plastic without hardening. In term of the shape of failure mode, the final deformed shapes of both simulation and test are illustrated in Figure 5.22. From the test result, the top steel plate penetrates into the specimen, which indicates that that top deformation of specimen is concentrated around the applied area. This can also be observed from the simulation. For the bottom of the slab, the deflection shape of simulation matches well with the test. Unfortunately, the crack pattern cannot be captured by this proposed model.

5.5.3 Structural Wall

5.5.3.1 Experiments

Parra-Montesinos et al. (2006) tested the structural wall constructed with HPFRCC under displacement reversals. In order to resist large displacement demands imposed by earthquake, the structural wall requires a substantial amount of transverse reinforcement at the boundary regions for the confinement. However, this would lead to difficulty in the construction process due to the congestion of the reinforcement. To ease this problem, HPFRCC used to replace concrete in critical section helps to eliminate the number of stirrups while not reducing displacement capacity.

- **Experimental Setup**

A structural wall with a span-to-wall ratio of 3.7 was tested under displacement reversals. As shown in Figure 5.23, a structural wall with the dimension of 40 in × 40 in × 136 in was subjected to displacement reversals at the top block through a 100-kip hydraulic actuator. The dimension of the top block was 16 in × 16 in × 52 in. The base block was 24 in × 24 in × 72 in and bolted to the strong floor. Lateral support was provided at mid-height of the wall to prevent out-of-plane movement.

- **Materials**

The wall was constructed with two different materials, i.e. normal concrete and HPFRCC with 2% volume fraction of 1.5-in long steel hooked fiber (Dramix ZP 305). The mixture proportions by weight of the matrix were 1: 0.48: 2: 0.48 (cement: water: sand: fly ash). The compressive strengths of concrete and HPFRCC were 7 and 6.5 ksi, respectively. The HPFRCC was used for the critical section of the wall whereas the normal concrete was used for the rest of the specimen. The critical section was defined as the location where the high strain demand occurred. Since the slender wall acted as cantilever, the critical section was located at the bottom of the wall. For this particular wall, the critical section was covered from the bottom of the wall up to 40 in (Figure 5.23).

As shown in Figure 5.24, the main reinforcements were aligned in two identical layers. Each layer composed of 3 of No.5 rebars with the spacing of 2.5 in located at the end of each side of the wall and 4 of No. 2 rebars with the spacing of 6 in located in the middle of the wall. The transverse reinforcements were No. 2 rebars with the spacing of 6 in. Since the bottom block and the critical section of the wall were constructed with two different materials, the cold joint at this section could not be avoided. To strengthen this cold joint, No.4 dowel bars were placed at the bottom concrete block and were extended 14 in into the wall section. The properties of the reinforcements are listed on Table 5.5.

5.5.3.2 Finite Element Model

- **Mesh Descriptions**

The finite element model of slender wall consists of two different element types, i.e. beam and solid elements. As shown in Figure 5.25, the beam element is used to represent main reinforcing steel bars, stirrups, and No. 9 bolts. The solid element is used to represent the matrix of the wall, top and bottom concrete blocks, and the steel plate that is used to apply the prescribed displacement. Based on given spacing of both main reinforcements and stirrups, the size of solid element of HPFRCC section is selected to be 2 in × 2 in × 1 in and that of concrete section of the wall is selected to be 2 in × 3 in × 1 in. The diagonal element length of HPFRCC section is 3 in. Therefore, for the wall part, the number of solid elements is 20 across the width × 4 through the height × 52 along the height. For top and bottom concrete blocks, to ensure the continuity between wall nodes and the top and bottom blocks, the size of solid elements of these blocks is dictated by that of the wall. Hence, the smallest element size of these blocks is the same size as used in the wall. Since full bond between reinforcement and matrix is assumed, the location and mesh size of beam elements are dictated by the size of the solid elements. The spacing between two layers of reinforcement is modified from 2.5 in to 2 in to simplify the meshing process.

A fixed boundary condition is enforced at the bottom nodes of the bolts. To let the top steel plate rotate freely in the z-direction (Figure 5.25), only one single line of nodes through the depth is subjected to prescribed horizontal displacement. In addition, the boundary condition at this nodal line is prevented from moving in the vertical and out-of-plane directions.

- **Material Models**

The structural wall specimen is constructed with three material models, namely modified HTC model, J_2 plasticity model, and linearly isotropic elastic model. The modified HTC model is used for the main wall section for both HPFRCC and concrete sections. For the HPFRCC section, the material parameters are divided into two sets. These two material sets are identical, except those parameters in tension. The material parameters for tension of the first set (DYNA1), are obtained by fitting with the tensile response given in the literature and the simulated response is shown in Figure 5.26a. For the second material set (DYNA2), the material parameters for tension are directly obtained from Table 5.3 without any modifications. As can be seen in Figure 5.26b, the simulated tensile response in DYNA2 is different from the experimental responses. The tensile strength in DYNA2 is four times higher than that in the literature but the overall response in DYNA2 is less ductile than in the literature. For compression, since the literature only provided the compressive strength, the material parameters for compression are obtained from Table 5.2 for 2% hooked fibers.

For the concrete section, the modified HTC model is reduced to the Drucker-Prager model by setting material parameters A, C, E_{htc} to zero. Other material parameters for compression are obtained by using the following well-known formula:

$$\frac{f'_{cc}}{f'_c} = 1 + 4.1 \times \frac{f_{CON}}{f'_c} \tag{5.10}$$

where f'_{cc} is the axial compressive strength of concrete under confining pressure f_{CON} and f'_c is the uniaxial compressive strength of concrete. The tensile response is assumed to be elastic with softening after the peak. The J_2 plasticity model is used for the reinforcements where the material parameters are given in Table 5.5. The input data required for defining the hardening function $f_h(\varepsilon^p_{eff})$ is the yield stress vs. the plastic strain. No reinforcement is provided at the top and bottom blocks because the deformation of these blocks are not the main concern in this simulation.

The linearly elastic isotropic material model is used for top and bottom concrete blocks as well as the top steel plate in which the prescribed displacement is applied. Since most deformation takes place at the wall section, the elastic model is sufficient to represent these parts. The material properties for both blocks are the same as used in the concrete section of the wall. For the top plate, the elastic property of No.9 bolt is applied.

5.5.3.3 Results and Discussions

Figure 5.27 shows the load-drift responses of the structural walls. The envelope curves of test results under cyclic loadings both positive and negative sides are plotted against the monotonic curve obtained from simulations. The overall trend of both simulated results is matched with the test. However, the initial stiffness of DYNA2 is much higher than the experimental results and DYNA1. This is due to the fact that the tensile response used in DYNA2 simulation is different from thetest result. The maximum load in DYNA1 is over-predicted by 20% but the corresponding drift is the same as in the test. Figure 5.28 shows the contour lines at various loading stages. The softening region starts to propagate from the location where the dowel bars are terminated. This location is the same as in the test where the major horizontal crack was formed (Figure 5.29). It should be noted that the test was performed under cyclic loading. Hence, the major horizontal crack was formed by propagation of two horizontal cracks that intersect at the center of the wall. However, the simulation was performed under monotonic loading and thus, the tension softening region occurred only on one side.

5.5.4 Coupling Beam

5.5.4.1 Experiments

HPFRCC coupling beams constructed as a part of the reinforced concrete structural wall systems were tested under displacement reversals in Wight et al (2007). During a large earthquake, the coupling beams, which are used to connect between two walls to form the structural wall system, are subjected to large inelastic deformation. The steel reinforcement detailing is required for high energy dissipation and retaining the integrity of the beams. However, this stringent detailing requires intensive labor and high cost. To reduce the congestion of the rebars, HPFRCC is therefore used to replace the steel confinement reinforcement.

- **Experimental Setup**

A coupling beam with the length-to-span ratio of 1.75 was tested under displacement reversals. With this aspect ratio, the coupling beam was subjected to not only high shear demand, but also flexural deformation under drift of the element. As shown Figure 5.30a, the coupling beam was subjected to cyclic displacements at the top concrete block through a 100-kip hydraulic actuator. A fixed boundary condition was provided by bolting the bottom concrete block to the strong floor. The overall dimensions of coupling beam with concrete blocks are given in Figure 5.30a.

- **Materials**

The coupling beam was constructed by using HPFRCC with 1.5% volume fraction of hooked fiber. The mixture compositions by weight of this matrix were 1: 0.875: 2.2: 1.2: 0.8: 0.005: 0.038 (cement: fly ash: sand: aggregate: water: super-plasticizer: viscosity modified agent (VMA)). The compressive strength of this matrix was 5.5 ksi. The main longitudinal reinforcements were placed into two identical layers. As shown in Figure 5.30b, each layer composed of 4 of No.4 rebars with a spacing of 11 in and 24 in apart from each other. In addition, 2 of No. 3 rebar with the spacing of 7 in apart from each other. The main diagonal reinforcements that were placed in the middle of the cross-section located between two layers of the main reinforcements composed of 4 of No.5 rebars with a spacing of 17 in and 21in apart from each other. Since the coupling beam and the blocks were constructed with two different materials, to provide load transition, all main reinforcements including the diagonal rebars were extended 18 in into concrete blocks on both sides. The web stirrups were No.3 rebars with the spacing indicated in Figure 5.30. Properties of reinforcements are listed on Table 5.6.

5.5.4.2 Finite Element Model

- **Mesh Description**

The coupling beam model is composed of solid and beam elements. Solid elements are used to represent HPFRCC and concrete matrices, and the steel plate whereas beam elements are used to represent steel reinforcing bars, stirrups, and bolts. The size of solid elements used in the HPFRCC matrix is dictated by the location of the diagonal bars. With the diagonal bar slope of 0.5, the size of HPFRCC solid elements is 1 in × 2 in × 1 in. In addition, full bond between concrete blocks and HPFRCC is assumed. The element size of concrete blocks along the width and the depth is controlled by HPFRCC section at the interface areas.

Slight changes in geometry were made to make the mesh fit. For example, the distance between the two outer diagonal bars is reduced from 20.75 in apart to 20 in. However, the inner diagonal bars are moved farther from 17 in to 18 in apart. For the main reinforcements, No. 3 rebars are moved from 7 in. to 8 in. apart from each other. Reinforcements in the top and bottom concrete blocks are excluded in this model.

Two bars are connected from the top concrete block to the strong floor to prevent the top block from rotating in the z-direction (Figure 5.31). In addition, 8 nodes of the bottom block located at the same location as in the test are enforced with a fixed boundary condition to represent contact with the fiber. A single line of nodes of the steel plate is pushed horizontally with the prescribed displacement and prevented to move in the vertical and out-of-plane directions.

- **Material Models**

The same set of material models as used in slender wall is used in this simulation with modification of material parameters. For the modified HTC model, the material parameters obtained from Table 5.2 and Table 5.3 for 1.5% hooked fibers are re-calibrated to fit with the data given in the literature. Figure 5.32 shows the comparison between the simulated responses and the test results. For the J_2 plasticity model, the material parameters are obtained from Table 5.6.

5.5.4.3 Results and Discussions

Figure 5.33 shows the load vs. drift response of the coupling beam. The envelope curves of both positive and negative loading directions are plotted against the response obtained from simulation under monotonic loading. The model successfully captured the overall trend of the response. The peak load is matched with the experimental result but the corresponding drift is over-predicted by 25%. This is due to the fact that the displacement reversals are applied in the experiment, which causes the crack to propagate from both directions, which in turn reduces the stiffness of the beam. In addition, the softening response in the experiment happens earlier than the simulation due to the same reason. Contour lines of the exponential softening parameter reveal that the coupling beam starts with the crack on tension on both top and bottom of the coupling beam. Figure 5.34 shows the hardening and softening contour lines at the final stage of loading. The tension softening propagates at the same location where the major cracks occur in the test.

5.6 Conclusion

This chapter covers the procedure to obtain the material parameters as well as verification of the plasticity macro-scale model for HPFRCC given in Chapter 4. The material parameters for compression yield function are obtained from three tests, namely uniaxial, biaxial, and triaxial compression tests whereas the material parameters for tension yield functions are obtained from uniaxial and biaxial tension. The remaining parameters are obtained by fitting the simulated response with the uniaxial responses. The softening response under compression shows little effect on the element size. However, the tensile softening response shows strong dependency on the size of the element. To compensate for this effect, the material parameters controlling the slope of tensile softening curve are written as a function of diagonal length of the element. Several exercises including a two-span continuous beam, a punching shear slab, a slender wall, and a coupling beam are conducted to verify the proposed model. The simulations are shown to capture the overall responses as well as the failure locations well.

Table 5.1 Steps to obtain material parameters

Steps to obtain material parameters
1. The compressive strength (f_c'), Young's modulus (E_c), and Poisson's ratio (ν) are obtained from uniaxial stress-strain compressive response.
2. Based on peak strengths under uniaxial, equal biaxial, and triaxial compressions, material parameters A, B, C, and D are obtained by using Eq. (5.4).
3. The hardening parameter for the compression yield funciton E_{htc} is obtained next from the initial condition k_0(Eq. (5.6)).
4. The softening parameter for the compression yield function $I_{1,trans}$ is directly obtained from triaxial compression test.
5. The effective plastic strains $\left(\varepsilon_{p,max}, \varepsilon_{p,int}, \text{and } \varepsilon_{p,ult}\right)$ and the slope of exponential softening parameter (s) are obtained by curve fitting with the uniaxial compressive response.
6. The tensile strength (f_t) is obtained from the uniaxial direct tension test.
7. The ratio between equal biaxial tension-tension and uniaxial tensile strength is obtained from biaxial tests.
8. The effective plastic strains $\left(\varepsilon_{p,1}, \varepsilon_{p,2}, \text{and } \varepsilon_{p,3}\right)$ and the softening slope (α) is obtained by curve fitting with the uniaxial tensile response.

Table 5.2 Material parameters of compression yield surface and its potential function

Parameter*	Mortar	Hooked			Spectra		
		1.0 %	1.5 %	2.0 %	1.0 %	1.5 %	2.0 %
f_c'	43.25	56.91	60.3	57.23	56.06	53.46	50.47
E_c	25463.3	25620.7	25723.4	35228.4	20359.84	25931.6	22024.2
A	2.8548	2.7212	2.702	2.7464	2.7663	2.7975	2.8174
B	0.7022	1.3331	1.5908	1.5878	1.7897	1.7449	1.6172
C	2.6419	1.6452	0.9484	2.1228	1.0053	1.5965	1.0293
D	0.3570	0.6767	0.8191	0.8322	0.9554	0.9339	0.8728
E_{htc}	-0.3570	-0.6767	-0.8191	-0.8322	-0.9554	-0.9399	-0.8728
$I_{1,trans}$	-301.26	-309.89	-318.37	-325.03	-329.51	-332.57	-326.04
k_0	0.37	0.37	0.37	0.37	0.37	0.37	0.37
$\varepsilon_{p,max}$	0.001	0.001	0.001	0.0015	0.002	0.001	0.001
$\varepsilon_{p,int}$	0.001	0.001	0.001	0.0015	0.002	0.001	0.001
$\varepsilon_{p,ult}$	0.005	0.007	0.008	0.006	0.011	0.008	0.006
ω	1.0	0.7	0.8	0.4	0.5	0.2	0.2
IMP	0.70	0.8	0.6	0.8	0.7	0.7	0.9
$a_{u,COMP}$	0.63	0.63	0.63	0.63	0.63	0.63	0.63
η	0.34	0.34	0.34	0.34	0.34	0.34	0.34
$\varepsilon_{v,max}$	-0.005	-0.005	-0.005	-0.005	-0.005	-0.005	-0.005
Ratio†	1.2‡	1.42	1.53	1.53	1.62	1.60	1.55

* Based on $25^{mm} \times 25^{mm} \times 25^{mm}$ single element and the unit of stress is MPa

† Ratio between biaxial compression-compression strength to uniaxial compressive strength (not the material parameter for yield function)

‡ Assumed value based on Hussein & Marzouk (2000)

Table 5.3 Material parameters of tension yield surface and its potential function

Parameter	Mortar	Hooked			Spectra		
		1.0 %	1.5 %	2.0 %	1.0 %	1.5 %	2.0 %
f_t	0.818	3.48	4.24	4	3.15	3.24	3.09
α†	1.0	1	1	1	1	1	1
k_1	-	0.7	0.9	0.7	0.9	0.9	0.9
$\varepsilon_{p,1}$	-	0.0005	0.002	0.0005	0.008	0.007	0.003
$\varepsilon_{p,2}$	-	0.0025	0.005	0.004	0.021	0.02	0.015
$\varepsilon_{p,3}$	-	0.018	0.018	0.018	0.035	2.70E-02	3.50E-02
$s^{\ddagger}$	-	0.0149d + 0.15	0.0084d + 0.45	0.0143d + 0.4	0.0156d + 0.1	0.0058d + 0.15	0.0143d + 0.4
$a_{u,ten}$	-	2	2	2	2	2	2

* Based on $25^{mm} \times 25^{mm} \times 25^{mm}$ single element and the unit of stress is MPa

† Since there is no existing data, the ratio between biaxial tension-tension strength and tensile strength is assumed to be 1.0. This assumption is based on the experimental results of the normal strength concrete under biaxial loadings (Hussein & Marzouk, 2000).

‡ d is diagonal length of solid element

Table 5.4 Material parameters of No. 3 rebar used in two-span continuous beam

ε_{eff}^{p} (-)	$f_h(\varepsilon_{eff}^{p})$ ksi (MPa)
0	60 (414)
0.04	105 (724)
1.00	105 (724)

Table 5.5 Properties of structural wall reinforcements

Steel No.	Nominal diameter in (mm)	Yield point		Ultimate point	
		Stress ksi (MPa)	Strain[1] (%)	Stress ksi (MPa)	Strain[2] (%)
#2	0.25 (6.35)	62.0 (427.48)	0.214	63.2 (435.75)	0.228
#4	0.50 (12.70)	92.3 (636.39)	0.318	111.8 (770.84)	1.878
#5	0.63 (15.88)	85.5 (589.50)	0.295	101.4 (699.13)	1.567

[1] Based on assumed Young’s modulus of 29000 ksi (200 GPa)
[2] Based on assumed tangent modulus of 1250 ksi (8618 MPa)

Table 5.6 Properties of coupling beam reinforcements

Steel No.	Nominal diameter in (mm)	Young’s modulus ksi (GPa)	Yield point		Ultimate point		Failure strain (%)
			Stress ksi (MPa)	Strain (%)	Stress ksi (MPa)	Strain (%)	
#3	0.375 (9.525)	28532 (196.72)	76.55 (527.79)	0.27	116.3 (801.86)	10.23	13.63
#4	0.5 (12.7)	25035 (172.61)	72.50 (499.87)	0.29	106.9 (737.05)	11.02	17.12
#5	0.625 (15.875)	23463 (161.77)	62.55 (431.27)	0.29	98.65 (680.17)	10.94	17.29

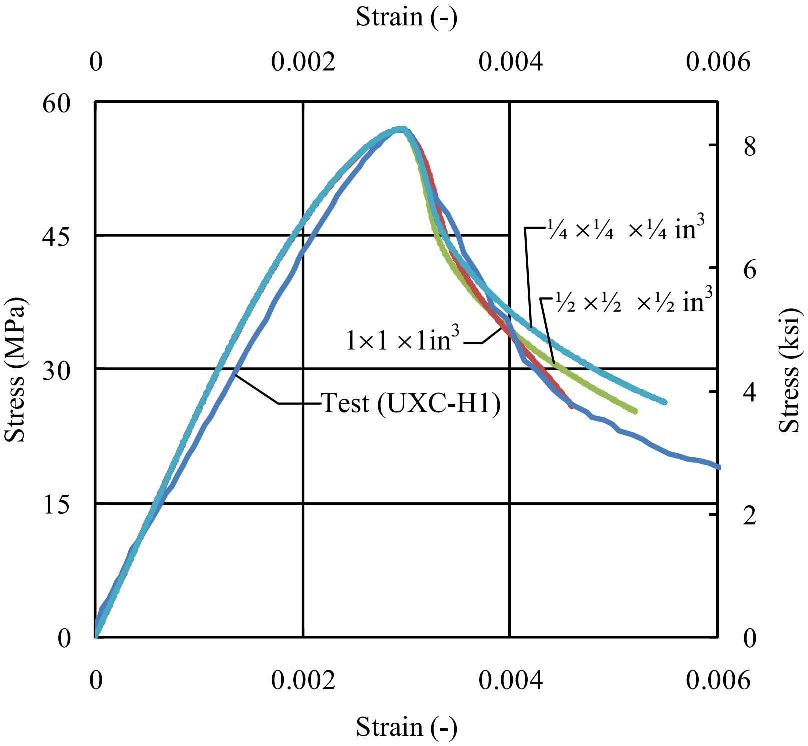

Figure 5.1 Mesh size dependency under compressive softening response (UXC-H1)

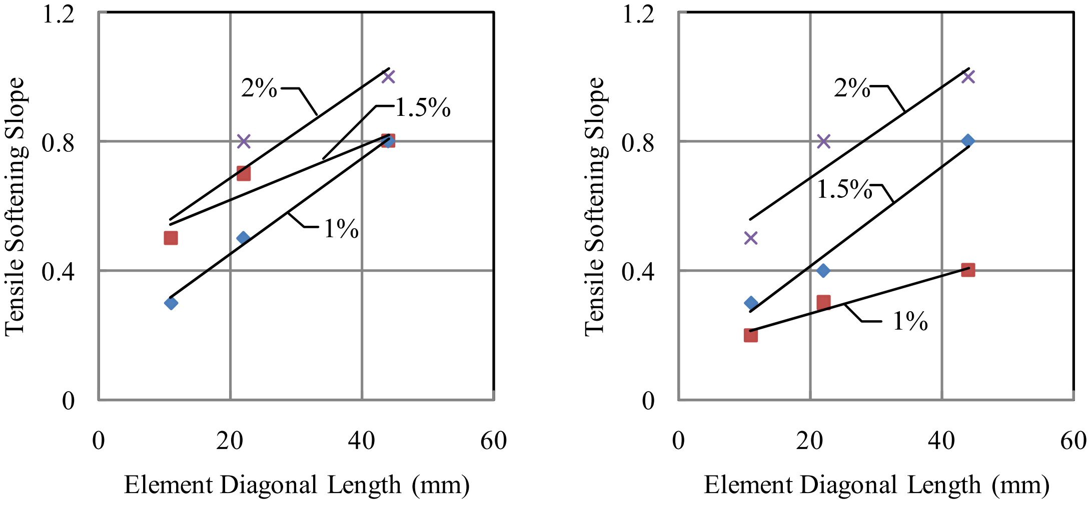

(a) Hooked fiber

(b) Spectra fiber

Figure 5.2Mesh size dependency under tensile softening response

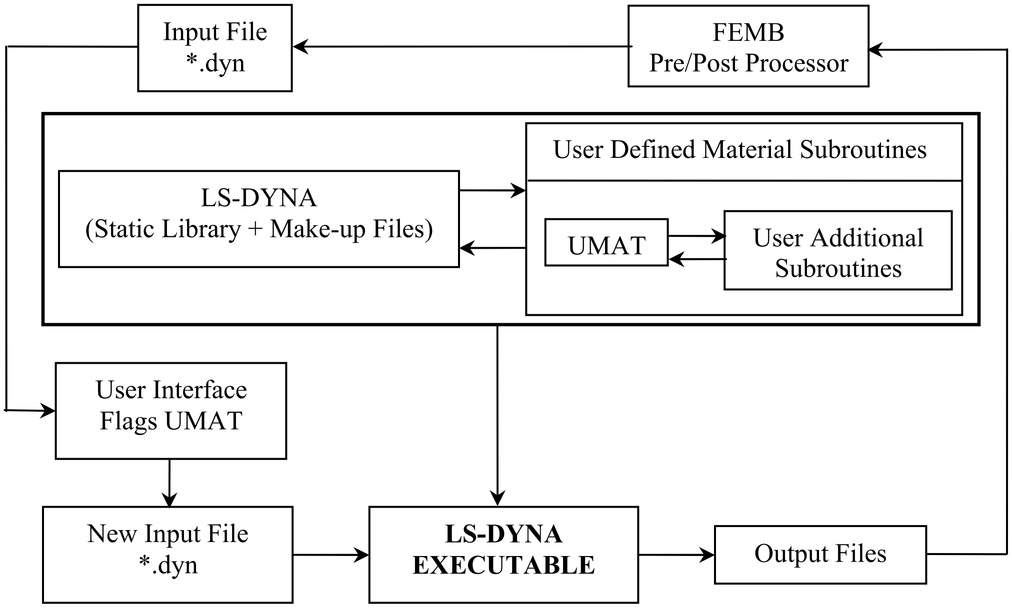

Figure 5.3 User-defined material in LS-DYNA (Moraes and Nicholson, 2001)

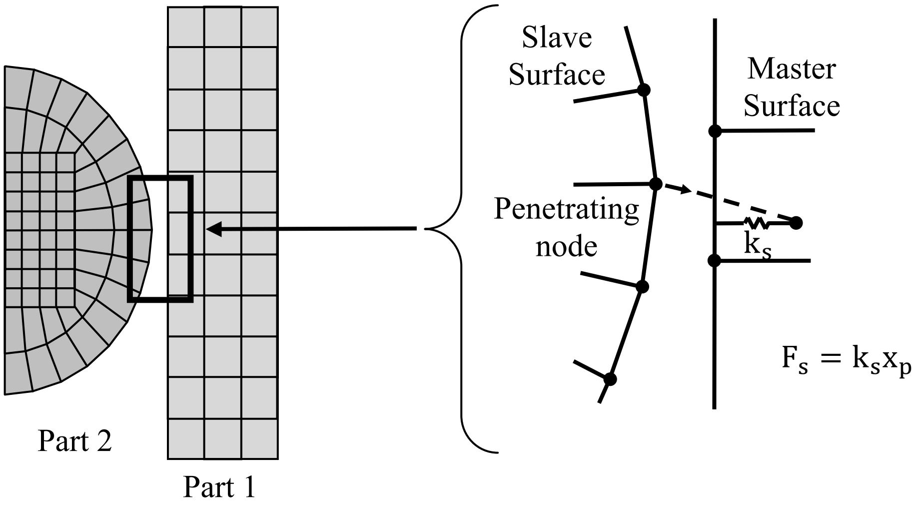

Figure 5.4 Penalty method for contact algorithm (Tavarez, 2001)

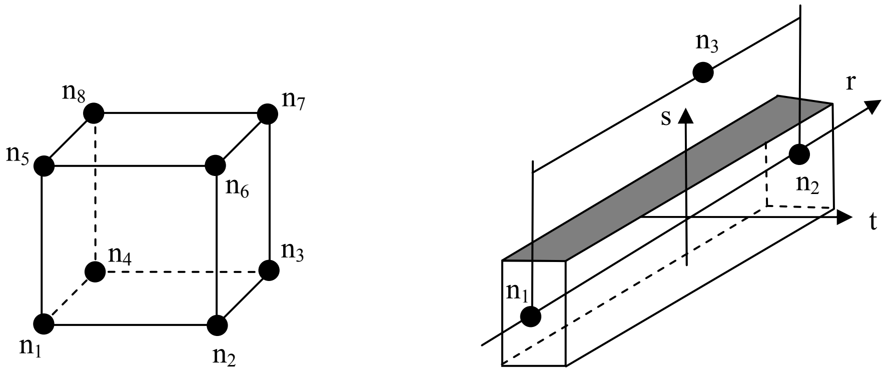

(a) 8-node solid element (b) Hughes-Liu beam element

Figure 5.5 Orientation of solid and beam elements used in LS-DYNA (Hallquist, 2007)

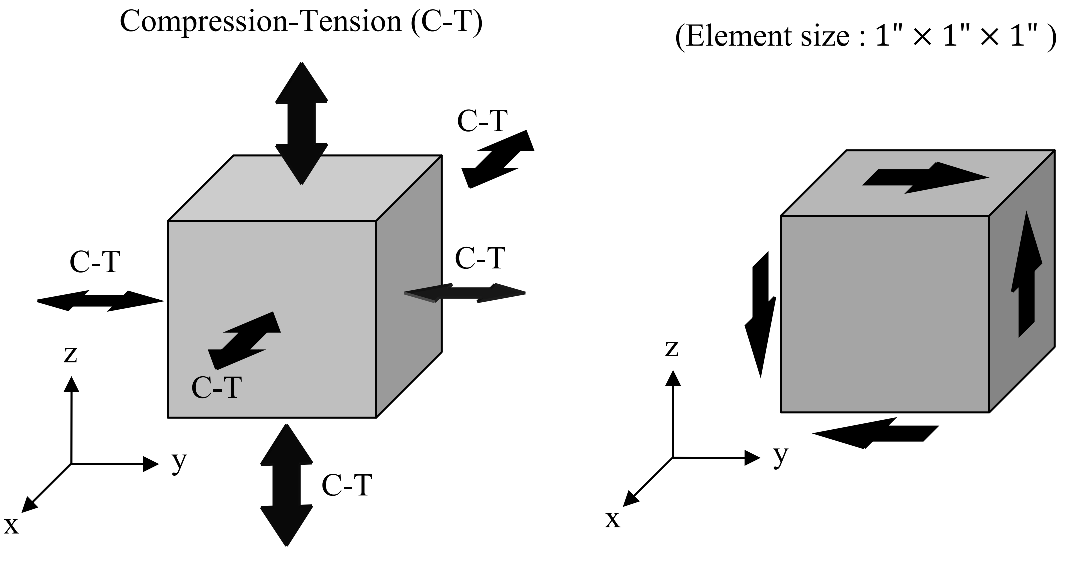

(a) Single element under multi-axial loading conditions

(b) Single element under pure shear loading condition (x-z plane)

Figure 5.6 Single element test under various loading conditions

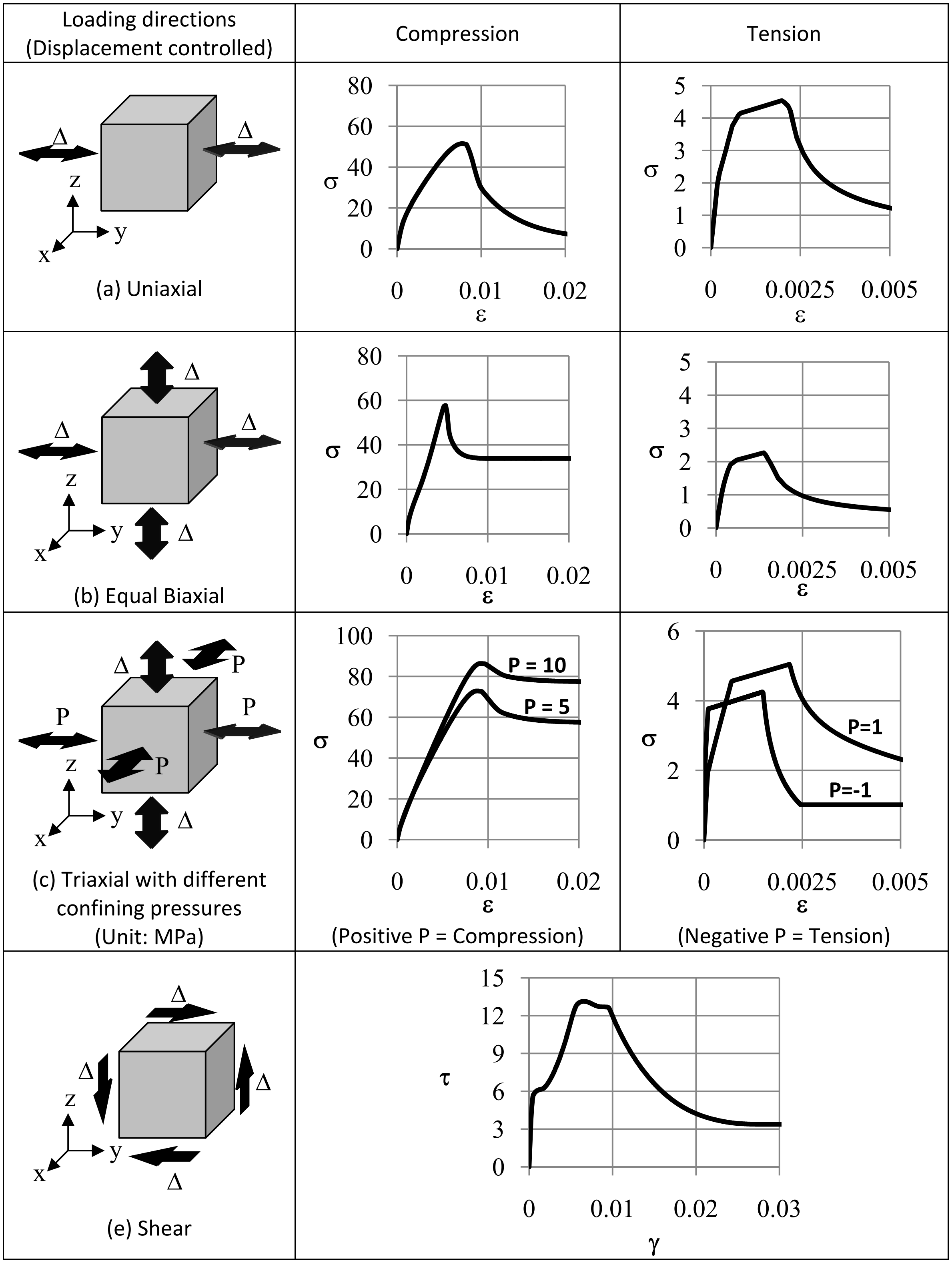

Figure 5.7 Stress-strain responses under various loading conditions

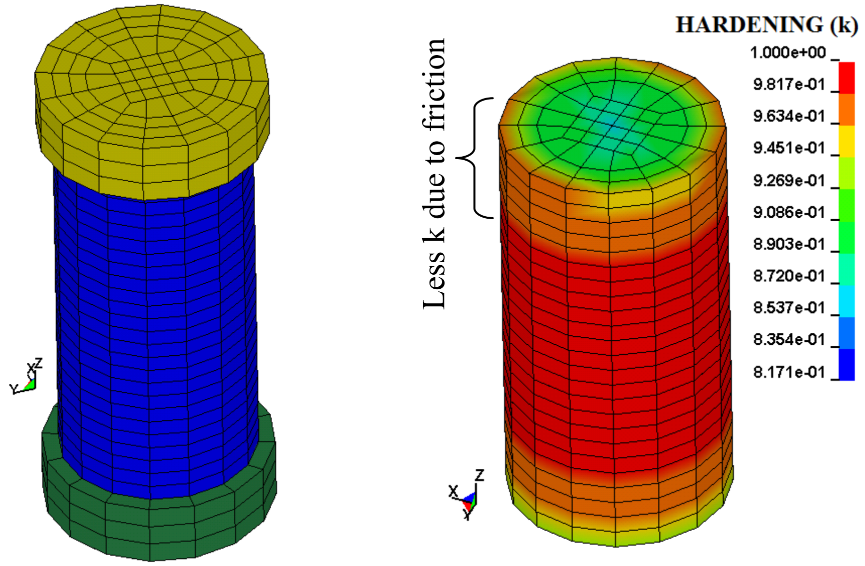

$(\varepsilon = 0, \mathrm{k_{max}} = 0.37)$
(At Initial Point)

$(\varepsilon = 0.40\%, \mathrm{k_{max}} = 1.00)$
(At the Peak Point)

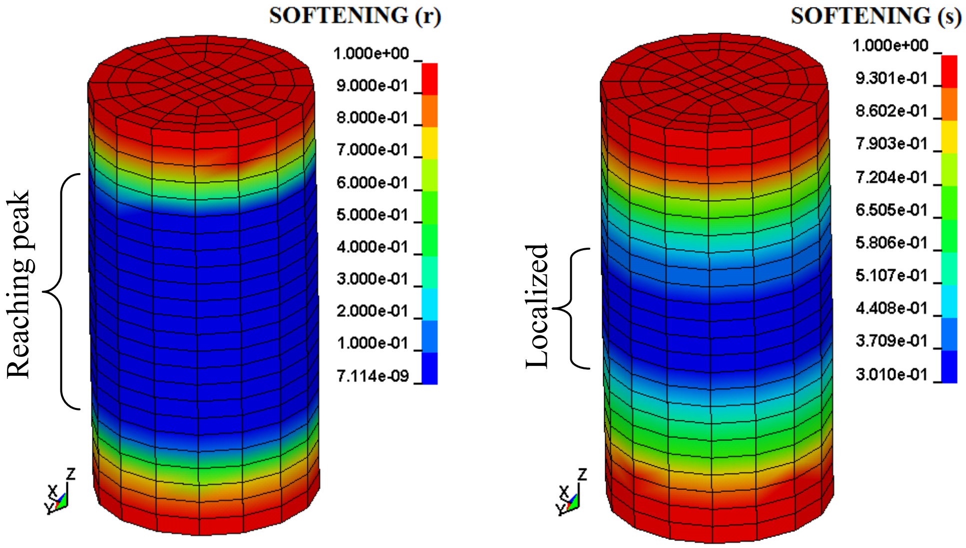

$(\varepsilon = 1.0\%, \mathrm{r_{min}} = 0.00)$
(Softening Region)

$(\varepsilon = 1.0\%, \mathrm{s_{min}} = 0.3)$
(Softening Region)

Figure 5.8 Contour plots of cylinder specimen at various loading stages

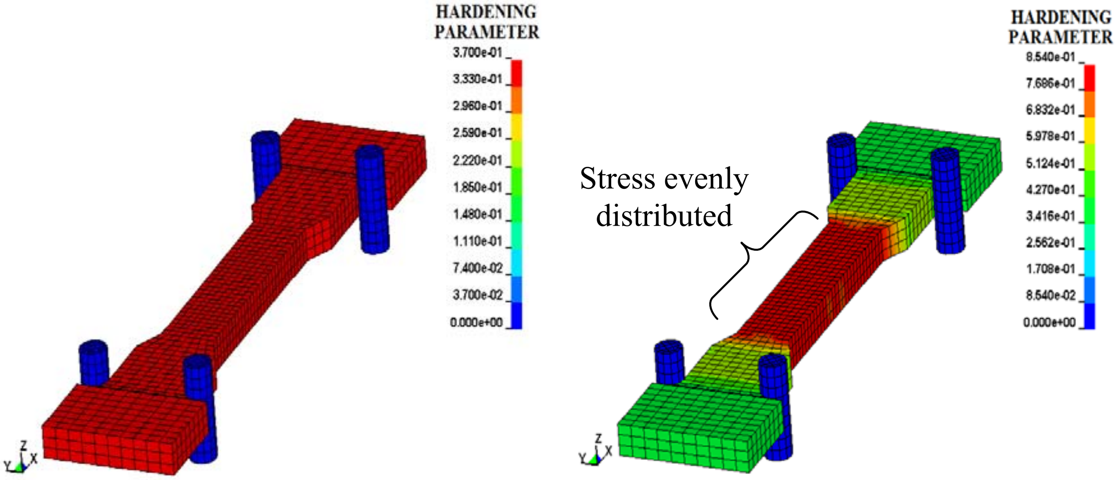

($\varepsilon = 0.0\%, \mathrm{k}_{\max} = 0.37$)
(At Initial Point)

($\varepsilon = 0.42\%, \mathrm{k}_{\max} = 0.85$)
(Hardening Region)

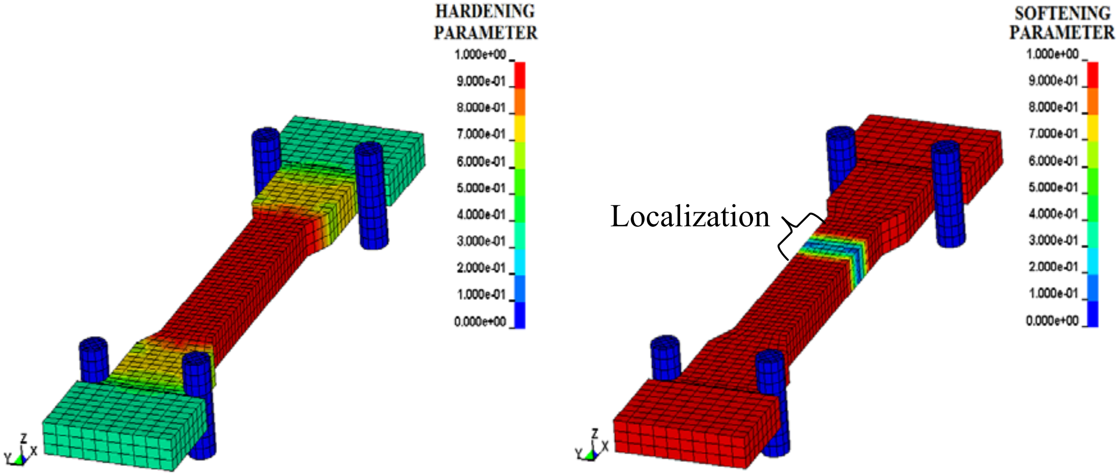

($\varepsilon = 1.3\%, \mathrm{k}_{\max} = 1.00$)
(At peak point)

($\varepsilon = 1.4\%, \mathrm{s}_{\min}$ & $\mathrm{r}_{\min} = 0.2$)
(Softening Region)

Figure 5.9 Contour plots of dog-bone specimen at various loading stages

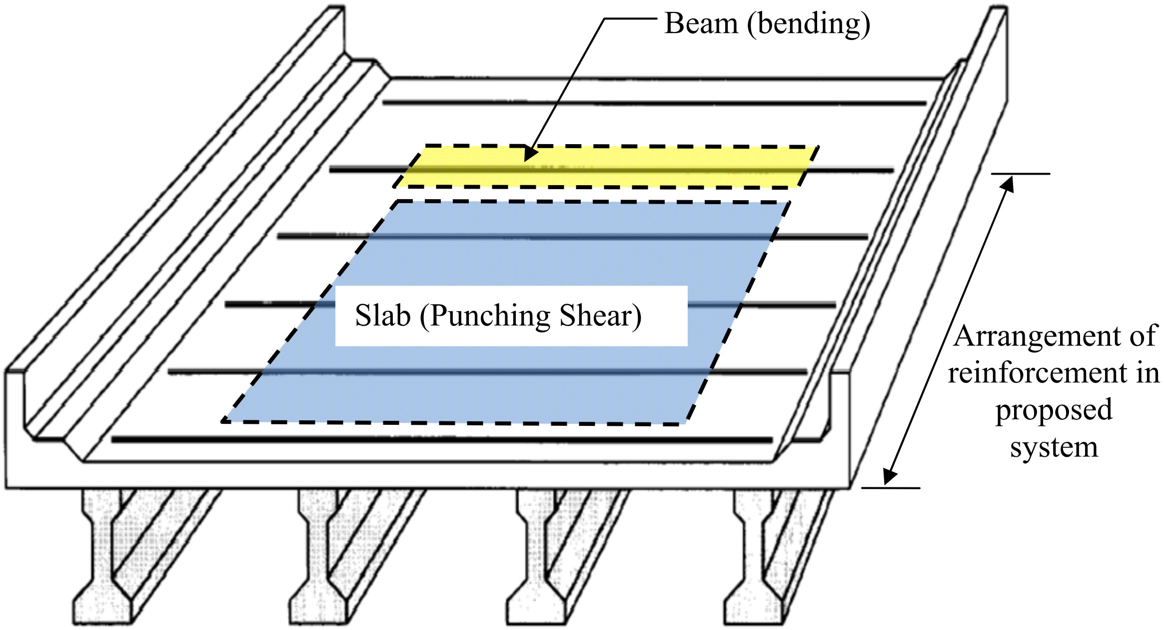

(a) Proposed bridge deck system

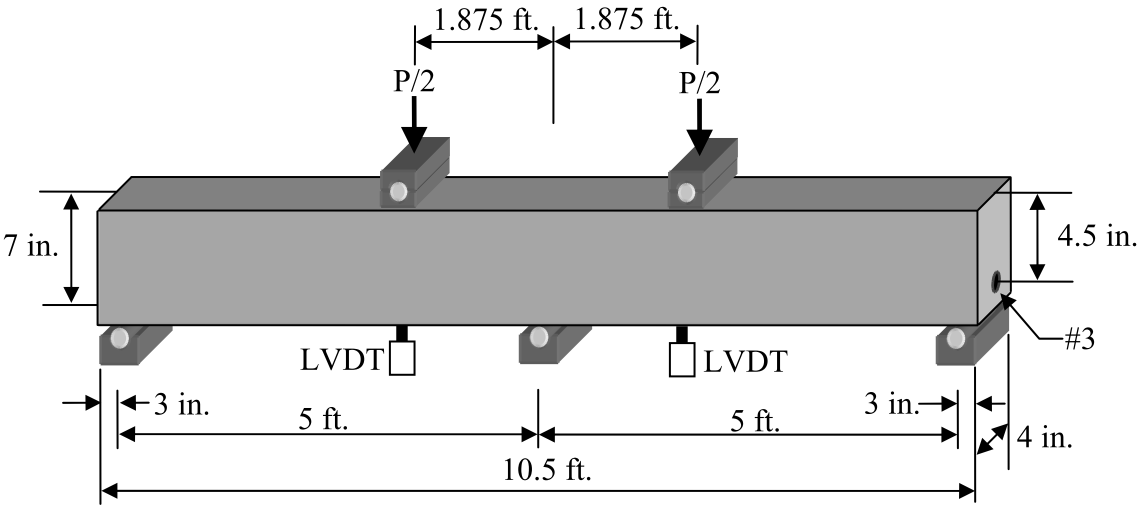

(b) Test setup

Figure 5.10 Continuous beam test setup (Chandrangsu, 2003)

TEST (H): Tensile strength of 0.66 ksi & TEST (L): Tensile strength of 0.53 ksi

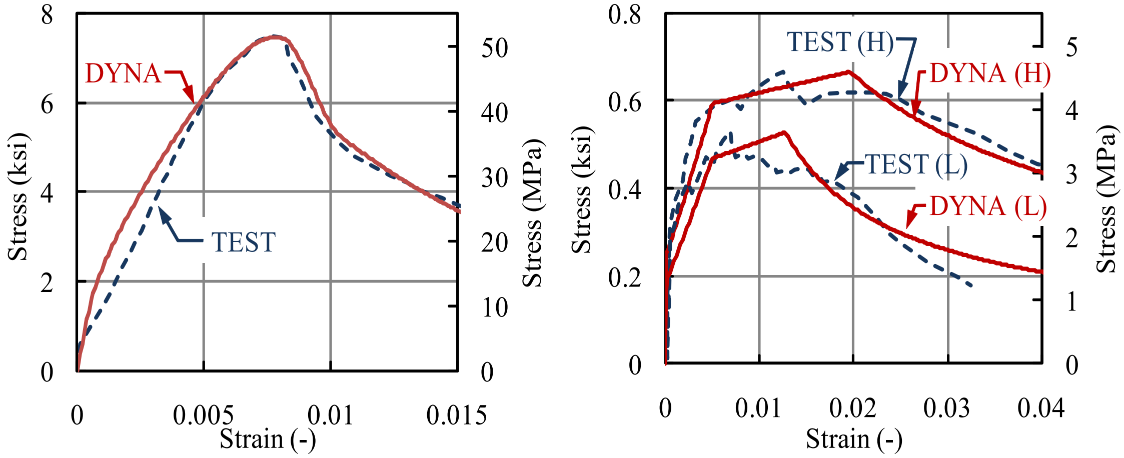

(a.1) Compression

(a.2) Tension

(a) Material parameters obtained from Chandrangsu (2003)

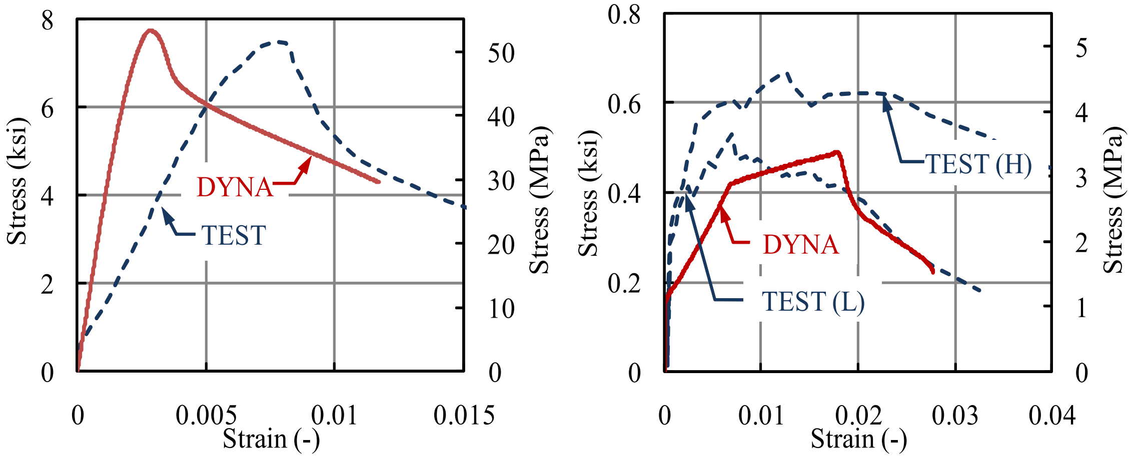

(b.1) Compression

(b.2) Tension

(b) Material parameters obtained from Table 5.2 and Table 5.3

Figure 5.11 Responses of HPFRCC with 1.5% Spectra fiber under uniaxial loadings

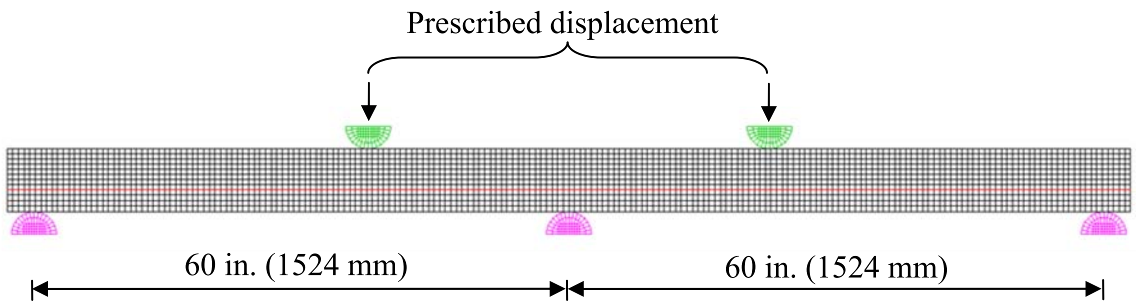

(a) Side view of the model

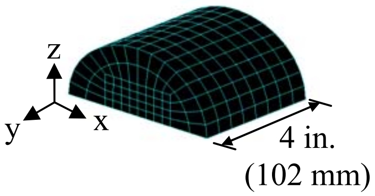

(b) Isometric view for support

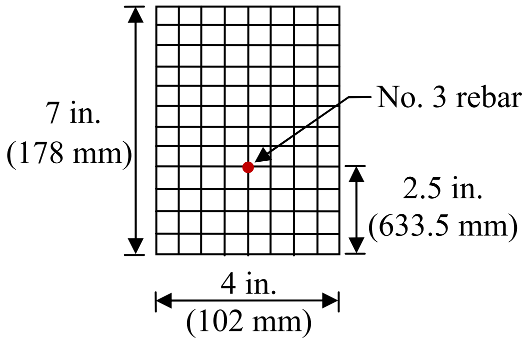

(c) Cross-section

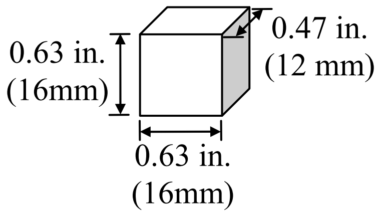

(d) Dimension of solid element for HPFRCC matrix

Figure 5.12 Finite element model of two-span continuous beam

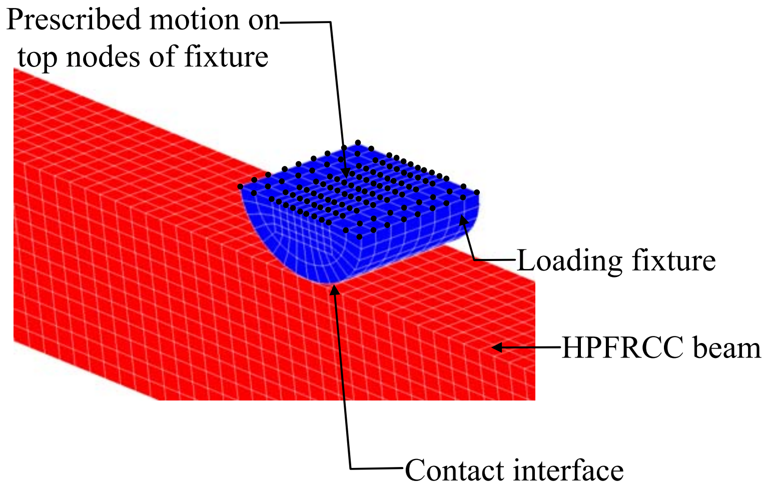

Figure 5.13 Prescribed displacement at the top nodes of loading fixtures

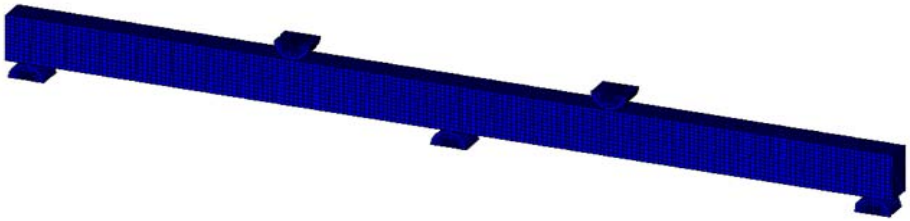

(a) Δ = 0 mm (0 in.)

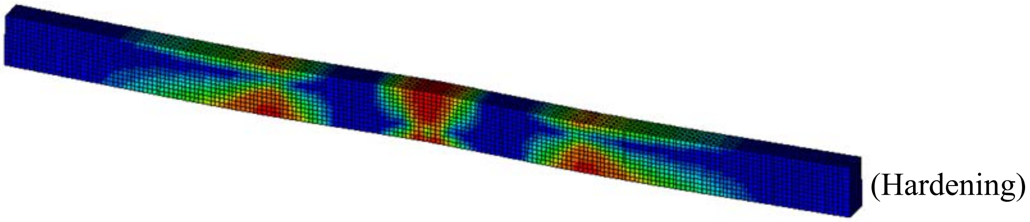

(b) Δ = 10 mm (0.39 in.)

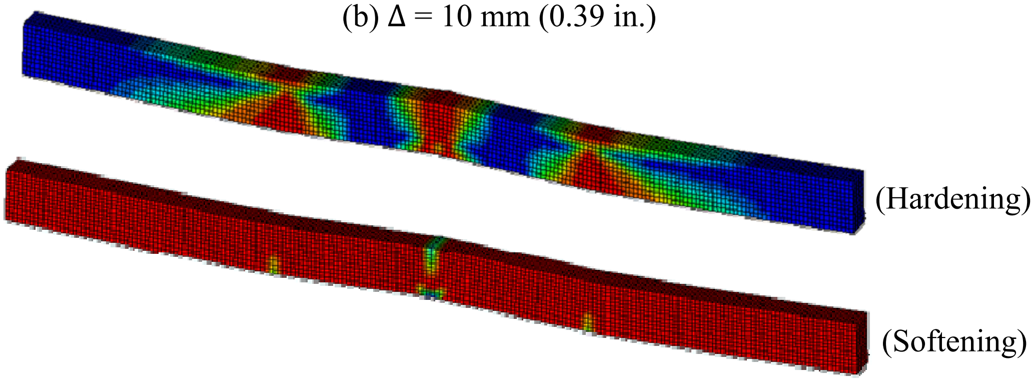

(c) Δ = 20 mm (0.79 in.)

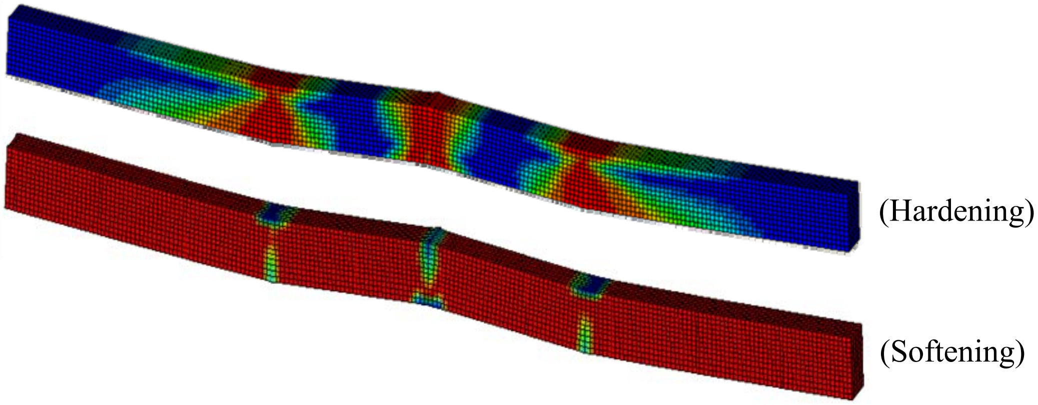

(d) Δ = 30 mm (1.18 in.)

Figure 5.14 Contour plots of the hardening and softening parameters at various loading stages (without magnification)

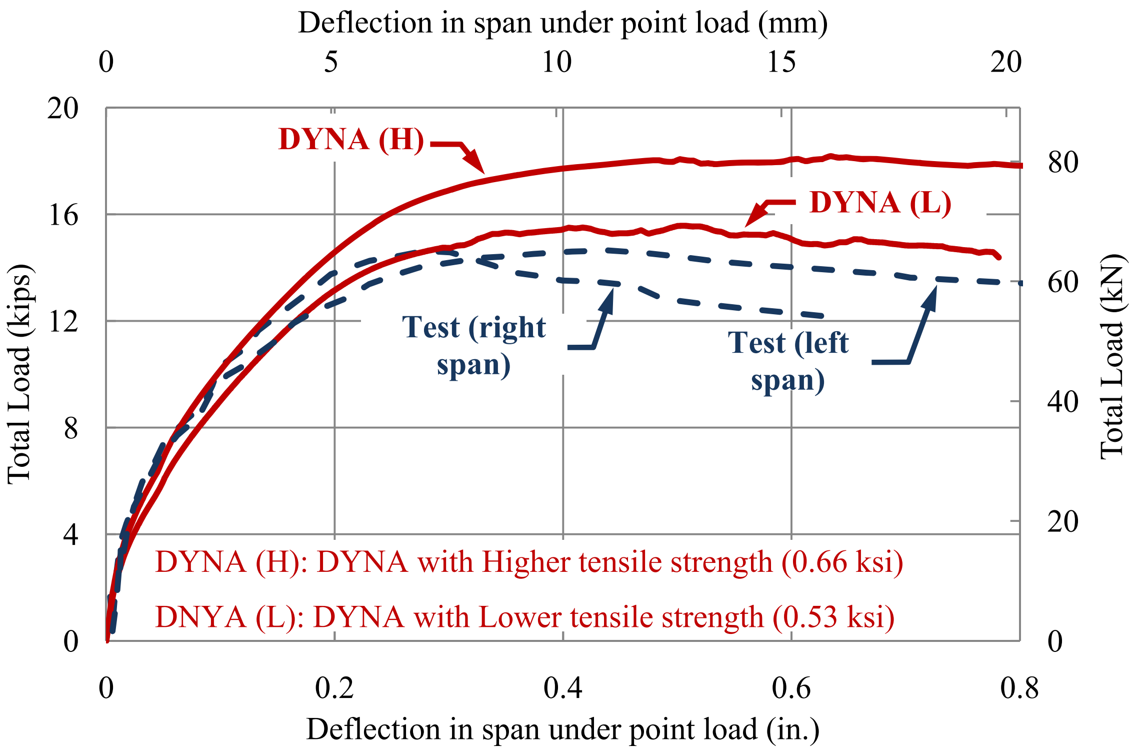

(a) Based on material parameters obtained from Chandrangsu (2003)

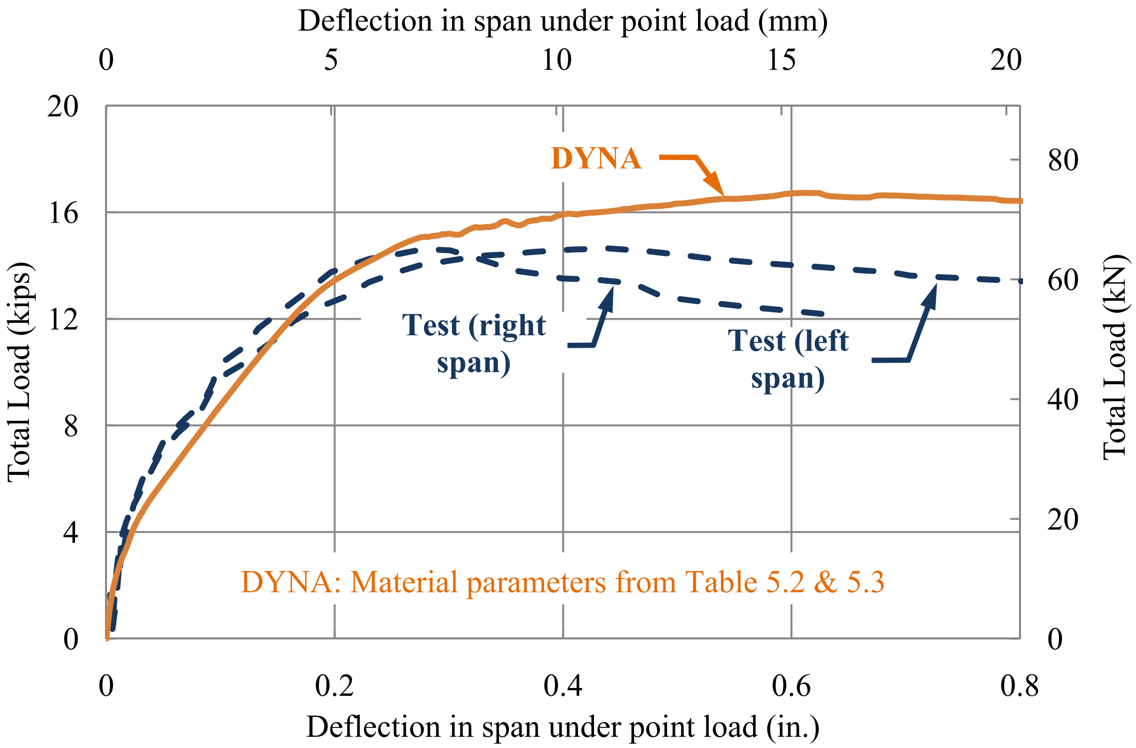

(b) Based on material parameters obtained from Table 5.2 and Table 5.3

Figure 5.15 Comparison of load-deflection curves between test results and simulations

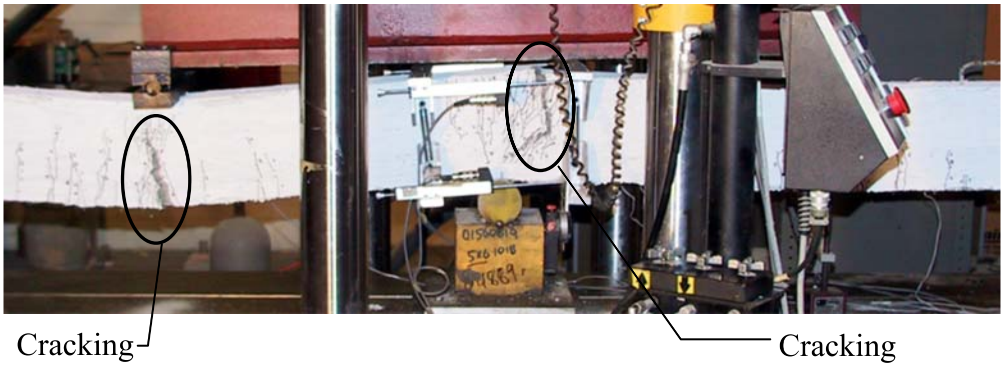

(a) Experiment

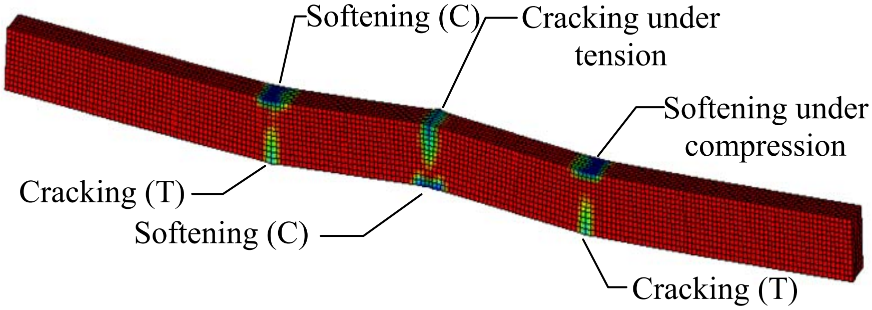

(b) Simulation

Figure 5.16 Deformed shape of continuous beam at the final stage

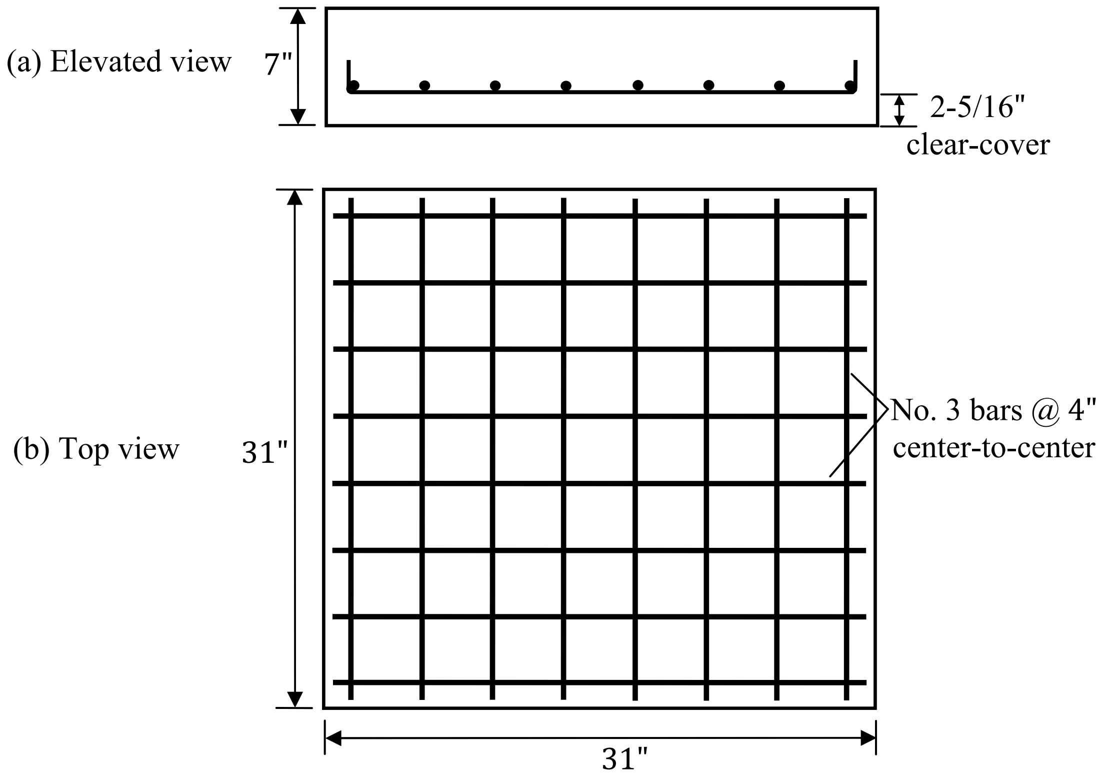

Figure 5.17 Reinforcement details of slab

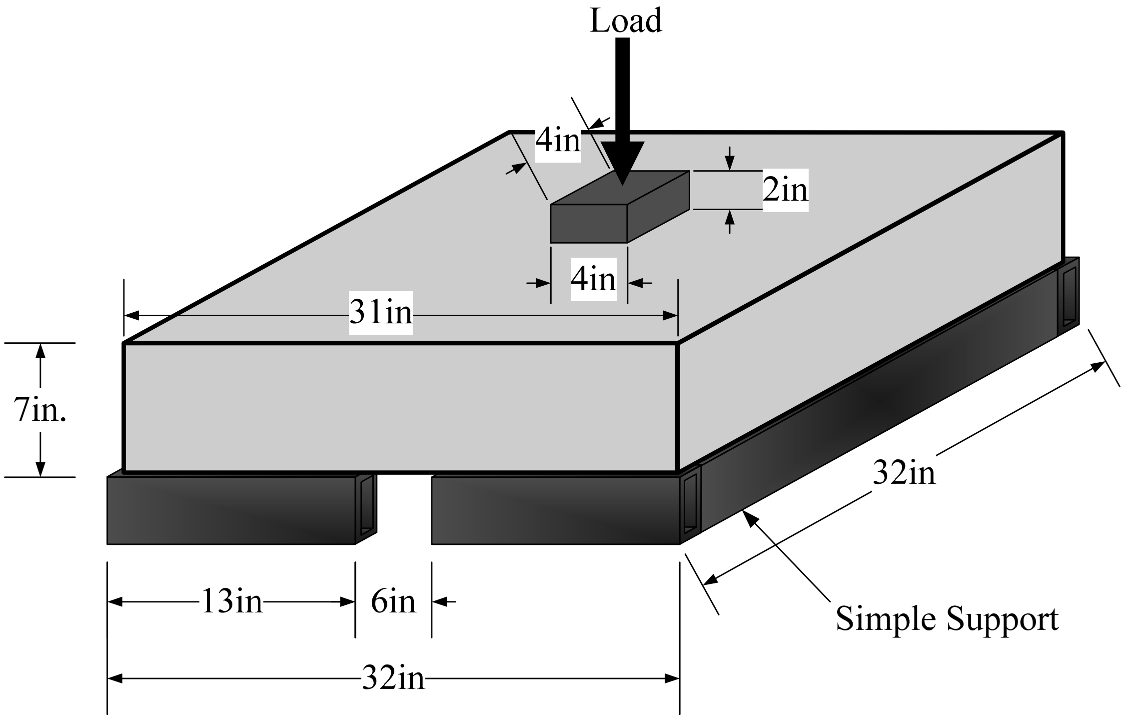

Figure 5.18 Punching shear slab test setup (Likhitruangsilp, 2006)

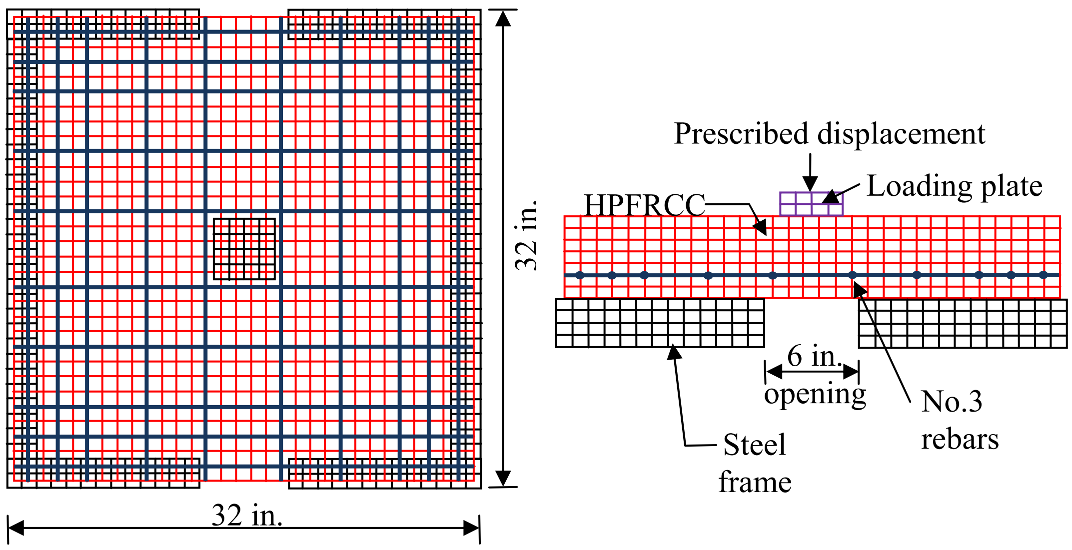

(a) Top view (b) Side view

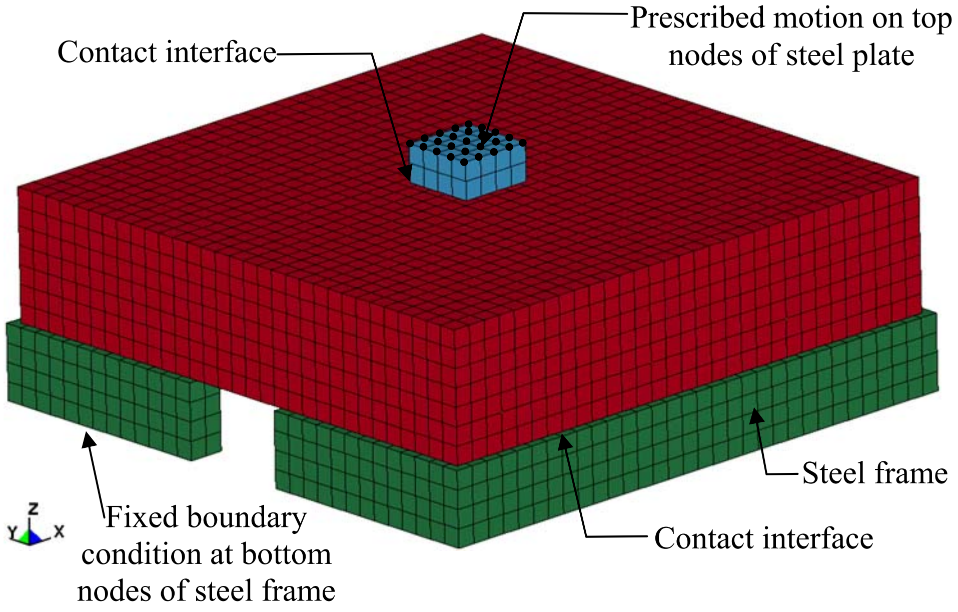

(c) Isometric view

Figure 5.19 Finite element model of punching shear slab

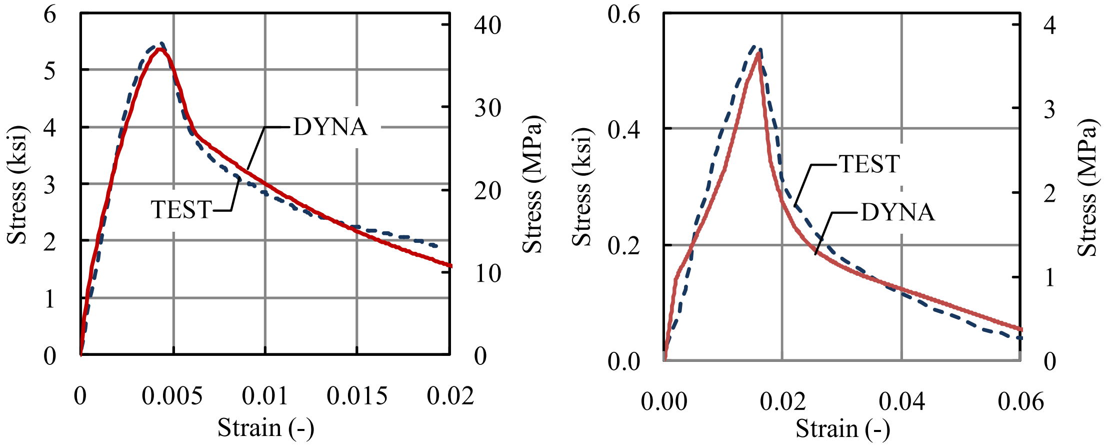

(a) Compression (b) Tension

Figure 5.20 Responses of HPFRCC with 1.75% Spectra fiber under uniaxial loadings

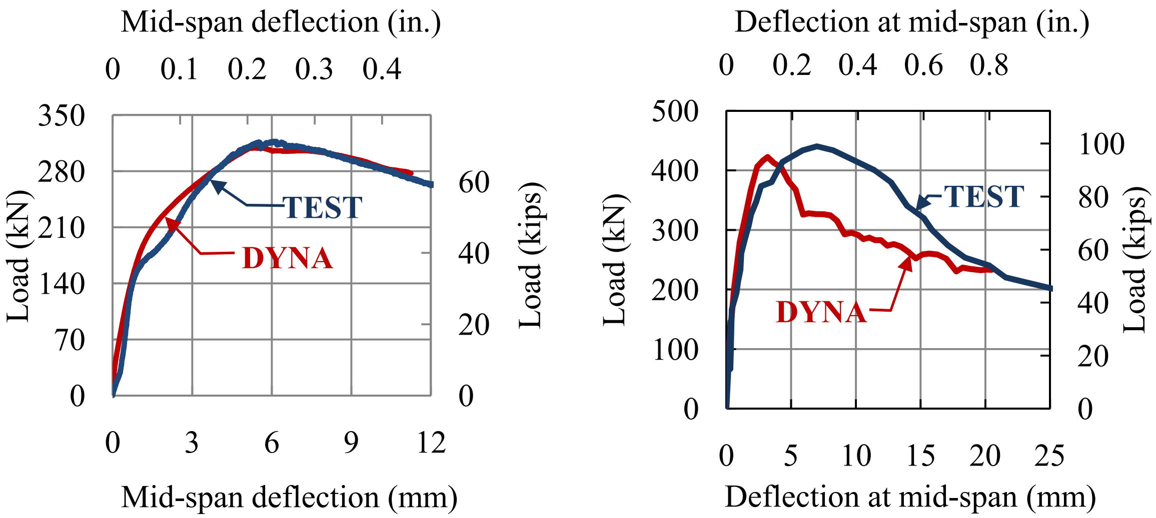

(a) No Reinforcement (0T-0L) (b) One layer of reinforcement (1T-1L)

Figure 5.21 Comparison of load-deflection at mid span between test and simulation

(Top)

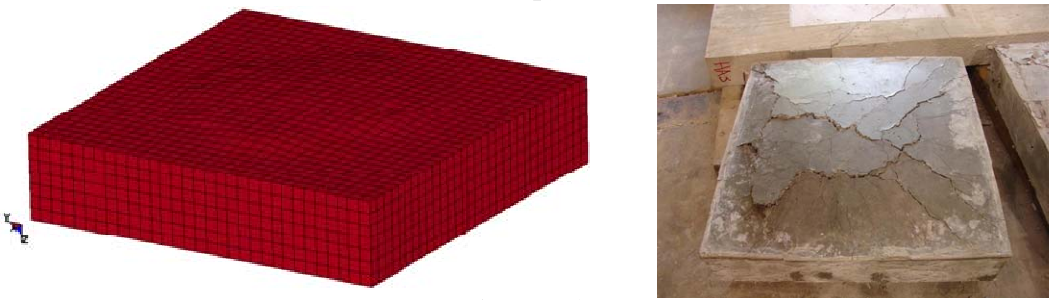

(Bottom)

(a) Simulation (b) Experiment

Figure 5.22 Deformed shape of slab at the final stage

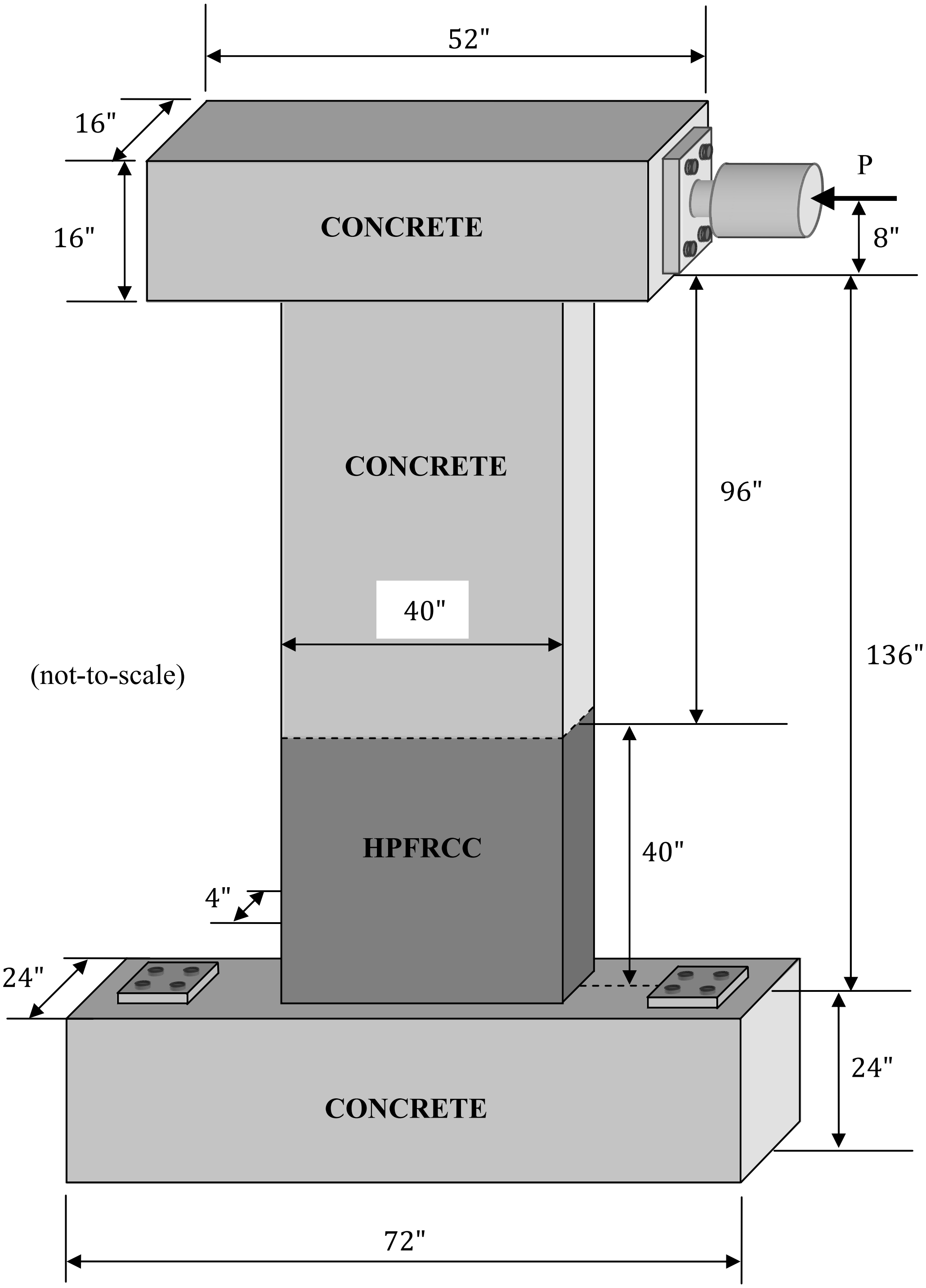

Figure 5.23 Slender wall test setup (Para-Montesinos et al, 2006)

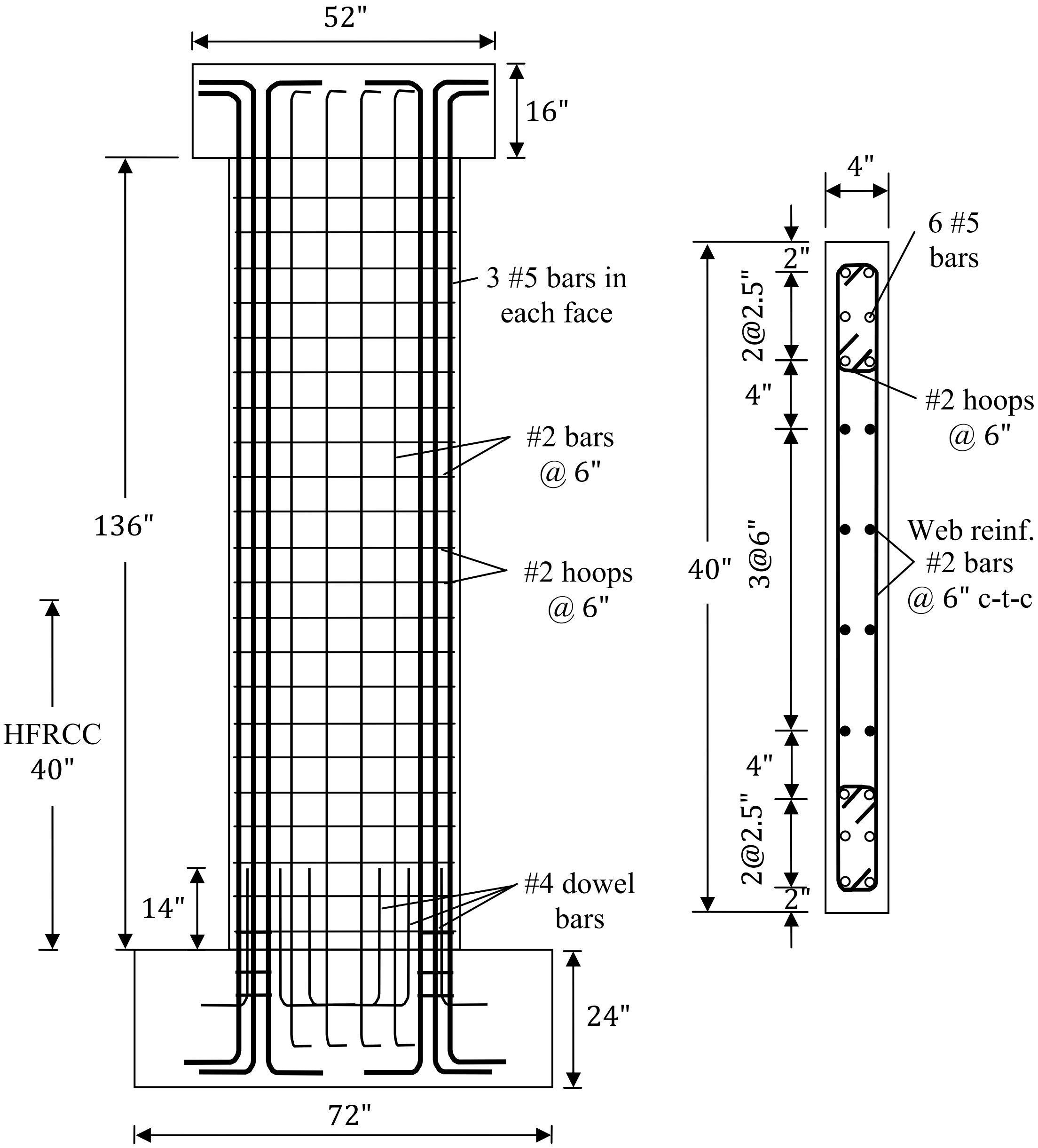

(a) Elevation view

(b) Cross-section

Figure 5.24 Reinforcement details of slender wall specimen (Para-Montesinos et al, 2006)

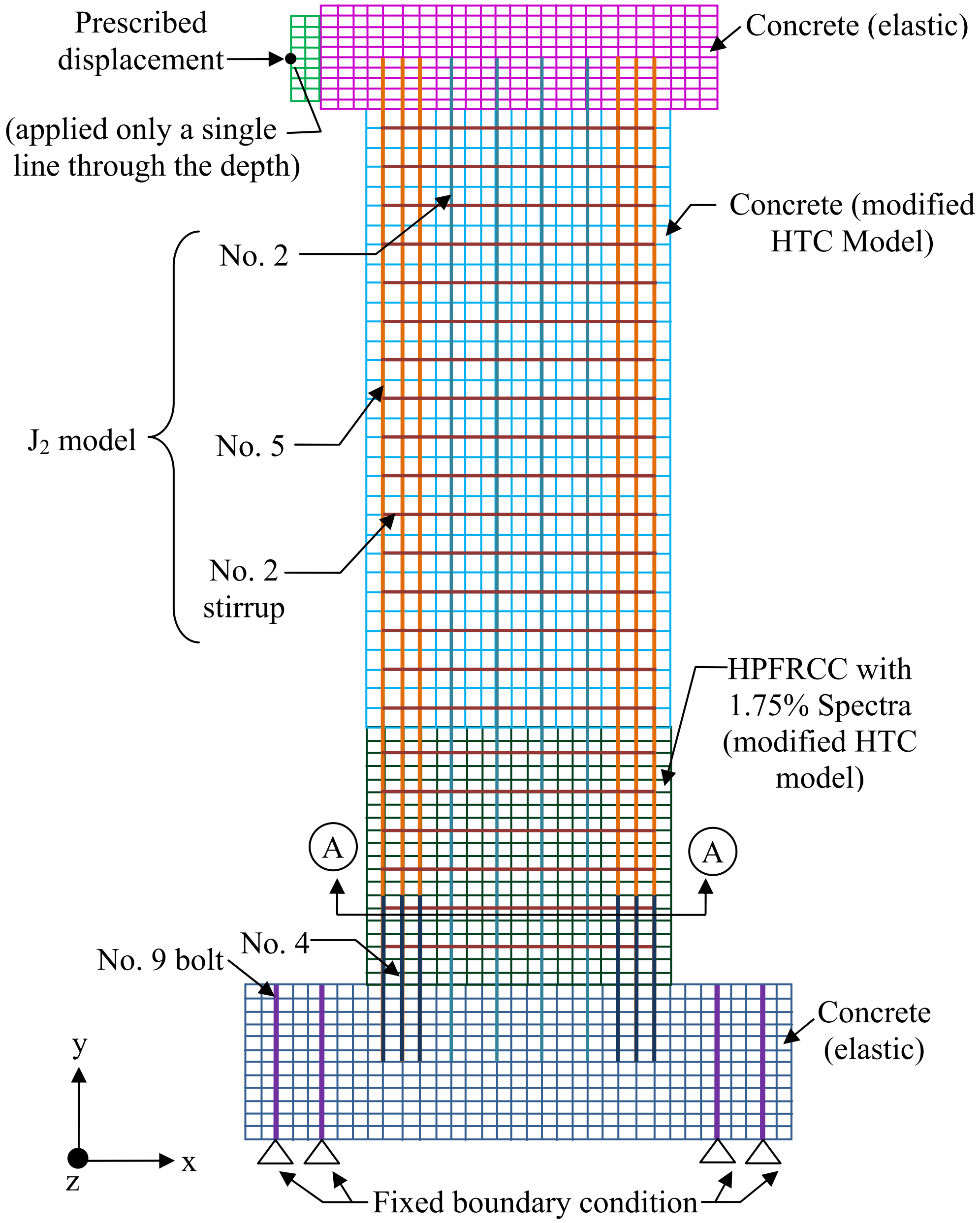

(a) Elevated view of slender wall

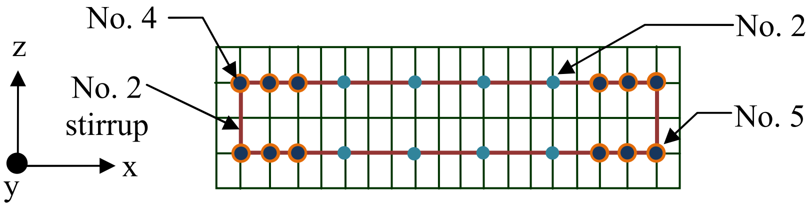

(b) Cross-section at HPFRCC section (A-A)

Figure 5.25 Finite element model of slender wall

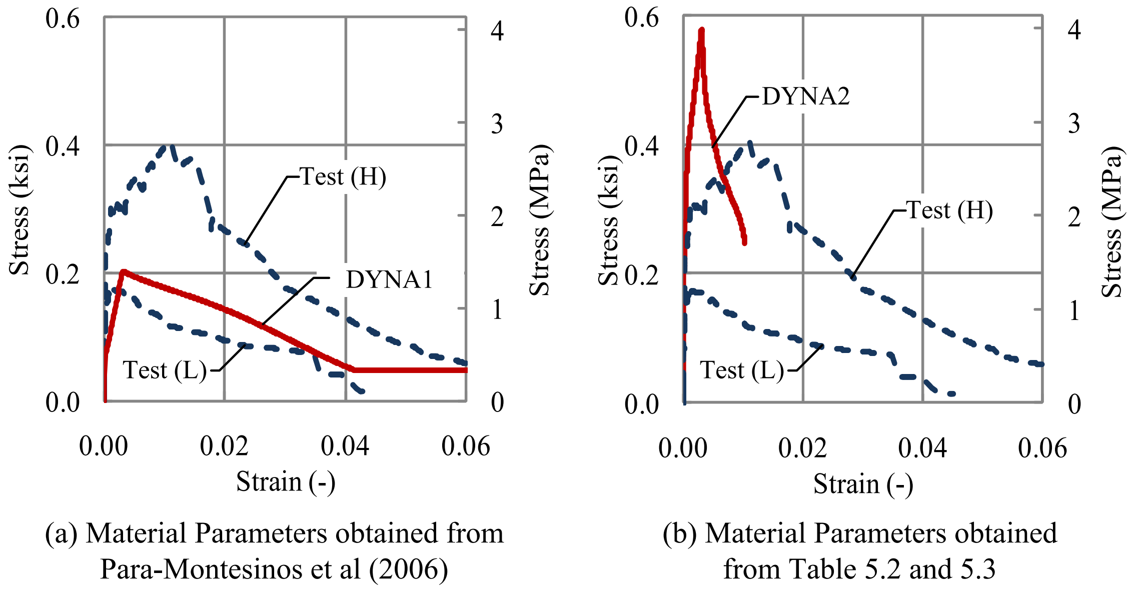

(a) Material Parameters obtained from Para-Montesinos et al (2006)

(b) Material Parameters obtained from Table 5.2 and 5.3

Figure 5.26 Responses of HPFRCC with 2.0 % hooked fiber under uniaxial tension

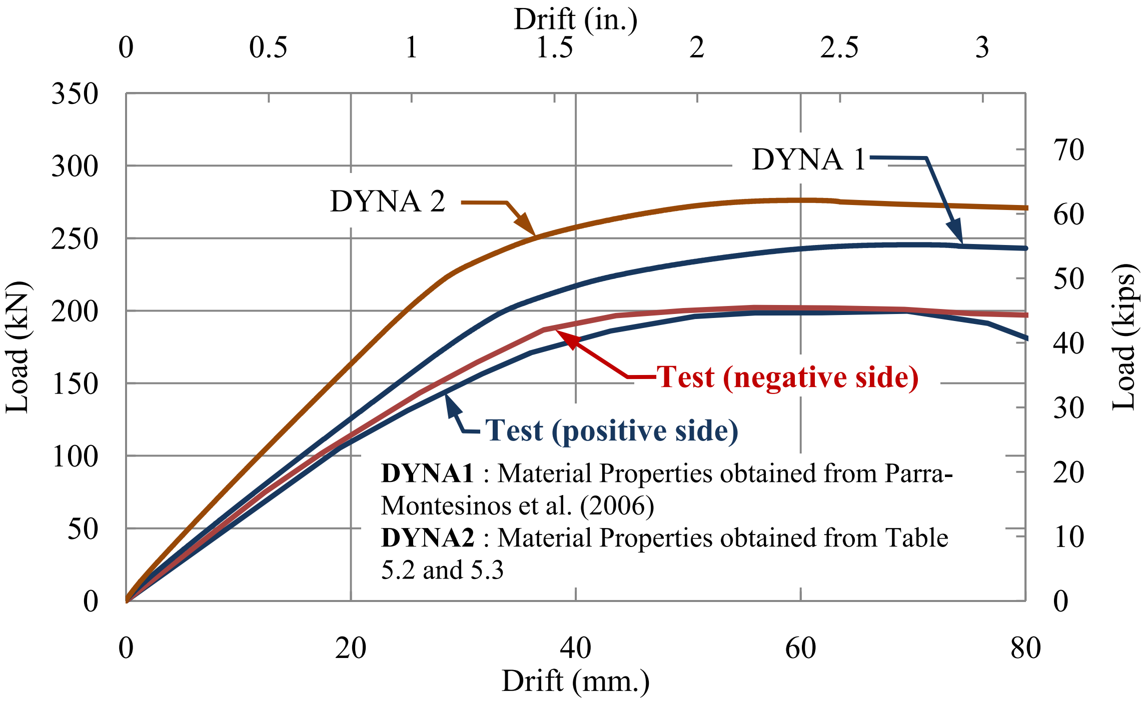

DYNA1 : Material Properties obtained from Parra-Montesinos et al. (2006)

DYNA2 : Material Properties obtained from Table 5.2 and 5.3

Figure 5.27 Lateral load Vs. drift response of slender wall

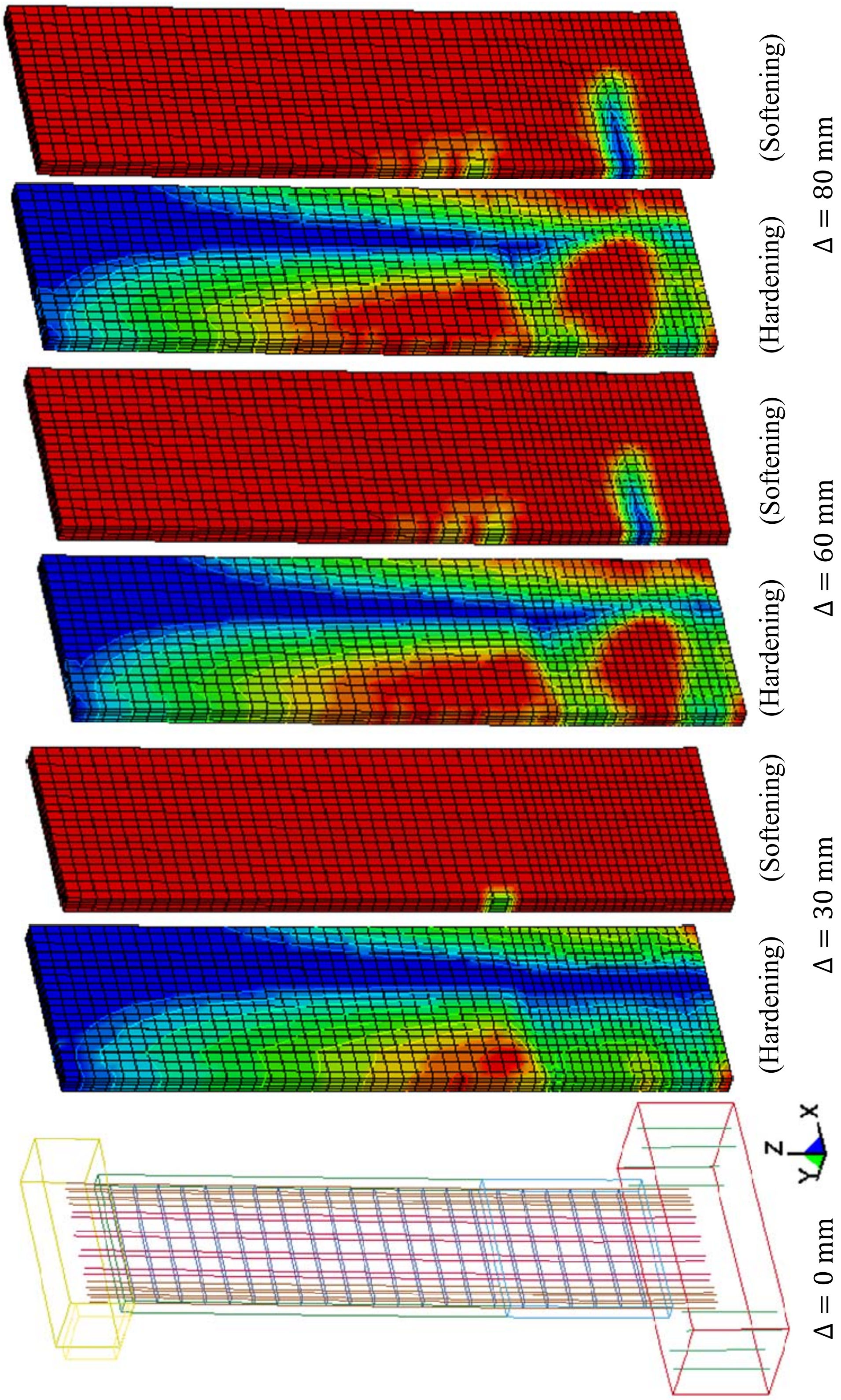

Figure 5.28 Deformed shape of slender wall at various loading stages

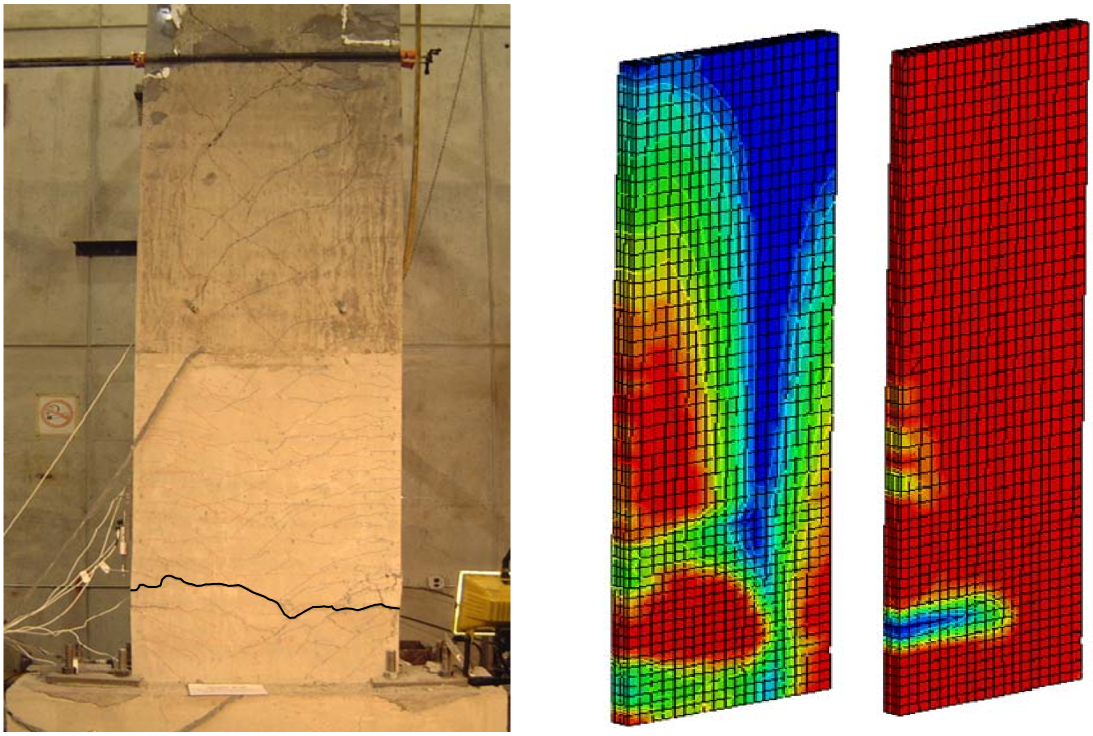

(Hardening) (Softening)

(a) At the end of testing

(b) Simulation

Figure 5.29 Deformed shape of the slab after testing

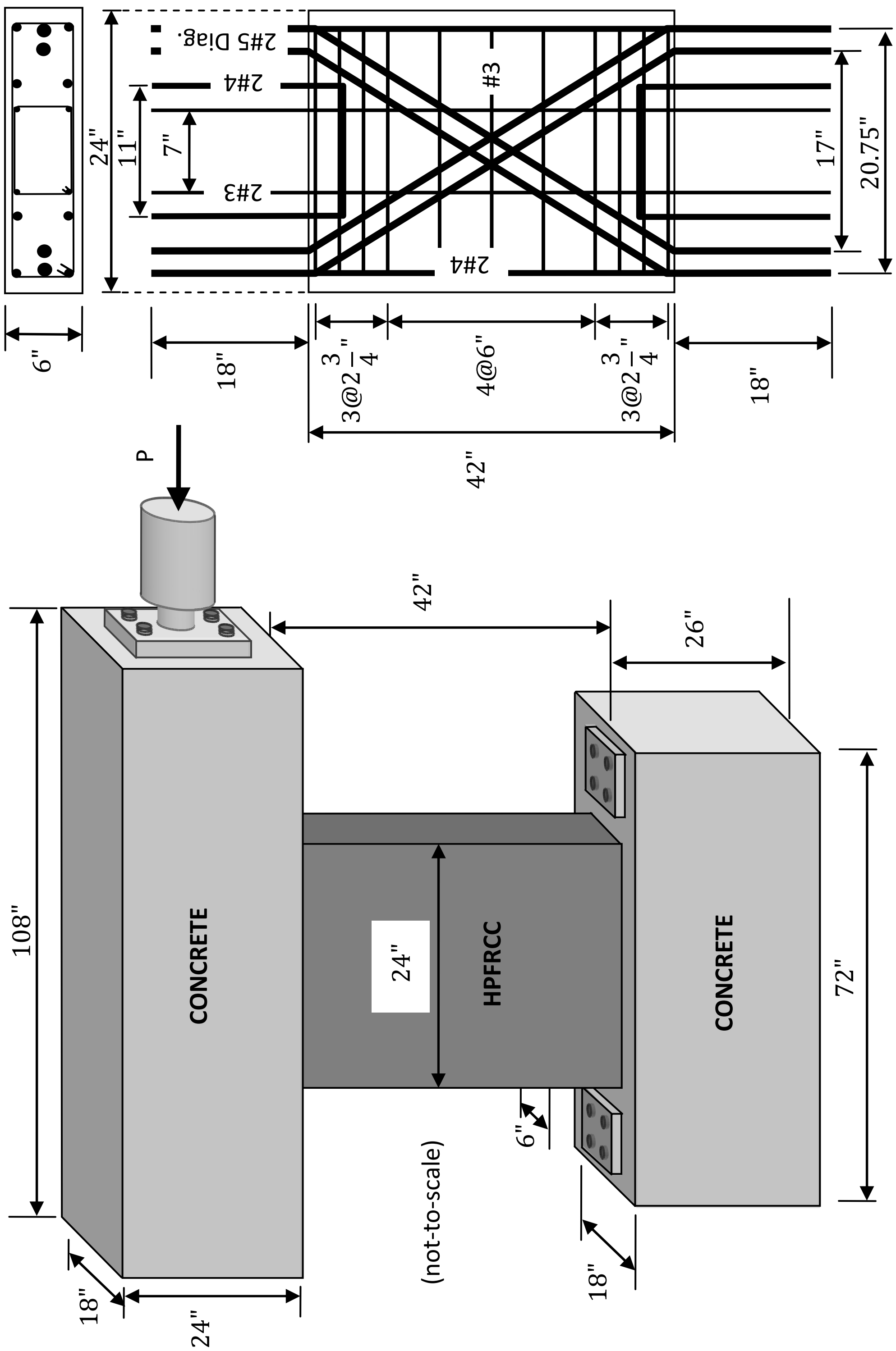

(a) Test setup

(b) Reinforcement Details

Figure 5.30 Coupling beam test setup and reinforcement details

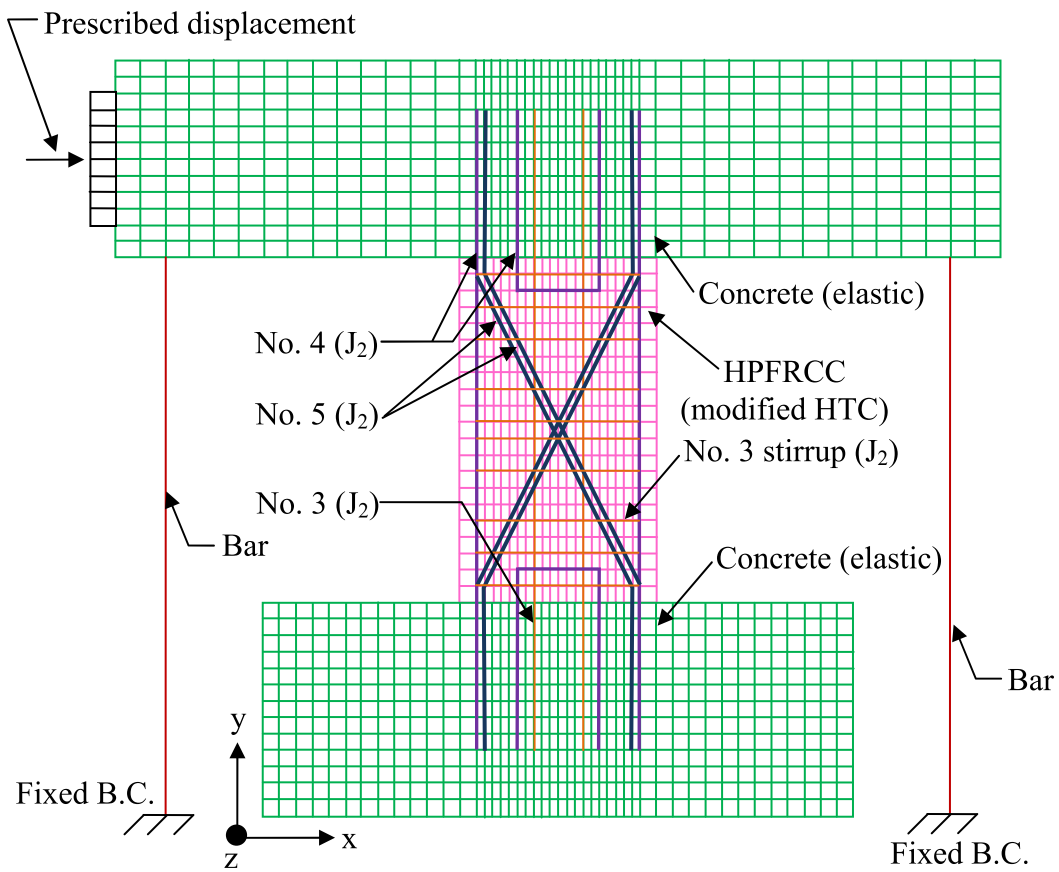

(a) Elevated view of coupling beam

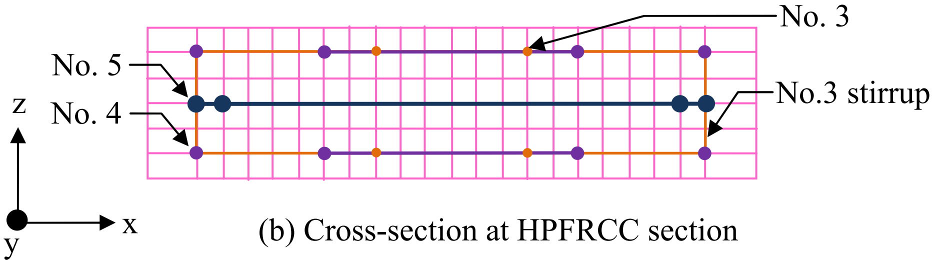

(b) Cross-section at HPFRCC section

Figure 5.31 Finite element model of coupling beam

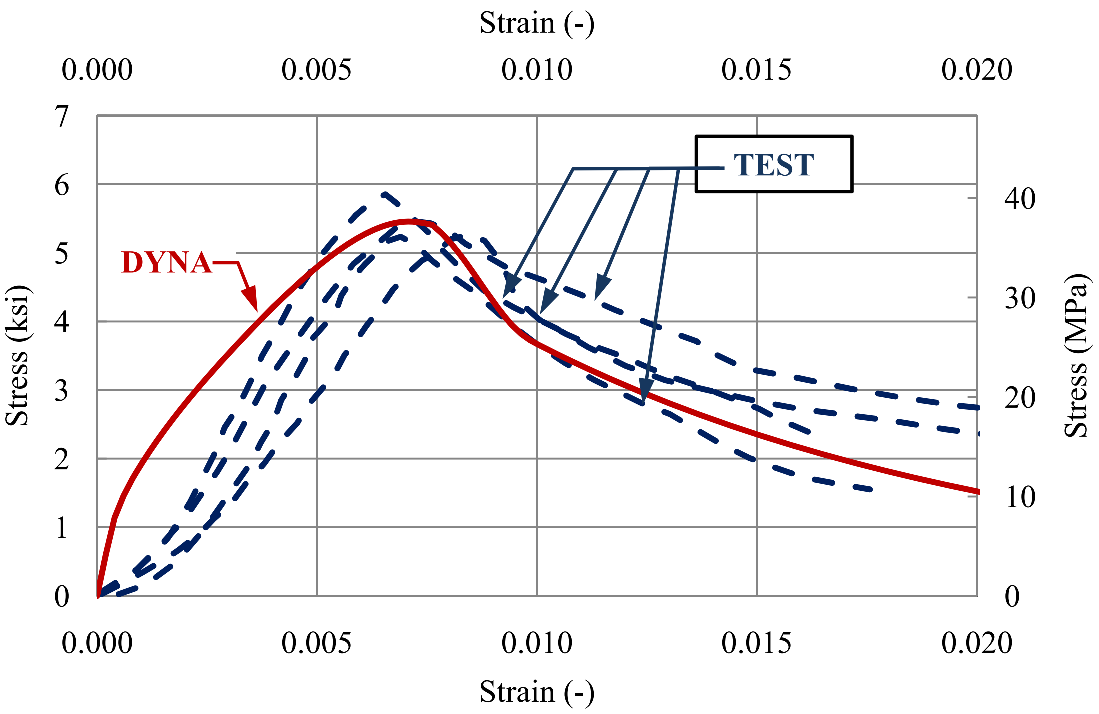

(a) Uniaxial compression

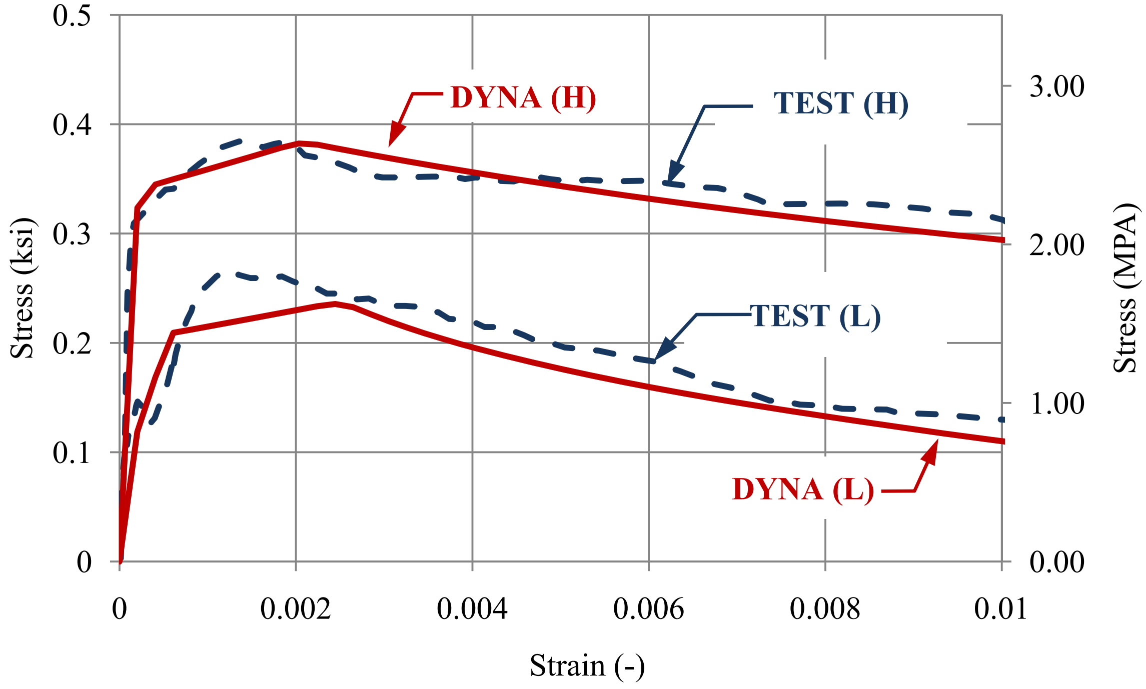

(b) Uniaxial tension

Figure 5.32 Responses of HPFRCC with 2% hooked fiber under uniaxial loadings

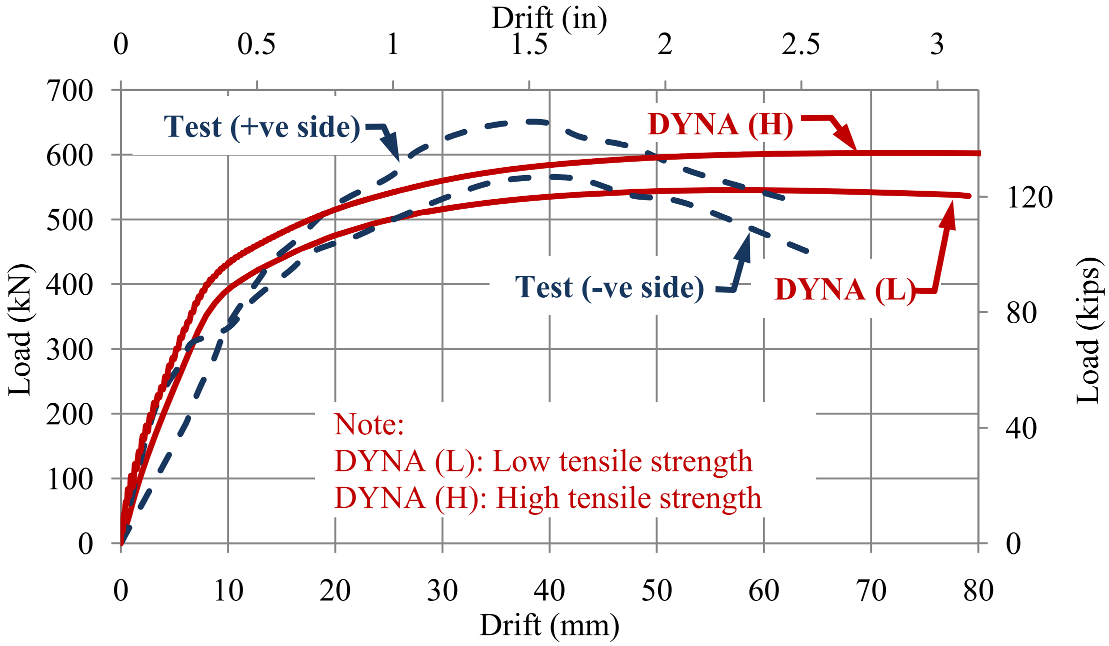

Figure 5.33 Lateral load Vs. drift of coupling beam

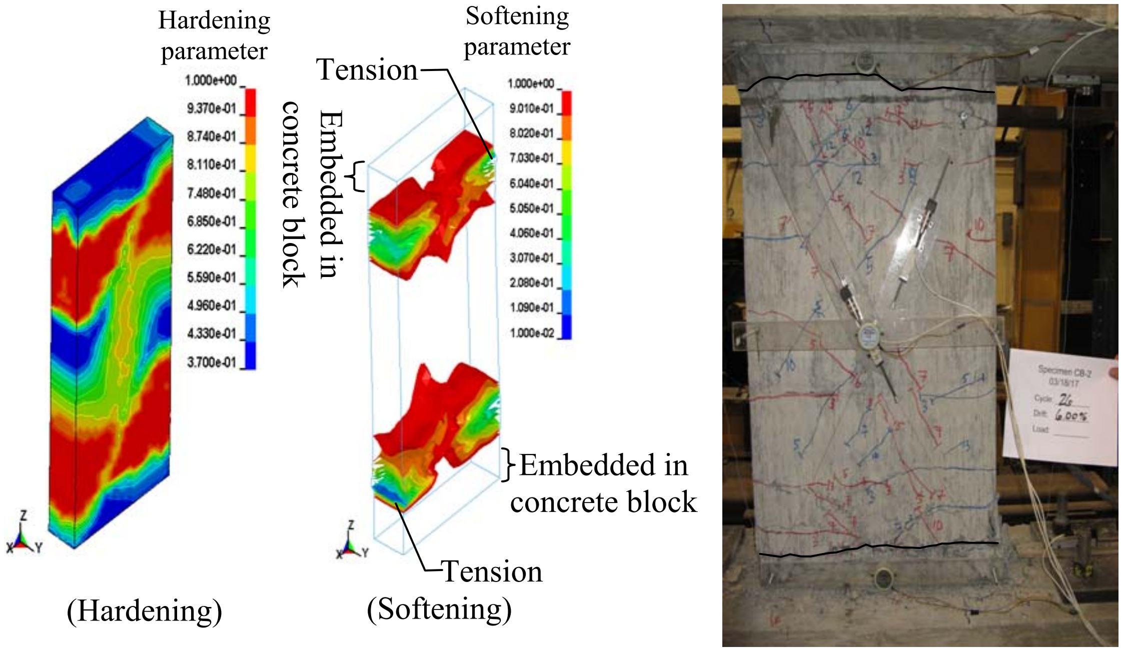

(a) Simulation

(b) Experiment

Figure 5.34 Final deformed shape of the coupling beam

CHAPTER 6

SUMMARY, CONCLUSIONS, AND FUTURE RESEARCH

6.1 Summary and Conclusions

The overall objective of this study is to develop a macro-scale, multi-axial constitutive model for High Performance Fiber Reinforced Cementitious Composites (HPFRCC). The developed model focuses on phenomenological behavior at the macro-scale level and captures responses such as cracking, softening, and hardening. An experimental program was conducted in order to gain a better understanding of the behavior of HPFRCC under basic loading combinations. Once the behavior of HPFRCC was understood from the experimental program, a material model was developed and verified in the analytical program of this research. Specifically, a macro-scale constitutive model for HPFRCC was developed and calibrated against the experimental results. The proposed model was then used to simulate several HPFRCC structural tests to validate its predictions.

6.1.1 Experimental Program

In the experimental program, two types of fibers, namely Hooked (H) and Spectra (S), with three different volume fractions, which are 1%, 1.5%, and 2%, were mixed with mortar having 8 ksi compressive strength.Hence, seven combinations including control mortar without fiber were considered in this study. For these seven material combinations, three loading paths including uniaxial, biaxial, and triaxial were selected for the test program. The following conclusions can be drawn from the test results:

- Under uniaxial tension, strain hardening behavior accompanied with multiple cracking was achieved in all specimens mixed with both types of fibers. Both strength and ductility of HPFRCC were generally improved compared with mortar without fiber.
- Inclusion of fibers increased ductility under all compressive loading paths except under triaxial compression with high confinement. This indicated that the shape of the compressive yield surface mostly depends on the strength of the matrix and not on the fiber content.
- Under uniaxial compression, the inclusion of fibers had little effect on the pre-peak response but significant effect on the peak and post-peak responses. Both strength enhancement and gradual softening were due to short fibers hindering lateral expansion, which in turn increased the confining pressure. Since mortar is a pressure dependent material, increasing confining pressure enhances both strength and ductility of the material.
- Under biaxial compression, although the shape of the failure surface of HPFRCC was found to be similar to concrete, the strength ratio between equal biaxial and uniaxial compressions significantly increased (1.5 and 1.6 for hooked and Spectra, respectively) when compared with regular concrete (1.1 and 1.2 for high strength and ordinary concrete, respectively). The enhancement was attributed to the fibers, which

prevented out-of-plane expansion, which in turn helped to improve the confinement and thus increased the compressive capacity.

- Under triaxial compression, the overall stress-strain response was not influenced by either types or volume contents of fibers. This was attributed to the heavy confinement provided by the steel tube which over shadowed the effect of fibers.

6.1.2 Analytical Program

The main objectives of the analytical program were to develop the material model for HPFRCC and to calibrate and verify the material model against actual structural tests that involved the use of HPFRCC. The macro-scale plasticity model was developed on the basis of the test results conducted in the experimental program. Unlike concrete, HPFRCC strain hardens after first cracking and then gradually softens once reaching the peak. This unique behavior of HPFRCC makes it a good candidate for a tension plasticity model. Due to clear differences in HPFRCC behavior under compression and tension, the proposed model was divided into two parts. Under compression, an existing four-parameter concrete model, which was originated by Hsieh et al. (1979) and later modified by Imran and Pantazopoulou (2001), was adjusted in the softening part of the yield function to accommodate the difference between mortar and HPFRCC. The inclusion of fibers in HPFRCC was evident in the ductility of the descending part of the stress-strain response. Under tension, the tensile yield surface was constructed by extending the compressive yield surface. In addition, three tensile loading combinations, namely uniaxial, biaxial, and triaxial tensions, were used to construct the new yield surface as well. The main reason for extending the compressive yield surface to tension is to make sure that continuity between compression and tension yield surfaces at every loading state exists. Internal parameters, i.e. hardening and softening parameters, were therefore shared by both yield functions to ensure continuity.

After developing the macro-scale plasticity model, the material parameters were calibrated using the test results given in Chapter 3. Then, several exercises, which included a two-span continuous beam, punching shear slab, slender wall, and coupling beam, were conducted to ensure that the model provides good results compared with test data. The procedure to obtain material parameters is: 1) six material parameters for the compression yield functions are obtained from uniaxial, biaxial, and triaxial compression tests; 2) two parameters for the tension yield functions are obtained from uniaxial and biaxial tension tests; 3) the remaining parameters, which control the shape of uniaxial compressive and tensile responses, are obtained by curve fitting with the uniaxial responses. The two material parameters (ω and γ) that control the slope of the softening response under compression and tension are dependent on the size and orientation of the elements. To get rid of the mesh dependency, these two parameters were expressed as the function of the diagonal length of the element. Comparisons to test results show that simulations using the proposed material model can capture the overall responses as well as the failure mode and location well.

In conclusion, a few characteristics of the proposed model can be drawn. First, a unique feature of the proposed yield surface for HPFRCC is that it contains a single yield surface covered both compression and tension. This will ensure numerical stability when crossing between compression and tension occurs. Second, the accumulated effective plastic strain (ε_p) defined as a scalar product of plastic strain tensors is used to measure the damage index for controlling the evolution of the plastic surfaces. The main advantage of defining ε_p this way is that the material parameters related to ε_p at various stages can directly be obtained by subtracting the elastic strain from the total strain under uniaxial responses. Third, the model can also be used for ordinary concrete by simply modifying the material parameters.

6.2 Future Research

This research has been mainly focused on the development of a macro-scale, multi-axial plasticity model for concrete. Some improvements and features can be added to increase the capability of the developed models:

- To reduce a number of material parameters and to simplify the compression yield function, two softening parameters can be combined into one parameter. This will subsequently reduce the components of the yield function. Instead of using a combination of Cosine and Exponential softeni0ng functions, a polynomial function can be used. Wang et al. (1978) proposed a second order polynomial function with four material constants to model the descending part. This polynomial function was constructed from three points, i.e. peak, inflection, and residual points. The inflection point located between the peak and residual point is in a way used to control the slope of the softening curve. Furthermore, they proposed the same form of polynomial function with another set of material parameters for the ascending part. This will help to further simplify the expression of both hardening and softening parameters.
- Instead of separately defining two effective plastic strains in compression and tension, the conjugate effective stress, which is tied with a single effective plastic strain, can be used (Shaw, 2008). An example of conjugate effective stress is comprised of J_2

and I_1 terms. The I_1 is used as the indicator of loading condition since I_1 is positive under tension and negative under compression. This conjugate effective stress is expressed as

$$\sigma_e = \frac{\sqrt{3J_2} + cI_1}{1 + c} \tag{6.1}$$

where c is the material parameters ranged from 0 to 1 for materials that are weak in tension. The uniaxial state of stress, σ_e can be rewritten as

$$\sigma_e = \frac{\sigma + c\sigma}{1 + c} = \sigma : \quad \text{for tension} \tag{6.2}$$

$$\sigma_e = \frac{\sigma - c\sigma}{1 + c} = \frac{(1 - c)}{(1 + c)}\sigma : \quad \text{for compression} \tag{6.3}$$

Clearly, σ_e under compression is different from tension. The value of ‘c’ is actually the strength ratio between compression and tension.

- This research has been mainly focused on the behavior under monotonic loading. However, the model could be extended to simulate behavior under cyclic loading with some modifications. These modifications may include the reductions of strength and stiffness due to permanent deformations. In contrast to the constant Young’s modulus used in this study, the Young’s modulus could be expressed in term of the effective plastic strain. Therefore, as permanent deformations accumulate, Young’s modulus is reduced and thus, decreases the unloading stiffness.

APPENDICES

APPENDIX A

STRESS-STRAIN RESPONSES OF HPFRCC UNDER VARIOUS LOADING CONDITIONS (SUPPLEMENT TO CHAPTER 3)

A.1 Uniaxial Compression Test

A.1.1 Uniaxial compression responses of mortar with hooked fiber

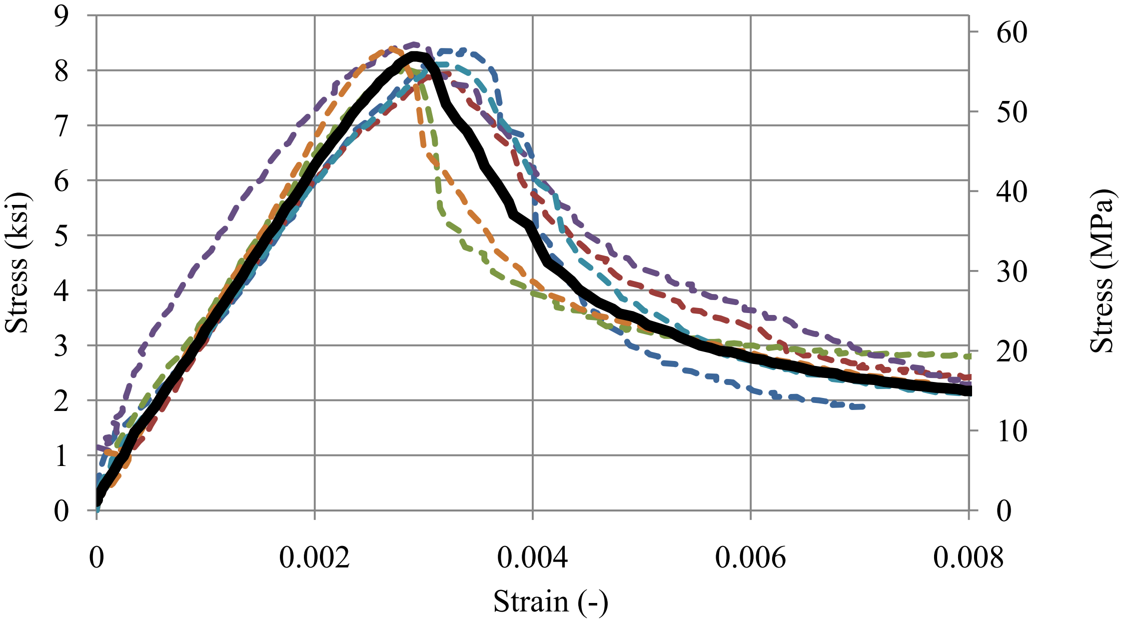

(a) UXC-H1

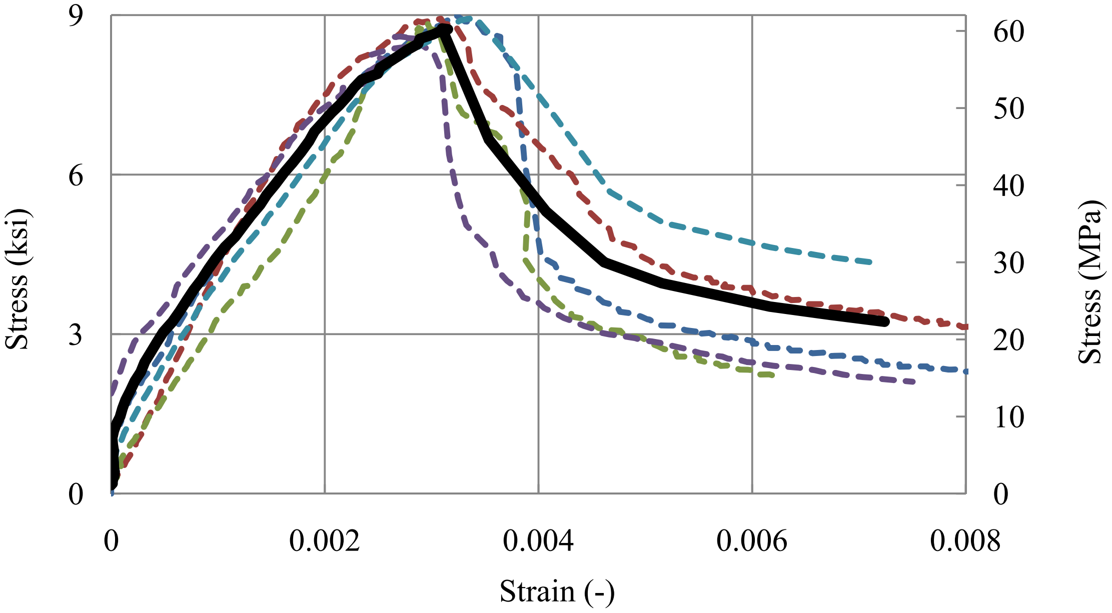

(b) UXC-H1.5

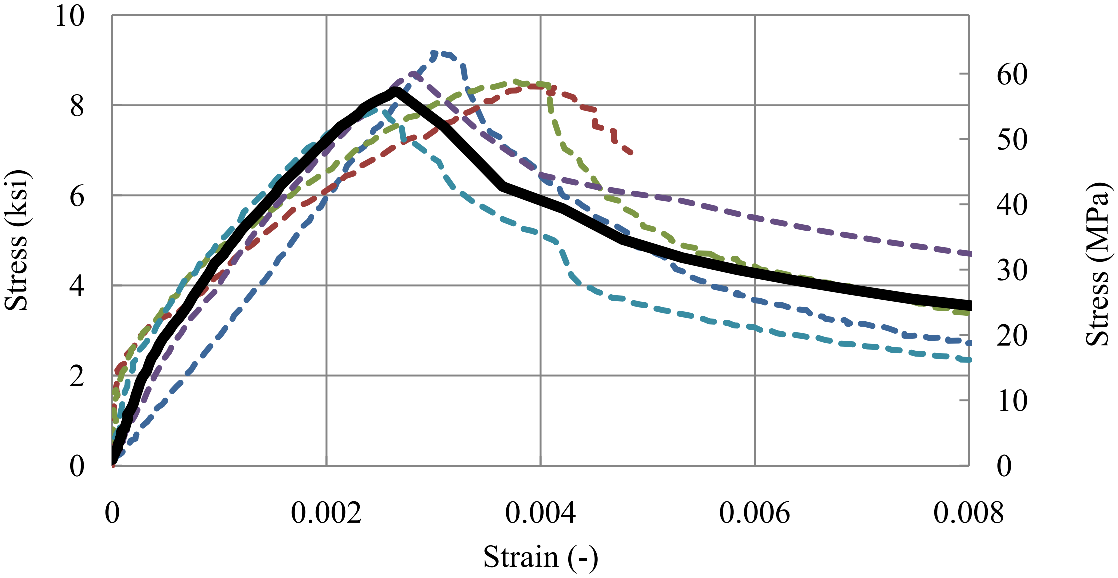

(c) UXC-H2

Figure A.1 Uniaxial compression response of mortar with hooked fiber: (a) 1.0% volume fraction; (b) 1.5% volume fractions; (c) 2.0% volume fractions

A.1.2 Uniaxial compression responses of mortar with Spectra fiber

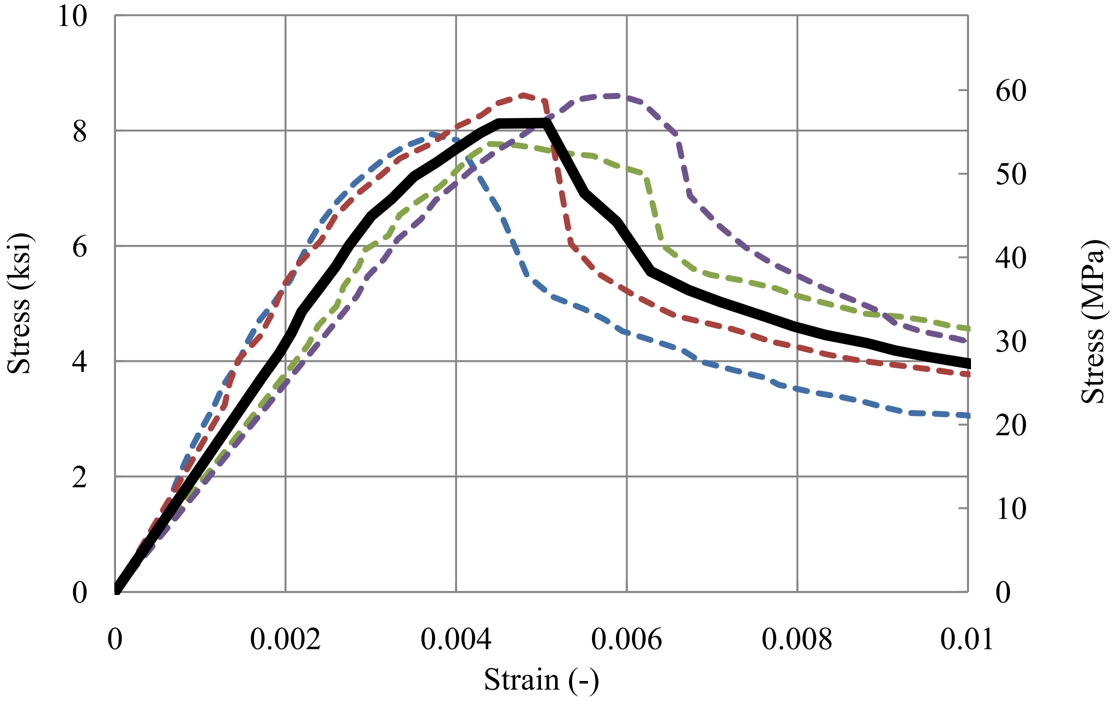

(a) UXC-S1

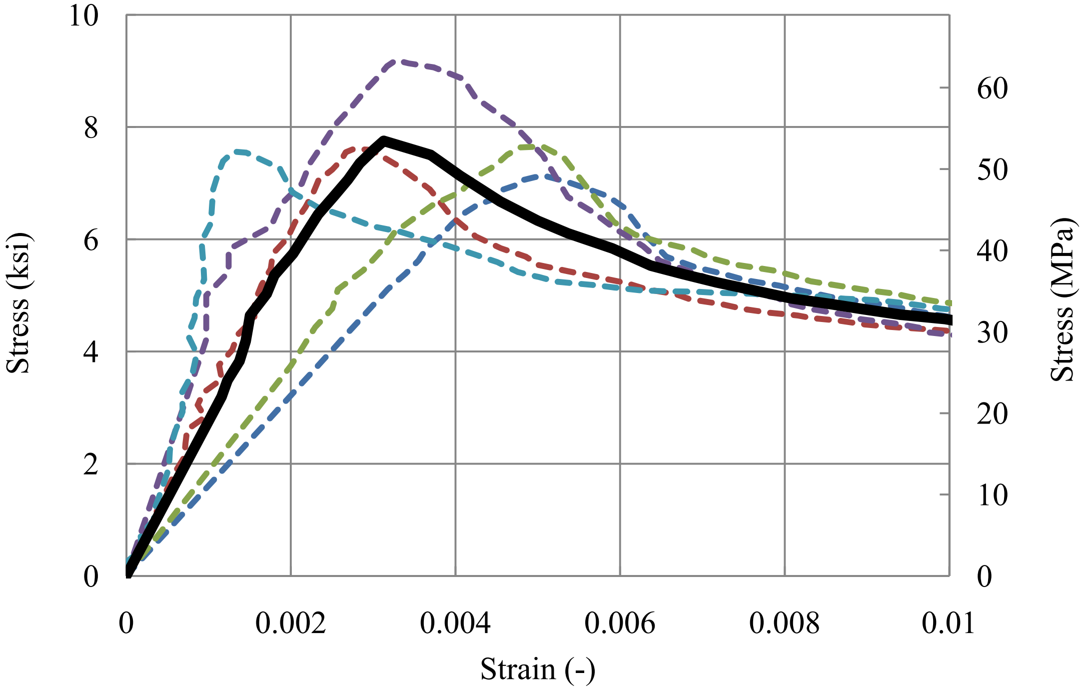

(b) UXC-S1.5

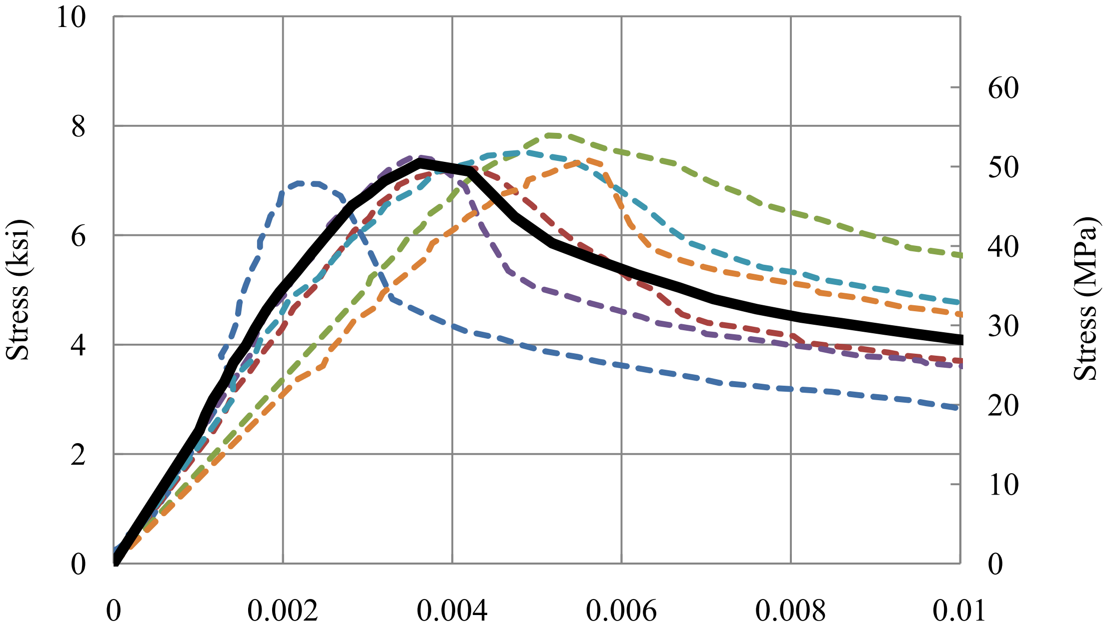

(c) UXC-S2

Figure A.2 Uniaxial compression response of mortar with Spectra fiber: (a) 1.0% volume fraction; (b) 1.5% volume fractions; (c) 2.0% volume fractions

A.1.3 Uniaxial compression responses of mortar

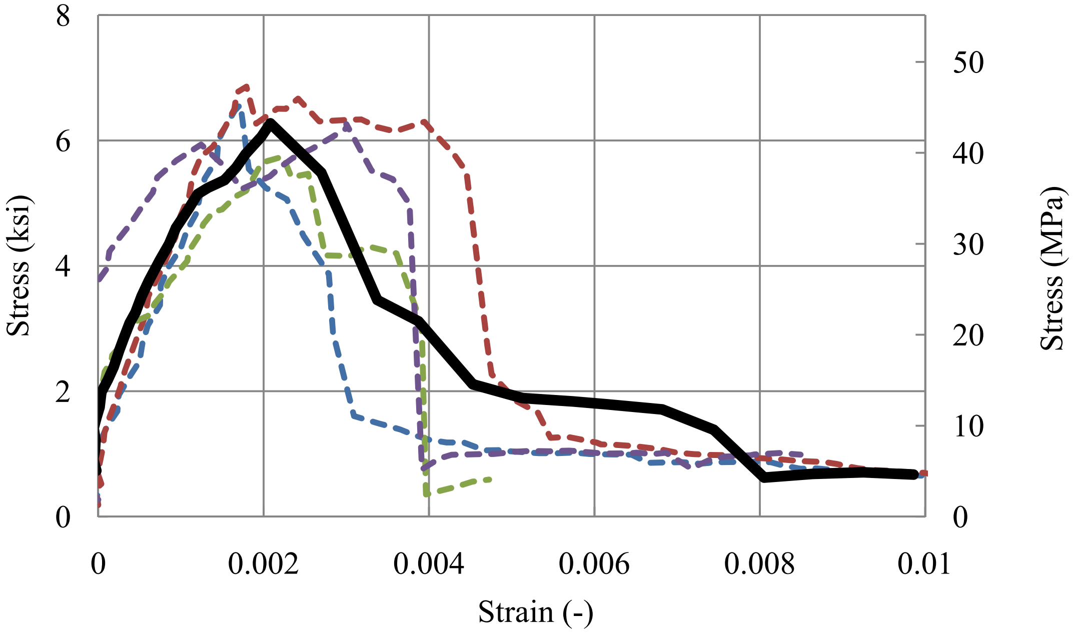

Figure A.3 Uniaxial compression response of mortar

A.2 Uniaxial Tension Test

A.2.1 Uniaxial tensile response of mortar with hooked fiber

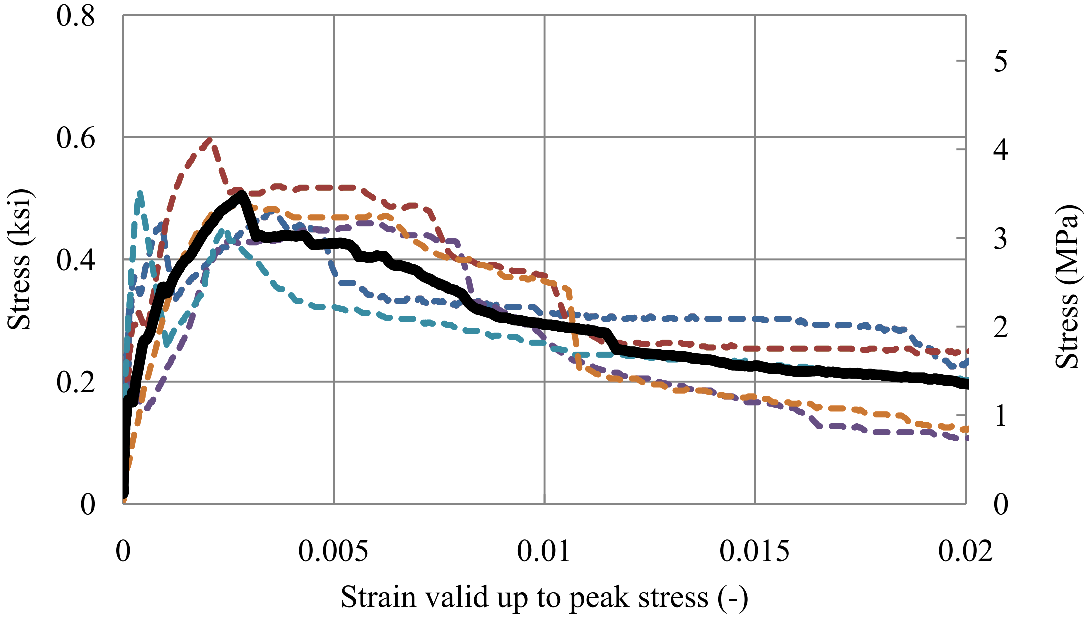

(a) UXT-H1

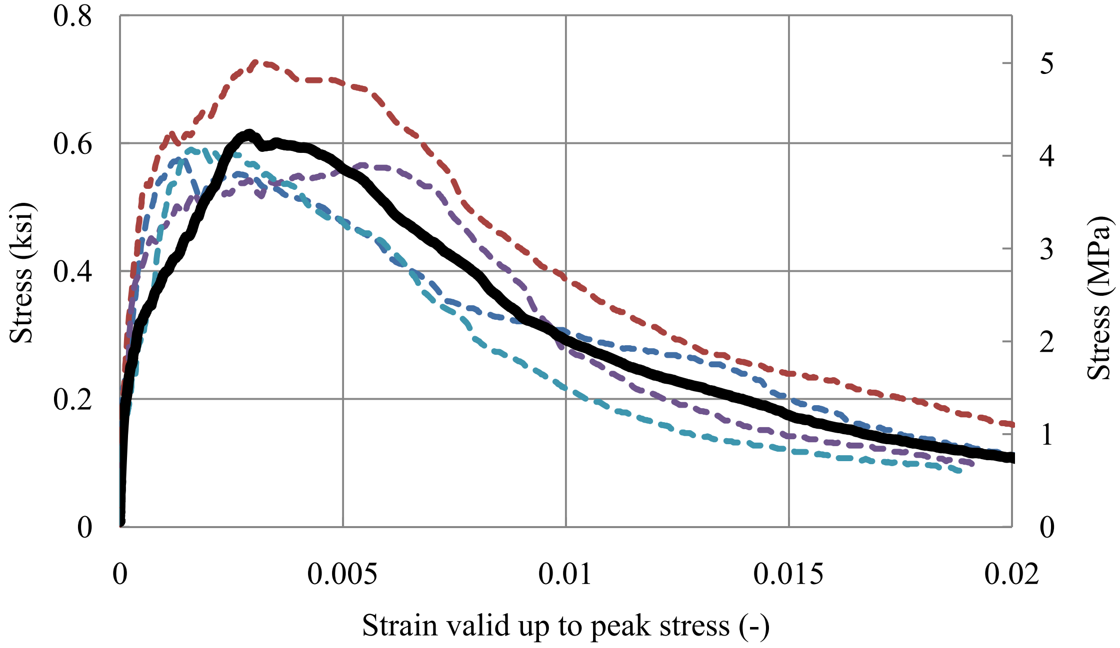

(b) UXT-H1.5

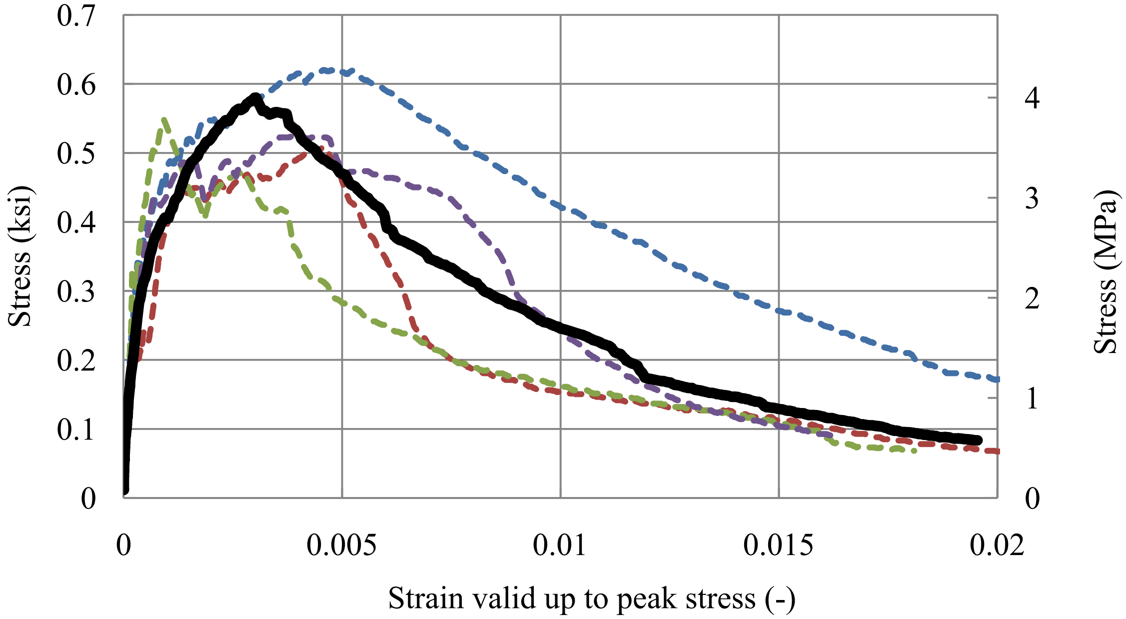

(c) UXT-H2

Figure A.4 Uniaxial tensile response of mortar with hooked fiber: (a) 1.0% volume fraction; (b) 1.5% volume fractions; (c) 2.0% volume fractions

A.2.1 Uniaxial tensile response of mortar with Spectra fiber

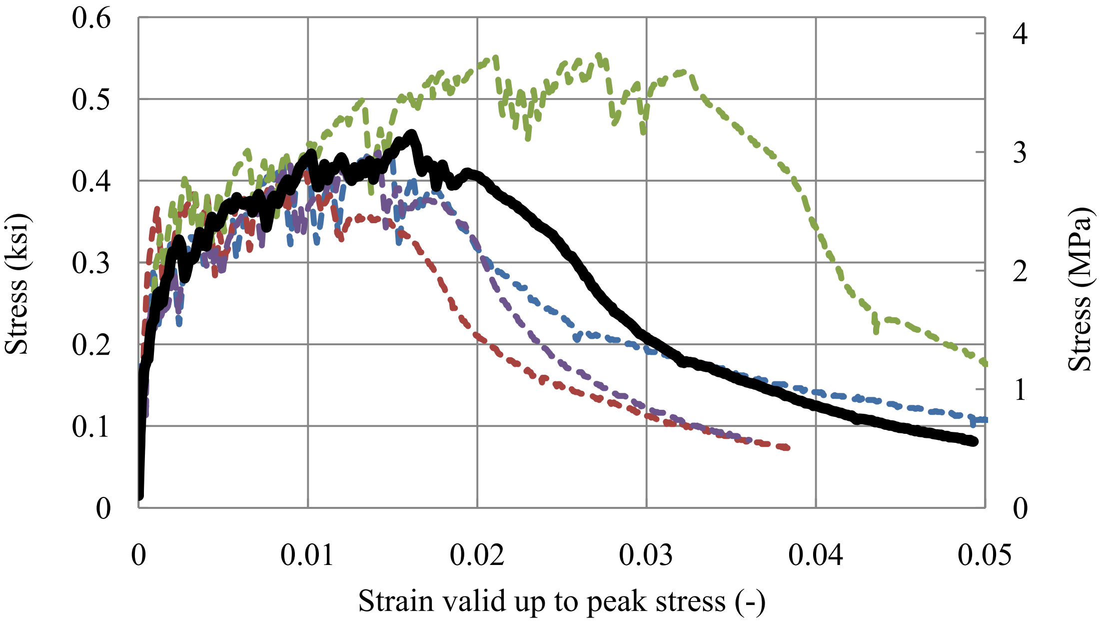

(a) UXT-S1

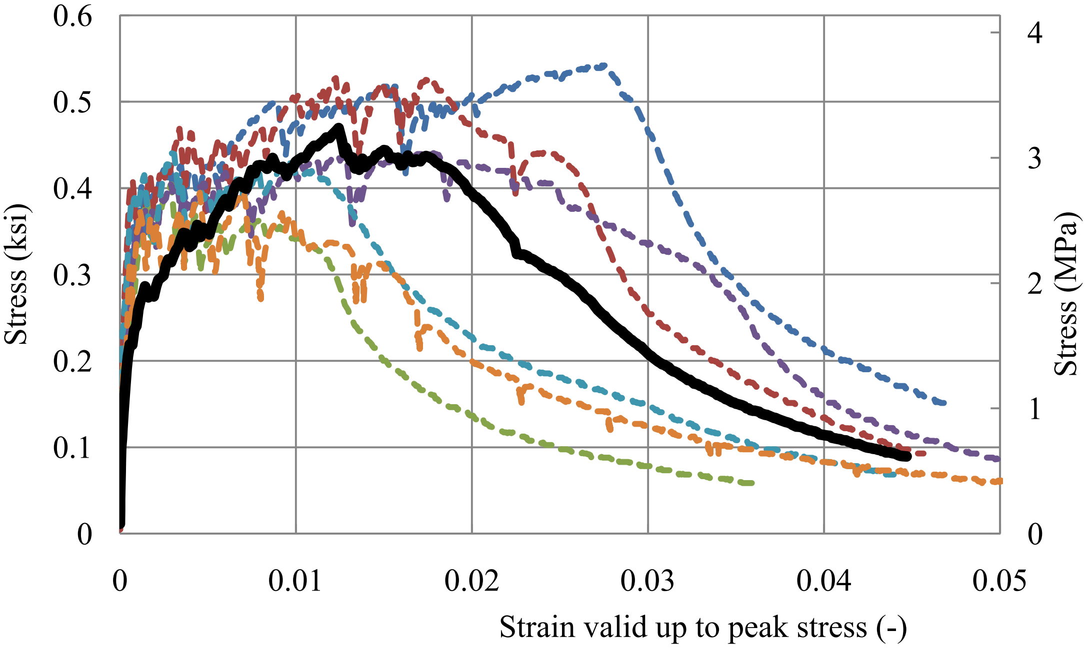

(b) UXT-S1.5

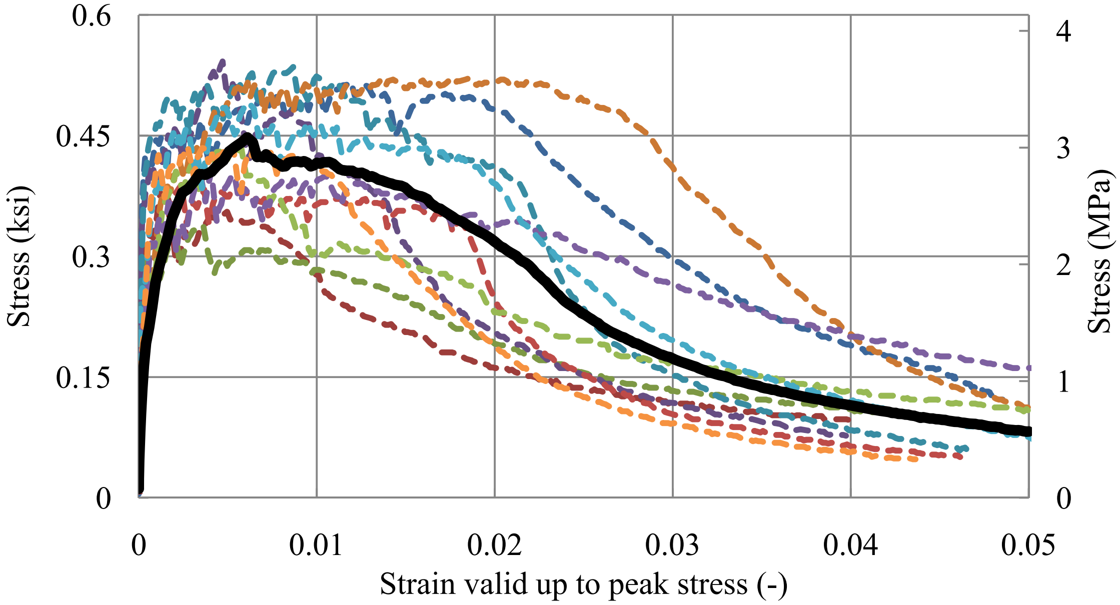

(c) UXT-S2

Figure A.5 Uniaxial tensile response of mortar with Spectra fiber: (a) 1.0% volume fraction; (b) 1.5% volume fractions; (c) 2.0% volume fractions

A.2.1 Uniaxial tensile response of mortar

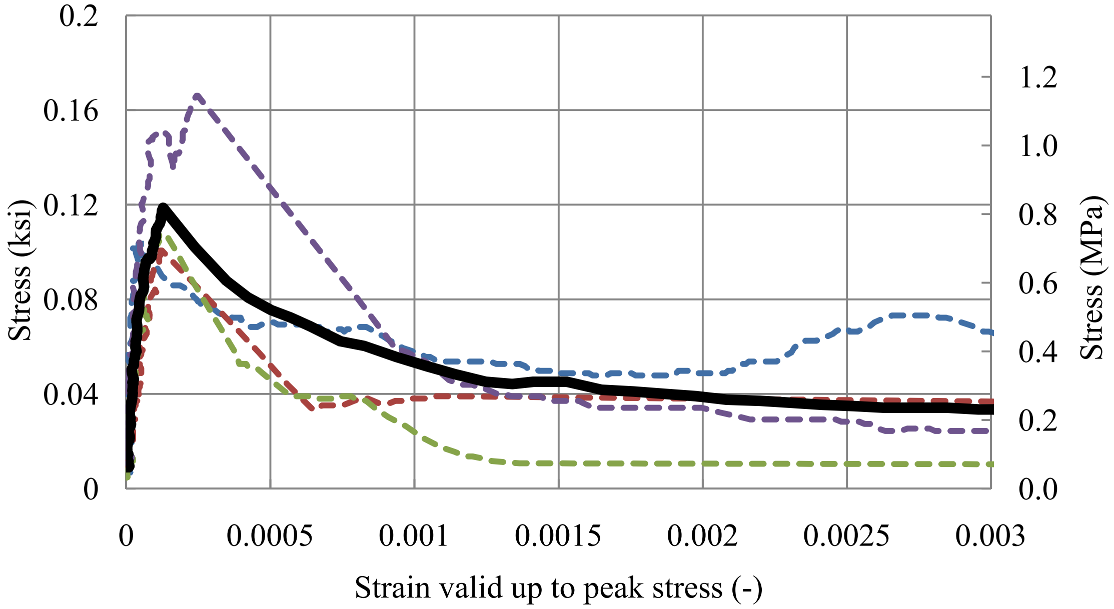

Figure A.6 Uniaxial tensile response of UXT-M

A.3 Triaixial Case

A.3.1 Triaxial compression under 6 ksi (41 MPa) confining pressure

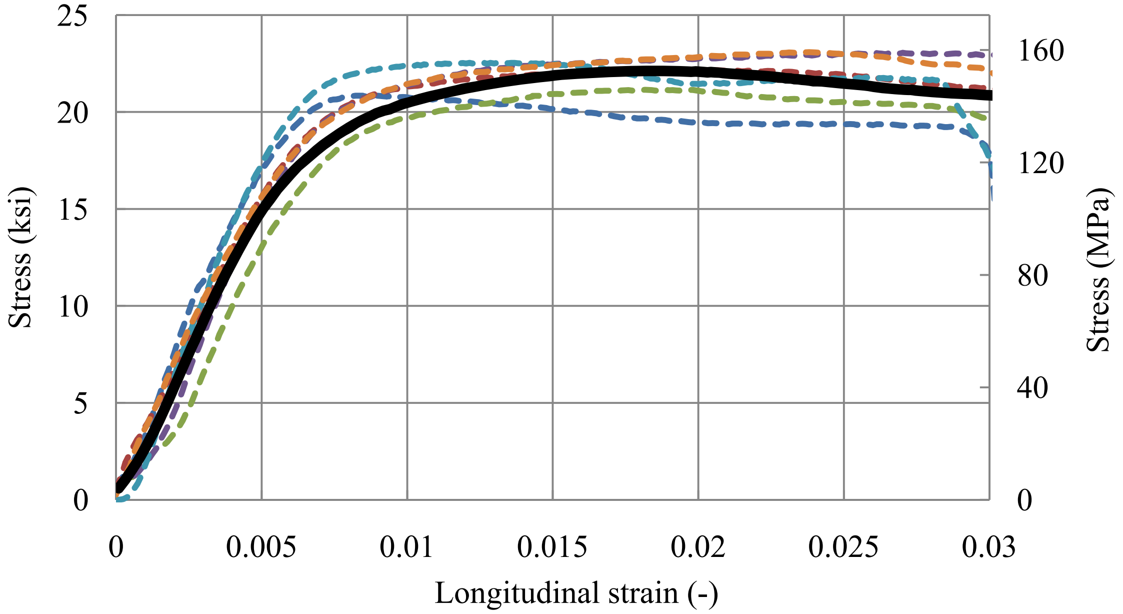

(a) Mortar with hooked fiber

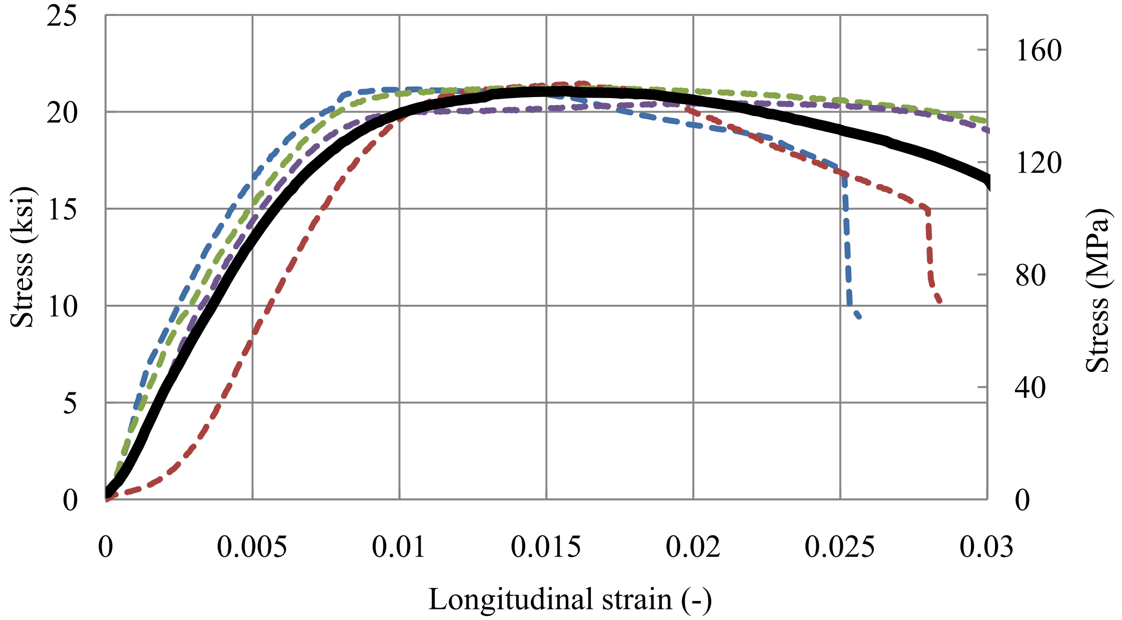

(b) Mortar with Spectra fiber

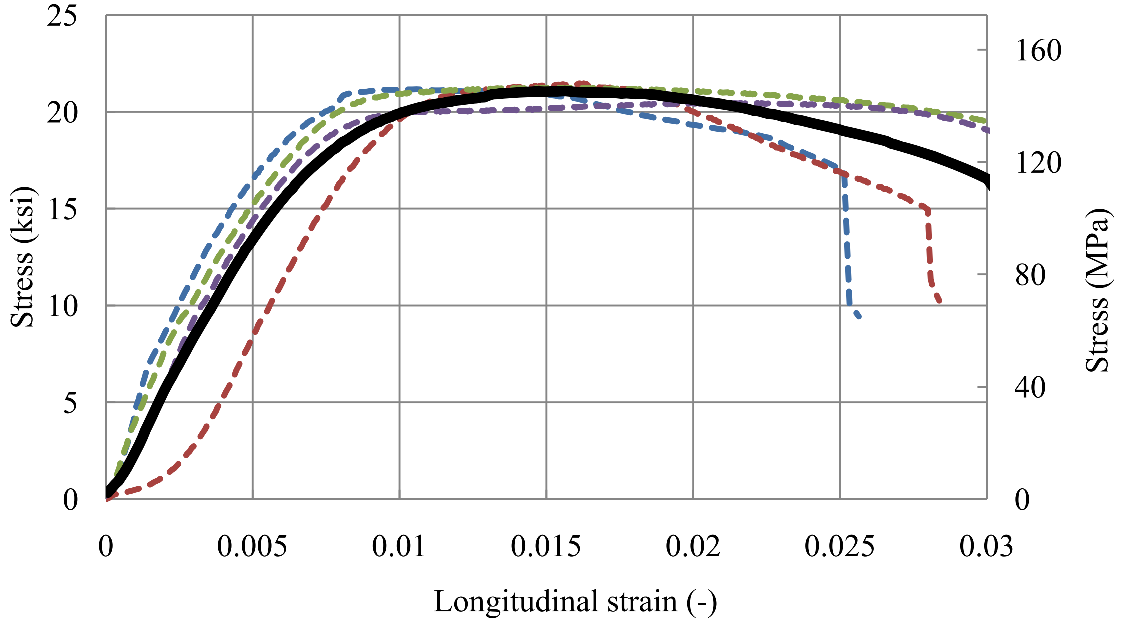

(c) Mortar

Figure A.7 Stress-strain response under triaxial compression test with confining pressure of 6 ksi (41 MPa)

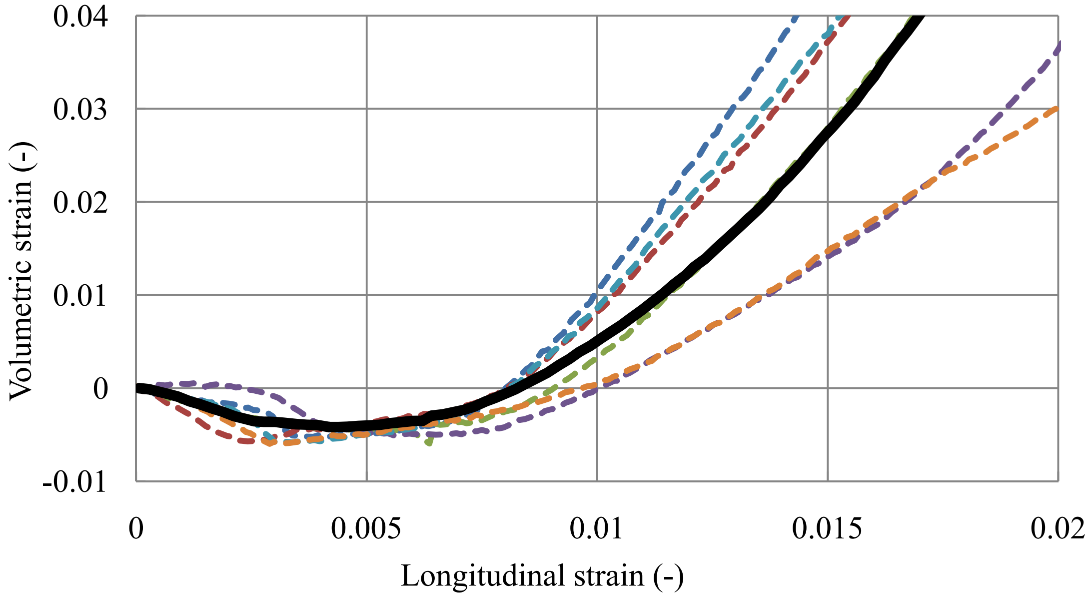

(a) Hooked fiber

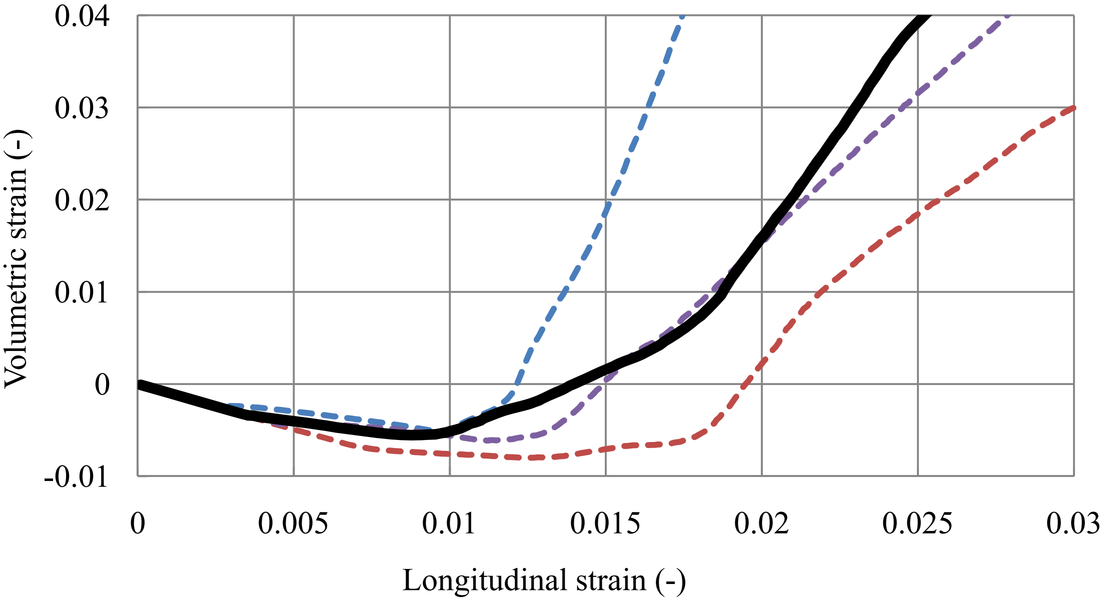

(b) Spectra fiber

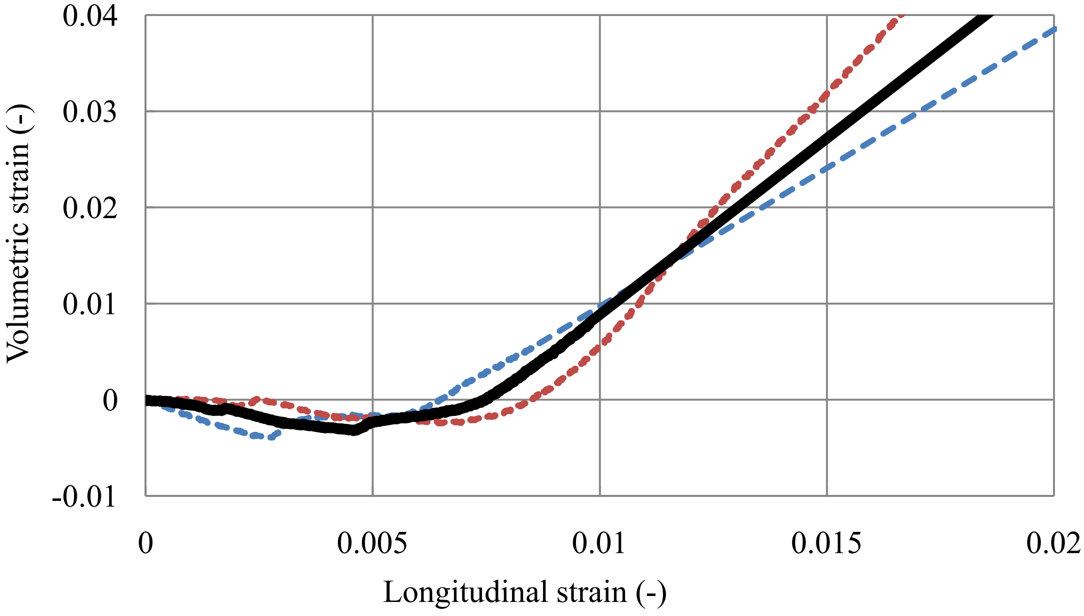

(c) Mortar

Figure A.8 Volumetric strain versus longitudinal strain responses of HPFRCC under confining pressure of 6 ksi (41 MPa): (a) Hooked; (b) Spectra; (c) Mortar

A.3.2 Triaxial compression under 6 ksi (41 MPa) confining pressure

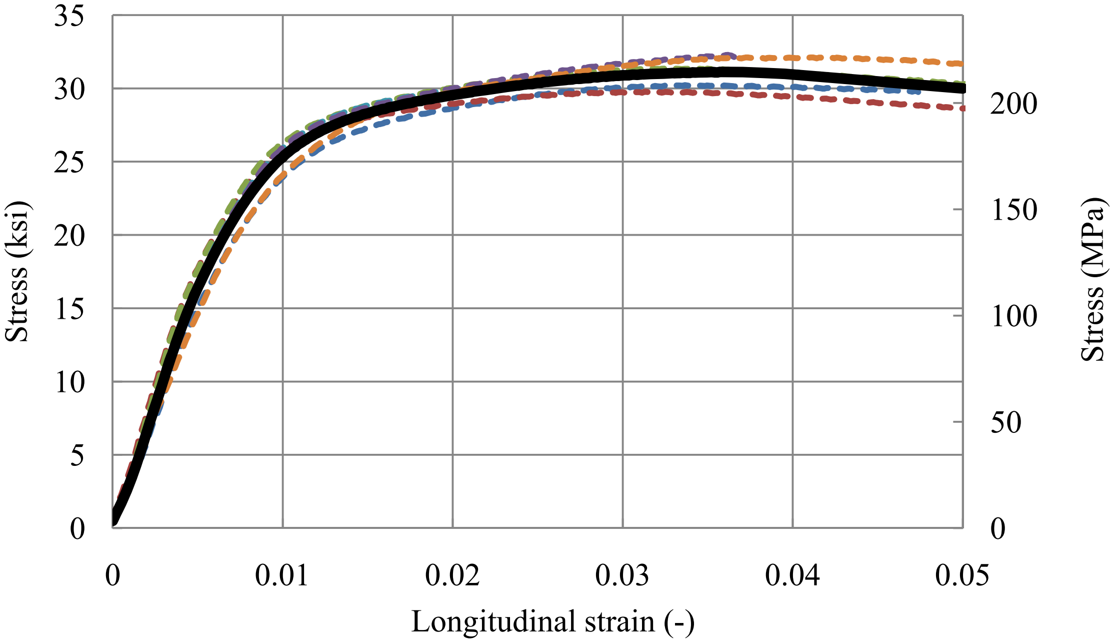

(a) Hooked fiber

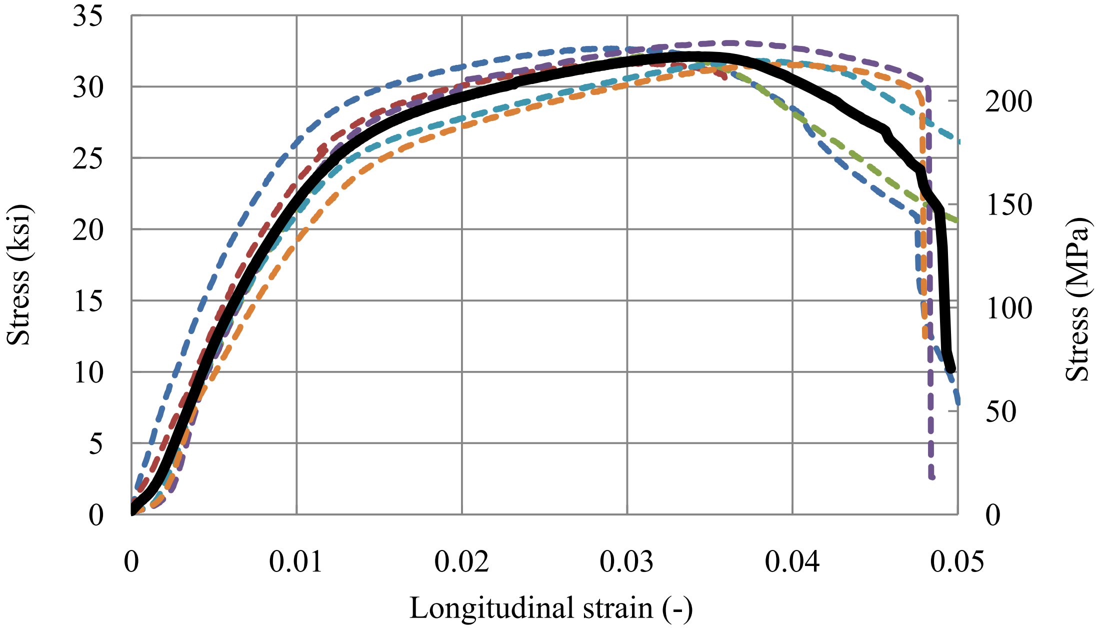

(b) Spectra fiber

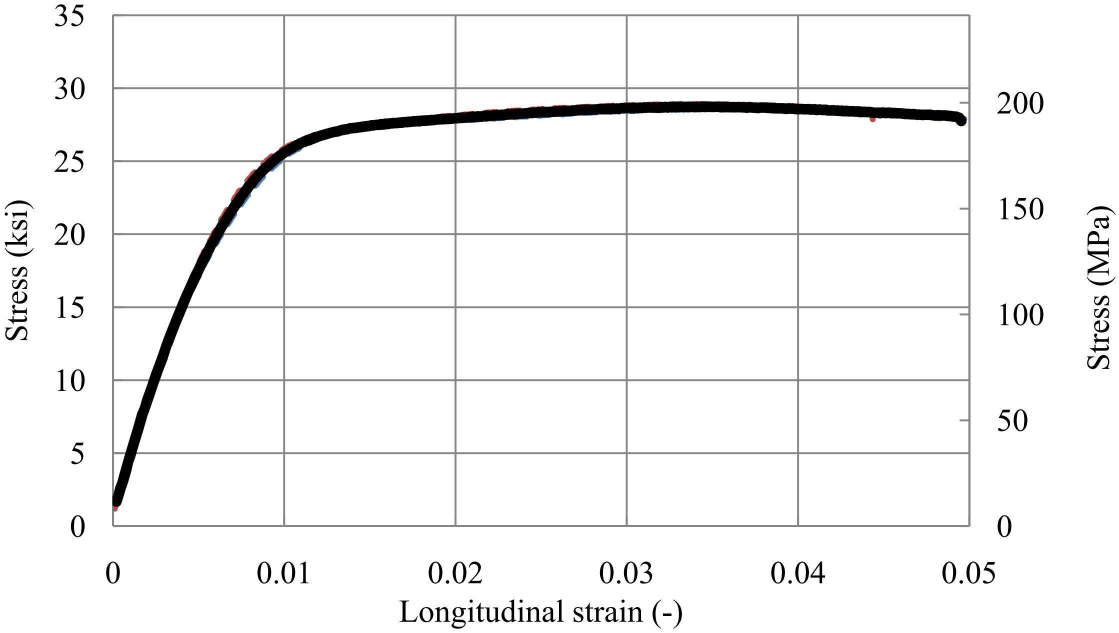

(c) Mortar

Figure A.9 Stress-strain response of HPFRCC under triaxial compression test with confining pressure of 7.5 ksi (52 MPa) (a) Hooked; (b) Spectra; (c) Mortar

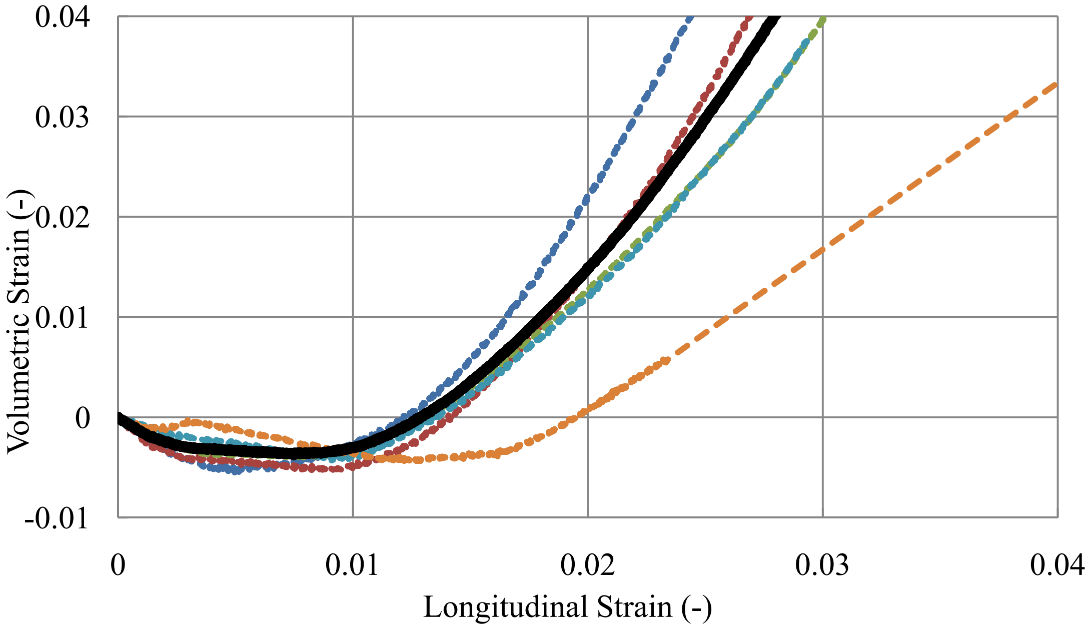

(a) Hooked fiber

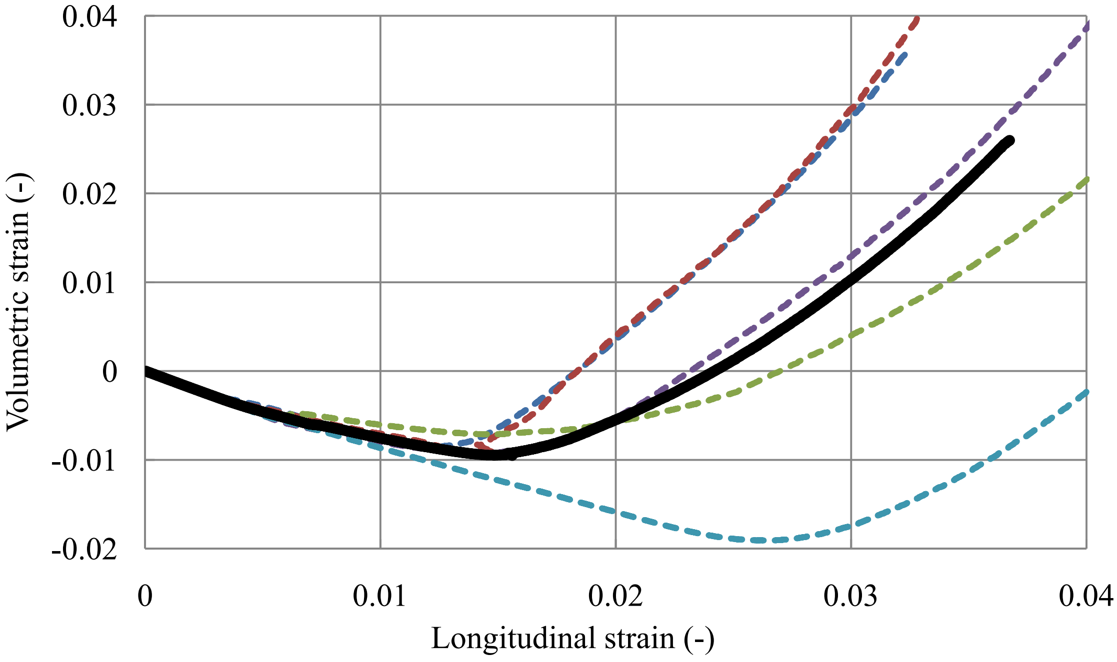

(b) Spectra fiber

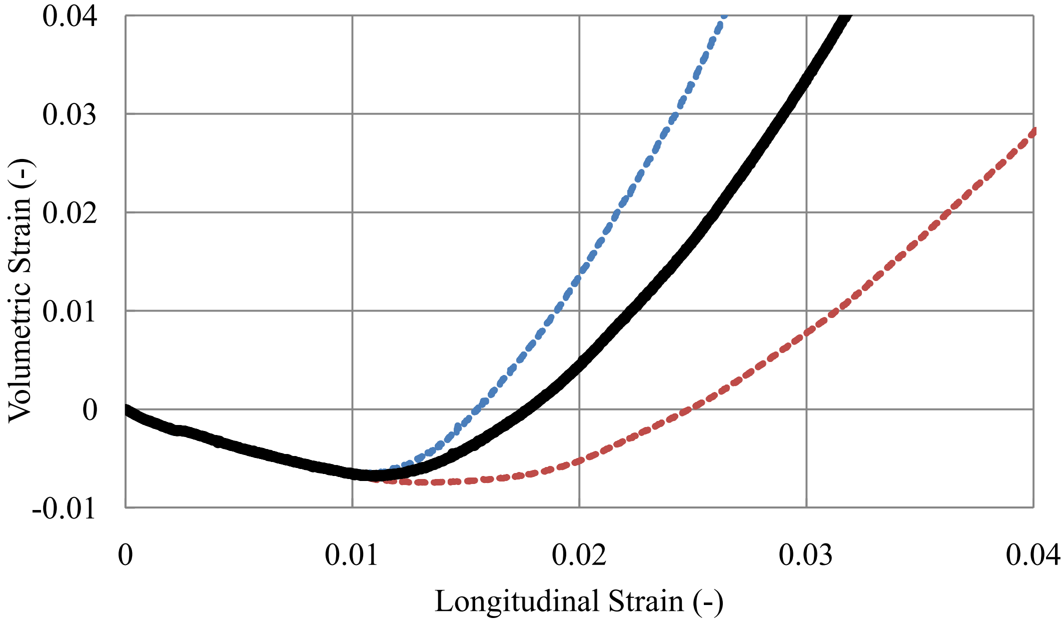

(c) Mortar

Figure A.10 Volumetric strain versus longitudinal strain responses of HPFRCC under confining pressure of 7.5 ksi (52 MPa) (a) Hooked; (b) Spectra; (c) Mortar

APPENDIX B

SUMMARY OF CLASSICAL PLASTICITY THEORY

The main intention of this section is only to give a brief review of general plasticity. A full treatment of plasticity can be found in most standard advanced mechanics textbooks, e.g. Chen (1982), Ottosen and Ristinmaa (2005).

B.1 Geometrical interpretation of stress invariants

A convenient way to visualize yield functions is to draw them in the Haigh-Westergaard (H-W) coordinate system because yield surfaces are mostly expressed in terms of invariants used as coordinates in this system. In this coordinate system, principal stress tensors, which are expressed as the axis in the Cartesian coordinate systems, are modified into three stress invariant components. These invariants are values of stress tensors that do not depend on the reference coordinate systems and can be derived from the characteristic equation:

$$|\boldsymbol{\sigma} - \sigma\delta| = \left|\sigma_{ij} - \sigma\delta_{ij}\right| = -\sigma^3 + I_1\sigma^2 - I_2\sigma + I_3 = 0 \qquad \text{(B.1)}$$

where

$$I_1 = \mathrm{tr}(\boldsymbol{\sigma}) = \sigma_{ii} \qquad : 1^{st}\text{Invariant} \qquad \text{(B.2.1)}$$

$$I_2 = \frac{1}{2}[\mathrm{tr}(\boldsymbol{\sigma})^2 - \mathrm{tr}(\boldsymbol{\sigma}^2)] = \frac{1}{2}[\sigma_{mm}\sigma_{nn} - \sigma_{mn}\sigma_{nm}] \qquad : 2^{nd}\text{ Invariant} \qquad \text{(B.2.2)}$$

$$I_3 = \det(\boldsymbol{\sigma}) = \frac{1}{6}\varepsilon_{ijk}\varepsilon_{pqr}\sigma_{ip}\sigma_{jq}\sigma_{kr} \qquad : 3^{rd}\text{Invariant} \qquad \text{(B.2.3)}$$

The deviatoric stress components, which are the components of stress that deviates from the hydrostatic axis, also have a characteristic equation, and again the coefficients are called invariants of the deviatoric stress tensors:

$$|\mathbf{S}-\sigma\boldsymbol{\delta}| = \left|S_{ij}-S\sigma_{ij}\right| = -S^3+J_1S^2+J_2S+J_3 = 0 \qquad \text{(B.3)}$$

where

$$J_1 = \mathrm{tr}(\mathbf{S}) = S_{ii} = 0 \qquad : 1^{st}\mathrm{Invariant} \qquad \text{(B.4.1)}$$

$$J_2 = \frac{1}{2}[\mathrm{tr}(\mathbf{S})^2 - \mathrm{tr}(\mathbf{S}^2)] = \frac{1}{2}\left[S_{ij}S_{ji} - S_{kk}S_{ll}\right] = \frac{1}{2}S_{ij}S_{ji} \quad : 2^{nd}\mathrm{Invariant} \qquad \text{(B.4.2)}$$

$$J_3 = \det(\mathbf{S}) = \frac{1}{3}S_{ij}S_{jk}S_{ki} \qquad : 3^{rd}\mathrm{Invariant} \qquad \text{(B.4.3)}$$

Consider an arbitrary stress component P $(\sigma_1, \sigma_2, \sigma_3)$ located at the cone shaped yield surface represented by dotted lines in Figure B.1a. The stress components at point P is decomposed into two terms: a hydrostatic term $(\xi, \overline{ON})$ and a deviatoric term $(\rho, \overline{NP})$. These two terms are considered in two separate planes in this coordinate system. The first plane known as the deviatoric or π-plane is the plane perpendicular to the hydrostatic axis. The hydrostatic axis represents the line where $\sigma_1 = \sigma_2 = \sigma_3$ and is denoted as n_i in Figure B.1a. The projections of the σ_1-, σ_2-, and σ_3-axes on the deviatoric plane are shown in Figure B.1b. At this plane, the deviatoric component is further decomposed into ρ and θ. The first subcomponent ρ is the magnitude of the deviatoric stress normal to the hydrostatic axis whereas the second subcomponent θ represents the loading condition of the current state of stress. The angle θ is always measured from $\pi/6$ departed from principal stress axis. The second plane is the meridian plane, which the plane perpendicular to the deviatoric plane. As shown in Figure B.1c, the horizontal and vertical axes of this plane are the hydrostatic component ξ and the deviatoric component ρ, respectively.

Mathematically, the position of arbitrary stress P in the principle stress coordinate systems $(\sigma_1, \sigma_2, \sigma_3)$ can be replaced with the Haigh-Westergaard coordinate systems (ξ, ρ, θ) as:

$$\xi = \frac{I_1}{\sqrt{3}}; \rho = \sqrt{2J_2}; \ \theta = \frac{1}{3}\sin^{-1}\left[\frac{-3\sqrt{3}}{2}\frac{J_3}{J_2^{3/2}}\right] \tag{B.5}$$

From Eq. (B.5), two unique properties of the Haigh-Westergaard components can be perceived. First, the component ρ is a positive definite value because the product of square root always gives a positive number. Second, the Lode angle θ, which is the product of the Arcsine function divided by three, has symmetrical properties in the deviatoric plane. This implies that any yield surfaces drawn in the deviatoric plane can be completely characterized within $-\pi/6 \leq \theta \leq \pi/6$ and the remaining sectors of the yield surface are repeated. Within the range of $-\pi/6$ to $\pi/6$, there are three meridian planes of interest when deriving the yield surfaces. They are the tensile meridian $(\theta = -\pi/6)$, the compressive meridian $(\theta = \pi/6)$, and the shear meridian $(\theta = 0)$.

B.2 Drucker's postulates and their consequences

Drucker (1950) showed that if the two conditions described below hold for a given mentioning, then the material is said to be stable. A stable material, in this context, is any material that always produces positive work when an external agency is inserted into the system (Shaw, 2004). The first condition states that with any given stress increment, the incremental strain must always generate positive work. Further, since the work increment is composed of elastic and inelastic parts and the elastic part is positive definite, it is sufficient to say that inelastic work is also positive definite. The first condition can be mathematically written as:

$$\Delta\sigma_{ij}\Delta\varepsilon_{ij} = \Delta\sigma_{ij}\left(\Delta\varepsilon^{e}_{ij} + \Delta\varepsilon^{p}_{ij}\right) \geq 0 \quad \text{or} \quad \Delta\sigma_{ij}\Delta\varepsilon^{p}_{ij} \geq 0 \tag{B.6}$$

Drucker's second condition applies when the material experiences cyclic loading. Two cases of uniaxial cyclic loadings are shown in Figure B.2. In the first case, the load starts from zero up to σ at point B followed by unloading to σ* or point A. In the second case, again the load starts from zero but does not unload at point B. The material is further loaded for Δσ up to point C followed by unloading to σ* at point D. The difference in strain between these two cases represents a permanent deformation or the plastic strain. It should be noted that this plastic strain is unrecoverable. To guarantee that a material is stable under cyclic loading, Drucker's second condition requires the shaded area ABCD to be greater than zero. Mathematically, the second condition can be expressed as:

$$(\sigma - \sigma^{*})\Delta\varepsilon^{p} + \frac{1}{2}\Delta\sigma\Delta\varepsilon^{p} \geq 0 \tag{B.7}$$

One special case for the second condition is a case in which σ is equal to σ*, then the first condition is recovered. In other words, if the stress σ is equal to σ*, then the first term of Eq. (B.7) becomes zero and Eq. (B.6) is recovered.

The Drucker's postulates are not applicable for softening materials because the slope of stress-strain curve is negative. In other words, with an increase in incremental strain, the corresponding incremental stress decreases. Therefore, the work increment for softening material will be negative.

The three consequences from Drucker's postulates (Shaw, 2004) can be described as follows: (1) the incremental plastic strain is normal to the current yield surface (Figure B.3a); (2) the yield surface must be convex (Figure B.3b); (3) incremental stress and the incremental plastic strain have a linear relationship.

B.3 Consistency condition and consistency parameter

The consistency condition states that any given set of stress tensors is said to be admissible if and only if those stress tensors are either inside or at the yield surface. In Figure B.4, the admissible domains in both one- and two-dimensional cases are shown in the shaded area. If the state of stress falls inside these shaded areas, then the stress tensors are admissible. This condition can also be mathematically written as:

$$\mathrm{F}(\boldsymbol{\sigma}, \mathbf{q}) \leq 0 \tag{B.8}$$

where $\boldsymbol{\sigma}$ represent the current state of stress tensors and $\mathbf{q}$ represent the internal parameters that are used to indicate the size of the admissible domain.

From Eq. (B.8), there are two possible scenarios for the admissible stress tensors. The first scenario is the circumstance when the state of stress falls inside the admissible domain and the yield function F is less than zero. The second scenario is the case when the state of stress is at the boundary of the admissible domain and the yield function F is equal to zero. The admissible domain can be defined as:

$$\mathrm{E}_\sigma = \{(\boldsymbol{\sigma}, \mathbf{q}) \in \mathrm{S} \times \mathrm{R}^\mathrm{m} | \mathrm{F}(\boldsymbol{\sigma}, \mathbf{q}) \leq 0\} = \mathrm{int}(\mathrm{E}_\sigma) \cup \partial \mathrm{E}_\sigma \tag{B.9}$$

where E_σ represents the admissible domain, the union $\mathrm{int}(\mathrm{E}_\sigma)$ and $\partial\mathrm{E}_\sigma$, which can be defined as

$$\partial \mathrm{E}_\sigma = \{(\boldsymbol{\sigma}, \mathbf{q}) \in \mathrm{S} \times \mathrm{R}^\mathrm{m} | \mathrm{F}(\boldsymbol{\sigma}, \mathbf{q}) = 0\} \qquad \text{: Boundary of } \mathrm{E}_\sigma \tag{B.10.1}$$

$$\mathrm{int}(E_\sigma) = \{(\boldsymbol{\sigma}, \mathbf{q}) \in S \times R^m | F(\boldsymbol{\sigma}, \mathbf{q}) < 0\} \quad : \text{Interior of } E_\sigma \tag{B.10.2}$$

where R^m is the real number in m-dimensional space. Focusing on the second case, where the current state of stress is on the current yield surface, the subsequent state of stress must also satisfy the consistency condition.

$$F\left(\boldsymbol{\sigma}^{(i+1)}, \mathbf{q}^{(i+1)}\right) = F\left(\boldsymbol{\sigma}^{(i)}, \mathbf{q}^{(i)}\right) + \Delta F\left(\boldsymbol{\sigma}^{(i)}, \mathbf{q}^{(i)}\right) \leq 0 \tag{B.11}$$

where the superscript (i) represents the current state and (i+1) represents the next state. Since the current state of stress is at the boundary, the current yield function is zero. Thus, the increment of the yield function must be less than or equal to zero and so Eq. (B.11) can be replaced as follows:

$$\Delta F(\boldsymbol{\sigma}, \mathbf{q}) \leq 0 \tag{B.12}$$

In Eq. (B.12), two possible outcomes can occur with a given set of incremental strains. The first occurs when the given incremental strains are under unloading condition; in this case the incremental yield function (ΔF) will be less than zero. The second occurs when the given incremental strains are under loading condition; the incremental yield function (ΔF) will be zero. As a consequence, by using Taylor's expansion up to the first order, the incremental form of the yield function can be expressed as:

$$\Delta F(\boldsymbol{\sigma}, \mathbf{q}) = \frac{\partial F}{\partial \boldsymbol{\sigma}} : \boldsymbol{\Delta\sigma} + \frac{\partial F}{\partial \mathbf{q}} \cdot \Delta \mathbf{q} = 0 \tag{B.13}$$

Furthermore, since the first outcome represents the unloading case, the next incremental stress tensors will be in the elastic region. Hence, the plastic component of the given incremental strain will be zero. However, the plastic component for the second outcome is not equal to zero. In other words, the increment of total strains for the second outcome is now composed of two components, i.e. the elastic and the plastic parts, and it can be mathematically expressed as:

$$\boldsymbol{\Delta\varepsilon}^{\mathrm{total}} = \boldsymbol{\Delta\varepsilon}^{\mathrm{e}} + \boldsymbol{\Delta\varepsilon}^{\mathrm{p}} \tag{B.14}$$

where the elastic component $\boldsymbol{\Delta\varepsilon}^{\mathbf{e}}$ is reversible and is the only component that is used to calculate the stress tensors. In contrast, the plastic component $\boldsymbol{\Delta\varepsilon}^{\mathbf{p}}$ represents permanent deformations that occur due to, for example, collapsing of air voids or the crushing of particles inside concrete when a compressive load is applied.

Since only the elastic strain components are used to calculate the stress tensors, the stress-strain relationship can be written as:

$$\boldsymbol{\Delta\sigma} = \mathbf{C}\colon \boldsymbol{\Delta\varepsilon}^{\mathrm{e}} \tag{B.15}$$

To write in an expression of incremental plastic strains, Eq. (4.14) is substituted into Eq. (B.15). The incremental stress tensors become

$$\boldsymbol{\Delta\sigma} = \mathbf{C}\colon \left(\boldsymbol{\Delta\varepsilon}^{\mathrm{total}} - \boldsymbol{\Delta\varepsilon}^{\mathrm{p}}\right) \tag{B.16}$$

where **C** is the forth-order stiffness tensor and subscripts ‘e’ and ‘p’ represent the elastic and the plastic components, respectively. Depending on the types of material, the elastic stiffness tensor **C** can have from 2 up to 21 independent variables. Since HPFRCC is homogeneous, the elastic behavior of HPFRCCs can be assumed to be linearly isotropic. Thus, only two independent variables are needed for the elastic stiffness matrix **C**:

$$\mathbf{C} = \mathrm{C}_{\mathrm{ijkl}} = \frac{\mathrm{E}}{(1+\nu)}\left[\frac{1}{2}\left(\delta_{\mathrm{ik}}\delta_{\mathrm{jl}} + \delta_{\mathrm{il}}\delta_{\mathrm{jk}}\right) + \frac{\nu}{1-2\nu}\delta_{\mathrm{ij}}\delta_{\mathrm{kl}}\right] \tag{B.17}$$

where E and ν represent Young’s modulus and Poisson’s ratio, respectively. Substituting the incremental stress tensors from Eq. (B.16) into Eq. (B.13), the incremental yield function can be rewritten as:

$$\Delta \mathrm{F} = \frac{\partial \mathrm{F}}{\partial \boldsymbol{\sigma}} : \mathbf{C} : \left(\boldsymbol{\Delta\varepsilon}^{\mathrm{total}} - \boldsymbol{\Delta\varepsilon}^{\mathrm{p}} \right) + \frac{\partial \mathrm{F}}{\partial \mathbf{q}} \cdot \boldsymbol{\Delta}\mathbf{q} = 0 \qquad \text{(B.18)}$$

The two unknowns in Eq. (B.18) are the incremental plastic strain tensors ($\boldsymbol{\Delta\varepsilon}^{\mathrm{p}}$) and the increment of internal variables ($\boldsymbol{\Delta}\mathbf{q}$). These two unknowns are defined as:

$$\boldsymbol{\Delta\varepsilon}^{\mathrm{p}} \equiv \gamma_{\mathrm{d}} \frac{\partial \mathrm{G}}{\partial \boldsymbol{\sigma}} \quad \& \quad \boldsymbol{\Delta}\mathbf{q} \equiv \gamma_{\mathrm{d}} \mathrm{M}(\mathrm{h}) \qquad \text{(B.19)}$$

where the parameter γ_{d} is the consistency parameter that indicates the magnitude of the incremental plastic strains. The parameter G represents the potential function that defines the plastic flow direction. The selection of the potential function G depends on the type of flow rules. If the associative flow rule is selected, the potential function is defined to be the same as the yield function ($\mathrm{G} = \mathrm{F}$). However, if the non-associative flow rule is used, the potential function is defined differently from the yield function ($\mathrm{G} \neq \mathrm{F}$). In the latter case, the plastic flow direction is not normal to the current yield surface. The incremental of the internal parameters ($\boldsymbol{\Delta}\mathbf{q}$) is defined as a function of ‘h’ (M( ) stands for Function). Some examples of ‘h’ are typically defined as:

$$\mathrm{h} = \sqrt{\frac{\partial \mathrm{G}}{\partial \boldsymbol{\sigma}} : \frac{\partial \mathrm{G}}{\partial \boldsymbol{\sigma}}} \quad \text{for the effective plastic strain } \varepsilon_{\mathrm{p}} \qquad \text{(B.20.1)}$$

$$\mathrm{h} = \boldsymbol{\sigma} : \frac{\partial \mathrm{G}}{\partial \boldsymbol{\sigma}} \quad \text{for the inelastic work } \mathrm{W}_{\mathrm{p}} \qquad \text{(B.20.2)}$$

Substituting the plastic incremental strains $\boldsymbol{\Delta\varepsilon}^{\mathrm{p}}$and the internal variables $\boldsymbol{\Delta}\mathbf{q}$ from Eq. (B.19) into Eq. (B.18), the consistency equation can be rewritten as:

$$\Delta \mathrm{F} = \frac{\partial \mathrm{F}}{\partial \boldsymbol{\sigma}} : \mathbf{C} : \left(\boldsymbol{\Delta\varepsilon} - \gamma_{\mathrm{d}} \frac{\partial \mathrm{G}}{\partial \boldsymbol{\sigma}} \right) + \frac{\partial \mathrm{F}}{\partial \mathbf{q}} \cdot \mathrm{M}(\mathrm{h}) = 0 \qquad \text{(B.21)}$$

By manipulating Eq. (B.21) to isolate the consistency parameter γ_d, the final equation becomes:

$$\gamma_d = \frac{\frac{\partial F}{\partial \boldsymbol{\sigma}} : \mathbf{C} : \boldsymbol{\Delta\varepsilon}}{\frac{\partial F}{\partial \boldsymbol{\sigma}} : \mathbf{C} : \frac{\partial G}{\partial \boldsymbol{\sigma}} - \frac{\partial F}{\partial \mathbf{q}} \cdot M(h)} \tag{B.22}$$

Once the consistency parameter is determined, the incremental plastic strains ($\boldsymbol{\Delta\varepsilon}^p$) and the increment of internal variables ($\boldsymbol{\Delta q}$) can be obtained from Eq. (B.19). Then the corresponding incremental stress tensors are determined from Eq. (B.16). Finally, the state of stress and the internal variables are updated.

B.4 Integration of constitutive equations

The main unknown in the plasticity model is the plastic component for a given set of incremental strains. Once the plastic component is determined, the elastic component can then be calculated by subtracting the plastic part from the total strain and the corresponding state of stress and the internal variables can finally be updated. From the definition of the incremental plastic strains, the incremental plastic strains are composed of two components, i.e. the consistency parameter (γ_d) and the plastic flow direction $\left(\frac{\partial G}{\partial \boldsymbol{\sigma}}\right)$. To calculate these components, first the plastic flow direction is defined and the corresponding consistency parameter is determined from the consistency condition. Depending on the calculation method, the plastic flow direction is defined from the variables of two different states, i.e. current $(\boldsymbol{\sigma}_n, \varepsilon_{p,n})$ or next $(\boldsymbol{\sigma}_{n+1}, \varepsilon_{p,n+1})$ state. For the current state, the plastic flow direction can be directly calculated from the given parameters. On the other hand, if the next state is involved in the calculation, trial-error iteration is required to calculate the plastic flow direction. To generalize the incremental plastic strain, Ortiz and Popov (1985) proposed the generalized mid-point rule in which the plastic flow direction can be obtained from a middle point between the current and the next state (Figure B.5):

$$\boldsymbol{\Delta\varepsilon}^{\mathrm{p}} \equiv \gamma_{\mathrm{d}} \frac{\partial \mathrm{G}_{\mathrm{n}+\alpha}}{\partial \boldsymbol{\sigma}} \tag{B.23}$$

where

$$\mathrm{G}_{\mathrm{n}+\alpha} = \mathrm{G}\left[(1-\alpha)\sigma_{\mathrm{n}} + \alpha\sigma_{\mathrm{n}+1}, (1-\alpha)\varepsilon_{\mathrm{p,n}} + \alpha\varepsilon_{\mathrm{p,n}+1}\right] \tag{B.24}$$

The parameter α is used to identify the location where the plastic flow is calculated. If the parameter α is equal to zero, the plastic flow is directly calculated from the current state of stress and the calculation method is said to be explicit. On the other hand, if the parameter α is greater than zero, the plastic flow direction is located between the current and the next states. Since the parameters in the next state remain unknown during the calculation, iteration is needed. Hence, the calculation method is said to be implicit. For the special case where the parameter α is one, the plastic flow direction is located at the next state. Once the location of the plastic flow direction is known, the consistency parameter is obtained from the consistency condition, which states that for any admissible state of stress, the corresponding yield function must be less than or equal to zero. For the case where the current state of stress is on the current yield surface ($\mathrm{F}_{\mathrm{n}} = 0$), the next loading incremental stress must give a zero incremental yield function($\Delta\mathrm{F}_{\mathrm{n}} = 0$) since the subsequent yield function is zero ($\mathrm{F}_{\mathrm{n}+1} = 0$).

Both integration methods were implemented in this work, i.e. explicit and implicit. For the former ($\alpha = 0$), the incremental form of the yield function is used to derive the consistency parameter. Since the yield function depends on two unknown parameters, i.e. stress tensors $(\boldsymbol{\sigma})$and the internal variables $\left(\varepsilon_\mathrm{p}\right)$, by applying the chain rule, the incremental yield function can be rewritten as:

$$\Delta\mathrm{F}\left(\boldsymbol{\sigma}, \varepsilon_\mathrm{p}\right) = \frac{\partial \mathrm{F}}{\partial \boldsymbol{\sigma}} : \boldsymbol{\Delta\sigma} + \frac{\partial \mathrm{F}}{\partial \varepsilon_\mathrm{p}} \cdot \Delta\varepsilon_\mathrm{p} \tag{B.25}$$

From the definition of the incremental stress and the effective plastic strain $\left(\Delta\varepsilon_\mathrm{p}\right)$ given earlier, the incremental yield function can be expanded in terms of the plastic strains:

$$\Delta\mathrm{F}\left(\boldsymbol{\sigma}, \varepsilon_\mathrm{p}\right) = \frac{\partial \mathrm{F}}{\partial \boldsymbol{\sigma}} : \mathbf{C} : (\boldsymbol{\Delta\varepsilon} - \boldsymbol{\Delta\varepsilon}^\mathbf{p}) + \frac{\partial \mathrm{F}}{\partial \varepsilon_\mathrm{p}} \cdot \sqrt{\boldsymbol{\Delta\varepsilon}^\mathbf{p} : \boldsymbol{\Delta\varepsilon}^\mathbf{p}} \tag{B.26}$$

For the explicit scheme where the plastic flow direction $\left(\frac{\partial \mathrm{G}}{\partial \boldsymbol{\sigma}}\right)$ is obtained from the current state of stress, the consistency condition becomes

$$\Delta\mathrm{F}\left(\sigma, \varepsilon_\mathrm{p}\right) = \frac{\partial \mathrm{F}}{\partial \boldsymbol{\sigma}} : \mathbf{C} : \left(\boldsymbol{\Delta\varepsilon} - \gamma_\mathrm{d} \frac{\partial \mathrm{G}}{\partial \boldsymbol{\sigma}}\right) + \frac{\partial \mathrm{G}}{\partial \varepsilon_\mathrm{p}} \cdot \gamma_\mathrm{d} \sqrt{\frac{\partial \mathrm{G}}{\partial \boldsymbol{\sigma}} : \frac{\partial \mathrm{G}}{\partial \boldsymbol{\sigma}}} = 0 \tag{B.27}$$

By rearranging above equation, the consistency parameter can be derived as a function of the current state:

$$\gamma_\mathrm{d} = \frac{\frac{\partial \mathrm{F}}{\partial \boldsymbol{\sigma}} : \mathbf{C} : \boldsymbol{\Delta\varepsilon}}{\frac{\partial \mathrm{F}}{\partial \boldsymbol{\sigma}} : \mathbf{C} : \frac{\partial \mathrm{G}}{\partial \boldsymbol{\sigma}} - \frac{\partial \mathrm{F}}{\partial \varepsilon_\mathrm{p}} \sqrt{\frac{\partial \mathrm{G}}{\partial \boldsymbol{\sigma}} : \frac{\partial \mathrm{G}}{\partial \boldsymbol{\sigma}}}} \tag{B.28}$$

It should be noted that since the consistency parameter for the explicit approach is solely based on the current state of stress, the stability or the accuracy of this method depends on a given set of incremental strains $(\boldsymbol{\Delta\varepsilon})$. Table B.1 summarizes the calculation steps for the explicit approach.

For the implicit method, the consistency parameter of the sub-increment (i) is derived from the yield function for the next state $\left(\mathrm{F}_{\mathrm{n+1}} \text{ or } \mathrm{F}\left(\boldsymbol{\sigma}_{\mathrm{n+1}}, \varepsilon_{\mathrm{p,n+1}}\right)\right)$. To simplify the equation of consistency parameter, the parameter α in Eq. (B.24) is one in this study. Notice that the yield function $\mathrm{F}_{\mathrm{n+1}}$ actually depends only on one unknown parameter γ_{d}. By expanding the yield function with respect to γ_{d}, the yield function becomes

$$\mathrm{F}_{\mathrm{n+1}} = \frac{\partial \mathrm{F}_{\mathrm{n+1}}}{\partial \gamma_{\mathrm{d}}} \cdot \Delta\gamma_{\mathrm{d}} \tag{B.29}$$

Or within the sub-increment during iteration, the yield function of the sub-increment (i) turns into:

$$\mathrm{F}_{\mathrm{n+1}}^{(\mathrm{i})} = \frac{\partial \mathrm{F}_{\mathrm{n+1}}^{(\mathrm{i})}}{\partial \gamma_{\mathrm{d}}} \cdot \left(\gamma_{\mathrm{d}}^{(\mathrm{i+1})} - \gamma_{\mathrm{d}}^{(\mathrm{i})}\right) \tag{B.30}$$

By rearranging the known parameters in step (i), the consistency for the next sub-increment (i+1) can be expressed as:

$$\gamma_{\mathrm{d}}^{(\mathrm{i+1})} = \gamma_{\mathrm{d}}^{(\mathrm{i})} - \frac{\mathrm{F}\left(\gamma_{\mathrm{d}}^{(\mathrm{i})}\right)}{\partial_{\gamma_{\mathrm{d}}} \mathrm{F}\left(\gamma_{\mathrm{d}}^{(\mathrm{i})}\right)} \tag{B.31}$$

where $\partial_{\gamma_{\mathrm{d}}} \mathrm{F}\left(\gamma_{\mathrm{d}}^{(\mathrm{i})}\right)$ is defined as $\frac{\partial \mathrm{F}\left(\gamma_{\mathrm{d}}^{(\mathrm{i})}\right)}{\partial \gamma_{\mathrm{d}}}$, which is the partial derivative of the yield function with respect to the consistency parameter (γ_{d}). Notice that this form is essentially the same form as the so-called Newton-Raphson method using derivatives (Press et al., 1997). By expanding the $\partial_{\gamma_{\mathrm{d}}} \mathrm{F}\left(\gamma_{\mathrm{d}}^{(\mathrm{i})}\right)$ term, the derivative becomes

$$\partial_{\gamma_{\mathrm{d}}} \mathrm{F}\left(\gamma_{\mathrm{d}}^{(\mathrm{i})}\right) = \frac{\partial \mathrm{F}\left(\gamma_{\mathrm{d}}^{(\mathrm{i})}\right)}{\partial \gamma_{\mathrm{d}}} = \left[\frac{\partial \mathrm{F}}{\partial \boldsymbol{\sigma}} : \frac{\partial \boldsymbol{\sigma}}{\partial \gamma_{\mathrm{d}}} + \frac{\partial \mathrm{F}}{\partial \varepsilon_{\mathrm{p}}} \cdot \frac{\partial \varepsilon_{\mathrm{p}}}{\partial \gamma_{\mathrm{d}}}\right]^{(\mathrm{i})} \tag{B.32}$$

By substituting the incremental stress equation and the definition of incremental plastic strain, the derivative $\partial_{\gamma_d}F(\gamma_d)$ becomes

$$\partial_{\gamma_d}F(\gamma_d) = \frac{\partial F}{\partial \boldsymbol{\sigma}} : \frac{\partial}{\partial \gamma_d}\left(\boldsymbol{\sigma}^{(t)} - \gamma_d^{(i)}\mathbf{C} : \frac{\partial G}{\partial \boldsymbol{\sigma}}\right) + \frac{\partial F^{(i)}}{\partial \varepsilon_p} \cdot \frac{\partial}{\partial \gamma_d}\left(\varepsilon_{p,n} + \gamma_d^{(i)}\sqrt{\frac{\partial G}{\partial \boldsymbol{\sigma}} : \frac{\partial G}{\partial \boldsymbol{\sigma}}}\right) \tag{B.33}$$

Since the trial state of stress $\left(\sigma^{(t)}\right)$ and the current effective plastic strain $\left(\varepsilon_{p,n}\right)$ do not depend on γ_d, the derivative $\partial_{\gamma_d}F(\gamma_d)$ is collapsed into:

$$\partial_{\gamma_d}F(\gamma_d) = -\frac{\partial F}{\partial \boldsymbol{\sigma}} : \mathbf{C} : \frac{\partial G}{\partial \boldsymbol{\sigma}} + \frac{\partial F}{\partial \varepsilon_p} \cdot \sqrt{\frac{\partial G}{\partial \boldsymbol{\sigma}} : \frac{\partial G}{\partial \boldsymbol{\sigma}}} \tag{B.34}$$

Therefore, the consistency parameter for the next sub-increment becomes

$$\gamma_d^{(i+1)} = \gamma_d^{(i)} + \frac{F\left(\gamma_d^{(i)}\right)}{\frac{\partial F}{\partial \boldsymbol{\sigma}} : \mathbf{C} : \frac{\partial G}{\partial \boldsymbol{\sigma}} - \frac{\partial F}{\partial \varepsilon_p} \cdot \sqrt{\frac{\partial G}{\partial \boldsymbol{\sigma}} : \frac{\partial G}{\partial \boldsymbol{\sigma}}}} \tag{B.35}$$

This formula is essentially the same as the cutting-plane algorithm proposed by Ortiz and Simo (1986). The basic concept behind their method is to use the elastic predictor to over-project the trial state of stress (σ_{n+1}^{trial}) to be outside the yield surface at the first trial step ($(i) = (0)$). Then, at each trial step (i), the plastic corrector ($\sigma_{n+1}^{(i)}$) at each trial step (i) is determined and used to slowly push the trial stress tensors back to the current yield surface (Figure B.6). Therefore, at the end of each trial step, the yield function slowly converges to zero and the iteration stops once the yield function reaches zero. The calculation step is shown on Table B.2 and the comparison between the explicit and the implicit methods are shown on Table B.3.

Table B.1 Calculation steps for explicit scheme

EXPLCIT APPROACH ($\alpha = 0$)

1. Calculate the trial state of stress $\boldsymbol{\sigma}^{(t)} = \boldsymbol{\sigma}_n + \mathbf{C}:\boldsymbol{\Delta\varepsilon}$
2. Calculate the trial yield surface $F\left(\sigma^{(t)}, \varepsilon_p^{(n)}\right)$
3. Check the trial yield surface
    a. IF $F\left(\boldsymbol{\sigma}^{(t)}, \varepsilon_p^{(n)}\right) \leq 0$ THEN update the next state of stress $\left(\boldsymbol{\sigma}_{n+1} = \boldsymbol{\sigma}^{(t)}\right)$and skip STEP 4
    b. IF $F\left(\sigma^{(t)}, \varepsilon_p^{(n)}\right) > 0$ THEN go to STEP 4
4. Plastic process
    a. Calculate the consistency parameter (γ_d)
    b. Calculate the incremental plastic strain ($\boldsymbol{\Delta\varepsilon}^p$)and the corresponding incremental stress ($\boldsymbol{\Delta\sigma}$).
    c. Calculate the increment of the effective plastic strain $\left(\Delta\varepsilon_p\right)$ and update internal variables (k, r, s, and a).

Note: for the explicit scheme, there is no need to calculate $F\left(\boldsymbol{\sigma}_{n+1}, \Delta\varepsilon_p^{(n+1)}\right)$

Table B.2 Calculation steps for implicit scheme

IMPLICIT APPROACH ($\alpha = 1$)

```
1. Calculate the trial state of stress $\boldsymbol{\sigma}^{(t)} = \boldsymbol{\sigma}_n + \mathbf{C}:\boldsymbol{\Delta\varepsilon}$
2. Calculate the trial yield function $F\left(\boldsymbol{\sigma}^{(t)}, \varepsilon_p^{(n)}\right)$
3. Check the trial yield function
    a. IF $F\left(\boldsymbol{\sigma}^{(t)}, \varepsilon_p^{(n)}\right) \leq 0$ THEN update the next state of stress $\left(\boldsymbol{\sigma}_{n+1} = \boldsymbol{\sigma}^{(t)}\right)$ and skip STEP 4
    b. IF $F\left(\sigma^{(t)}, \varepsilon_p^{(n)}\right) > 0$ THEN go to STEP 4
4. Plastic Process (at sub-increment (i))
    a. Determine $F\left(\gamma_d^{(i-1)}\right), \partial_{\gamma_d} F\left(\gamma_d^{(i-1)}\right)$
    b. Determine $\gamma_d^{(i)} = \gamma_d^{(i-1)} - \frac{F\left(\gamma_d^{(i-1)}\right)}{\partial_{\gamma_d} F\left(\gamma_d^{(i-1)}\right)}$
    c. Update $\boldsymbol{\sigma}^{(i)} = \boldsymbol{\sigma}^{t} - \gamma_d^{(i)} C:\frac{\partial G}{\partial \boldsymbol{\sigma}}$
    d. Update $\varepsilon_p^{(i)} = \varepsilon_{p,n} + \gamma_d^{(i)} \sqrt{\frac{\partial G}{\partial \boldsymbol{\sigma}}:\frac{\partial G}{\partial \boldsymbol{\sigma}}}$
    e. Update history variables (k, r, and s)
    f. Check $F\left(\gamma_d^{(i)}\right) \leq \mathrm{TOL}$
        i. IF YES, STOP
        ii. IF NO, REPEAT STEP a.
```

Note: Initial condition (0): $\gamma_d^{(0)} = 0$ $\boldsymbol{\sigma}^{(0)} = \boldsymbol{\sigma}^{(t)}$ $\varepsilon_p^{(0)} = \varepsilon_{p,n}$

Table B.3 Comparison between explicit and implicit schemes

	Explicit Scheme ($\alpha = 0$)	Implicit Scheme ($\alpha = 1$)
1. Consistency condition	$\Delta \mathrm{F}\left(\boldsymbol{\sigma}_{\mathrm{n}}, \varepsilon_{\mathrm{p,n}}\right) = 0$	$\mathrm{F}\left(\boldsymbol{\sigma}_{\mathrm{n+1}}, \varepsilon_{\mathrm{p,n+1}}\right) = 0$
2. Consistency parameter (γ_{d})	$\gamma_{\mathrm{d}} = \dfrac{\partial_{\boldsymbol{\sigma}} \mathrm{F}_{\mathrm{n}} : \mathbf{C} : \boldsymbol{\Delta\varepsilon}}{\partial_{\boldsymbol{\sigma}} \mathrm{F}_{\mathrm{n}} : \mathbf{C} : \partial_{\boldsymbol{\sigma}} \mathrm{G}_{\mathrm{n}} - \partial_{\varepsilon_{\mathrm{p}}} \mathrm{F}_{\mathrm{n}} \sqrt{\partial_{\boldsymbol{\sigma}} \mathrm{G}_{\mathrm{n}} : \partial_{\boldsymbol{\sigma}} \mathrm{G}_{\mathrm{n}}}}$	$\gamma_{\mathrm{d}}^{(\mathrm{i})} = \gamma_{\mathrm{d}}^{(\mathrm{i-1})} + \dfrac{\mathrm{F}_{\mathrm{n+1}}^{(\mathrm{i-1})}}{\partial_{\boldsymbol{\sigma}} \mathrm{F}_{\mathrm{n+1}}^{(\mathrm{i-1})} : \mathbf{C} : \partial_{\boldsymbol{\sigma}} \mathrm{G}_{\mathrm{n+1}}^{(\mathrm{i-1})} - \partial_{\varepsilon_{\mathrm{p}}} \mathrm{F}_{\mathrm{n+1}}^{(\mathrm{i-1})} \cdot \sqrt{\partial_{\boldsymbol{\sigma}} \mathrm{G}_{\mathrm{n+1}}^{(\mathrm{i-1})} : \partial_{\boldsymbol{\sigma}} \mathrm{G}_{\mathrm{n+1}}^{(\mathrm{i-1})}}}$
3. Plastic strain increment $(\boldsymbol{\Delta\varepsilon}^{\mathrm{p}})$	$\boldsymbol{\Delta\varepsilon}^{\mathrm{p}} = \gamma_{\mathrm{d}}\, \partial_{\boldsymbol{\sigma}} \mathrm{G}_{\mathrm{n}}$	$\boldsymbol{\Delta\varepsilon}^{\mathrm{p}^{(\mathrm{i})}} = \gamma_{\mathrm{d}}^{(\mathrm{i})}\, \partial_{\boldsymbol{\sigma}} \mathrm{G}_{\mathrm{n+1}}^{(\mathrm{i-1})}$
4. Equivalent plastic strain increment $(\Delta\varepsilon_{\mathrm{p}})$	$\Delta\varepsilon_{\mathrm{p}} = \gamma_{\mathrm{d}} \sqrt{\partial_{\boldsymbol{\sigma}} \mathrm{G}_{\mathrm{n}} : \partial_{\sigma} \mathrm{G}_{\mathrm{n}}}$	$\Delta\varepsilon_{\mathrm{p}}^{(\mathrm{i})} = \gamma_{\mathrm{d}}^{(\mathrm{i})} \sqrt{\partial_{\boldsymbol{\sigma}} \mathrm{G}_{\mathrm{n+1}}^{(\mathrm{i-1})} : \partial_{\boldsymbol{\sigma}} \mathrm{G}_{\mathrm{n+1}}^{(\mathrm{i-1})}}$
5. Stability condition	Depending on given incremental strain $(\boldsymbol{\Delta\varepsilon})$	Unconditional
Note	$\partial_{\boldsymbol{\sigma}} \mathrm{F}_{\mathrm{n}} = \dfrac{\partial \mathrm{F}\left(\boldsymbol{\sigma}_{\mathrm{n}}, \varepsilon_{\mathrm{p,n}}\right)}{\partial \boldsymbol{\sigma}}, \partial_{\boldsymbol{\sigma}} \mathrm{G}_{\mathrm{n}} = \dfrac{\partial \mathrm{G}\left(\boldsymbol{\sigma}_{\mathrm{n}}, \varepsilon_{\mathrm{p,n}}\right)}{\partial \boldsymbol{\sigma}}$ and $\partial_{\varepsilon_{\mathrm{p}}} \mathrm{F}_{\mathrm{n}} = \dfrac{\partial \mathrm{F}\left(\boldsymbol{\sigma}_{\mathrm{n}}, \varepsilon_{\mathrm{p,n}}\right)}{\partial \varepsilon_{\mathrm{p}}}$	(i) represents the sub-incremental step where $\mathrm{F}_{\mathrm{n+1}}^{(\mathrm{i})} = \mathrm{F}\left(\gamma_{\mathrm{d}}^{(\mathrm{i})}\right)$ and $\mathrm{G}_{\mathrm{n+1}}^{(\mathrm{i})} = \mathrm{G}\left(\gamma_{\mathrm{d}}^{(\mathrm{i})}\right)$ $\partial_{\boldsymbol{\sigma}} \mathrm{F}_{\mathrm{n+1}}^{(\mathrm{i})} = \dfrac{\partial \mathrm{F}\left(\gamma_{\mathrm{d}}^{(\mathrm{i})}\right)}{\partial \boldsymbol{\sigma}}$ and $\partial_{\boldsymbol{\sigma}} \mathrm{G}_{\mathrm{n+1}}^{(\mathrm{i})} = \dfrac{\partial \mathrm{G}\left(\gamma_{\mathrm{d}}^{(\mathrm{i})}\right)}{\partial \boldsymbol{\sigma}}$

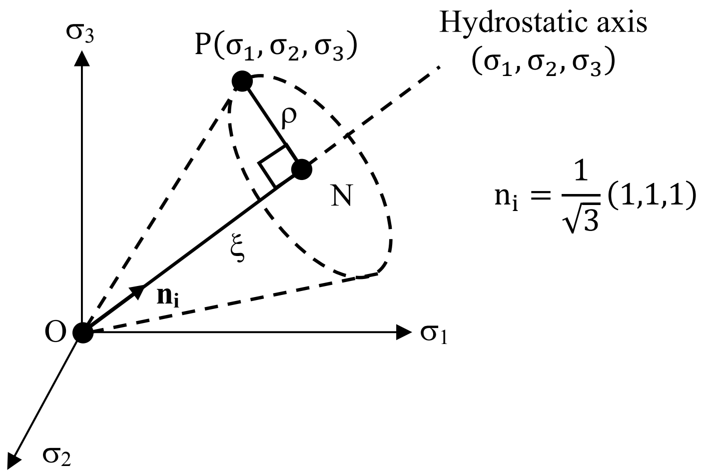

(a) The Haigh-Westergaard coordinate system

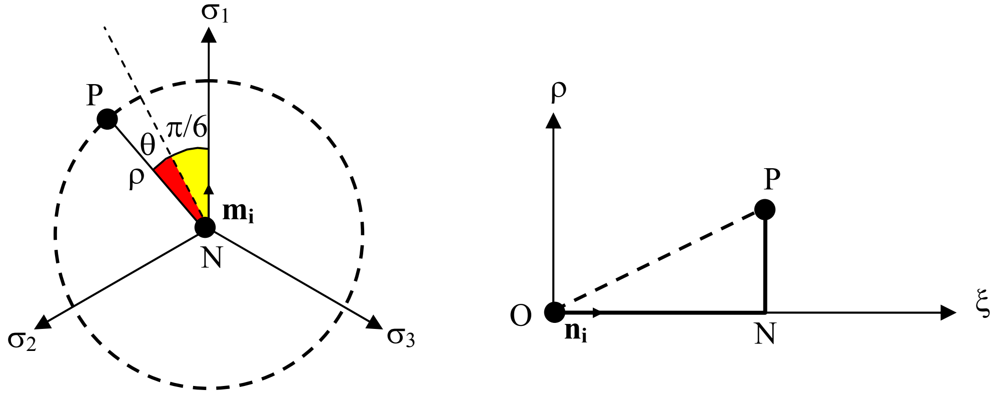

(b) Deviatoric plane perpendicular to the hydrostatic axis

(c) Meridian plane

Figure B.1 Geometric representation of the stress state in the principal stress space (Ottosen and Ristinmaa, 2005)

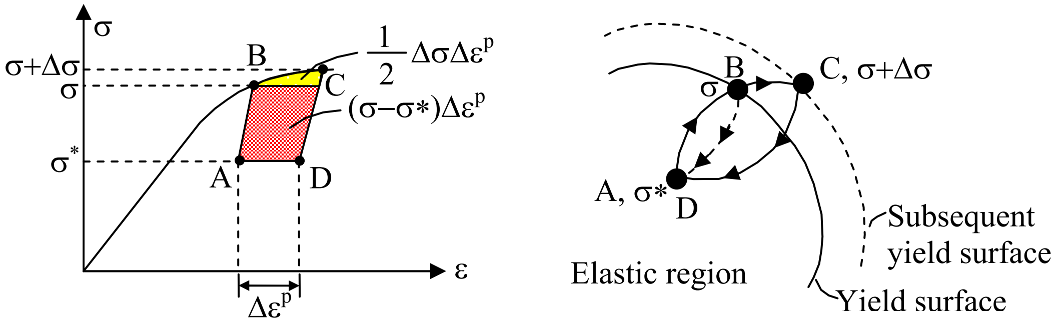

Figure B.2 Stress cycle for stable materials produced by external agency must always give the positive work (shaded area ABCD >0) (Ottosen & Ristnimaa, 2005)

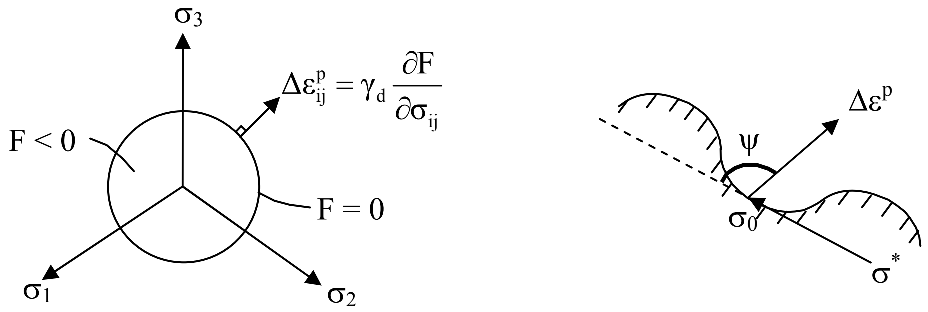

(a) The first consequence of the Drucker's postuate is the normality condition

(b) Yield surface that does not satisfy the convexity condition.

Figure B.3Graphical representations of the Drucker's postulates and their consequences (Shaw, 2004)

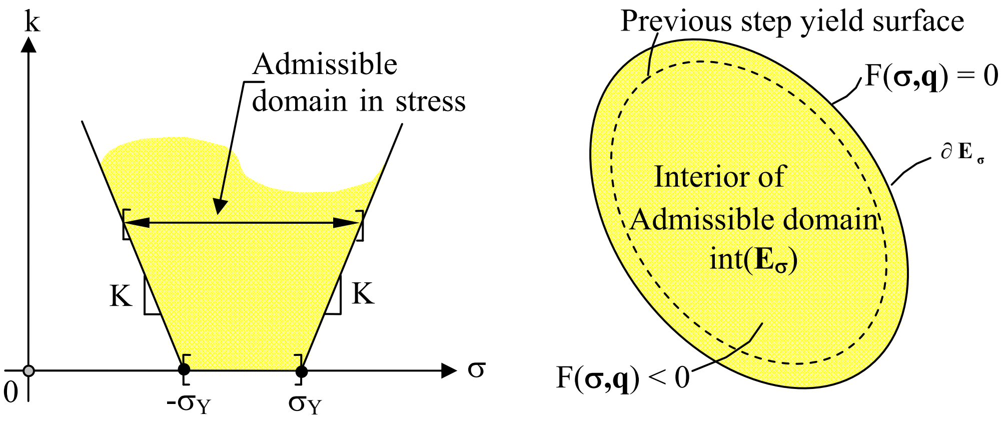

(a) One-dimensional model

(b) Two-dimensional model

Figure B.4 Elastic range and admissible domain in stress space (Simo & Hughes, 2001)

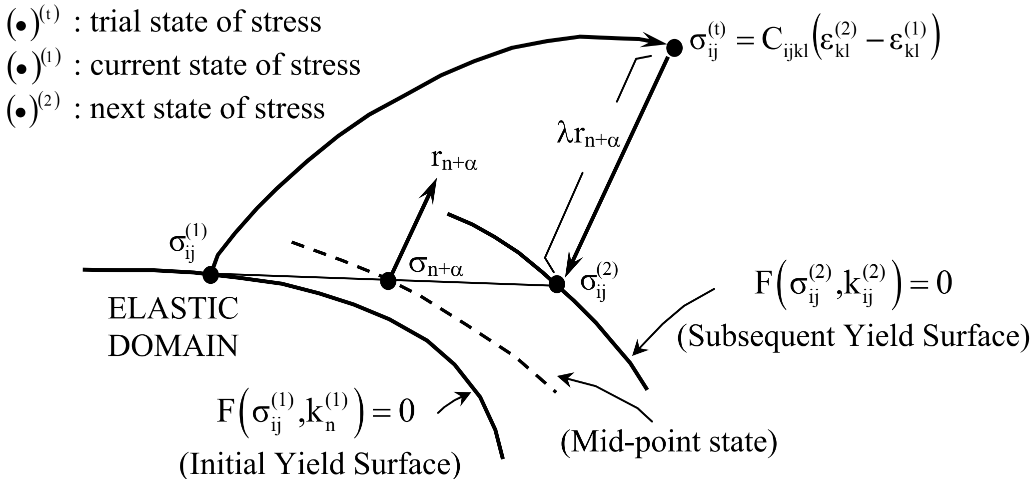

Figure B.5 Geometric interpretation of the generalized midpoint rule (Ortiz and Popov, 1985)

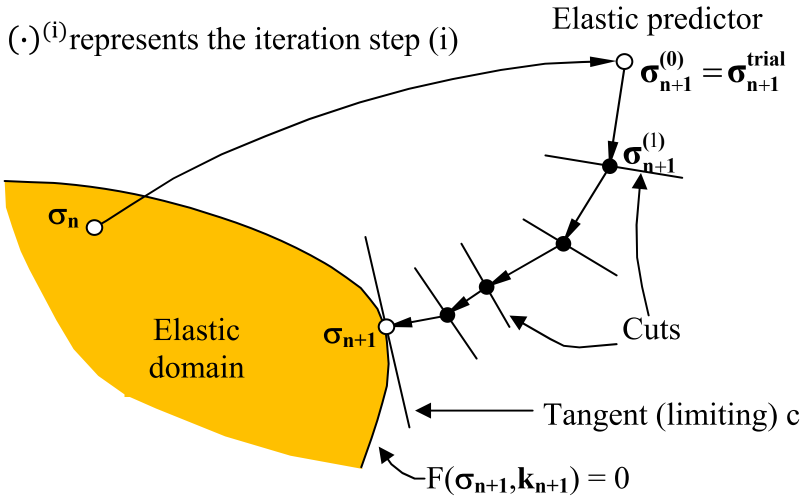

Figure B.6 Geometric interpretation for the case of perfect plasticity of a general return mapping algorithm based on an elastoplastic split of the constitutive equations (Ortiz & Simo, 1986)

APPENDIX C

DERIVATION OF CONSISTENCY PARAMETER

This appendix covers derivation of the consistency parameters for both compression and tension that involves tensorial manipulations such as double contraction, and dot products. Moreover, the derivatives of yield and potential functions with respect to stress tensors are discussed in this section as well. Before deriving the consistency parameter, the invariants of stress tensors and the derivatives of invariants with respect to stress tensors are discussed.

C.1 Invariants of stress tensors

$\mathrm{I}_1 = \mathrm{tr}(\boldsymbol{\sigma}) = \sigma_{\mathrm{ii}}$: First invariant of stress tensors

$\mathbf{S} = \boldsymbol{\sigma} - \frac{\mathrm{I}_1}{3}\boldsymbol{\delta}$: Deviatoric stress tensors

$\mathrm{S}_{\mathrm{ij}} = \sigma_{\mathrm{ij}} - \frac{\sigma_{\mathrm{kk}}}{3}\delta_{\mathrm{ij}}$: Deviatoric stress tensors (index notation)

$\mathrm{J}_2 = \frac{1}{2}\mathbf{S}:\mathbf{S} = \frac{1}{2}\mathrm{S}_{\mathrm{ij}}\mathrm{S}_{\mathrm{ji}}$: Second invariant of deviatoric stress tensors

$\mathrm{J}_3 = \det(\mathbf{S}) = \frac{1}{3}\mathrm{S}_{\mathrm{ij}}\mathrm{S}_{\mathrm{ik}}\mathrm{S}_{\mathrm{kj}}$: Third invariant of deviatoric stress tensors

$\sin(3\theta) = -\frac{3\sqrt{3}\mathrm{J}_3}{2\mathrm{J}_2^{3/2}}$: Lode angle

C.2 Derivatives of Invariants with respect to stress tensors

$$\frac{\partial \mathrm{I}_1}{\partial \boldsymbol{\sigma}} = \frac{\partial(\sigma_{\mathrm{kk}})}{\partial \sigma_{\mathrm{ij}}} = \delta_{\mathrm{ik}}\delta_{\mathrm{jk}} = \delta_{\mathrm{ij}} = \boldsymbol{\delta}$$

: Derivative of first invariant with respect to stress tensors

$$\frac{\partial \mathrm{J}_2}{\partial \boldsymbol{\sigma}} = \frac{\partial \mathrm{J}_2}{\partial \mathbf{S}} \cdot \frac{\partial \mathbf{S}}{\partial \boldsymbol{\sigma}} = \frac{\partial\left(\frac{1}{2}\mathbf{S}:\mathbf{S}\right)}{\partial \mathbf{S}} \cdot \frac{\partial \mathbf{S}}{\partial \boldsymbol{\sigma}}$$

: Derivative of second invariant with respect to stress tensors

$$\frac{\partial \mathrm{J}_2}{\partial \sigma_{\mathrm{ij}}} = \frac{\partial\left(\frac{1}{2}\mathrm{S}_{\mathrm{kl}}\mathrm{S}_{\mathrm{lk}}\right)}{\partial \mathrm{S}_{\mathrm{mn}}} \cdot \frac{\partial \mathrm{S}_{\mathrm{mn}}}{\partial \sigma_{\mathrm{ij}}} = \mathrm{S}_{\mathrm{ij}}$$

: Derivative of second invariant with respect to stress tensors (index notation)

$$\frac{\partial \mathrm{J}_3}{\partial \boldsymbol{\sigma}} = \frac{\partial \mathrm{J}_3}{\partial \mathbf{S}} \cdot \frac{\partial \mathbf{S}}{\partial \boldsymbol{\sigma}} = \frac{\partial(\det(\mathbf{S}))}{\partial \mathbf{S}} \cdot \frac{\partial \mathbf{S}}{\partial \boldsymbol{\sigma}} \equiv \mathbf{t}$$

: Derivative of third invariant with respect to stress tensors

$$\frac{\partial \mathrm{J}_3}{\partial \sigma_{\mathrm{ij}}} = \frac{\partial\left(\frac{1}{3}\mathrm{S}_{\mathrm{mn}}\mathrm{S}_{\mathrm{ma}}\mathrm{S}_{\mathrm{an}}\right)}{\partial \mathrm{S}_{\mathrm{kl}}} \cdot \frac{\partial \mathrm{S}_{\mathrm{kl}}}{\partial \sigma_{\mathrm{ij}}} = \mathrm{S}_{\mathrm{in}}\mathrm{S}_{\mathrm{nj}} - \frac{2}{3}\mathrm{J}_2\delta_{\mathrm{ij}} \equiv \mathrm{t}_{\mathrm{ij}}$$

: Derivative of third invariant with respect to stress tensors (index notation)

C.3 Compression Yield Function $(\mathrm{F_C})$ and Potential Function $(\mathrm{g_C})$

Recall compression yield and potential function given in Chapter 4. The compression yield function composes of three parts, i.e. hardening (F_1), Cosine softening (F_2), and Exponential softening (F_3). The potential function used here is the Drucker-Prager yield function used to control the amount of volumetric strain.

- Compression yield function

$$\mathrm{F_c}(\boldsymbol{\sigma}, \mathrm{k}, \mathrm{r}, \mathrm{s}) = \mathrm{F}_1(\boldsymbol{\sigma}, \mathrm{k}) + \mathrm{F}_2(\boldsymbol{\sigma}, \mathrm{r}) + \mathrm{F}_3(\boldsymbol{\sigma}, \mathrm{s})$$

where

$$\mathrm{F}_1(\boldsymbol{\sigma}, \mathrm{k}) = \frac{\mathrm{A}}{\mathrm{kf}_\mathrm{c}'}\mathrm{J}_2 + \mathrm{B}\sqrt{\mathrm{J}_2} + \mathrm{Ck}\sigma_1 + \mathrm{DkI}_1 + \mathrm{E}_{\mathrm{htc}}\frac{(1-\mathrm{k})}{\mathrm{kf}_\mathrm{c}'}\mathrm{I}_1^2 - \mathrm{kf}_\mathrm{c}'$$

$$\mathrm{F}_2(\sigma, \mathrm{r}) = -(1-\mathrm{Imp})(1-\mathrm{r})\left(\frac{\mathrm{I}_1}{\mathrm{I}_{1,\mathrm{trans}}} - 1\right)\mathrm{f}_\mathrm{c}'$$

$$\mathrm{F}_3(\sigma, \mathrm{s}) = -\mathrm{Imp}(1-\mathrm{s})\left(\frac{\mathrm{I}_1}{\mathrm{I}_{1,\mathrm{trans}}} - 1\right)\mathrm{f}_\mathrm{c}'$$

where

$$\sigma_1 = \frac{\mathrm{I}_1}{3} + \frac{2\sqrt{\mathrm{J}_2}}{\sqrt{3}}\sin\left(\theta + \frac{2\pi}{3}\right)$$

: Maximum principal stress

- Compression potential function

$$\mathrm{g_C}(\boldsymbol{\sigma}, \varepsilon_\mathrm{p}) = \mathrm{a_C}\frac{\mathrm{I}_1}{\sqrt{3}} + \sqrt{2\mathrm{J}_2} - \mathrm{c_C}$$

where

$$a_C = \frac{a_u}{(1-\eta)}\left(\frac{\varepsilon_p}{\varepsilon_{p,max}} - \eta\right)$$

a_u = Slope of volumetric strain (ε_v) vs. normal strain without confinement

η = Ratio of $\varepsilon_p/\varepsilon_{p,max}$ at zero slope $(a = 0)$

C.4 Derivative of Compression Yield Function with respect to Stress Tensor ($\partial F_C / \partial \boldsymbol{\sigma}$)

By using chain rule, the derivative of yield function with respect to stress tensors can be decomposed into three parts based on invariants, i.e. first invariant I_1 (A_1), second invariant J_2 (A_2), and third invariant J_3 (A_3). The derivatives of invariants with respect to stress tensors are given in C.2

$$\frac{\partial F_C}{\partial \boldsymbol{\sigma}} = \frac{\partial F_C}{\partial I_1}\cdot\frac{\partial I_1}{\partial \boldsymbol{\sigma}} + \frac{\partial F_C}{\partial J_2}\cdot\frac{\partial J_2}{\partial \boldsymbol{\sigma}} + \frac{\partial F_C}{\partial J_3}\cdot\frac{\partial J_3}{\partial \boldsymbol{\sigma}}$$

$$\frac{\partial F_C}{\partial \boldsymbol{\sigma}} = A_1\boldsymbol{\delta} + A_2\mathbf{S} + A_3\mathbf{t}$$

where

$$A_1 = \frac{\partial F_C}{\partial I_1} = \frac{Ck}{3} + Dk + 2E_{htc}\frac{(1-k)}{kf_c'}I_1 - \frac{(1-Imp)(1-r)f_c'}{I_1^{trans}} - \frac{Imp(1-s)f_c'}{I_1^{trans}}$$

$$A_2 = \frac{\partial F_C}{\partial J_2} = \frac{A}{kf_c'} + \frac{B}{2\sqrt{J_2}} + \frac{3Ck\cos\left(\theta + \frac{2\pi}{3}\right)}{2\,(\cos 3\theta)}\frac{J_3}{J_2^2} + \frac{Ck}{\sqrt{3J_2}}\sin\left(\theta + \frac{2\pi}{3}\right)$$

$$A_3 = \frac{\partial F_C}{\partial J_3} = -\frac{Ck\cos\left(\theta + \frac{2\pi}{3}\right)}{(\cos 3\theta)J_2}$$

$$\mathbf{t} = \frac{\partial J_3}{\partial \boldsymbol{\sigma}}$$

Note that the $A_2$and A_3 terms contained $\cos 3\theta$ as denominator, which causes zero dividing, will be discussed later.

C.5 Derivative of yield function with respect to effective plastic strain $(\partial F_C / \partial \varepsilon_p)$

Besides having the derivatives of yield function with respect to the stress tensors, the derivatives of yield function with respect to effective plastic strain $(\partial F_C / \partial \varepsilon_p)$ are also of interest. Based on the number of internal variables, $\partial F_C / \partial \varepsilon_p$ are divided into three components, i.e. hardening (B_1), Cosine softening (B_2), and Exponential softening (B_3). Unlike $\partial F_C / \partial \boldsymbol{\sigma}$, not all components are required for each loading step. For example, if the effective plastic strain (ε_p) is less than $\varepsilon_{p,max}$ (under hardening regime), only B_1 is required and all other components are set zero.

$$\frac{\partial F_C}{\partial \varepsilon_p} = \frac{\partial F_C}{\partial k} \cdot \frac{\partial k}{\partial \varepsilon_p} + \frac{\partial F_C}{\partial r} \cdot \frac{\partial r}{\partial \varepsilon_p} + \frac{\partial F_C}{\partial s} \cdot \frac{\partial s}{\partial \varepsilon_p}$$

$$\frac{\partial F_C}{\partial \varepsilon_p} = B_1 H_1 + B_2 H_2 + B_3 H_3$$

where

$$B_1 = \frac{\partial F_C}{\partial k} = \frac{\partial F_1}{\partial k} = -\frac{A}{k^2 f_c'} J_2 + C\sigma_1 + DI_1 - \frac{E_{htc} I_1^2}{k^2 f_c'} - f_c'$$

$$B_2 = \frac{\partial F_C}{\partial r} = \frac{\partial F_2}{\partial r} = (1 - \mathrm{Imp}) \left(\frac{I_1}{I_1^{trans}} - 1 \right) f_c'$$

$$B_3 = \frac{\partial F_C}{\partial s} = \frac{\partial F_3}{\partial s} = \mathrm{Imp} \left(\frac{I_1}{I_1^{trans}} - 1 \right) f_c'$$

$$H_1 = \frac{\partial k}{\partial \varepsilon_p} = (1 - k_0) \left[\frac{1}{\sqrt{\varepsilon_p \varepsilon_{p,max}}} - \frac{1}{\varepsilon_{p.max}} \right]$$

$$H_2 = \frac{\partial r}{\partial \varepsilon_p} = \frac{-\pi}{2\left(\varepsilon_{p,ult} - \varepsilon_{p,max}\right)} \sin\left[\frac{\pi\left(\varepsilon_p - \varepsilon_{p,max}\right)}{\varepsilon_{p,ult} - \varepsilon_{p,max}}\right]$$

$$H_3 = \frac{\partial s}{\partial \varepsilon_p} = \frac{-\omega}{\left(\varepsilon_{p,ult} - \varepsilon_{p,int}\right)} \mathrm{Exp}\left[\frac{-\omega\left(\varepsilon_p - \varepsilon_{p,int}\right)}{\varepsilon_{p,ult} - \varepsilon_{p,int}}\right]$$

C.5 Derivative of potential function with respect to stress tensors ($\partial g_C / \partial \boldsymbol{\sigma}$)

The last derivative required for obtaining the consistency parameter is the derivative of potential function with respect to stress tensors ($\partial g_C / \partial \boldsymbol{\sigma}$). This component is also used to determine the plastic strain tensors.

$$\frac{\partial g_C}{\partial \boldsymbol{\sigma}} = \frac{\partial}{\partial \boldsymbol{\sigma}}\left(a_C \frac{I_1}{\sqrt{3}} + \sqrt{2J_2} - c_C\right)$$

$$\frac{\partial g_C}{\partial \boldsymbol{\sigma}} = \frac{a_C}{\sqrt{3}} \boldsymbol{\delta} + \frac{1}{\sqrt{2J_2}} \mathbf{S}$$

C.6 Consistency Parameter for Compression

Based on the assumption that the material in the elastic range is linearly isotropic, the first term in denominator of the consistency parameter equation becomes

$$\frac{\partial F_C}{\partial \boldsymbol{\sigma}} : \mathbf{C} : \frac{\partial g_C}{\partial \boldsymbol{\sigma}} = \frac{\partial F_C}{\partial \sigma_{ij}} C_{ijkl} \frac{\partial g_C}{\partial \sigma_{kl}}$$

$$= \left(A_1 \delta_{ij} + A_2 S_{ij} + A_3 t_{ij}\right)\left(2G\left[\frac{1}{2}\left(\delta_{ik}\delta_{jl} + \delta_{il}\delta_{jk}\right) + \frac{\nu}{1-2\nu}\delta_{ij}\delta_{kl}\right]\right)\left(\frac{a_C}{\sqrt{3}}\delta_{kl} + \frac{1}{\sqrt{2J_2}} S_{kl}\right)$$

$$\frac{\partial F_C}{\partial \boldsymbol{\sigma}} : \mathbf{C} : \frac{\partial g}{\partial \boldsymbol{\sigma}} = 2G\left[A_1 a_C \sqrt{3} \frac{(1+\nu)}{(1-2\nu)} + A_2 \sqrt{2J_2} + A_3\left(\frac{3J_3}{\sqrt{2J_2}}\right)\right]$$

Note: For linearly isotropic elastic material, **C** is written as:

$$C_{ijkl} = 2G\left[\frac{1}{2}\left(\delta_{ik}\delta_{jl} + \delta_{il}\delta_{jk}\right) + \frac{\nu}{1-2\nu}\delta_{ij}\delta_{kl}\right]$$

Back to the discussion related to $\cos(3\theta)$ in A_2 and A_3 terms in section C.4 and consider the last two term of $\frac{\partial F}{\partial \boldsymbol{\sigma}}:\mathbf{C}:\frac{\partial g}{\partial \boldsymbol{\sigma}}$ for the compression:

$$A_2\sqrt{2J_2} + A_3\left(\frac{3J_3}{\sqrt{2J_2}}\right) = \left(\frac{A}{kf_c'} + \frac{B}{2\sqrt{J_2}} + \frac{3Ck\cos\left(\theta + \frac{2\pi}{3}\right)}{2\,(\cos 3\theta)}\frac{J_3}{J_2^2} + \frac{Ck}{\sqrt{3J_2}}\sin\left(\theta + \frac{2\pi}{3}\right)\right)\sqrt{2J_2}$$

$$+\left(-\frac{Ck\cos\left(\theta + \frac{2\pi}{3}\right)}{(\cos 3\theta)J_2}\right)\left(\frac{3J_3}{\sqrt{2J_2}}\right)$$

$$= \sqrt{2J_2}\left[\frac{A}{kf_c'} + \frac{B}{2\sqrt{J_2}} + \frac{Ck}{\sqrt{3J_2}}\sin\left(\theta + \frac{2\pi}{3}\right)\right]$$

$$= \frac{A}{kf_c'}\sqrt{2J_2} + \frac{B}{\sqrt{2}} + \frac{\sqrt{2}Ck}{\sqrt{3}}\sin\left(\theta + \frac{2\pi}{3}\right)$$

Therefore, the first term of denominator of the consistency parameter equation becomes

$$\frac{\partial F_C}{\partial \boldsymbol{\sigma}}:\mathbf{C}:\frac{\partial g_C}{\partial \boldsymbol{\sigma}} = 2G\left[A_1 a_C\sqrt{3}\frac{(1+\nu)}{(1-2\nu)} + \frac{A}{kf_c'}\sqrt{2J_2} + \frac{B}{\sqrt{2}} + \frac{\sqrt{2}Ck}{\sqrt{3}}\sin\left(\theta + \frac{2\pi}{3}\right)\right]$$

By substituting $\partial g_C / \partial \boldsymbol{\sigma}$ into the second term of denominator, it becomes

$$\frac{\partial F_C}{\partial \varepsilon_p}\sqrt{\frac{2}{3}\frac{\partial g_C}{\partial \boldsymbol{\sigma}}:\frac{\partial g_C}{\partial \boldsymbol{\sigma}}} = (B_1H_1 + B_2H_2 + B_3H_3)\sqrt{\frac{2}{3}(a_c^2 + 1)}$$

C.7 Tension Yield Function (F_T) and Potential Function (g_T)

Recall the tension yield and potential functions given in Chapter 4.

- Tension yield function (F_T)

$$F_T(\sigma, k, r, s) = x' I_1^2 + \left[(y' + z')\sqrt{rs} - z'\right]I_1 + kz' - d\sqrt{J_2}$$

where

$$x' = f_t[(2\alpha - 1)\beta - 2]\sqrt{J_{2,1}} + \sqrt{3}f_t^2[1 + (\alpha - 1)\beta]$$

$$y' = f_t^2\left[8 - 2\beta(2\alpha - 1) - \beta^2(2\alpha - 1)^2\right]\sqrt{J_{2,1}} - 3\sqrt{3}f_t^3[1 + (\alpha - 1)\beta]$$

$$z' = 3f_t^3[1 - (2\alpha - 1)\beta][(2\alpha - 1)\beta - 2]\sqrt{J_{2,1}}$$

$$d = 3f_t^3[1 - (2\alpha - 1)\beta][(2\alpha - 1)\beta - 2]$$

$$\beta \equiv (\sin\theta) + \frac{1}{2}$$

$$\sqrt{J_{2,1}} = \sqrt{J_{2,HTC}} = \frac{2c'}{-b' - \sqrt{b'^2 - 4a'c'}}$$

where

$$a' = \frac{A}{kf_c'}$$

$$b' = B + \frac{2Ck}{\sqrt{3}}\sin\left(\theta + \frac{2\pi}{3}\right)$$

$$c' = -kf_c' + [(1 - \mathrm{Imp})(1 - r)f_c'] + [\mathrm{Imp}(1 - s)f_c']$$

- Tension potential function (g_T)

$$g_T = a_T\frac{I_1}{\sqrt{3}} + \sqrt{2J_2} - c_T$$

where

a_T = material parameter controlled slope of volumetric strain with respect to normal strain

C.8 Derivative of Tension Yield Function with respect to Stress Tensor ($\partial F_T / \partial \boldsymbol{\sigma}$)

The same derivation in compression is repeated here for tension.

$$\frac{\partial F_T}{\partial \boldsymbol{\sigma}} = A_1'\boldsymbol{\delta} + A_2'\mathbf{S} + A_3'\mathbf{t}$$

where

$$A_1' = \frac{\partial F_T}{\partial I_1} = 2x'I_1 + (y' + z')\sqrt{rs} - z'$$

$$A_2' = \frac{\partial F_T}{\partial J_2} = \left\{I_1^2\frac{\partial x'}{\partial \theta} + I_1\left[\left(\frac{\partial y'}{\partial \theta} + \frac{\partial z'}{\partial \theta}\right)\sqrt{rs} - \frac{\partial z'}{\partial \theta}\right] + k\frac{\partial z'}{\partial \theta} - \sqrt{J_2}\frac{\partial d}{\partial \theta}\right\}\frac{\partial \theta}{\partial J_2} - \frac{1}{2}\frac{d}{\sqrt{J_2}}$$

$$= \left\{I_1^2\frac{\partial x'}{\partial \theta} + I_1\left[\left(\frac{\partial y'}{\partial \theta} + \frac{\partial z'}{\partial \theta}\right)\sqrt{rs} - \frac{\partial z'}{\partial \theta}\right] + k\frac{\partial z'}{\partial \theta} - \sqrt{J_2}\frac{\partial d}{\partial \theta}\right\}\left(\frac{3\sqrt{3}}{4\cos(3\theta)}\frac{J_3}{J_2^{\frac{5}{2}}}\right) - \frac{1}{2}\frac{d}{\sqrt{J_2}}$$

$$= [*]\left(\frac{3\sqrt{3}}{4\cos(3\theta)}\frac{J_3}{J_2^{\frac{5}{2}}}\right) - \frac{1}{2}\frac{d}{\sqrt{J_2}}$$

$$A_3' = \frac{\partial F_T}{\partial J_3} = \left\{I_1^2\frac{\partial x'}{\partial \theta} + I_1\left[\left(\frac{\partial y'}{\partial \theta} + \frac{\partial z'}{\partial \theta}\right)\sqrt{rs} - \frac{\partial z'}{\partial \theta}\right] + k\frac{\partial z'}{\partial \theta} - \sqrt{J_2}\frac{\partial d}{\partial \theta}\right\}\frac{\partial \theta}{\partial J_3}$$

$$= \left\{I_1^2\frac{\partial x'}{\partial \theta} + I_1\left[\left(\frac{\partial y'}{\partial \theta} + \frac{\partial z'}{\partial \theta}\right)\sqrt{rs} - \frac{\partial z'}{\partial \theta}\right] + k\frac{\partial z'}{\partial \theta} - \sqrt{J_2}\frac{\partial d}{\partial \theta}\right\}\left(-\frac{\sqrt{3}}{2\cos(3\theta)}\frac{1}{J_2^{3/2}}\right)$$

$$= [*]\left(-\frac{\sqrt{3}}{2\cos(3\theta)}\frac{1}{J_2^{3/2}}\right)$$

C.9 Derivative of yield function with respect to effective plastic strain $(\partial F_T / \partial \varepsilon_p)$

$$\frac{\partial F_T}{\partial \varepsilon_p'} = \frac{\partial F_T}{\partial k}\cdot\frac{\partial k}{\partial \varepsilon_p'} + \frac{\partial F_T}{\partial r}\cdot\frac{\partial r}{\partial \varepsilon_p'} + \frac{\partial F_T}{\partial s}\cdot\frac{\partial s}{\partial \varepsilon_p'}$$

$$\frac{\partial F_T}{\partial \varepsilon_p'} = B_1'H_1' + B_2'H_2' + B_3'H_3'$$

where

$$B_1' = \frac{\partial F_T}{\partial k} = I_1^2\frac{\partial x'}{\partial k} + I_1\left[\left(\frac{\partial y'}{\partial k} + \frac{\partial z'}{\partial k}\right)\sqrt{rs} - \frac{\partial z'}{\partial k}\right] + k\frac{\partial z'}{\partial k} + z' - \sqrt{J_2}\frac{\partial d}{\partial k}$$

$$B_2' = \frac{\partial F_T}{\partial r} = I_1^2 \frac{\partial x'}{\partial r} + I_1 \left[\left(\frac{\partial y'}{\partial r} + \frac{\partial z'}{\partial r} \right) \sqrt{rs} + \frac{1}{2} (y' + z') \sqrt{\frac{s}{r}} - \frac{\partial z'}{\partial r} \right] + k \frac{\partial z'}{\partial r} - \sqrt{J_2} \frac{\partial d}{\partial r}$$

$$B_3' = \frac{\partial F_T}{\partial s} = I_1^2 \frac{\partial x'}{\partial s} + I_1 \left[\left(\frac{\partial y'}{\partial s} + \frac{\partial z'}{\partial s} \right) \sqrt{rs} + \frac{1}{2} (y' + z') \sqrt{\frac{r}{s}} - \frac{\partial z'}{\partial s} \right] + k \frac{\partial z'}{\partial s} - \sqrt{J_2} \frac{\partial d}{\partial s}$$

$$H_1' = \frac{\partial k}{\partial \varepsilon_p'} = \begin{cases} \dfrac{(k_1 - k_0)}{\varepsilon_{p,1}'} & : 0 \le \varepsilon_p' \le \varepsilon_{p,1}' \\[2ex] \dfrac{(1 - k_1)}{\left(\varepsilon_{p,2}' - \varepsilon_{p,3}'\right)} & : \varepsilon_{p,1}' < \varepsilon_p' \le \varepsilon_{p,2}' \end{cases}$$

$$H_2' = H_3' = \frac{\partial r}{\partial \varepsilon_p'} = \frac{\partial s}{\partial \varepsilon_p'} = -\frac{\gamma}{\left(\varepsilon_{p,3}' - \varepsilon_{p,2}'\right)} \mathrm{Exp} \left[\frac{-\gamma\left(\varepsilon_p' - \varepsilon_{p,2}'\right)}{\left(\varepsilon_{p,3}' - \varepsilon_{p,2}'\right)} \right] \qquad : \ \varepsilon_{p,2}' < \varepsilon_p' \le \varepsilon_{p,3}'$$

- Derivative of internal parameters with respect to hardening parameter (k)

$$\frac{\partial x'}{\partial k} = f_t[(2\alpha - 1)\beta - 2] \frac{\partial \sqrt{J_{2,1}}}{\partial k}$$

$$\frac{\partial y'}{\partial k} = f_t^2 \left[8 - 2\beta(2\alpha - 1) - \beta^2 (2\alpha - 1)^2\right] \frac{\partial \sqrt{J_{2,1}}}{\partial k}$$

$$\frac{\partial z'}{\partial k} = 3 f_t^3 [1 - (2\alpha - 1)\beta][(2\alpha - 1)\beta - 2] \frac{\partial \sqrt{J_{2,1}}}{\partial k}$$

$$\frac{\partial d}{\partial k} = 0$$

$$\frac{\partial \sqrt{J_{2,1}}}{\partial k} = \frac{\left[\left(-b' - \sqrt{b'^2 - 4a'c'}\right) \dfrac{\partial (2c')}{\partial k} \right] - \left[(2c') \dfrac{\partial\left(-b' - \sqrt{b'^2 - 4a'c'}\right)}{\partial k} \right]}{\left(-b' - \sqrt{b'^2 - 4a'c'}\right)^2}$$

$$= \frac{1}{b' + \sqrt{b'^2 - 4a'c'}} \left\{ (2f_c') + \left[\left(\frac{2c'}{\sqrt{b'^2 - 4a'c'}} \right) \left(\frac{2C}{\sqrt{3}} \sin\left(\theta + \frac{2\pi}{3}\right) \right) \right] \right\}$$

- Derivative of internal parameters with respect to softening parameter (r)

$$\frac{\partial x'}{\partial r} = f_t[(2\alpha - 1)\beta - 2] \frac{\partial \sqrt{J_{2,1}}}{\partial r}$$

$$\frac{\partial y'}{\partial r} = f_t^2\left[8 - 2\beta(2\alpha - 1) - \beta^2(2\alpha - 1)^2\right]\frac{\partial\sqrt{J_{2,1}}}{\partial r}$$

$$\frac{\partial z'}{\partial r} = 3f_t^3[1 - (2\alpha - 1)\beta][(2\alpha - 1)\beta - 2]\frac{\partial\sqrt{J_{2,1}}}{\partial r}$$

$$\frac{\partial d}{\partial r} = 0$$

$$\frac{\partial\sqrt{J_{2,1}}}{\partial r} = \left[\left(\frac{2}{\left(b' + \sqrt{b'^2 - 4a'c'}\right)}\right) + \left(\frac{4a'}{\left(b' + \sqrt{b'^2 - 4a'c'}\right)^2\sqrt{b'^2 - 4a'c'}}\right)\right](1 - \mathrm{Imp})f_c'$$

- Derivative of internal parameters with respect to softening parameter (s)

$$\frac{\partial x'}{\partial s} = f_t[(2\alpha - 1)\beta - 2]\frac{\partial\sqrt{J_{2,1}}}{\partial s}$$

$$\frac{\partial y'}{\partial s} = f_t^2\left[8 - 2\beta(2\alpha - 1) - \beta^2(2\alpha - 1)^2\right]\frac{\partial\sqrt{J_{2,1}}}{\partial s}$$

$$\frac{\partial z'}{\partial s} = 3f_t^3[1 - (2\alpha - 1)][(2\alpha - 1)\beta - 2]\frac{\partial\sqrt{J_{2,1}}}{\partial s}$$

$$\frac{\partial d}{\partial s} = 0$$

$$\frac{\partial\sqrt{J_{2,1}}}{\partial s} = \left[\left(\frac{2}{\left(b' + \sqrt{b'^2 - 4a'c'}\right)}\right) + \left(\frac{4a'}{\left(b' + \sqrt{b'^2 - 4a'c'}\right)^2\sqrt{b'^2 - 4a'c'}}\right)\right](\mathrm{Imp})f_c'$$

C.10 Derivative of potential function with respect to stress tensors ($\partial g_T / \partial\boldsymbol{\sigma}$)

$$\frac{\partial g_T}{\partial\boldsymbol{\sigma}} = \frac{\partial}{\partial\boldsymbol{\sigma}}\left(a_T\frac{I_1}{\sqrt{3}} + \sqrt{2J_2} - c_T\right)$$

$$\frac{\partial g_T}{\partial\boldsymbol{\sigma}} = \frac{a_T}{\sqrt{3}}\boldsymbol{\delta} + \frac{1}{\sqrt{2J_2}}\mathbf{S}$$

C.11 Consistency Parameter for Tension

By assuming that the material in the elastic range to be linearly isotropic as in the compression, the first term in denominator of the consistency parameter equation becomes

$$\frac{\partial F_T}{\partial \boldsymbol{\sigma}} : \mathbf{C} : \frac{\partial g_T}{\partial \boldsymbol{\sigma}} = \frac{\partial F_T}{\partial \sigma_{ij}} C_{ijkl} \frac{\partial g_T}{\partial \sigma_{kl}}$$

$$= \left(A'_1 \delta_{ij} + A'_2 S_{ij} + A'_3 t_{ij}\right) \left(2G\left[\frac{1}{2}\left(\delta_{ik}\delta_{jl} + \delta_{il}\delta_{jk}\right) + \frac{\nu}{1-2\nu}\delta_{ij}\delta_{kl}\right]\right) \left(\frac{a_T}{\sqrt{3}}\delta_{kl} + \frac{1}{\sqrt{2J_2}} S_{kl}\right)$$

$$\frac{\partial F_T}{\partial \boldsymbol{\sigma}} : \mathbf{C} : \frac{\partial g_T}{\partial \boldsymbol{\sigma}} = 2G\left[A'_1 a_T \frac{(1+\nu)}{(1-2\nu)} + A'_2\sqrt{2J_2} + A'_3\left(\frac{3J_3}{\sqrt{2J_2}}\right)\right]$$

Now consider the last two term containing A'_2 and A'_3 terms,

$$A'_2\sqrt{2J_2} + A'_3\left(\frac{3J_3}{\sqrt{2J_2}}\right) = \left[[*]\left(\frac{3\sqrt{3}}{4\cos(3\theta)} \frac{J_3}{J_2^{\frac{5}{2}}}\right) - \frac{1}{2}\frac{d}{\sqrt{J_2}}\right]\sqrt{2J_2} + \left[[*]\left(-\frac{\sqrt{3}}{2\cos(3\theta)} \frac{1}{J_2^{\frac{3}{2}}}\right)\right]\left(\frac{3J_3}{\sqrt{2J_2}}\right)$$

$$= -\frac{d}{\sqrt{2}}$$

Therefore, the first equation of denominator in consistency parameter equation becomes

$$\frac{\partial F_T}{\partial \boldsymbol{\sigma}} : \mathbf{C} : \frac{\partial g_T}{\partial \boldsymbol{\sigma}} = 2G\left[A'_1 a_T \sqrt{3} \frac{(1+\nu)}{(1-2\nu)} - \frac{d}{\sqrt{2}}\right]$$

By Substituting $\partial g_T / \partial \boldsymbol{\sigma}$ into the second term of denominator in consistency parameter equation, it becomes

$$\frac{\partial F_T}{\partial \varepsilon_p} \sqrt{\frac{2}{3} \frac{\partial g_T}{\partial \boldsymbol{\sigma}} : \frac{\partial g_T}{\partial \boldsymbol{\sigma}}} = \left(B'_1 H'_1 + B'_2 H'_2 + B'_3 H'_3\right) \sqrt{\frac{2}{3}\left(a_T^2 + 1\right)}$$

BIBLIOGRAPHY

BIBLIOGRAPHY

1. ACI Committee 318, Building Code Requirements for Reinforced Concrete and Commentary, ACI 319R-05, American Concrete Institute, Farmington Hills, 2005

2. Ahmad, S. H., and Shah, S. P., "Complete Triaxial Stress-Strain Curves for Concrete," ASCE Journal of Structural Division, Vol. 108, No. ST4, Apr 1982, pp. 728-742

3. Aifantis, E. C., "The Physics of Plastic Deformation," International Journal of Plasticity, Vol. 3, 1987, pp. 211-247

4. Aifantis, E.C., "On the Role of Gradients in the Localization of Deformation and Fracture," International Journal of Engineering Science, Vol. 30, No. 10, Oct 1992, pp. 1279-1299

5. Alwan, J.M., Naaman, A.E., and Hansen, W., "Pull-out Work of Steel Fibers from Cementitious Composites: Analytical Investigation," Cement and Concrete Composites, Vol. 13, No. 4, 1991, pp. 247-255

6. Alwan, J. M., Modeling of the Mechanical Behavior of Fiber-reinforced Cement Based Composites under Tensile Loads, Ph.D. Dissertation, University of Michigan, Ann Arbor, 1994

7. American Association of State Highway and Transportation Officials, AASHTO LRFD Specification for Highway Bridge Design, Washington, D. C., 2000

8. ASTM International, "Standard test method for preparation and testing of controlled low strength material (CLSM) test cylinders D4832-02," ASTM International, 1-5

9. Balana, T.A., Spacone, E., and Kwon, M., "A 3D Hypoplastic Model for Cyclic Analysis of Concrete Structures," Journal of Engineering Structures, Vol. 23 (4), Apr 2001, pp. 333-342

10. Baluch, M. H., Qureshy, A. B., and Azad, A. K., "Fatigue Crack Propagation in Plain Concrete," Society for Experimental Mechanics Inc, 1987, pp. 112-119

11. Barzegar, F., and Maddipudi, S., "Three-dimensional modeling of concrete structures I: Plain concrete," Journal of Structural Engineering, Vol. 123, No. 10, Oct 1997, pp. 1339-1346

12. Bazant, Z. P., "Microplane Model for Strain-Controlled Inelastic Behavior," Mechanics of Engineering Materials, International Conference on Constitutive Laws for Engineering Materials: Theory and Application, Tucson, AZ, USA , 1984, pp. 45-59

13. Bazant, Z. P., Adley, M. D., and Xiang, Y. "Finite Strain Analysis of Deformations of Quasibrittle Material during Missile Impact and Penetration," Advances in Failure Mechanisms in Brittle Materials, Vol. 75, 1996, pp. 163-169

14. Bazant, Z. P., Caner, F. C., Carol, I., and Adley, M. D., and Akers, S. A., "Microplane Model M4 for concrete I: Formulation with Work-Conjugate Deviatoric Stress," Journal of Engineering Mechanics, Vol. 126, No. 9, Sep 2000, pp. 944-953

15. Bazant, Z. P., and Oh, B. H., "Microplane Model for Progressive Fracturing," Proceedings of the 4th Engineering Mechanics Division Specialty Conference, Indiana, USA, Vol. 2, 1983, pp. 956-959

16. Bazant, Z. P., and Oh, B. H., "Microplane Model for Progressive Fracture of Concrete and Rock," Journal of Engineering Mechanics, Vol. 111, No. 4, April 1985, pp. 559-582

17. Bazant, Z. P., and Ozbolt, J., "Nonlocal Microplane Model for Fracture, Damage, and Size Effect in Structures," Journal of Engineering Mechanics, Vol. 116, No. 11, Nov 1990, pp. 2485-2505

18. Bazant, Z. P., and Prat, P. C., "Microplane Model for Brittle-Plastic Material: I. Theory," Journal of Engineering Mechanics, Vol. 114, No. 10, Oct 1988, pp. 1672-1688

19. Bazant, Z. P., and Schell, W. F., "Fatigue Fracture of High-Strength Concrete and Size Effect," ACI Materials Journal, Vol. 90, No. 5, Sep-Oct 1993, pp. 472-478

20. Bazant, Z. P., and Tsubaki, T., "Total Strain Theory and Path-Dependence of Concrete," Journal of Engineering Mechanics, Vol. 106, No. 6, December 1980, pp. 1151-1173

21. Bazant, Z. P.,and Xu, K., "Size Effect in Fatigue Fracture of Concrete," ACI Materials Journal, Vol. 88, No. 4, Jul-Aug 1991, pp. 390-399

22. Benssousan, A., Lions, J. L., and Papanicoulau, G., Asymptotic Analysis for Periodic Structures, North-Holland, Amsterdam, 1978, 700 pages

23. Bolander, J. E. Jr., and Saito, S., "Discrete Modeling of Short-fiber Reinforcement in Cementitious Composites," Advanced Cement Based Materials, Vol. 6, No. 3-4, Oct-Nov 1997, pp. 76-86

24. Carol, I., Part, P. C., and Bazant Z. P., "New Explicit Microplane Model for Concrete: Theoretical Aspects and Numerical Implementation," International Journal of Solids and Structures, Vol. 29, No. 9, 1992, pp. 1173-1191

25. Chandrangsu, K., Innovative bridge deck with reduced reinforcement and strain-hardening fiber reinforced cementitious composites, Ph.D. Dissertation, University of Michigan, Ann Arbor, 2003

26. Chang, T. Y., Taniguchi, H., and Chen, W. F., "Nonlinear Finite Element Analysis of Reinforced Concrete Panels," Journal of Structural Engineering, Vol. 113, No. 1, January 1987, pp. 122-140

27. Chen, A. C. T., and Chen, W. F., "Constitutive Relations for Concrete," Journal of Engineering Mechanics Division, Vol. 101, No. 4, August 1975, pp. 465-481

28. Chen, W. F., Plasticity in Reinforced Concrete, McGraw-Hill Education, January 1982, 474 pages

29. Cofer, W. F., and Kohut, S. W., "A General Nonlocal Microplane Concrete Material Model for Dynamic Finite Element Analysis," Computers and Structures, Vol. 53, No. 1, October 1994, pp. 189-99

30. de Borst, R. Pamin, J., Peerlings, R.H.J., and Sluys, L.J., "On Gradient-Enhanced Damage and Plasticity Models for Failure in Quasi-Brittle and Frictional Materials," Computational Mechanics, Vol. 17, No. 1-2, Dec. 1995, pp. 130-141

31. Demeke, A., and Tegos, I.A., "Steel Fiber Reinforced Concrete in Biaxial Stress Tension-Compression Conditions," ACI Materials Journal, Vol. 91, No. 5, Sept-Oct 1994, pp. 579-584

32. DiMaggio, F.L., and Sandler, I. S., "Material Model for Granular Soils," Journal of Engineering Mechanics Division, Vol. 97, No. EM3, 1971, pp. 935-950

33. Feenstra, P. H.; Rots, J. G.; Arnesen, A.; Teigen, J. G.; and Hoiseth, K. V., "A 3D Constitutive Model for Concrete Based on Co-Rotational Concept," Computational Modelling of Concrete Structures, R. de Borst, N. Bióanió, H. Mang, and G. Meschke, eds., Proceedings of the EURO-C 1998 Conference on Computational Modelling of Concrete Structures, Austria, pp. 13-22.

34. Gabet, T., Vu, X.H., Malecot, Y., and Daudeville, L., "A New Experimental Technique for the Analysis of Concrete under High Triaxial Loading," Journal de Physique IV (Proceedings), Vol. 134, Aug. 2006, pp. 635-40

35. Geudes, J. M., Nonlinear Computational Models for Composites Materials using Homogenization, Ph.D. Dissertation, University of Michigan, Ann Arbor, 1990

36. Grassl, P., Lundgren, K., and Gylltoft, K., "Concrete in Compression: a Plasticity Theory with a Novel Hardening Law," International Journal of Solids and Structures, Vol. 39, No. 20, October 2002, pp. 5205-5223

37. Grassl, P., “Modelling of Dilation of Concrete and its Effect in Triaxial Compression,” Finite Elements in Analysis and Design, Vol. 40, No. 9-10, June 2004, pp. 1021-1033

38. Griffith, A. A., “The Phenomena of Rupture and Flow in Solids,” Philosophical Transactions, Series A, Vol. 221, 1920, pp. 163-198

39. Hallquist, J. O., LS-DYNA Keyword User’s Manual Version 971, May 2007, 2206 pages

40. Han, T.S., Feenstra, P.H., and Billington, S.L., “Simulation of Highly Ductile Cement-based Composites”, ACI Structural Journal, 100(6), 2003, pp. 749-757

41. Hill, R., the Mathematical Theory of Plasticity, Oxford, Clarendon Press, 1950, 356 pages

42. Hillerborg, A., Modéer, M., and Petersson, P. E., “Analysis of crack formation and crack growth in concrete by means of fracture mechanics and finite elements,” Cement and Concrete Research, Vol. 6, No. 6, November 1976, pp. 773-781

43. Hodge, P.G., “A new method of analyzing stresses and strains in work hardening plastic solids,” Journal of Applied Mechanics, Vol. 24, 1957, pp. 482–483

44. Hsieh, S. S., Ting, E. C., and Chen, W. F., “Elastic-Fracture Model for Concrete,” Proceeding ASCE Engineering Mechanics Division Specification Conference, 3rd, Austin, TX, USA, Sep. 17-19 1979, pp. 437-440

45. Hu, X. D., Day, R., and Dux, P., “Biaxial Failure Model for Fiber Reinforced Concrete,” Journal of Material in Civil Engineering, Vol. 15, No. 6, Dec 2003, pp. 609-615

46. Hutchinson, J. W., :Singular Behavior at the End of a Tensile Crack Tip in a Hardening Material,” Journal of the Mechanics and Physics of Solids, Vol. 16, 1968, pp. 13-31

47. Hussein, A., and Marzouk, H., “Behavior of High-Strength Concrete under Biaxial Stresses,” ACI Materials Journal, Vol. 97, No. 1, Jan/Feb 2000, pp. 27-36

48. Imran, I., Applications of Non-Associated Plasticity in Modelling the Mechanical Response of Concrete, Ph.D. Thesis, University of Toronto, Canada, 1994

49. Imran, I., and Pantazopoulou, S.J., “Experimental Study of Plain Concrete unde Triaxial Stress,” ACI Materials Journal, Vol. 93, No. 6, Nov-Dec 1996, pp. 589-601

50. Imran, I., and Pantazopoulou, S. J., “Plasticity Model for Concrete under Triaxial Compressions,” Journal of Engineering Mechanics, Vol. 127, No.3, March 2001, pp. 281-290

51. Irwin, G. R., "Onset of Fast Crack Propagation in High Strength Steel and Aluminum Alloys," Sagamore Research Conference Proceedings, Vol. 2, 1956, pp. 289-305

52. Kabele, P., "New Development in Analytical Modeling of Mechanical Behavior of ECC," Journal of Advanced Concrete Technology, V. 1, No. 3, November 2003, pp. 253-264

53. Kanda, T., and V.C. Li, "Interface Property and Apparent Strength of a High Strength Hydrophilic Fiber in Cement Matrix," ASCE Journal Materials in Civil Engineering, Vol. 10, No. 1, 1998, pp. 5-13

54. Kim, J. K., Yi, S. T., Park, C. K., and Eo, S. H., "Size Effect on Compressive Strength of Plain and Spirally Reinforced Concrete Cylinders," ACI Structural Journal, Vol. 96, No. 1, Jan-Feb 1999, pp. 88-94

55. Krajcinovic, D., "Constitutive Theory of Damaging Materials," ASME Journal of Applied Mechanics, Vol. 50, 1983, pp. 355-360

56. Kupfer, H., Hilsdorf, H. K., Rusch, H., "Behavior of Concrete under Biaxial Stresses," ACI Journal, Vol. 66, No. 8, Aug. 1969, pp. 656-66

57. Lade, P.V., "Three-parameter Failure Criterion for Concrete," Journal of the Engineering Mechanics Division, Vol. 108, No. EM5, October 1982, pp. 850-863

58. Lan, S., and Guo, Z., "Biaxial Compression Behavior of Concrete under Repeated Loading," Journal of Material in Civil Engineering, Vol. 11, No. 2, 1999, pp. 105-115

59. Lan, S., and Guo, Z., "Experimental Investigation of Multiaxial Compressive Strength of Concrete under Different Stress Paths," ACI Materials Journal, Vol. 94, No. 5, Sep-Oct 1997, pp. 427-434

60. Lee, S. K., Song, Y. C., Han, S. H., "Biaxial Behavior of Plain Concrete of Nuclear Containment Building," Nuclear Engineering and Design, Vol. 227, No. 2, Jan. 2004, pp. 143-153

61. Leguillon, D., and Sánchez-Palencia, E., "Fracture in Heterogeneous Material Weak and Strong Singularities," P. Ladeveze and O. C. Zienkiewicz ed. New Advances in Computational Structural Mechanics, Amsterdam, Elsevier, 1992

62. Lemaitre, J., A Course on Damage Mechanics, Springer, 2nd rev., 1992, 228 pages.

63. Leung, C. K. Y., and Geng, P. Y., "Micromechanical modeling of softening behavior in steel fiber reinforced cementitious composites," International Journal of Solids and Structures, Vol. 35, No. 31-32, November 1998, pp. 4205-4222

64. Li, Q., and Ansari, F., "Mechanics of Damage and Constitutive Relationships for High-Strength Concrete in Triaxial Compression," Journal of Engineering Mechanics, Vol. 125, No. 1, Jan 1999, pp. 1-10

65. Li, V.C., Chan, C.M., and Leung, C.K.Y., "Experimental Determination of the Tension-softening Curve in Cementitious Composites," Cement and Concrete Research, Vol. 17, No.3, 1987, pp. 441-452

66. Liu, J., and Foster, S. J., "A Three-Dimensional Finite Element Model for Confined Concrete Structures," Computers & Structures, Vol. 77, No. 5, 2000, pp. 441-51

67. Li, V.C., and Leung, C.K.Y., "Steady State and Multiple Cracking of Short Random Fiber Composites," ASCE Journal of Engineering Mechanics, Vol. 188, No. 11, 1992, pp. 2246-2264

68. Lin, G., Lu, J., Wang, Z., and Xiao, S., "Study on the Reduction of Tensile Strength of Concrete due to Triaxial Compressive Loading History," Magazine of Concrete Research, Vol. 54, No. 2, April 2002, pp. 113-124

69. Li, V.C., Wang, Y., and Becker, S., "A Micromechanical Model of Tension-Softening and Bridging Toughening of Short Random Fiber Reinforced Brittle Matrix Composites," Journal Mechanics and Physics of Solids, Vol. 39, No. 5, 1991, pp. 607-625

70. Lokuge, W.P., Sanjayan, J.G., and Setunge, S., "Triaxial Test Results of High-Strength Concrete Subjected to Cyclic Loading," Magazine of Concrete Research, Vol. 55, No. 4, August 2003, pp. 321-329

71. Maalej, M., and Li, V.C., "Introduction of Strain Hardening Engineered Cementitious Composites in the Design of Reinforced Concrete Flexural Members for Improved Durability," ACI Structural Journal, Vol. 92, No. 2, March-April 1995, pp. 167-176

72. Mahboubi, A., and Ajorloo, A., "Experimental Study of the Mechanical Behavior of Plastic Concrete in Triaxial Compression," Cement and Concrete Research, Vol. 35, No. 2, Feb. 2005, pp. 412-19

73. Moraes and Nicholson, "Simulation of projectile impact using continuum damage mechanics", ASME Pressure Vessels and Piping Conference, 2001, pp. 39-46

74. Marshall, D.B., and Cox, B.N., "J-Integral Method for Calculating Steady-State Matrix Cracking Stresses in Composites," Mechanics of Materials, Vol. 7, No. 2, Nov 1988, pp. 127-133

75. Minelli, F., and Vecchio, F. J., "Compression Field Modeling of Fiber-reinforced Concrete Members under Shear Loading," ACI Structural Journal, Vol. 106, No. 2, March/April 2006, pp. 244-252

76. Naaman, A. E., Reinhardt, H. W., "Characterization of High Performance Fiber Reinforced Cement Composites," High Performance Fiber Reinforced Cement Composites (HPFRCC 2), Edited by Naaman, A. E., and Reinhardt, H. W., 1996,1-23

77. Needleman, A., "Material Rate Dependence and Mesh Sensitivity in Localization Problems," Computer Methods in Applied Mechanics and Engineering, Vol. 67, No. 1, Mar 1988, pp. 69-85

78. Ngo, D., A Network Topological Approach to Finite Element Analysis of Progressive Crack Growth in Concrete Members, Ph. D. Thesis, University of California, Berkeley, 1975

79. Ngo, D., and Scordelis, A.C., "Finite element analysis of reinforced concrete beams," ACI Journal, Vol. 64, No. 3, Mar 1967, pp. 152-163

80. Ohtani, Y. C., and Chen, W. F., "Hypoelastic-Perfectly Plastic Model for Concrete Materials," Journal of Engineering Mechanics, Vol. 113, No. 2, December 1987, pp. 1840-1860

81. Olesen, J. F., "Fictitious Crack Propagation in Fiber-Reinforced Concrete Beams," Journal of Engineering Mechanics, V. 127, No. 3, March 2001, pp. 272-280

82. Ottosen, N. S., "a Failure Criterion for Concrete," Journal of Engineering Mechanics Division, Vol. 103, No. 4, August 1977, pp. 527-535

83. Ottosen, N. S. and Ristinmaa, M., The Mechanics of Constitutive Modeling, Elsevier Science, July 2005, 700 pages.

84. Ouyang, C., and Shah, S. P., "Toughening of High Strength Cementitious Matrix Reinforced by Discontinuous Short Fibers," Cement and Concrete Research, Vol. 22, No. 6, Nov 1992, pp. 1201-1215

85. Pantazopoulou, S.J., and Zanganeh, M., "Triaxial Tests of Fiber-Reinforced Concrete," Journal of Materials in Civil Engineering, Vol. 13, No. 5, Sept/Oct 2001, pp. 340-348

86. Paris, P., and Erdogan, F., "Critical Analysis of Crack Propagation Laws," ASME Transactions Journal of Basic Engineering, Vol. 85, No. 4, December 1963, pp. 528-534

87. Parra-Montesinos, G. J., *Seismic behavior, strength and retrofit of exterior RC column-to-steel beam connections*, Ph.D. Dissertation, University of Michigan, Ann Arbor, 2000

88. Parra-Montesinos, G.J., Canbolat, B. A., and Jeyaraman, G. R., "Relaxation of Confinement Reinforcement Requirements in Structural Walls Through the Use of

Fiber Reinforced Cement Composites," *8th National Conference on Earthquake Engineering, San Francisco*, CA, April 2006

89. Perdikaris, P. C., and Calomino, A. M., "Crack Growth in Concrete under Fatigue," Soc for Experimental Mechanics Inc, 1986, pp. 1-6

90. Peerlings, R.H.J., de Borst, R., Brekelmans, W.A.M., and Geers, M.G.D., "Gradient-Enhanced Damage Modelling of Concrete Fracture," Mechanics of Cohesive-Frictional Materials, Vol. 3, No. 4, Oct. 1998, pp. 323-342

91. Pijaudier-Cabot, G., and Bazant, Z. P., "Nonlocal Damage Theory," Journal of Engineering Mechanics, Vo. 113, No. 10, Oct. 1987, pp. 1512-1533

92. Pivonka, P., Lacknew, R., and Mang, H. A., "Concrete Subjected to Triaxial Stress States: Application to Pull-Out Analyses," Journal of Engineering Mechanics, Vol. 130 (12), December 2004, pp. 1486-1498

93. Prager, W., "A new method of analyzing stresses and strains in work hardening plastic solids," Journal of Applied Mechanics, 23, 1956, pp. 493–496

94. Reis, J. M. L., Ferreira, A. J. M., "The Influence of Notch Depth on the Fracture Mechanics Properties of Polymer Concrete," International Journal of Fracture, Vol. 124, No. 1-2, November 2003, pp. 33-42

95. Rice, J. R., "A Path Independent Integral and the Approximate Analysis of Strain Concentration by Notches and Cracks," Journal of Applied Mechanics, Vol. 35, 1968, pp. 379-386

96. Rice, J. R., and Rosengren, G. F., "Plane Strain Deformation near a Crack Tip in a Power-Law Hardening Material," Journal of the Mechanics and Physics of Solids, Vol. 16, 1968, pp. 1-12

97. Sánchez-Palencia, E., Nonhomogeneous Media and Vibration Theory, Lecture Notes in Physics vol. 127, Springer-Verlag, Berlin, 1980

98. Schreyer, H. L., and Babcock, S. M., "Third-Invariant Plasticity for Low-Strength Concrete," Journal of Engineering Mechanics, Vol. 111, No. 4, April 1985, pp. 545-558

99. Schwer, L. E., and Murray, Y. D., "Three-invariant smooth cap model with mixed hardening," International Journal for Numerical and Analytical Methods in Geomechanics, Vol. 18, No. 10, Oct 1994, pp. 647-688

100. Schwer, L. E., "Geomaterial Modeling with LS-DYNA" Geomaterial Modeling Course Pack, LSTC, 2002, 250 pages

101. Seow, P. E. C., and Swaddiwudhipong, S., "Failure Surface for Concrete under Multiaxial Load – a Unified Approach," Journal of Material in Civil Engineering, Vol. 17, No. 2, March-April 2005, pp. 219-228

102. Sfer, D, Carol, I., Gettu, R., and Etse, G., "Study of the Behavior of Concrete under Triaxial Compression," Journal of Engineering Mechanics, Vol. 128, No. 2, February 2002, pp. 156-163

103. Shah, S. P., and Jeng, Y. S., "Fracture Resistance of Steel Fiber Reinforced Concrete," Swedish Cement & Concrete Research Inst, 1985, pp. 273-297

104. Simo, J.C., "A Framework for Finite Strain Elastoplasticity based on Maximum Plastic Dissipation and the Multiplicative Decomposition. I. Continuum Formulation," Computer Methods in Applied Mechanics and Engineering, Vol. 66, No. 2, Feb. 1988, pp. 199-219

105. Simo, J. C. and Hughes, T. J. R., Computational Inelasticity (Interdisciplinary Applied Mechanics) Vol. 7, Springer, July 2000, 392 pages.

106. Simo, J. C., and Ju, J. W., "Strain- and stress-based continuum damage models: I. Formulation," International Journal of Solids and Structures, Vol. 23, No. 7, 1987, pp. 821-840

107. Simo, J. C., Ju, J., Pister, K. S., and Taylor, R. L., "Assessment of Cap Model: Consistent Return Algorithms and Rate-Dependent Extension," Journal of Engineering Mechanics, Vol. 114, No. 2, Feb 1988, pp. 191-218

108. Sluys, L.J., and de Borst, R., "Wave Propagation and Localization in a Rate-Dependent Cracked Medium-Model Formulation and One-Dimensional Examples," International Journal of Solids and Structures, Vol. 29, No. 23, 1992, pp. 2945-58

109. Smith, S. S., William, K. J., Gerstle, K. H., and Sture, S., "Concrete over the Top, or: Is There Life After Peak?," ACI Material Journal, Vol. 86, No. 5, September-October 1989, pp. 491-497

110. Soranakom, C., and Mobasher, B., "Flexural Modeling of Strain Softening and Strain Hardening Fiber Reinforced Concrete," High Performance Fiber Reinforced Cement Composites (HPFRCC 5), Mainz, Germany, July 2007, pp. 155-164

111. Spoelstra, M. R., and Monti, G., " FRP-Confined Concrete Model," Journal of Composites for Construction, Vol. 3, No. 3, 1999, pp. 143-150

112. Stang, H., Li, Z., and Shah, S. P., "Pullout Problem Stress versus Fracture Mechanic Approach," Journal of Engineering Mechanics, Vol. 116, No. 10, October 1990, pp. 2136-2150

113. Stang, H., and Olesen, J. F. "On the interpretation of bending tests on FRC-materials" Fracture Mechanics of Concrete Structures, Vol.1, 1998, pp. 511-520

114. Su, E. C. M., and Hsu, T. T. C., "Biaxial Compression Fatigue and Discontinuity of Concrete," ACI Material Journal, Vol. 85, No. 3, May-Jun 1988, pp. 178-188

115. Subramaniam, K. V., and Shah, S. P., "Biaxial Tension Fatigue Response of Concrete," Cement and Concrete Composites, Vol. 25, No. 6, August 2003, pp. 617-623

116. Sujivorakul, C., Development of High Performance Fiber Reinforced Cement Composites using Twisted Polygonal Steel Fibers, Ph.D. Dissertation, University of Michigan, Ann Arbor, 2002

117. Tavarez, F. A., Simulation of Behavior of Composite Grid Reinforced Concrete Beams using Explicit Finite Element Methods, Master Thesis, University of Wisconsin, Madison, 2001

118. Torrenti, J.M., and Djebri, B., "Behaviour of Steel-Fibre-Reinforced Concretes under Biaxial Compression Loads," Cement and Concrete Composites, Vol. 17, No. 4, 1995, pp. 261-266

119. Toutanji, H.A., El-Korchi, T., Katz, R.N., and Leatherman, G.L., "Behavior of Carbon Fiber Reinforced Cement Composites in Direct Tension," Cement and Concrete Research, Vol. 23, No. 3, May 1993, pp. 618-626

120. Triantafyllidis, N. and Maker, B., "On the Comparison between Microscopic and Macroscopic Instability Mechanisms in a Class of Fiber Reinforced Composites," Journal of Applied Mechanics, 52, 1985, pp. 794-800

121. Tschegg, E.K., Elser, M., and Stanzl-Tschegg, S.E., "Biaxial Fracture Tests on Concrete - Development and Experience," Cement & Concrete Composites, Vol. 17, No. 1, 1995, pp. 57-75

122. Van Mier, J.G.M., and Van Vliet, M.R.A., "Uniaxial Tension Test for the Determination of Fracture Parameters of Concrete: State of the Art," Engineering Fracture Mechanics, Vol. 69, No. 2, Dec. 2002, pp. 235-247

123. Van Vliet, M.R.A., and Van Mier, J.G.M., "Experimental Investigation of Concrete Fracture under Uniaxial Compression," Mechanics of Cohesive-Frictional Materials, Vol. 1, No. 1, Jan. 1996, pp. 115-127

124. Well, A. A., "Unstable Crack Propagation in Metals: Cleavage and Fast Fracture," Proceeding of the Crack Propagation Symposium, Vol. 1, Paper 84, Cranfield, UK, 1961

125. Wu, J.F., Shephard, M. S., Dvorak, G. J., and Bahei-El Din, Y.A., "A Material Model for the Finite Element Analysis of the Metal Matrix Composites," Journal of Computer Science and Technology, 35, 347, 1989

126. Yan, D., and Lin, G., “Dynamic Behavior of Concrete in Biaxial Compression,” Magazine of Concrete Research, Vol. 59, No. 1, Jan. 2007, pp. 45-52

127. Yin, W.S., Su, E. C. M., Mansur, M.A., and Hsu, T. T. C., “Biaxial Tests of Plain and Fiber Concrete,” ACI Materials Journal, Vol. 86, No. 3, May-June 1989, pp. 236-243

128. Ziegler, H., “A modification of Prager's hardening rule,” Quarterly of Applied Mechanics, Vol. 17, 1959, pp. 55–65

129. Zhang, J., Li, V.C., and Stang, H., “Size Effect on Fatigue in Bending of Concrete,” Journal of Materials in Civil Engineering, Vol. 13, No. 6, November /December 2001, pp. 446-453